Adsorption/diffusion interplay in hierarchical zeolites : understanding the role of external surface and additional porosity

Izabel Cristina Medeiros Costa

N°d'ordre NNT : 2019LYSE1022

THESE de DOCTORAT DE L'UNIVERSITE DE LYON

opérée au sein de

l'Université Claude Bernard Lyon 1

Ecole Doctorale N° ED206

Ecole Doctorale de Chimie de l'Université Lyon

IFP Energies Nouvelles, Direction Catalyse et Séparation

Département Séparation

Spécialité de doctorat : Chimie

Soutenue publiquement le 28/02/2019, par :

Izabel Cristina Medeiros Costa

Adsorption/diffusion interplay in hierarchical zeolites: Understanding the role of external surface and additional porosity

---

Devant le jury composé de :

M. Jallut, Christian	Professeur Université Lyon 1	Président
M. Denayer, Joeri	Professeur Université de Bruxelles (Belgique)	Rapporteur
Mme. Mintova, Svetlana	DR CNRS ENSICAEN	Rapporteure
Mme. Bourrelly, Sandrine	MC Aix-Marseille Université	Examinatrice
Mme. Lebeau, Bénédicte	DR CNRS Université de Haute Alsace	Examinatrice
Mme. Laroche, Catherine	Ingénieure de Recherche IFPEN	Directrice de thèse
M. Coasne, Benoit	DR CNRS Université Grenoble Alpes	Co-directeur de thèse
M. Perez Pellitero, Javier	Ingénieur de Recherche IFPEN	Promoteur de thèse

Title: Adsorption/diffusion interplay in hierarchical zeolites: Understanding the role of external surface and additional porosity

Abstract

The performance of xylene separation processes using nanoporous adsorbents is related to both the transport and selectivity properties of the used faujasite zeolites (BaX). Conventional zeolites exhibit a large volume of micropores and a good selectivity to paraxylene (*px*). However, intracrystalline diffusion is a slow process which limits the efficiency of the zeolites. Therefore, the use of hierarchical zeolites has been proposed as an alternative to improve transport properties by the introduction of an additional porous network. In this thesis, two types of BaX hierarchical zeolites are considered: Nanoparticles aggregates (NA - aggregates of small particles with mesopores between them) and Layer-like zeolite (LL - array of zeolite layers, with the presence of inter and intra-layers mesopores). In order to better understand the role played by the external surface and by the additional porosity in hierarchical zeolites (NA and LL), these zeolites were characterized in terms of quantity and quality of the external surface by the application of different characterization techniques (X-ray diffraction, N_2 adsorption, porosimetry, microscopy, infrared and nuclear magnetic resonance). The xylene adsorption and diffusion were evaluated in gas and liquid phase, by means of thermogravimetry and batch experiments, respectively. Through the experiments in liquid phase, it is noticed that the xylene diffusion in hierarchical zeolites is considerably improved. On the other hand, a significant loss in *px*-selectivity in hierarchical BaX zeolites is observed compared to conventional BaX zeolites. The study of diffusion in gas phase allowed the identification of surface barriers, which are not present in the liquid phase. This may be an indication that, when the concentration around the surface is large (liquid phase), the passage of molecules across the surface is less/not disturbed. This reinforces the interest of using hierarchical zeolite for xylene separation which is carried out in liquid phase.

Titre: Couplage entre adsorption et diffusion dans les zéolithes à porosité hiérarchisée: Effet de la surface externe et de la porosité supplémentaire

Résumé

La performance des procédés de séparation des xylènes utilisant des adsorbants nanoporeux est liée aux propriétés de transport et de sélectivité des zéolithes faujasite du type BaX. Les zéolithes conventionnelles présentent un grand volume de micropores et une bonne sélectivité vis-à-vis du paraxylène. Cependant, la diffusion intracristalline est un processus lent qui limite l'efficacité des zéolithes. Par conséquent, l'utilisation de zéolithes hiérarchiques a été proposée comme alternative pour améliorer les propriétés de transport par l'introduction d'un réseau poreux supplémentaire. Dans cette thèse, deux types de zéolithes hiérarchiques BaX sont considérés: les agrégats de nanoparticules (NA - des agrégats de petites particules avec des mésopores entre eux) et les zéolithes *Layer-Like* (LL), formées par un réseau de couches zéolitiques (présentant des mésopores entre les couches et au sein des couches). Afin de mieux comprendre le rôle joué par la surface externe et par la porosité supplémentaire dans les zéolithes hiérarchiques (NA et LL), ces zéolithes ont été caractérisées en termes de quantité et de qualité de la surface externe par différentes techniques de caractérisation (diffraction des rayons X, adsorption de N_2, porosimétrie, microscopie, infrarouge et résonance magnétique nucléaire). L'adsorption et la diffusion des xylènes ont été évaluées par thermogravimétrie et par batch, en phase gazeuse et liquide, respectivement. Les expériences réalisées en phase liquide permettent d'observer une amélioration importante de la diffusion des xylènes dans les zéolithes hiérarchiques. Néanmoins, une perte significative de la para-sélectivité dans les zéolites BaX hiérarchiques est observée par rapport aux zéolites BaX conventionnelles. L'étude de la diffusion en phase gazeuse a permis d'identifier des barrières de surface, qui sont absentes en phase liquide. Cela peut indiquer qu'à forte concentration , le passage des molécules à travers la surface est moins perturbé. Ceci renforce l'intérêt d'utiliser les zéolithes hiérarchiques pour la séparation des xylènes qui est opérée en phase liquide.

Acknowledgment

I would like to thank the catalysis and separation direction at IFPEN for allowing me to carry out this thesis. Especially Julia, the head of the separation department. I thank my supervisors, who have always been willing to help … without whom this work would not be possible. I thank them for believed in me and for the encouragement and sympathy. I also thank the jury members for accepting the mission to contribute to the improvement of this work.

I thanks all from separation department for the warm and friendly welcome. Even without speaking French at the beginning, I counted on the understanding of all, who spared no effort to help me. I leave a special thanks to Maria, Hèlène, Danielle, Morgane, Jean-Pierre(s), Marc, Sonia, Laetitia, Emily, Elise, Sandra, Aurelie, Michel, Thierry, Angelique, Fabrice, Manu, Alex, Sophie … It was a real pleasure to share all these moments with you. Thanks also to people who helped me with the analysis and synthesis - Bogdan, Eric, Fred, Leonor … Thanks also to friends I met during this period, in particular Raquel, Hugo, Luis, Cristina, Angel, Alejandra, Belinda, Larissa, Ana Rita, Rafaela, July, Rick, Elsy, Marisa, Damien, Esther, Xiaoiu… Being with you was always a reason for happiness. Thanks also to the Brazilian friends that I met in Lyon - Tatu, David, Helaine, Cinthia, Julia and Lucas. You were my ray of sunshine.

Thanks also to the University of Alicante and Professor Joaquin Silvestre who welcomed me for a month to perform the calorimetry experiments. Thanks also to the friends I made in Alicante, Carlos Cuadrado, Jesus and Snezana. We had a good time together.

I dedicate this work to my parents, above all, for their unconditional love, for the great effort devoted to my achievements and for the constant encouragement … To the memory of my grandparents, whose example of humility taught me a lot about life. To my nephews, for the joy they bring to my life … I've missed them every day in these three years. For my family and family-in-law, for supporting my decisions and always being willing to help. I also dedicate this work to Edwyn, for the love and companionship of always … for sharing the joys, for making me smile in the sad days and for the strength in the difficult moments.

Abstract ..... **III**

Résumé ..... **IV**

Acknowledgment ..... **V**

Introduction **9**

1. Bibliography **12**

1.1. Xylene separation using zeolites 12

1.1.1 Importance of paraxylene (px) 12

1.1.2 Zeolites 13

1.1.2.1 Faujasite-type zeolite 14

1.1.2.2 Xylene selectivity in faujasite-type zeolite 16

1.1.2.3 Improving adsorptive and diffusion performance of zeolites 20

1.1.2.4 Hierarchical zeolites 21

1.2. Xylene adsorption and diffusion - fundamentals 25

1.2.1 Thermodynamics of adsorption 25

1.2.1.1 General aspects about adsorption in porous solids 25

1.2.1.2 Henry's law 27

1.2.1.3 Langmuir adsorption isotherm 27

1.2.1.4 Dubinin-Radushkevich adsorption isotherm 28

1.2.1.5 Differential enthalpy of adsorption 29

1.2.2 Diffusion in porous materials 29

1.2.2.1 Fundamental laws of diffusion 29

1.2.2.2 Transport and self-diffusion 30

1.2.2.3 Diffusion mechanisms 30

1.2.2.4 External resistance to mass transfer 33

1.3. Xylene adsorption and diffusion - measurements 35

1.3.1 Gas phase approach 35

1.3.1.1 Thermogravimetric and calorimetric measurements 35

1.3.1.2 Thermogravimetry and uptake curves 37

1.3.1.3 Pulsed field gradient nuclear magnetic resonance (PFG NMR) 40

1.3.2 Liquid phase approach 41

1.3.2.1 Xylene selectivity and diffusion in faujasite 41

1.3.2.2 Adsorption kinetics in batch experiments 42

1.3.2.3 Breakthrough curves 44

1.3.2.4 Zero length column 46

2. Materials and methods **47**

2.1. Zeolites 48

2.2. Characterization techniques 49

2.2.1 Surface area 49

2.2.1.1 X-ray diffraction 49

2.2.1.2 X-ray fluorescence 50

2.2.1.3 N_2 adsorption 50

2.2.1.4 Mercury intrusion 50

2.2.1.5 Electron microscopy and tomography 51
2.2.1.6 Scanning electron microscopy 51
2.2.1.7 Transmission electron microscopy 51
2.2.1.8 Electron tomography 51
2.2.1.9 ^{1}H 2D exchange spectroscopy nuclear magnetic resonance 52
2.2.2 Surface chemistry 53
2.2.2.1 Fourier-transform infrared spectroscopy 53
2.2.2.2 Nuclear magnetic resonance 53

2.3. Xylene adsorption and diffusion 54
2.3.1 Thermogravimetric analyses 54
2.3.1.1 Apparatus 54
2.3.1.2 Desorption of samples 55
2.3.1.3 Diffusion experiments 56
2.3.1.4 Adsorption isotherms 56
2.3.2 Pulsed field gradient NMR 57
2.3.3 Liquid batch experiments at ambient temperature 58
2.3.3.1 Preliminary tests on NaX zeolite 59
2.3.3.2 Adsorption and diffusion on a BaX zeolite 61
2.3.3.3 Method to estimate the amount of xylene adsorbed in the zeolite 63

3. Characterization of conventional and hierarchical X-type zeolites 65

3.1. NaX zeolite 65
3.1.1 Surface area 65
3.1.1.1 X-Ray diffraction and fluorescence 65
3.1.1.2 Microscopy techniques and tomography 68
3.1.1.3 Textural characterization 73
3.1.2 Surface chemistry 89
3.1.2.1 Nuclear magnetic resonance (NMR) 89
3.1.2.2 Fourier-transform infrared spectroscopy (FTIR) 91

3.2. BaX zeolite 93
3.2.1 Surface area 93
3.2.1.1 X-Ray diffraction and fluorescense 93
3.2.1.2 Textural characterization 95
3.2.2 Surface chemistry 102
3.2.2.1 Fourier-transform infrared spectroscopy (FTIR) 102

3.3. Conclusions on characterization 103

4. Xylene adsorption in conventional and hierarchical zeolites 105

4.1. Adsorption in partially saturated medium 105
4.1.1 Modeling of adsorption isotherms 108
4.1.2 Isosteric adsorption enthalpies $\Delta Hads$ 112

4.2. Adsorption in saturated zeolites 114
4.2.1 Selectivity with NaX zeolites 114
4.2.2 Selectivity on BaX zeolites 121

4.3. Conclusions on adsorption properties 125

5. Xylene diffusion in conventional and hierarchical zeolites 126

5.1. Counter-diffusion in saturated medium 126

5.1.1 Counter-diffusion of px in the presence of mx or ox 126

5.1.2 Comparison with pure px 135

5.2. Diffusion in partially saturated medium 138

5.2.1 Thermogravimetric technique 138

5.2.2 Pulsed field gradient nuclear magnetic resonance (PFG - NMR) 144

5.3. Conclusions on diffusion properties 148

6. Study of the surface adsorption by molecular simulation 150

6.1. Grand canonical Monte Carlo (GCMC) methodology 151

6.2. Force field implementation 152

6.2.1 Xylene adsorption in NaLSX and BaLSX for bulk-crystal systems 152

6.2.2 Xylenes force field 153

6.2.3 NaLSX and BaLSX force field 154

6.2.4 Xylene adsorption in NaLSX and BaLSX systems bearing an interface 154

6.2.4.1 Surface selection and preparation 155

6.2.4.2 Surface force field 156

6.3. Xylene adsorption in NaLSX and BaLSX 156

6.3.1 Xylene adsorption in NaLSX and BaLSX bulk-crystal systems 157

6.3.2 Xylene adsorption in NaLSX and BaLSX systems bearing an interface 159

6.3.3 Configurational analysis of the adsorption in the interface 162

6.4. Conclusions on molecular simulation 168

Conclusions and perspectives 169

References **174**

Introduction

This study concerns the use of hierarchical zeolites for xylene separation. Among the different xylene isomers, paraxylene (*px*) is the most consumed isomer by the petrochemical industry, which justifies the need for improving this separation process. The efficiency of xylene separation is controlled by a combination of the adsorbent properties involving the selectivity, the adsorption capacity and the diffusion time. These properties may vary according to the type of adsorbent used. Nowadays, the adsorbent employed for xylene separation is the microporous faujasite zeolite. While these zeolites present interesting xylene-selectivities resulting from confinement in their micropores, the access through diffusion to such porosity leaves room for improvement. Thus, in an attempt to improve transport properties in the xylene separation process, the use of hierarchical faujasite zeolites is investigated in this thesis.

In addition to micropores, hierarchical zeolites also present meso/macropores (pore diameter larger than 2nm) that contribute to the reduction of the diffusion pathway length, hence enhancing access to micropores. The synthesis of hierarchical zeolites is usually accompanied by a significant increase in their external surface area. So far, the impact of this large external surface area on the xylene separation process has remained poorly understood. Therefore, the objective of this thesis is to better understand the role played by each porosity and surface domain (micro/meso/macropores and external surface) on xylene adsorption and diffusion in hierarchical zeolites. To do so, the characterization of such materials and the selection of the most appropriate methods to probe adsorption and diffusion are essential steps.

In this thesis, two types of faujasite hierarchical zeolites are being considered: nanoparticle aggregates (NA) and layer-like zeolite (LL). The NA zeolite is formed by the aggregation of small crystals presenting mesoporosity between them. The LL zeolite is formed by an array of faujasite zeolite layers, which leads to the formation of inter and intra-layer mesopores. Both NaX and BaX forms are studied in order to obtain more insights into the effect of the hierarchization of zeolites for respectively non-selective zeolites (NaX) and *px*-selective zeolites (BaX).

In Chapter 1, the NA and LL hierarchical zeolites are described in more detail. In addition, a review on xylene adsorption and diffusion in faujasite-type zeolites is presented. The last part of this literature survey is dedicated to the description of techniques to measure xylene adsorption and diffusion in zeolites.

Furthermore, in Chapter 2, the methodologies of selected techniques for the study of xylene adsorption and diffusion are described. In this chapter, the methods used to characterize the zeolitic structures are also presented.

Chapter 3 is dedicated to the results of the different characterization techniques applied to assess both the quantity and the quality of the external surface and other relevant features for xylene separation. Among the characterization techniques, N_2 physisorption and mercury intrusion porosimetry are used to evaluate the external surface area, microporous volume and pore size distribution. The analysis of pore accessibility is also evaluated through hysteresis scanning curves in the context of nitrogen physisorption experiments. The connectivity between different pore domains is investigated through ^{1}H 2D exchange spectroscopy (^{1}H EXSY) NMR, using *px* as a probe molecule. The meso/macropores array is investigated by means of scanning/transmission electron microscopy and electron tomography. The chemistry of the surface is also investigated. As silanol groups are present in the adsorbent (particularly at the external surface), infrared spectroscopy (IR) and nuclear magnetic resonance (NMR) techniques are used to probe the presence of such silanol groups at the external surface area of the hierarchical zeolites.

The hierarchical and conventional zeolites are also examined in terms of xylene adsorption and diffusion. For this purpose, in Chapter 4, xylene adsorption isotherms are evaluated for the gas phase by means of thermogravimetry and co-adsorption measurements are performed using liquid phase batch experiments.

The diffusion characterization is presented in Chapter 5. Diffusion, like adsorption, is analyzed through batch experiments in liquid phase and through thermogravimetry in the gas phase. The evaluation of the diffusion allows the observation of possible differences between behaviors in the gas phase and in the liquid phase, i.e. in partially saturated and in fully saturated media. Diffusion was further investigated by means of pulsed field gradient nuclear magnetic resonance (PFG NMR): this technique, which is capable of measuring very small displacements of the adsorbed molecules, allows an accurate determination of the intracrystalline diffusion

coefficient. In addition, the variation of the diffusion time is interpreted to identify the presence of diffusion barriers.

Finally, in Chapter 6, a theoretical study is carried out. The molecular simulation using the Monte Carlo method in the Grand Canonical ensemble is used to further study the effects of surface adsorption on *px*-selectivity in NaX and BaX zeolites. Two simulation studies were performed: xylene adsorption in bulk-crystal phase NaX and BaX zeolites (only considering microporous phase) and xylene adsorption in NaX and BaX zeolites through a model considering both the external surface and the microporous phase.

1. Bibliography

This literature survey is divided in two main parts: 1.1. xylene separation using zeolites - this part introduces the importance of xylene separation and the advantages of using hierarchical zeolites and 1.2. xylene adsorption and diffusion - this part presents the main models and techniques for the measurement of xylene adsorption and diffusion in zeolites.

1.1. Xylene separation using zeolites

In this section, the importance of paraxylene (*px*) separation will be briefly introduced. *px* is usually found in a mixture of C_8 isomers, which includes metaxylene (*mx*) and orthoxylene (*ox*). These isomers differ from each other by the position of the methyl groups attached to the benzene ring. *px* posseses methyl groups at positions (1,4); *ox* (1,2) and *mx* (1,3). After introducing xylene, a description of the zeolites - more specifically faujasite-type zeolites, which are the adsorbents used in xylene separation - will be carried out. The xylene-selectivity and description of *px* and *mx* adsorption in BaX and NaX zeolites will be discussed. In the last part of this section, the motivation to use hierarchical zeolites will be presented as well as a brief survey on the types of hierarchical zeolites used in this thesis.

1.1.1 *Importance of paraxylene (px)*

The separation of compounds in the chemical industry is one of the first steps for the production of high-value-added supplies for our society. The optimization of a given process can therefore lead to a significant reduction of production costs. Among important materials involved in our day-to-day needs, we can emphasize the importance of polyethylene terephthalate resins (also known as PET) and textile fibers, used in many processes such as production of bottles, plastic packaging and clothes. *px* is the precursor molecule behind the production of those materials - the oxidation of *px* generates the terephthalic acid, which yields the polyethylene terephthalate by condensation with ethylene glycol[1].

px is found in a mixture of C_8 aromatic isomers that comprises other xylene molecules and ethylbenzene. These isomers are mainly obtained from catalytic reforming units (96%) followed by steam cracking (4%). The percentage of *px* in the mixture is about 20% only. However, the consumption of xylene is mainly centered on *px* - around 80% of the isomers are

finally consumed as *px*. These numbers show that it is indeed important to perform efficient paraxylene separation and further xylene isomerization[1].

px separation cannot be done through conventional distillation, since xylene isomers present very similar boiling points. Separation is therefore achieved through adsorption in a faujasite-type zeolite using a simulated moving bed (SMB) process. In what follows, a brief description of zeolites (especially the faujasite zeolite) and its application to xylene separation will be presented.

1.1.2 *Zeolites*

Zeolites are defined as crystalline porous materials whose porous structure is formed by tetrahedra of silicon and aluminium linked by oxygen atoms[2]. However, a modern definition of zeolites, by the *International Mineralogical Association,* describes them as crystalline structures formed by the union of tetrahedra composed by a central cation and oxygen atoms in the vertices[3]. The silicon tetrahedra composing the zeolite structures are electrically neutral but, when Si (IV) atoms are substituted by atoms such as aluminium Al (III), the structure becomes negatively charged. According to Lowenstein's rule, two or more aluminium tetrahedra cannot be connected directly[4]. The negative charge generated by the aluminium tetrahedron must be compensated by a cation. These cations are not fixed in specific positions and they can move along the lattice structure. These cations can also be replaced by other cations, therefore leading to the ion exchange property of zeolites[5]. Ion exchange may cause some modifications in the properties of zeolites such as their stability, selectivity, adsorption and catalytic activity. Therefore, it is possible to adjust the properties of zeolites for a specific application by using this ion exchange property[6].

The crystalline structure of zeolites is made up of internal voids such as pores, channels and cavities. This feature confers to these materials a large specific area, which is responsible for the adsorption capacity of zeolites. The length of the rings and cavities of zeolitic structure is the main factor that determines the sizes of the molecules that can be adsorbed.

1.1.2.1 *Faujasite-type zeolite*

The zeolites X and Y possess the same structure which is representative of faujasite. The main difference between these two zeolites is related to their Si/Al ratio. The denomination is as follows: zeolite X for a Si/Al ratio between 1 and 1.5 and Si/Al ratio > 1.5 for zeolite Y. The faujasite-type zeolite is based on primary building units (PBU's) (TO_4) where the "T" central atom represents a Si^{4+} or Al^{3+} which is surrounded by four O^{2-}. These primary units can be linked to form the secondary building units which are linked again to form cages or channels. In faujasite zeolites, a combination of six 4-membered-rings and eight 6-membered-rings secondary units leads to the formation of the sodalite cage[7]. This polyhedron is composed by fourteen faces, which delimit an empty inner space of a diameter of 0.64 nm. The 6-membered-rings in the sodalite cage form the β-cage, which has an access diameter of 0.22 nm. Another secondary building unit (SBU) found in faujasite-type zeolite structure is the hexagonal prism (D6R), which is formed by two parallel 6-rings (S6R) linked by six oxygen bonds[2].

In the faujasite framework, four β-cages of sodalite are linked with four nearest sodalite cages through four D6R units. The process of faujasite formation, starting with the appearance of the primary building units, is represented in Figure 1. The sodalite cages are linked together to create the α-cages (also referred to as supercages). These supercages have an internal diameter of 1.3 nm, which is accessible through windows with a diameter of 0.74 nm composed by 12-membered-rings[8]. Figure 1 shows the three different sites that countercations occupy in faujasite. Sites I and I′ are located at the D6R faces linking the sodalite cages. Sites II and II′ are located at the open hexagonal (S6R) faces. Finally, sites III and III' are located at the surface of the supercage. A more detailed description about cation distributions can be found in Table 1.

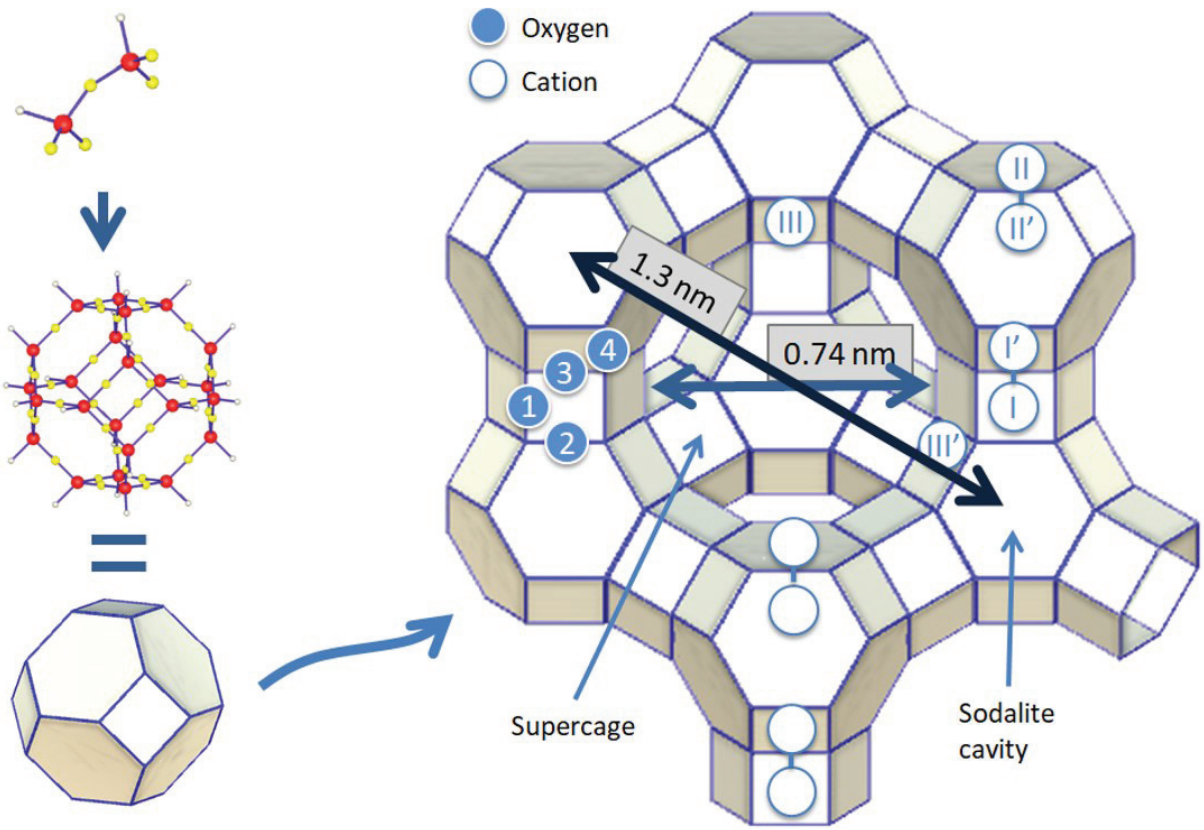

Figure 1. Construction of the faujasite structure from the primary building units (TO4). The array of sodalites creates a supercage with a 12-membered-rings window. The faujasite structure on the right presents the position of countercations and of nonequivalent oxygen atoms (1-4). (*Adapted from Refs.* [7,9]).

Table 1. Relation between nature, number and localization of cationic sites per unit cell in a faujasite zeolite. *From Ref.* [9].

Site	Cations/ unit cell	Cavity	Definition
Site I	16	Hexagonal prism	In the hexagonal prism. When in the center of the prism, octahedral coordination with neighbouring oxygen atoms.
Site I'	32	Sodalite cage	In the sodalite cage, close to the hexagonal window.
Site II'	32	(β cage)	In the sodalite cage, close to the hexagonal window to the supercage.
Site II	32	Supercage	In the center of the hexagonal window between the sodalite cage and the supercage.
Site II*	32		In the supercage, close to the hexagonal window to the sodalite cage. Generally considered as site II.
Site III	48		In the supercage, close to square windows between two other square windows.
Site III'	96 or 192		In the supercage, close to square windows between two other square windows or inside the supercage wall.

1.1.2.2 *Xylene selectivity in faujasite-type zeolite*

The capacity of zeolites to adsorb molecules is related to their internal void space composed by channels and pores. Adsorption is a phenomenon very important to the chemical industry in general. It permits the separation of components of a mixture, being a useful alternative when distillation is not possible (for example in the case of xylene separation). For efficient separation, the adsorbent must be selective towards one component of the mixture with respect to the other. The selectivity α_B^A is defined as:[10]

$$\alpha_B^A = \frac{X_A \cdot Y_B}{X_B \cdot Y_A} \qquad \text{(Eq 1)}$$

where X_A and X_B represent the molar fractions of compounds A and B in the adsorbed phase while Y_A and Y_B represent the molar fractions in the fluid phase. When the selectivity factor is ~1, there is no preferential adsorption between the two components of the mixture. However, when the selectivity factor value is smaller or larger than 1, there is preferential adsorption. As will be discussed in this thesis, favored adsorption is originated from both entropic and enthalpic effects.

Figure 2 shows the *px*/*mx* selectivity as a function of the loading for BaX and NaX zeolites. At low loadings, both faujasite zeolites do not exhibit favorable selectivity towards any of the isomers. This is explained by the fact that, in the low loading region of the adsorption isotherm, the selectivity is governed by the interactions between the aromatic ring of xylenes and the cations (enthalpic adsorption). However, close to saturation, the BaX zeolite presents an increased *px*-selectivity. In the latter case, the dominant effect is related to the number of adsorption configurations available for each type of isomers. *i.e.* a better accommodation of the adsorbed molecules inside the α cages - the affinity is then driven by entropy. In contrast, the NaX zeolite presents a non-selective behavior independent of the loading.

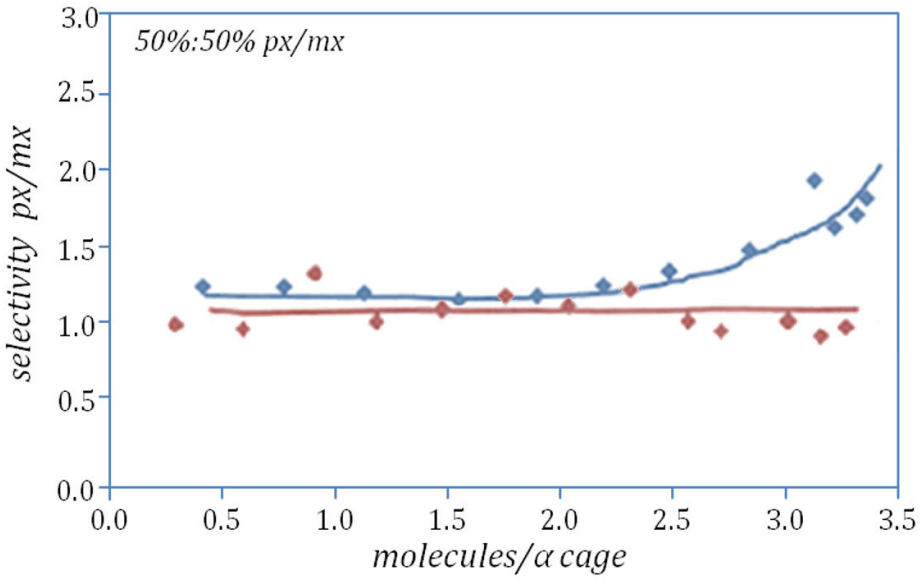

Figure 2. *px*-selectivity in BaX (blue) and NaX (red) zeolites as a function of the loading in the α cages. The selectivity was measured at 150°C for a 50%:50% *px/mx* mixture (*Adapted from Ref.* [11]).

After total filling of the α cages, adsorption only takes place at the external surface of the zeolite. The selectivity of the external surface should present an enthalpic character governed by the interaction between the adsorbate and the groups present at the external surface of the zeolite (such as the interaction with silanol groups). The external surface selectivity of faujasite Y zeolites was previously investigated by Bellat et al.[12] In this study, the *mx* molecule was found to be preferentially adsorbed at the external surface compared to *px*. The external surface of zeolites presents indeed a polar structure owing to the presence of silanol groups[13,14], anionic charges and cations that generate local electrostatic fields. In turn, these electrostatic fields interact with molecular dipoles and, thus, contribute to the preferential adsorption of polar molecules[15].

The adsorption capacity in faujasite is frequently given in terms of the number of adsorbed molecules/α cage. Depending on the loading of these cages, it is possible to find different configurations for the adsorbed isomers. For the zeolite BaX, calorimetry and neutron diffraction studies by Mellot et al. (1995)[16] suggest the following behavior for *mx* and *px* location inside the α cages (Figure 3 and Figure 4)

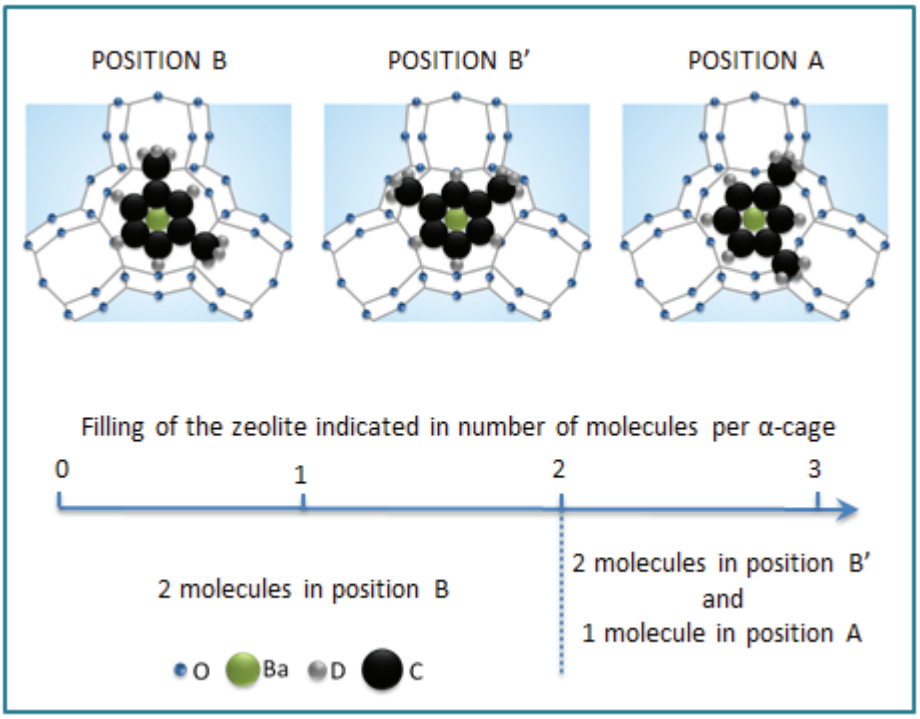

Figure 3. Positioning of the *mx* molecules within the α cages in the BaX faujasite according to the loading of the α cages. First and second *mx* are located in position B. When the third molecule is adsorbed in position A, reorientation of the first and second *mx* in position B' occurs. (*Adapted from Ref.* [16]).

Upon loading of the first two molecules, the differential enthalpy of adsorption for *px* and *mx* are close because the adsorption of both isomers occurs within the α cage next to the cation in site II. Only a difference with respect to the position of the isomers is observed. In the case of *mx,* the molecules (0-2 molecules/α cage) are adsorbed in position B (Figure 3) whereas for *px* the position A is adopted (Figure 4(a)). Adsorption of the third *mx* molecule leads to a slight decrease in the enthalpy of adsorption. In addition, adsorption of the third *mx* molecule (adsorbed in position A) requires a rearrangement of previously adsorbed molecules to minimize adsorbate-adsorbate repulsion (Figure 3). However, upon the adsorption of the third *px* molecule, a significant drop in the enthalpy of adsorption is observed. This suggests the appearance of a new – less energetic – adsorption site for *px*. The location of this site was later described by Lachet *et al.*[17] and Pichon[18] as being located in the center of the dodecagonal window at a non-cationic site (whose stabilization occurs by electrostatic interactions between the xylene molecule and the oxygen in the framework[19]) (Figure 4 (b-c)).

The study by Descours about the co-adsorption of *px* and *mx* through IR spectroscopy allowed a better understanding of the selective character of BaX zeolites. At high loadings, a

strong rearrangement of the *mx* molecules is necessary which does not seem to affect the adsorption and configuration of *px* molecule[20].

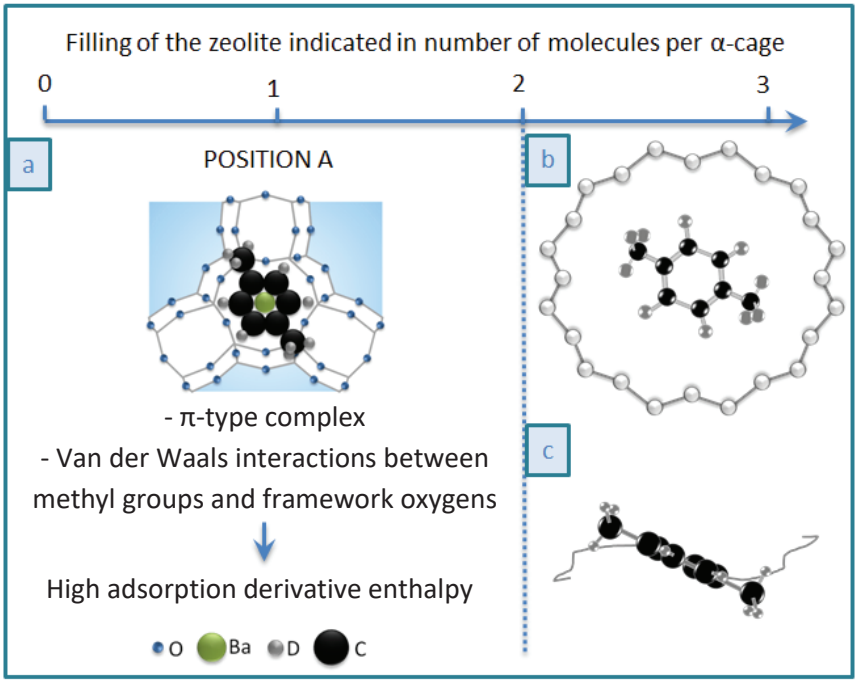

Figure 4. Positioning of the *px* molecules within the α cages according to the loading of the α cages. The first and second *px* are adsorbed in position according to Mellot et al.[16] (a). The third *px* molecule is adsorbed in the center of the dodecagonal window at a non-cationic site: front view (b) and side view (c)[19]. (*Adapted from Refs.* [16,19]).

In contrast to the BaX zeolite, the NaX zeolite is not selective towards a specific isomer. With this zeolite, two adsorption sites energetically equivalent for *px* or *mx* were identified experimentally[20,21]. The site SIII (occupied by Na^+) is the first being occupied at low loadings, independently of the xylene isomer. In order to allow the adsorption of the second xylene molecule, the first one must be redistributed in a position a little farther from the cation. This second site is classified as non-cationic and is located between sites SII and SIII. A third site was later found using molecular simulation by Lachet et al.[17] and identified as a window site (Figure 5)[17].

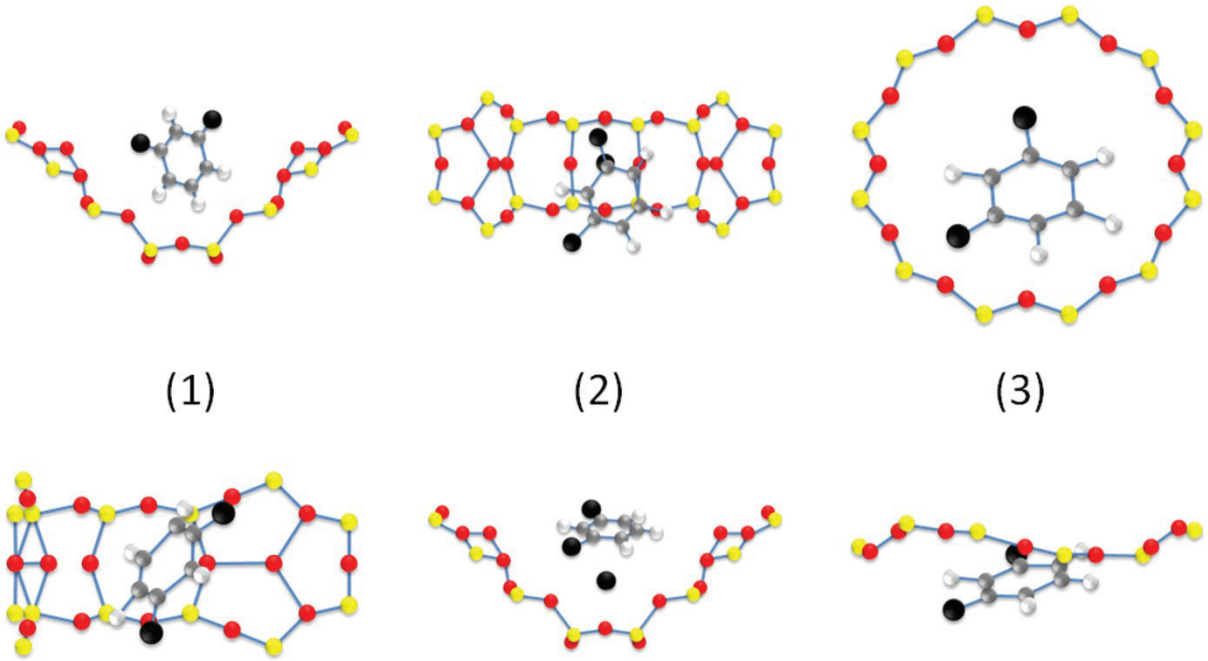

Figure 5. Positioning of *mx* molecules adsorbed in NaX zeolite according to the loading of the α cages [(1), (2) and (3)]. The adsorption of the first *mx* molecule takes place at site III (1). However, upon adsorption of the second *mx* in site III, the first *mx* molecule is relocated to site II/III (2). The third *mx* molecule is then adsorbed in a window site (3). (*Adapted from Refs.* [17,20]).

1.1.2.3 *Improving adsorptive and diffusion performance of zeolites*

As discussed earlier, zeolites have a fascinating structure composed by channels and cavities accessible to a wide range of molecules. Zeolites also exhibit several important properties such as a large specific surface area, microporosity, shape selectivity, hydrothermal stability, acidity and others. These properties are responsible for an extensive variety of zeolite applications such as in catalysis and separation. Nevertheless, the performance of zeolites can be hampered by some obstacles related to accessibility features. In conventional zeolites, the diffusion is a slow process as it occurs in micropores (diffusion is of the order of 10^{-15} m^2/s for xylenes in faujasite). Bulky molecules (or molecules near the range of micropore openings) are commonly limited by steric hindrance and, hence, exhibit very slow intracrystalline diffusion. Based on these limitations, some strategies have been developed to increase accessibility in zeolites. These strategies comprise a variety of synthesis methodologies capable to generate a secondary porosity in zeolitic materials (in most cases mesoporosity). These strategies lead to the formation of hierarchical zeolites[22].

The presence of this secondary porosity in hierarchical zeolites also leads to increased external surface areas and, hence, an increase in the number of active sites without or with less steric hindrance. These zeolites are therefore of special interest for catalytic applications. In addition, the new meso/macro pores provide new paths, facilitating access to the interior of the zeolite - *i.e.* decreasing the pathlength of intracrystalline diffusion[22,23]. Instead of diffusing through a large microporous crystal, the adsorbate molecules may also make use of facilitated access routes (meso/macropores) in order to fill the entire microporous space, making therefore the overall diffusion faster. Accordingly, in most cases, it is expected that hierarchical zeolites present improved catalytic and adsorption properties when compared with conventional ones. Therefore, understanding the synergistic effect of meso/macropores and micropores in such materials, along with the role played by the external surface during adsorption and transport, is of great interest.

1.1.2.4 *Hierarchical zeolites*

The term hierarchical zeolite refers to zeolitic materials, *i.e.* microporous materials, which present a secondary porosity (macroporous and/or mesoporous). The characteristics of the secondary porosity such as pore size and pore connectivity are governed by the synthesis route. Reviews regarding the different synthesis approaches are already available in the literature[22,24–26]. A brief explanation about the different routes leading to hierarchical zeolites studied in this thesis will be presented in what follows.

Nanoparticle aggregates (NA) - In several applications, the use of nanoparticles is seen as the solution to reduce diffusion problems since the pathlength is reduced. However, it is important to note that the handling of nanoparticles is not simple, especially during the filtration step. Therefore, the agglomeration of nanoparticles appears as an interesting alternative to improve the manipulation of this type of material. Nanoparticles aggregates are obtained by the aggregation of nanozeolite crystals and are characterized by the presence of intercrystalline macro and/or mesoporosity. In the literature, some works related to the synthesis of faujasite nanocrystal aggregates, where the aggregation of such crystals occurs during the synthesis, have been reported[27]. Valtchev et al.[28] have detailed the process of obtaining aggregated nanozeolites at ambient temperature. In this work, the formation mechanism of the nanozeolites was studied and two main steps were reported: (1) the chemical evolution of the gel with the induction step from the first nuclei and (2) the formation of aggregates and crystal growth-crystallization.

Another method allowing the agglomeration of faujasite zeolite crystals is described in the US patent 2012/022758S1320[29]. In this case, small crystals form aggregates of about 1 μm and some porosity is present between such crystals (although the mesopore volume remains low). The synthesis in this case is performed with an ageing step at room temperature (16 h) and subsequent static crystallization at 98°C.

In the structure of the nanoparticle aggregates it is common to observe a porous core with denser edges. Thanks to the approach mentioned above, for the nanoparticles aggregates synthesized at ambient temperature[28], a better understanding of the origin of a more porous center can be reached. The presence of such porous heart in the nanoparticulate aggregates can be linked to the characteristics of the different synthesis steps. The nuclei formed during the induction step are first aggregated and some pores are then created between such nuclei. Then, the crystalline growth surrounding the aggregates takes place, which gives rise to larger microporous phase around the porous center[28].

Layer-like zeolite – The synthesis of faujasite-type layer-like zeolite (or nanosheets assembly) was reported by Inayat et al.[30] in 2012. This approach is based on a one-step synthesis consisting in the addition of an organosilane surfactant known as TPHAC (3-(trimethoxydilyl) propyl hexadecyl dimethyl ammonium chloride) to the synthesis gel. This simple method allows one to obtain a hierarchical material without evidence of amorphous phase and presenting interconnected micro, meso and macroporosities. The material structure consists of a layer-like faujasite arranged in a house of card structure forming a ball shape (Figure 6 (a)). These balls present a larger size when compared with conventional X zeolite crystals[19,31]. However, other similarities such as the triangular face observed for the faujasite crystals can be identified in the hierarchical material. The triangular face, as well as the 4-fold symmetry of the cuboctahedron, was identified as a general trend for cubic crystals. The arrangement of faujasite nanosheets was attributed to the disposition of four {111} planes arranged with angles 70.5° and 109.5° (Figure 6 (b))[31].

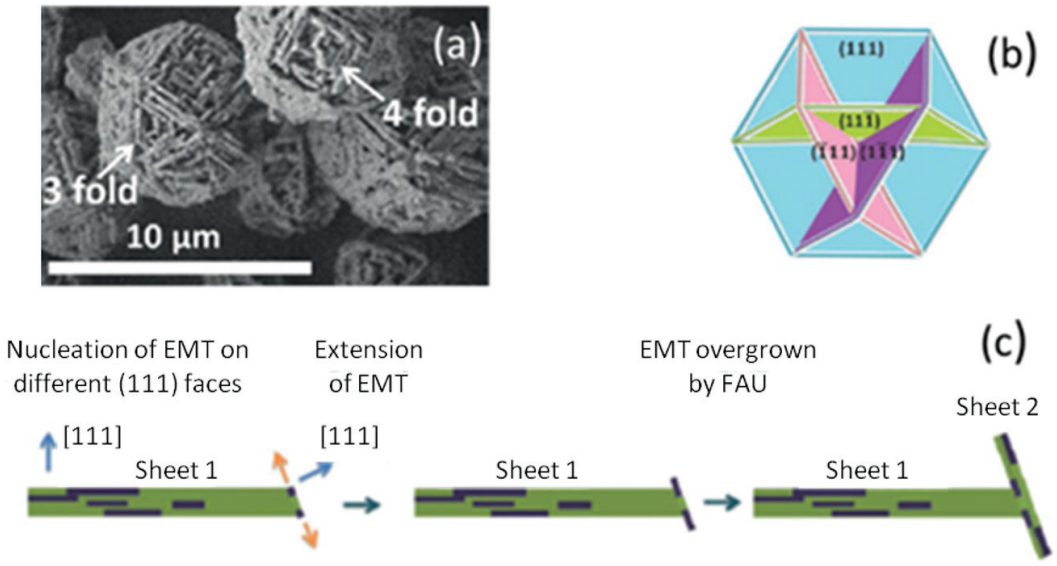

Figure 6. (a) SEM images showing ball-shaped faujasite nanosheet assemblies (3-fold and 4-fold symmetry); (b) Proposed model of interpenetrated plates demonstrating 3-fold and 4-fold symmetry; (c) Mechanism of formation of a faujasite nanosheet assembly. (*Adapted from Ref.* [31]).

A possible explanation for the formation of the faujasite nanosheet morphology relies on the occurrence of EMT zeolite islands located at the plate edges. The zeolite EMT presents a hexagonal morphology whose structure is analogous to zeolite faujasite. It is formed by the connection between faujasite sheets through 6-membered rings, forming two types of supercavities[32]. The presence of EMT seems to favor anisotropic growth. As illustrated in Figure 6 (c), the presence of EMT facilitates the growth of faujasite sheets in directions forming an angle of about 70.5° with respect to a preformed faujasite sheet. Further growth of such sheets will produce interpenetration and the formation of the structure described in Figure 6 (b). According to the mechanism proposed, after a long synthesis time, the void in the structure in Figure 6 (b) is filled by the nanosheets and the material reaches the final configuration as observed using scanning electron microscopy (SEM) (Figure 6 (a))[31]. The resulting material therefore exhibits micro and mesoporosity inside the nanosheets, and their array creates an external macroporosity between them. These micro, meso and macro domains are connected. Therefore, considering the arrangement of pores in this hierarchical material, two different routes can be proposed regarding the access to the microporous region: (a) flow passing through macro-, meso-, and micropores and (b) direct access from macropores to micropores. Accordingly, it is expected that some diffusion-limited applications should be improved through the use of this hierarchical material.

Later, in 2015, Inayat et al.[33] have shown that the addition of inorganic salts was also able to direct structural modifications during the synthesis of faujasite zeolite (therefore creating a hierarchical zeolite with a layer-like morphology). The influence of salts such as zinc nitrate and lithium carbonate was studied during the synthesis of nanosheet assembly: both favor the formation of EMT which, as already discussed, is responsible for the formation of the layer-like morphology of the faujasite. The substitution of TPHAC by the inorganic salts generates a similar type of material presenting an interlayer porosity (although intracrystalline mesoporosity was not found in the materials obtained using inorganic salts). The effect of the lithium salt was found to induce the crystallization of a larger amount of EMT and, also, to lead to a final structure which seems to be more open than that obtained using zinc nitrate. In turn, the use of zinc nitrate leads to a material similar to the conventional faujasite zeolite in terms of textural properties (large micropore volume/low mesopore volume). This can be explained by the formation of an internal compact core constituted by microporous faujasite zeolite. In conclusion, analyzing the use of the two described inorganic salts, the material synthesized in presence of lithium carbonate presents a larger amount of mesopores probably due to a larger amount of EMT phase. On the other hand, comparing the textural properties of the materials obtained using the synthesis with TPHAC and lithium salt, it is observed that, even if the mesopore size is similar (around 7 nm), the mesopore volume is almost twice larger when the organic directing agent is used. Although the presence of intracrystalline mesopores was not evidenced and the mesoporosity is lower, the material synthesized by a non-organic route still presents interesting characteristics due to the porosity between the nanosheets. This is expected to facilitate the access of molecules to the microporous domains. Moreover, it is of fundamental importance to consider that, through this organic-free methodology, the risks to the environment and production costs are reduced. Indeed, organic directing agents are a source of environmental contamination and the presence of such agents in the synthesis generally involves a costly additional step (calcination) to eliminate this organic content after the synthesis of the zeolite.

1.2. Xylene adsorption and diffusion - fundamentals

In this section, some aspects about the adsorption thermodynamics will be presented – driving forces, models for adsorption isotherms and calculation of enthalpy of adsorption. Then, the diffusion mechanisms in porous media will be discussed. Finally, in the last part of this section, some works on xylene adsorption and diffusion will be presented as well as the main methods used in the literature for gas phase and liquid phase measurements.

1.2.1 *Thermodynamics of adsorption*

Adsorption is a spontaneous process at constant temperature and pressure which means that the corresponding Gibbs free energy (ΔG) is negative. Adsorption results in a decrease in the entropy since the molecules that were before in the bulk gas or liquid phase lose a certain degree of freedom when adsorbed on a solid surface (therefore, ΔS is negative upon adsorption). Considering the Gibbs free energy expression in (Eq 2), it is possible to deduce that the adsorption process is exothermic so that the enthalpy of adsorption should present a negative value to ensure the negative sign of ΔG (representative of a spontaneous process).

$$\Delta G = \Delta H - T\Delta S \qquad \text{(Eq 2)}$$

1.2.1.1 ***General aspects about adsorption in porous solids***

An adsorption system is composed of the adsorbent, a fluid phase and an interfacial layer separating the two first. The adsorbent is a porous solid or a solid with a large specific surface area while the fluid phase is a gas or liquid. The fluid molecules are called adsorptive. The adsorption is defined by IUPAC as "*the phenomena in which the adsorptive is brought into contact with the surface of a solid (adsorbent), contributing to the enrichment of one or more components (adsorbate) in this interfacial layer*"[34]. When the molecules of the fluid penetrate the surface layer into the structure of the bulk solid, the term absorption is used. The term sorption is also used as a general manner to refer to both adsorption and absorption[34,35]

Porous solids are extensively used as adsorbents in adsorption processes. Figure 7 shows a possible representation of a crystal containing a variety of pore types[35]. At the external surface, it is possible to observe roughness (R) (different from pores by being wider than deep). There are some pores accessible to the exterior (open pores - B, T or I) and others closed (C). In the case of open pores, the access to the exterior can occur through only a single entry, as in the case of blind pores (B), or through both sides of the crystal surface where the pore is open (through T pores). It is also important to note that blind pores do not present interconnectivity (I). The characteristics of these varieties of pores are very important as they govern the adsorption and transport properties of a porous adsorbent.

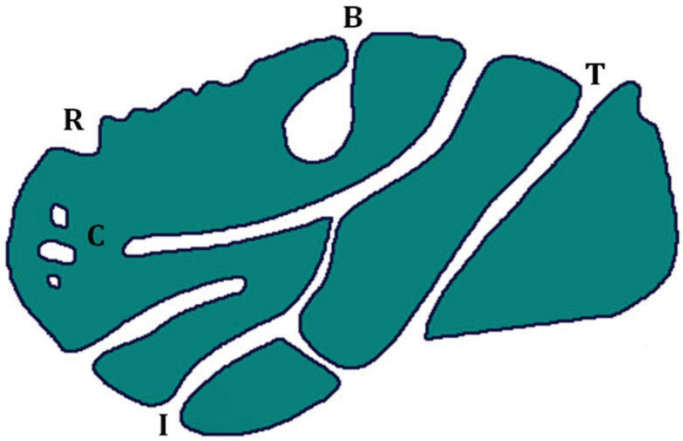

Figure 7. Porous material showing various types of pores. The letters indicate the type/name of the pores classified by Rouquerol et al.[35], where (C) denotes closed pores, (B) blind pores, (T) through pores, (I) refers to interconnectivities between pores and (R) surface roughness. (*Adapted from Ref.* [35]).

There are also distinct interactions between the adsorbate and the adsorbent. Physisorption occurs through less specific and weaker intermolecular forces than chemisorption (only the latter involves a chemical bond between the adsorbate and adsorbent)[10]. These main differences lead to distinct features between both processes. Physisorption presents low enthalpy of adsorption, consists in a non-activated reversible process and involves both monolayer or multilayer formation. In contrast, chemisorption shows a larger enthalpy of adsorption, consists of an activated and irreversible process, and involves only monolayer formation[10]. This thesis involves xylene separation which occurs through physisorption so that all further discussion in this chapter will be focused on it.

1.2.1.2 *Henry's law*

At low coverage, it is expected that the molecules adsorbed in the adsorption sites of a uniform surface do not interact with each other. Thus, the equilibrium between fluid phase and adsorbed phase is assumed to be linear and the adsorbed amount q is dependent on concentration c or pressure P. This is commonly described using Henry's law[10,35]:

$$q = Kc \quad \text{or} \quad q = K'P \qquad \text{(Eq 3)}$$

where q and c are expressed in moles/volume unit.

1.2.1.3 *Langmuir adsorption isotherm*

The Langmuir model[10,35] assumes that all adsorption sites are energetically equivalent and that there is no interaction between molecules adsorbed in neighboring sites. Moreover, it is assumed that the solid surface is composed of q^s equivalent sites available to adsorption (only one molecule can be adsorbed per site)[10]. The amount of occupied sites relative to the total amount of sites can be expressed as surface coverage (θ):

$$\theta = q/q^s \qquad \text{(Eq 4)}$$

The fraction of unoccupied sites is (1 - θ), which, along with the pressure P, defines the adsorption rate: $K_a P(1 - \theta)$. The desorption rate in turn is θK_d. The equilibrium condition is obtained by writing that the adsorption and desorption rates are equal:

$$K_a P(1 - \theta) = \theta K_d \qquad \text{(Eq 5)}$$

where K_a and K_d are the adsorption and desorption rate constants, respectively. Rearranging this equation and considering the adsorption equilibrium constant $b = K_a / K_d$, the Langmuir model can be expressed as[35]:

$$\theta = q/q^s = bP/(1 + bP) \qquad \text{(Eq 6)}$$

At low coverage, θ in the Langmuir model reduces to Henry's law. However, at high loadings, once all the available sites are almost filled by the adsorbate, θ→1. The Langmuir model can also be represented in its linear form[10]:

$$\frac{P}{q} = \frac{P}{q^s} + \frac{1}{bq^s} \quad \text{(Eq 7)}$$

The parameters q^s and b can be obtained by the slope/interception of $\frac{p}{q}$ versus p.

1.2.1.4 *Dubinin-Radushkevich adsorption isotherm*

The Dubinin-Radushkevich (DR)[36–38] model is often used to describe adsorption in microporous materials such as carbons and zeolites. This equation correlates the adsorption affinity A (Polanyi theory) and the fractional filling of the micropores (W/W_0):

$$\Theta = W/W_0 = exp[(A/E)^2] \quad \text{(Eq 8)}$$

where E is the characteristic energy of the fluid-solid system that can be expressed as $E = \beta E_0$. β is a scaling factor and E_0 is the characteristic energy for a standard system (adsorbate + solid). By defining the Polanyi adsorption potential as $A = -RT \ln (P_{sat}/P)$, where P_{sat} is the saturation pressure at the temperature T, (Eq 8) can be rewritten as:

$$W/W_0 = exp\{-[RT \ln(P_{sat}/P)]^2/(\beta E_0)^2\} \quad \text{(Eq 9)}$$

By using $\left[D = B\left(\frac{T}{\beta}\right)^2\right]$, (Eq 9) can be expressed in its linear form as:

$$\log W = \log W_0 - D[\log(P_{sat}/P)]^2 \quad \text{(Eq 10)}$$

where $B = 2.303\, R^2 E_0$.

The DR isotherm does not reduce to Henry's law at low pressures. For that reason, some failures are expected in the low pressure region. By plotting $[T \log (P_{sat}/P)]^2$ *versus* $\log W$, it is possible to identify a linear region where the DR model can be applied. The D value can be obtained from the slope of the curve while W_0 is the intercept with the y axis. The fit can also present more than one linear range, making possible to calculate different values for D and W_0 for the same system[36,38].

1.2.1.5 *Differential enthalpy of adsorption*

Differential enthalpy of adsorption is the amount of energy released to the surrounding after the transfer of a molecule from the bulk phase to an adsorbed position[10,39]. For pure-component adsorption, considering an ideal gas, the differential enthalpy Δh_{ads} is defined as:

$$\Delta h_{ads} = R\left[\frac{\partial ln(P)}{\partial(1/T)}\right]_n \quad \text{(Eq 11)}$$

where R is the ideal gas constant while T and P are the pressure and temperature when the loading corresponds to n adsorbed molecules. Investigating the energy characteristics of adsorption may bring new insights to the understanding of the observed changes in the adsorption of different molecules[40].

1.2.2 *Diffusion in porous materials*

1.2.2.1 *Fundamental laws of diffusion*

The degree of molecular motion can be characterized using the diffusivity which can be described using the self-coefficient D_s. The latter relates the molecular flow J and the concentration gradient ∇C according to Fick's first law[41-43]

$$J = -D_s \nabla C \quad \text{(Eq 12)}$$

This equation has a negative sign indicating that the flow occurs from the high concentration to the low concentration regions. Fick's second law for diffusion represents the correlation between variation in concentration in the porous medium as a function of time (mass conservation):

$$\frac{\partial C}{\partial \mathrm{t}} = D_s \nabla C \quad \text{(Eq 13)}$$

Later, Einstein proposed a correlation between diffusion and the random motion of particles observed earlier by Brown (Brownian motion). Einstein showed that the mean square displacement of particles moving according to a random motion is a linear function of time t and self-diffusivity D_s:

$$\langle r^2(t)\rangle = 6D_s t \quad \text{(Eq 14)}$$

1.2.2.2 *Transport and self-diffusion*

The transport diffusivity D_t is a variable related to the mass transfer rate which is induced by a potential gradient as a driven force[10,41]. The transport diffusivity consists in a net particle transport and can be derived from Fick's second law (Eq 13). It is important to highlight that transport diffusivity is a non-equilibrium process with a gradient in the overall particle concentration. Diffusion in porous materials can also be measured under equilibrium conditions following the diffusion of labelled molecules. In this specific case, we are referring to self-diffusion D_s which is defined in (Eq 12). In this case, mass transfer is related to the random motion of molecules and it can be determined from the mean square displacements of a large number of molecules. Self-Diffusion in micropores materials will be addressed in the following section.

1.2.2.3 *Diffusion mechanisms*

Diffusion in porous media can occur through different mechanisms depending on the pore size. The three mechanisms of gas diffusion in zeolites are presented in Figure 8: *Configurational, Knudsen and Molecular diffusion.* In the case of diffusion in the liquid phase, the mechanisms are the same except for the Knudsen diffusion which only applies to the gas phase.

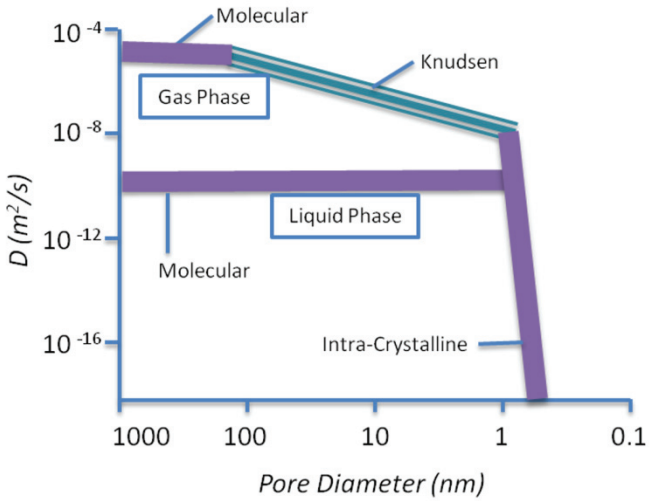

Figure 8. Effect of pore diameter on diffusivity. Intracrystalline diffusion is observed in gas and liquid phase for pore diameters below 1 nm. In gas phase, Knudsen diffusion is observed in the range of mesopores and molecular diffusion in macropores. For diffusion in liquid phase, only molecular diffusion is observed for both meso and macropores. (*Adapted from Ref.* [42]).

Diffusion in Micropores - Micropore or configurational diffusion is characterized by the motion of molecules through pores of molecular dimensions (such as micropores). As a result, there is a significant interaction between diffusing molecules and porous structure compared with other diffusion mechanisms. In this case, the diffusion process is also affected by steric hindrance usually involved in such small pores. It is also important to note that this is an activated process where the molecules move through "jumps" between the adsorption sites. The self-diffusion coefficient that describes the diffusion of a molecule adsorbed in micropores at equilibrium conditions can be described according to Arrhenius' equation:

$$D_s = D_* exp\left(\frac{-E_a}{RT}\right) \quad \text{(Eq 15)}$$

where D_s is the self-diffusion coefficient, D_* is the pre-exponential factor, E_a is the activation energy, R is the ideal gas constant and T is the temperature.

Diffusion in meso-macropores - Knudsen diffusion is a mechanism where transport resistance is due to collisions of molecules with the pore walls. In mesopores, the interaction of adsorbate molecules with the pore wall is smaller compared with that observed in the case of configurational diffusion. However, the collisions of molecules with the walls are frequent in gaseous phase, for which the pore diameter is smaller than the mean free path of molecules. The Knudsen diffusion coefficient can be expressed as:

$$D_k = \frac{2}{3} r \left(\frac{8RT}{\pi M}\right)^{\frac{1}{2}} \quad \text{(Eq 16)}$$

where r is the mean pore radius, R is ideal gas constant, T is the temperature and M is the molecular weight of the diffusing molecules. In the liquid phase, the *Knudsen diffusion* is negligible since the molecule mean free path is much smaller than the pore size. Therefore, in the case of liquid phase, the diffusion regime in mesopores corresponds to *molecular diffusion* as described below.

Molecular diffusion is predominant in macroporous materials or in mesoporous materials when the liquid phase is involved, *i.e.* when the pore diameter is large compared to the mean free path of the molecules (collisions between molecules in the fluid phase are more frequent than collision with pore walls). As the system mostly behaves as if there were no pore walls, it is assumed that there are only collisions between fluid phase molecules[10].

The pore diffusivity D_p is defined as:

$$D_p = \frac{D_m}{\tau} \quad \text{(Eq 17)}$$

where D_m is the bulk molecular diffusivity and $\tau \geq 1$ is the tortuosity. The tortuosity is the factor which accounts for the deviations in the trajectory of diffusing molecules caused by the pore walls. For a gas binary mixture, D_m is given by Chapman-Eskog equation:

$$D_m = \frac{0.00158T^{\frac{3}{2}}\left(\frac{1}{M_1} + \frac{1}{M_2}\right)^2}{P\sigma_{12}^2\Omega\left(\frac{\epsilon}{kT}\right)} \quad \text{(Eq 18)}$$

where M represents the molecular weight, P is the pressure (atm), σ_{12} is the collision diameter (Å). Ω is a function of $\left(\frac{\epsilon}{kT}\right)$ where ϵ is the fluid-fluid energy, k is Boltzmann's constant and T is the temperature. The molecular diffusivity D_m in the liquid phase can be estimated using the Wilke-Chang equation:

$$D_m = \frac{7.4 \times 10^{-8} T\sqrt{\alpha_{SV} M_{SV}}}{\eta_{SV} V^{0.6}} \quad \text{(Eq 19)}$$

where T is the absolute temperature, α is the association coefficient, M is the molecular weight, η is the viscosity, and V is the molar volume at the normal boiling point.

In addition to the mechanisms described above, there is another contribution to diffusion in macropores: *surface diffusion*. In this case, diffusion occurs in a similar way to configurational diffusion but the molecule is attracted by the potential field imposed by the pore walls. A flux of molecules is observed through the layer formed by the adsorbed phase at the macropore surface. Despite the mobility of the adsorbed layer being lower than in the fluid phase, if the thickness of the layer is large, the contribution of surface diffusion to overall diffusion can be non-negligible. The contribution of surface diffusion to the overall diffusivity in meso and macropores is dependent on the product KD_{surf}:

$$D = D_p + KD_{surf}\left(\frac{1 - \varepsilon_p}{\varepsilon_p}\right) \quad \text{(Eq 20)}$$

where ε_p represents the porosity (microporous volume), K is the Henry constant, D_p denotes the contributions from Knudsen, molecular diffusion and also Poiseuille flow (if significant) and D_{surf} is the surface diffusivity.

1.2.2.4 *External resistance to mass transfer*

External fluid film – An external resistance to mass transfer can take place due to the hydrodynamic conditions controlling the fluid film around the particles. The hydrodynamic conditions control the thickness of the layer, which governs the diffusion surrounding the boundary pellet particle[41]. The external resistance is expressed in terms of a mass transfer coefficient (k_f):

$$J = k_f(c - c_s^*) \quad \text{(Eq 21)}$$

where c is the concentration in the fluid phase and c_s^* is the concentration of the fluid film at equilibrium with the adsorbed phase at the surface of the crystal. The representation of an adsorbent pellet, its external mass transfer and internal resistance are represented in Figure 9 (a). The amount of adsorbed molecules in the fluid phase is small compared to the adsorbed amount inside the adsorbent particle. Therefore, the concentration in the fluid film can be described by a linear regime, where the time to reach equilibrium is much smaller than in the interior of the particle (Figure 9 (b)).

Resistance at the external surface of the particles - In addition to the internal diffusional resistance described in the previous section, another contribution can arise due to external resistance in the particles. There is a resistance at the external surface of the particles that is frequently reported in the literature. The origin of this surface resistance is still debated but it was identified by some authors as partial blockage of pores at the surface[43], distortion of the crystal structure at the surface[44] or even the presence of an impermeable layer composing the surface[45]. The surface resistance is not a phenomenon with a clear origin which means that, depending on the zeolitic material and used synthesis route, the origin of the surface resistance varies.

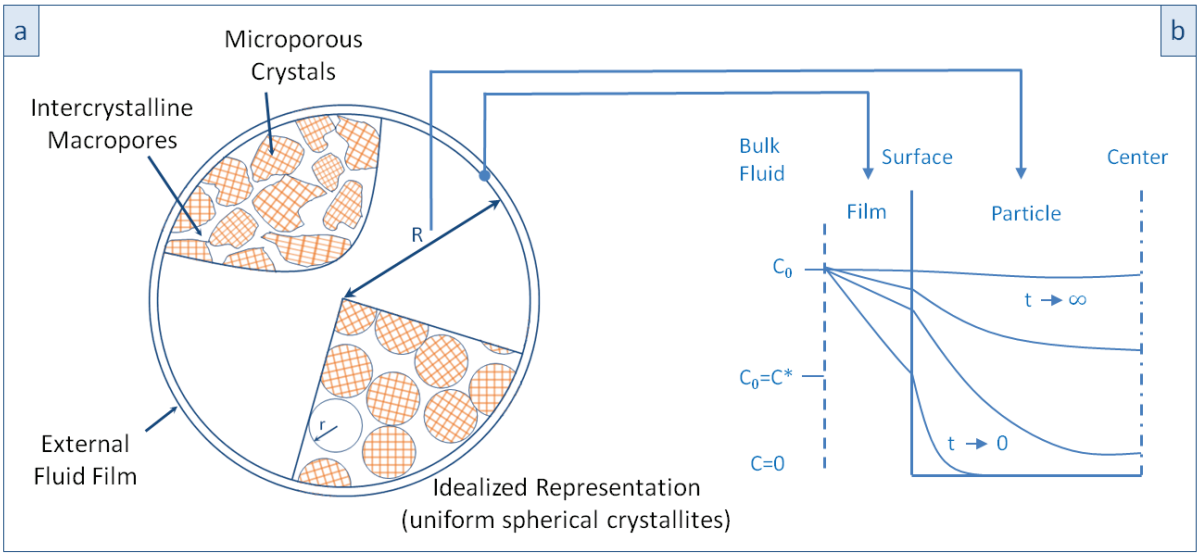

Figure 9. (a) Ideal adsorbent pellet showing the external resistance to mass transfer and internal diffusional resistance; (b) concentration profile of sorbate under the influence of an external fluid film and internal diffusion control. (*Adapted from Ref.* [10]).

The expression for mass transfer resistance at the external surface is quite similar to mass transfer resistance in the external fluid film. However, in the case of the external surface, the mass transfer coefficient in the fluid phase is replaced by the surface permeability coefficient α_s[41]:

$$J = \alpha_s(q^* - q) \qquad \text{(Eq 22)}$$

where α_s is the surface permeability for the film adsorbed at the surface, q^* represents the adsorbed phase concentration at the crystal surface and q is the concentration of adsorbed molecules within the particle. In the case of zeolites, the fluid film resistance must be negligible since the intraparticle resistance is usually slower than diffusion in the external fluid film. However, surface resistance can lead to a rate controlling transport in the case of zeolites[41].

Model for indirect adsorption - when the adsorbate interacts with the surface of the adsorbent crystals, the adsorption mechanism should be represented by indirect adsorption: the molecules are first adsorbed at the surface of the crystals and, after this first adsorption step, the molecules diffuse in an adsorbed state in direction to the pore entrances and finally penetrate in the structure of the particles. It is important to note that, according to this model, the larger the concentration of adsorbed molecules at the surface, the faster the diffusion. Hence, the diffusive properties should be significantly affected by the temperature and concentration of the fluid phase[46]. Regardless of the specific origin of surface resistance, it is clear that such resistance is

a result of a set of phenomena that hinder the penetration of molecules into the structure. Among these impediment sources, a strong interaction between the chemical groups at the crystal surface and the adsorbate molecules can lead to significant retention times. This causes limitations in the penetration of molecules into the pores. In order to get more insights about this indirect adsorption, surface characterization of the materials must be performed and compared with the results for diffusion. In so doing, it will be possible to identify if there is a direct relationship between these two phenomena.

1.3. Xylene adsorption and diffusion - measurements

1.3.1 *Gas phase approach*

For the study of xylene adsorption and diffusion in zeolites, several works used thermal analysis such as thermogravimetry to obtain adsorption isotherms and calorimetry to obtain adsorption enthalpies. Thermogravimetry can also be used to obtain uptake curves and define apparent diffusion coefficients. More recently, the PFG NMR technique - which allows probing microporous diffusion and surface barriers - was also applied for the determination of diffusion coefficients in hierarchical zeolites. Throughout this section, some works on these issues will be discussed.

1.3.1.1 *Thermogravimetric and calorimetric measurements*

A large number of studies on the adsorption and diffusion of xylenes in the gas phase have been done using thermogravimetry[47–53]. By using a thermobalance and applying specific conditions of temperature and pressure, the mass adsorbed in a zeolite can be measured as a function of time and at equilibrium. In this analysis, the adsorption of xylenes can be done at different conditions, therefore allowing the study of adsorption isotherms and isobars. Information on the enthalpy of adsorption can also be obtained using this technique (See Section 1.2.1.5).

Bellat et al. studied the adsorption of xylenes at the outer surface of Y-type zeolites[12]. In this work, adsorption isotherms of *px* and *mx* were obtained at 25°C. To differentiate

adsorption at the external surface (m_{ext}) and in the micropores (m_{μ}), a linear model correlating the mass adsorbed with the thickness *t* of a xylene film adsorbed at the surface of a reference material (alumina) was used:

$$m = m_{\mu} + m_{ext} \quad \text{(Eq 23)}$$

$$m = m_{\mu} + \rho S t \quad \text{(Eq 24)}$$

where ρ is the liquid density of xylene at 25°C and S is the external surface of the zeolite. The results showed that the adsorption of xylene in the micropores is about 3.5 molecules/α cage and that the adsorption of *mx* at the surface prevails in comparison to *px.* This suggests that the external surface of the zeolites is selective to the most polar isomer (*mx*).

Xylene co-adsorption was further analyzed by means of thermogravimetry in a BaX zeolite. However, this time, a more complex system with the gas outlet coupled to a chromatograph[11] was used. As can be seen in Figure 10 (a), the adsorbed amount of *px* is slightly larger than for *mx*. Using this analysis, the selectivities as a function of the loading could be obtained. At low loadings, the BaX zeolite was not selective for any of the xylene isomers. However, above 2 molecules/α cage, the *px*-selectivity increases abruptly (Figure 10 (b)). In these analyses, it was also observed that some of the pre-adsorbed water in the zeolite is replaced by xylene molecules when the adsorbed amount of xylene exceeds 2 molecules/α cage. It is also interesting to note that the presence of pre-adsorbed water increases the selectivity up to a factor 2 at high loadings. For optimum *px*-selectivity in BaX zeolites, the amount of water was estimated to be around 6%[18].

The adsorption of pure *px* and *mx* and of a *px/mx* equimolar mixture was further studied in the BaX zeolite by means of differential calorimetry[11]. As seen in Figure 11, the enthalpies of adsorption are mainly constant with α cage loading and, once filling is complete, the heat of adsorption decreases rapidly towards the enthalpy of vaporization of the pure xylenes. The data for the pure xylenes are very similar, except for a decrease of the *mx* enthalpy of adsorption at loadings larger than 2.3 molecules/α cage (near the point where the adsorption starts being selective to *px*). The behavior of the enthalpy of adsorption for the xylene mixture is similar to that for pure xylenes, except for the range between 1.6 - 2.8 molecules/α cage - which present larger adsorption enthalpies in the case of the mixture[20].

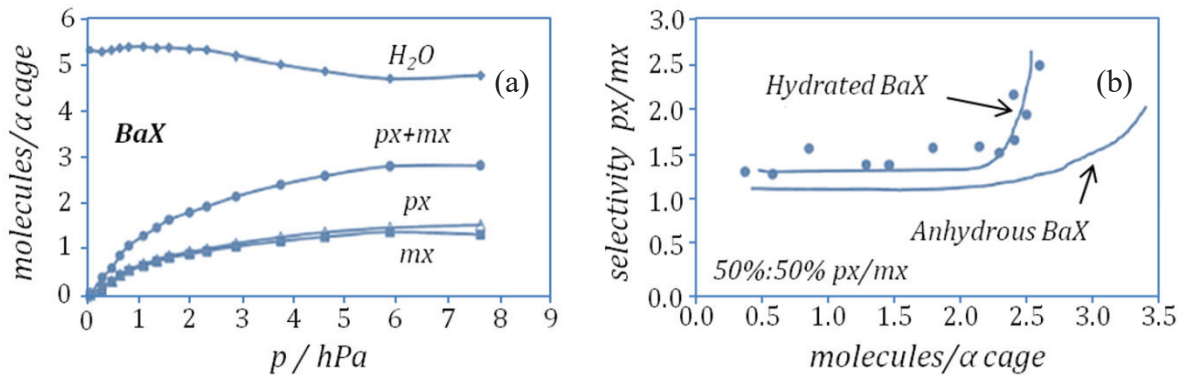

Figure 10. (a) Co-adsorption isotherms of xylenes in partially hydrated BaX zeolite at 150°C. (b) Comparison of the selectivities between anhydrous and partially hydrated BaX zeolite at 150°C. The curves were obtained for a 50%:50% *px/mx* mixture. (*Adapted from Ref.* [11]).

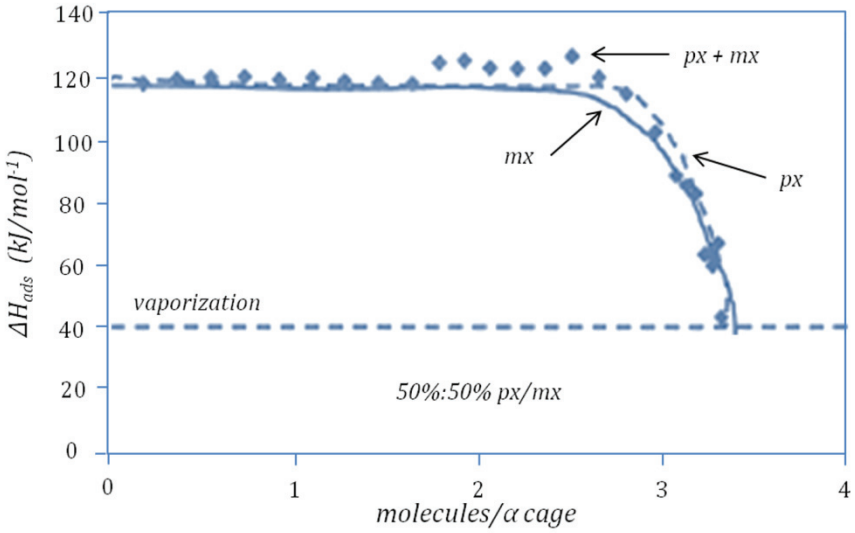

Figure 11. Differential enthalpy of adsorption for *px*, *mx* and 50%:50% *px/mx* mixture in a BaX zeolite at 150°C. (*Adapted from Ref.* [11]).

1.3.1.2 *Thermogravimetry and uptake curves*

The thermogravimetric analysis can be used to measure diffusion through uptake curves. For this, the gain in mass of a sample submitted to a partial pressure of a specific adsorbate is measured as a function of time. In the case of a microporous zeolite exposed to a sorbate

concentration, and considering a spherical shape for the zeolite crystals, Fick's law can be written as follows in a system where the diffusivity is constant:

$$\frac{\partial q}{\partial t} = D_c \left(\frac{\partial^2 q}{\partial r^2} + \frac{2}{r} \frac{\partial q}{\partial r} \right) \quad \text{(Eq 25)}$$

It is important to note that the system is considered isothermal, or at least that the heat transfer is assumed to be fast, so that it does not impact the adsorption rate. If the adsorption in the system is not significant enough to cause large changes in the concentration of the fluid phase around the particles, the curve can be described in terms of fractional uptake as:

$$\frac{m_t}{m_\infty} = 1 - \frac{6}{\pi^2} \sum_{n=1}^{\infty} \frac{1}{n^2} exp\left(- \frac{n^2 \pi^2 D_c t}{r_c^2} \right) \quad \text{(Eq 26)}$$

where m_t is the mass adsorbed at a given time *t*, m_∞ is the mass adsorbed under equilibrium, r_c is the crystal radius and D_c is the intracrystalline diffusivity.

It is also possible to simplify (Eq 26) in the short and long-time regimes. For a mass fraction $\frac{m_t}{m_\infty}$ greater than 70%, the expression above is simplified to the long-time model where only the first term is significant for the description of the uptake curve:

$$\frac{m_t}{m_\infty} = 1 - \frac{6}{\pi^2} exp\left(- \frac{\pi^2 D_c t}{r_c^2} \right) \quad \text{(Eq 27)}$$

By using the linear form of this long-time equation with an intercept at $ln\ (\frac{6}{\pi^2})$, the slope of the straight line provides the apparent diffusion coefficient. For mass fractions lower than 30%, another simple model, called short-time model, can be applied:

$$\frac{m_t}{m_\infty} = \frac{6}{\sqrt{\pi}} \left(- \frac{D_c t}{r_c^2} \right)^{1/2} \quad \text{(Eq 28)}$$

In this case, the linear plot of $\frac{m_t}{m_\infty}$ as a function of $\sqrt{t}$ passing through the origin (0,0) provides a slope from which the diffusion coefficient can also be obtained.

The diffusion of xylenes has already been studied through gravimetric measurements in faujasite-type zeolites[54]. In this study, the zeolite crystals were quite large - 100 µm NaX and 250 µm natural faujasite. The diffusivity values determined for both zeolites were similar, around 6×10^{-13} m²/s at 170°C. Through the use of such large crystals, the elimination of

problems such as heat and mass transfer issues and the negligible effect of surface barriers, the diffusion measured by this technique is expected to be consistent with self-diffusion measurements by NMR[55]. However, measurements by NMR for the *px* molecule indicated diffusivity of about 5×10^{-10} m²/s at 120°C for NaX zeolites. The analysis of uptake curves has also been used for the assessment of diffusion in hierarchical zeolites (for a hierarchical ZSM-5/2,2 dimethylbenzene system)[56]. Special attention in this work was paid to investigating surface resistance in hierarchical zeolites since this class of zeolites present a large external surface area.

The technique of measuring diffusion through thermogravimetry is a macroscale technique able to measure apparent diffusion (which includes surface resistance). The overall time for apparent diffusion was established from a linear correlation between intracrystalline diffusivity and surface permeability as[44,56]:

$$t_{diff} = \frac{r_c^2}{D_{app}} = \frac{r_c^2}{D_c} + \frac{r_c}{3\alpha_s} \qquad \text{(Eq 29)}$$

where D_{app} and D_c are, respectively, the apparent and intracrystalline diffusion coefficient. α_s is the surface permeability. By using the correlation in (Eq 29), Gueudré et al. were able to analyze both types of resistance by treating the zeolites with HCl and HF acids to eliminate surface resistance. The surface barrier was successfully identified. In addition, it was found to present a negligible effect on the diffusion of 2,2 dimethylbenzene in hierarchical ZSM-5 zeolite[56]. The use of acids is an interesting solution to evaluate surface resistance. However, special care should be taken with the textural characterization of these materials after the treatment since dealumination and generation of mesopores can occur.

As could be observed for some examples, the analysis of uptake curves measured by thermogravimetry allows obtaining valid information about diffusion in zeolites. However, special attention should be paid to the experimental conditions so that heat transfer and extracrystalline resistance to mass transfer can be reduced. One way to verify that the system is free of mass and heat transfer effects is to vary the adsorbent mass and check whether the different uptake curves overlap[10,46]. Another way to evaluate if the system can be considered isothermal (free of heat effects) is to observe whether the intersection of the curve corresponds to that described by (Eq 28). The effects of heat transfer on the diffusivity can be reduced by decreasing the concentration step of the uptake measurement[10].

1.3.1.3 *Pulsed field gradient nuclear magnetic resonance (PFG NMR)*

The layer-like faujasite zeolite was the first hierarchical zeolite characterized by PFG NMR in the literature[57]. The diffusivity of hexane molecule was obtained by means of a correlation between the intensity of the NMR signal (S) with another term accounting for the diffusivity (D), duration (δ) and amplitude (g) of gradient pulse and gyromagnetic ratio of the nuclei (γ):

$$\frac{S(\gamma\delta g, t)}{S_0} = \exp(-\gamma^2\delta^2 g^2 D t) \qquad \text{(Eq 30)}$$

By plotting the data according to (Eq 30), two characteristic decays were identified (Figure 12). A fast decay assigned to molecules diffusing between different particles and a slower decay representative of diffusion in an individual crystal. By increasing the observation time, it is possible to observe a larger contribution in the first part of the graph, evidencing a greater number of molecules diffusing between different crystals. When dealing with the second range of the graph, *i.e.* for molecules diffusing inside the same crystal, no significant difference was found for the zeolite diffusivity upon changing the observation time. Moreover, for the second decay in the case of the hierarchical material, a larger diffusivity compared to that for the conventional NaX was observed. According to the authors, the faster diffusivity for the hierarchical zeolite leads to molecular displacements that exceed the thickness of the nanosheets[57].

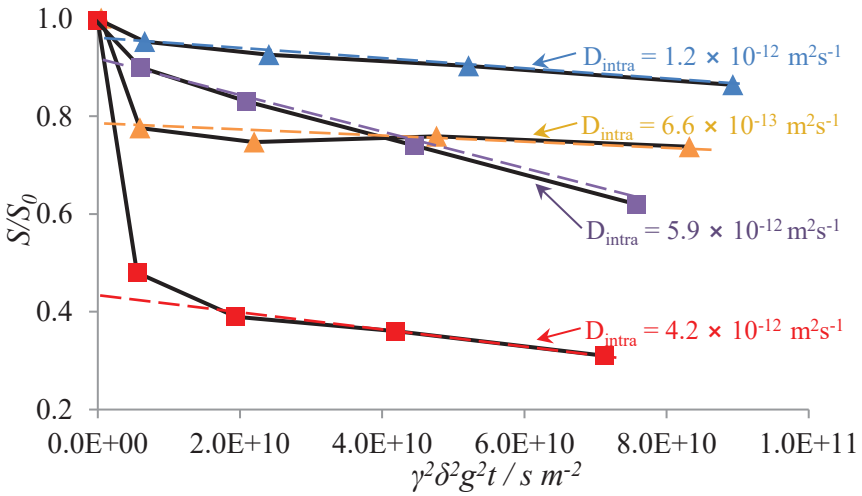

Figure 12. PFG NMR curves for cyclohexane in conventional NaX (triangles) and layer-like NaX zeolite (squares) for different observation times (blue and purple - 5ms; red and orange - 160ms) at 25°C. Diffusivities are presented for each type of zeolite and for different diffusion times. (*Adapted From Ref.* [57]).

Recently, Guenneau and coworkers[58] provided evidence for the interconnectivity between the microporous and mesoporous domains in a hierarchical zeolite (which was synthesized by pseudomorphic transformation of a faujasite zeolite). The resulting faujasite-type hierarchical zeolite was found to present similar mesopores to those of MCM-41. By using PFG NMR, the effective diffusivity was determined for mesoporous faujasite, parental materials (MCM-41 and zeolite faujasite) and a physical mixture of MCM-41 and zeolite faujasite (with the same amount of micro/meso as in mesoporous faujasite). The results showed that diffusivity for the mechanical mixture present two diffusion regimes, each of them being very close to that observed for the parental MCM-41 and microporous faujasite. On the other hand, diffusivity for mesoporous faujasite was intermediate between those for pure microporous and mesoporous materials. The presence of such intermediate diffusivity in mesoporous faujasite is an evidence of physical connectivity between the two domains (micro and meso). In this way, PFG NMR was shown to be effective in proving the existence of interconnectivity in mesoporous zeolites and also distinguishing between a true hierarchical porous material and a simple mixture.

1.3.2 *Liquid phase approach*

1.3.2.1 *Xylene selectivity and diffusion in faujasite*

The composition of liquid mixtures can be readily determined using chromatography. The change in the composition of a solution in the presence of a zeolite may, in turn, be useful in determining key properties for the separation of xylenes (such as diffusion and selectivity). The diffusion is related to the access of a given molecule to the micropores of the zeolite where it is adsorbed. The diffusion is therefore directly related to the time it takes for the molecules to be adsorbed in the micropores. Furthermore, the efficiency of the xylene separation process is defined by the product between adsorption capacity and selectivity divided by the effective diffusion time.

The study of diffusion in liquid phase corresponds, in fact, to a measurement of counter-diffusion. The use of a solvent is usually needed so that the variations in the liquid phase concentration can be observed with accuracy along the experiment. Considering a zeolite pre-saturated with a solvent, the counter-diffusion consists in the release of the solvent and

adsorption of the adsorbate. Some studies indicate that the critical diameter of molecules used as a solvent may lead to very large differences in estimating the counter-diffusion coefficient[59]. By comparing the counter-diffusion in NaY systems of molecules with different critical diameters (with cyclohexane as solvent), Moore and Katzer have identified that the counter-diffusion coefficient is correlated with the critical diameter of the largest molecule in the counter-diffusion system (Figure 13). The diffusion coefficient decreases by four orders of magnitude as the critical molecular diameter increases from 0.675 to 0.92 nm. Furthermore, studies performed by Ruthven suggest that the use of a linear paraffin with respect to a cyclic hydrocarbon as solvent leads to a larger counter-diffusion coefficient[42,60]. When using a saturated NaX zeolite in *n*-hexane, the benzene counter-diffusion coefficient obtained was similar to that of unilateral gas phase diffusion for benzene (direct diffusion measurement when no counter-diffusing molecule is used)[61].

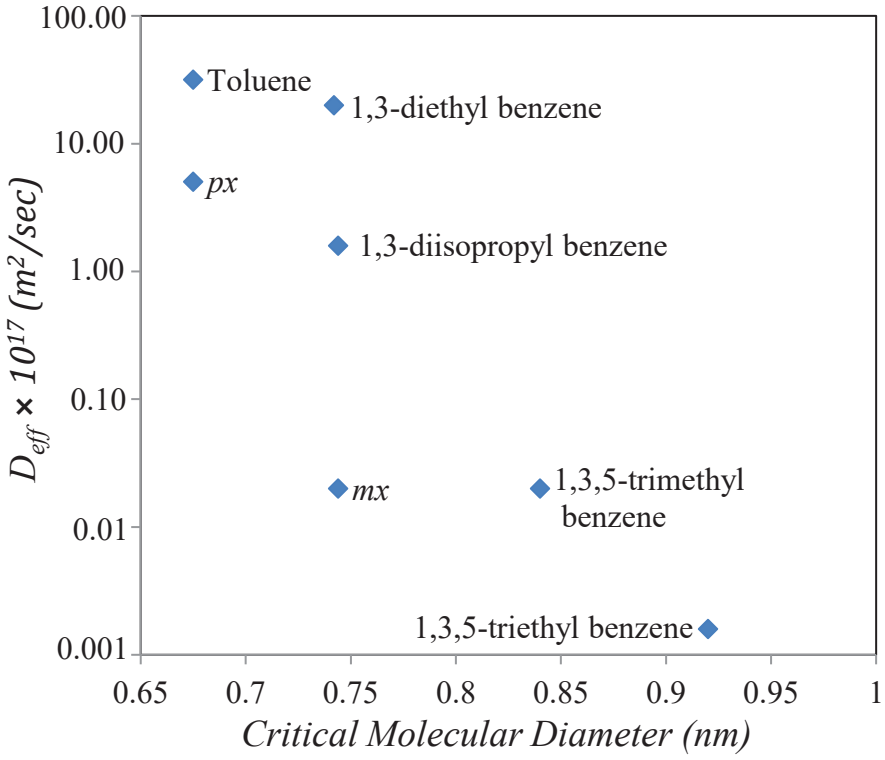

Figure 13. Correlation between the critical diameter of molecules and their counter-diffusion coefficients in cyclohexane-saturated NaY at 25°C. (*Adapted from Ref.* [59]).

1.3.2.2 *Adsorption kinetics in batch experiments*

One of the simplest ways to probe the diffusion of a given adsorbate is to measure the kinetics of adsorption through batch experiments. In a closed system, the adsorbent is placed in

contact with a solvent and then exposed to a given concentration of the adsorbate. Due to the changes in the liquid phase composition, it is possible to determine the amount of molecules adsorbed in the system as a function of time. This method is simple to apply but the diffusion properties can only be measured in systems where the diffusion is sufficiently slow. It has been suggested that the maximum diffusion coefficient that can be observed in crystals around 1 μm is of the order of 10^{-16} m²/s[62]. In the literature, there are studies carried out in closed batch systems to determine the diffusion of xylenes in faujasite-type zeolites. Moore and Katzer[59] identified the *px* and *mx* counter-diffusion coefficients for 1.1 μm NaY zeolite : respectively, $D \sim 10^{-16}$ m²/s and $D \sim 10^{-18}$ m²/s (the temperature of the test was 25°C and the solvent employed was cyclohexane). Later, Minceva and Rodrigues[63] obtained a micropore counter-diffusion coefficients for a Ba faujasite-type zeolite in a pellet shape (it is not specified in the study if X or Y zeolite was used) of 8×10^{-19} m²/s and 1.5×10^{-18} m²/s for *px* and *ox*, respectively. The tests were realized at 25°C and the solvent used was isooctane.

In order to obtain uptake curves in liquid phase batch experiments, the adsorbed amount as a function of time is calculated from the difference in adsorbate concentration in the liquid phase. In this case, since concentrations change in liquid phase occur, a correction to (Eq 26) must be applied as proposed by Crank[64]:

$$\frac{m_t}{m_\infty} = 1 - 6\sum_{n=1}^{\infty} \frac{\exp\left(\frac{-D_c p_n^2 t}{r_c^2}\right)}{\frac{9\Lambda}{(1-\Lambda)+(1-\Lambda)p_n^2}} \qquad \text{(Eq 31)}$$

where p_n is given by the non-zero roots of

$$\tan p_n = \frac{3p_n}{3 + (\frac{1}{\Lambda - 1})p_n^2} \qquad \text{(Eq 32)}$$

and Λ corresponds to the change in the concentration of the fluid phase by taking into account the initial concentration of the adsorbate C_0 and the concentration of adsorbate at equilibrium C_∞:

$$\Lambda = \frac{(C_0 - C_\infty)}{C_0} \qquad \text{(Eq 33)}$$

1.3.2.3 *Breakthrough curves*

Breakthrough experiments allow the characterization of the adsorbent in terms of selectivity and diffusion. These experiments are based on the principle of liquid phase chromatography and are widely used to test adsorbents for xylene separation[60,65–67]. In this type of experiments, a column is filled with an adsorbent that is initially saturated with a solvent. Subsequently, the feed mixture is injected in the column and the concentration of adsorbed solvent starts to decrease while the adsorbed feed concentration increases (Figure 14 (a)). This occurs because the molecules present in the feed are replacing the solvent molecules in the adsorbent. This process continues until the feed concentration is reached at the outlet of the column. During desorption, the opposite behavior is observed - the desorbent displaces the feed molecules previously adsorbed (Figure 14 (b)).

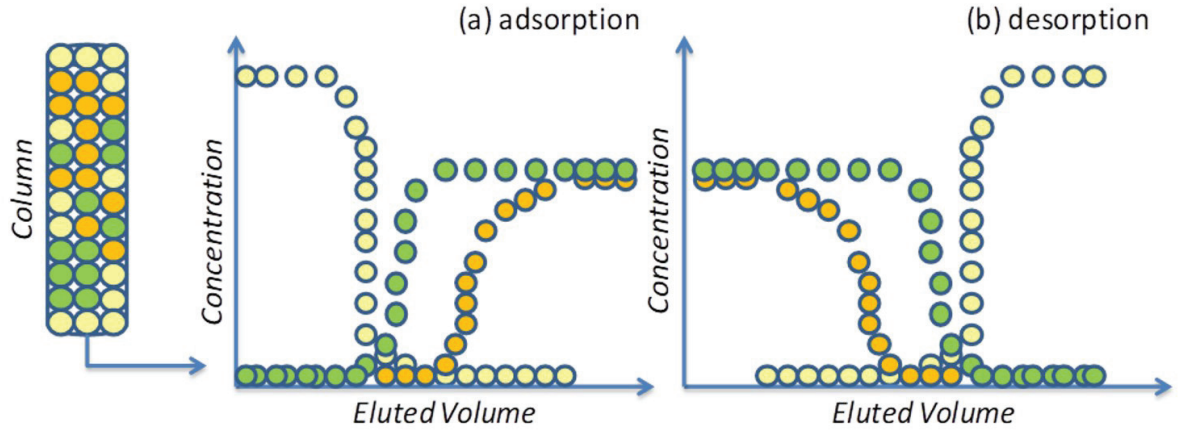

Figure 14. Breakthrough curve where the concentration of the solvent (yellow circles) decreases while concentration of xylene isomers in the adsorbent (green and orange circles) is enhanced (a) and reverse breakthrough curve showing opposite behavior (b). (*Adapted from Ref.* [68]).

It is possible to distinguish between the volume retained in the column and the volume collected at the output. The volume retained in the column corresponds to the microporous volume V_{μ} and the non-selective volume V_{ns} expressed as:

$$V_{ns} = V_{dead} + V_p + V_b \qquad \text{(Eq 34)}$$

where V_{dead} is the dead volume, V_p is the macroporous and mesoporous volume and V_b is the interparticle volume. V_p and V_b are determined by the introduction of a tracer in the feed - the tracer is a molecule that can access the same sites as the adsorbate but it is not strongly adsorbed in the micropores (measurement with the tracer therefore provides the non-selective volume). The selective volume V_{μ} can then be calculated using the following equation:

$$V_\mu = V_{input} - V_{output} - V_{ns} \quad \text{(Eq 35)}$$

Therefore, the selectivity of a specific adsorbate (*e.g. px*) with respect to another adsorbate (*i*) can be expressed in terms of adsorbed amount in the selective volume (V_μ) relative to the volume ratio (x) of molecules in the fluid phase mixture:

$$\alpha_{p-x/i} = \frac{V\mu_{p-x}/x_{p-x}}{V\mu_i/x_i} \quad \text{(Eq 36)}$$

The height equivalent to a theoretical plate (HETP) is a useful tool to describe mass transfer in adsorption columns. The HETP is defined as the distance in the column over which the fluid change from one state (fully saturated with solvent) to the other (fully saturated with feed). The HETP is expressed using moment analysis. Through the first and second moments, μ and σ, we can evaluate the adsorption equilibrium constant and the overall mass transfer resistance, respectively. The HETP as a function of first and second moments is defined as:

$$HETP = \frac{\sigma^2}{\mu^2} L = 2v \left(\frac{\in}{1-\in}\right) \frac{1}{kK} \left[1 + \frac{\in}{(1-\in)}\right]^{-2} \quad \text{(Eq 37)}$$

By plotting HETP *versus* the interstitial velocity *v,* the slope of the curve provides the overall mass transfer resistance $\frac{1}{kK}$. In turn, the mass transfer resistance is expressed as a series of resistance existing around and inside the pellet adsorbent (Eq 38). The first term is related to the hydrodynamic film around the particles. The second term is due to the resistance in extruded particles arising from the presence of the macropores. The third term corresponds to the micropore resistance:

$$\frac{1}{kK} = \frac{R_p}{3k_f} + \frac{R_p^2}{15 \in_p D_p} + \frac{r_c^2}{15KD_c} \quad \text{(Eq 38)}$$

where the first term can be lumped with the second term, since it accounts only for a small contribution to the total of the first and second terms[68]. Macropore diffusional resistance can be accessed through the tracer analysis. Then, the resistance in micropores is estimated by subtracting the macropore contributions from the global resistance:

$$\left(\frac{1}{kK}\right)_{micro} = \left(\frac{1}{kK}\right)_{adsorbate} - \left[\left(\frac{1}{kK}\right)_{tracer} \times \left(\frac{D_{tracer}}{D_{adsorbate}}\right)\right] \quad \text{(Eq 39)}$$

1.3.2.4 *Zero length column*

The zero length column (ZLC) method was initially designed to measure intracrystalline gas phase diffusion[69]. The basis of the method consists in exposing the adsorbent to a given adsorbate concentration until equilibrium is reached. Thereafter, an inert gas is used to purge the system and promote desorption of the adsorbate. A sufficiently high gas flow is used so that the concentration at the surface of the adsorbent is zero. The concentration of adsorbate in the effluent is measured in the outlet stream so that the desorption rate can be obtained. As many applications occur in the liquid phase, the ZLC method was later adapted[70]. Benzene desorption measurements were then performed by purging with liquid hexane in an X zeolite[70,71]. The ZLC method has been widely used since its invention for micro and mesoporous materials but especially in gas phase applications[72–75]. The ZLC method has also been used in the study of the diffusion in hierarchical zeolites[76,77]. However, no selectivity measurement can be made with this method. In the ZLC method, the solution model of the desorption curve is similar to that proposed by Crank[64]:

$$\frac{M_t}{M_\infty} = 1 - \sum_{n=1}^{\infty} \frac{6L^2 exp(-\frac{\beta_n^2 Dt}{R^2})}{\beta_n^2[\beta_n^2 + L(L-1)]} \quad \text{(Eq 40)}$$

where L is defined as:

$$L = \left(\frac{1}{3}\right)\left(\frac{Purge\ Flow\ rate}{Crystal\ Vol}\right)\left(\frac{R^2}{KD}\right) \quad \text{(Eq 41)}$$

At very high purge flow rates, the concentration surrounding the particle is maintained close to zero, $L \rightarrow \infty$, $\beta_n \rightarrow n\pi$ and the desorption curve is given by:

$$\frac{C}{C_0} = \frac{2}{L}\sum_{n=1}^{\infty} exp(-\frac{n^2\pi^2 Dt}{R^2}) \quad \text{(Eq 42)}$$

At longer times, where only the first term is taken into account, the solution becomes:

$$ln\left(\frac{C}{C_0}\right) = ln\left(\frac{2}{L}\right) - \frac{\pi^2 Dt}{R^2} \quad \text{(Eq 43)}$$

As a result, D/R^2 and L can be determined respectively from the slope and intercept of a plot of C/C_0 *versus* t.

2. *Materials and methods*

This chapter presents the hierarchical and conventional zeolites used throughout this thesis. Then, the techniques used to characterize these materials in terms of surface quantity and quality are presented. The last part of this chapter is devoted to describing the methods used to study xylene adsorption and diffusion within nanoporous media. Both gas phase thermogravimetry techniques and batch liquid experiments will be used for adsorption and diffusion measurements. In addition, the diffusion will also be studied by the means of pulsed-field nuclear magnetic resonance (PFG-NMR). The methods are summarized in Figure 15.

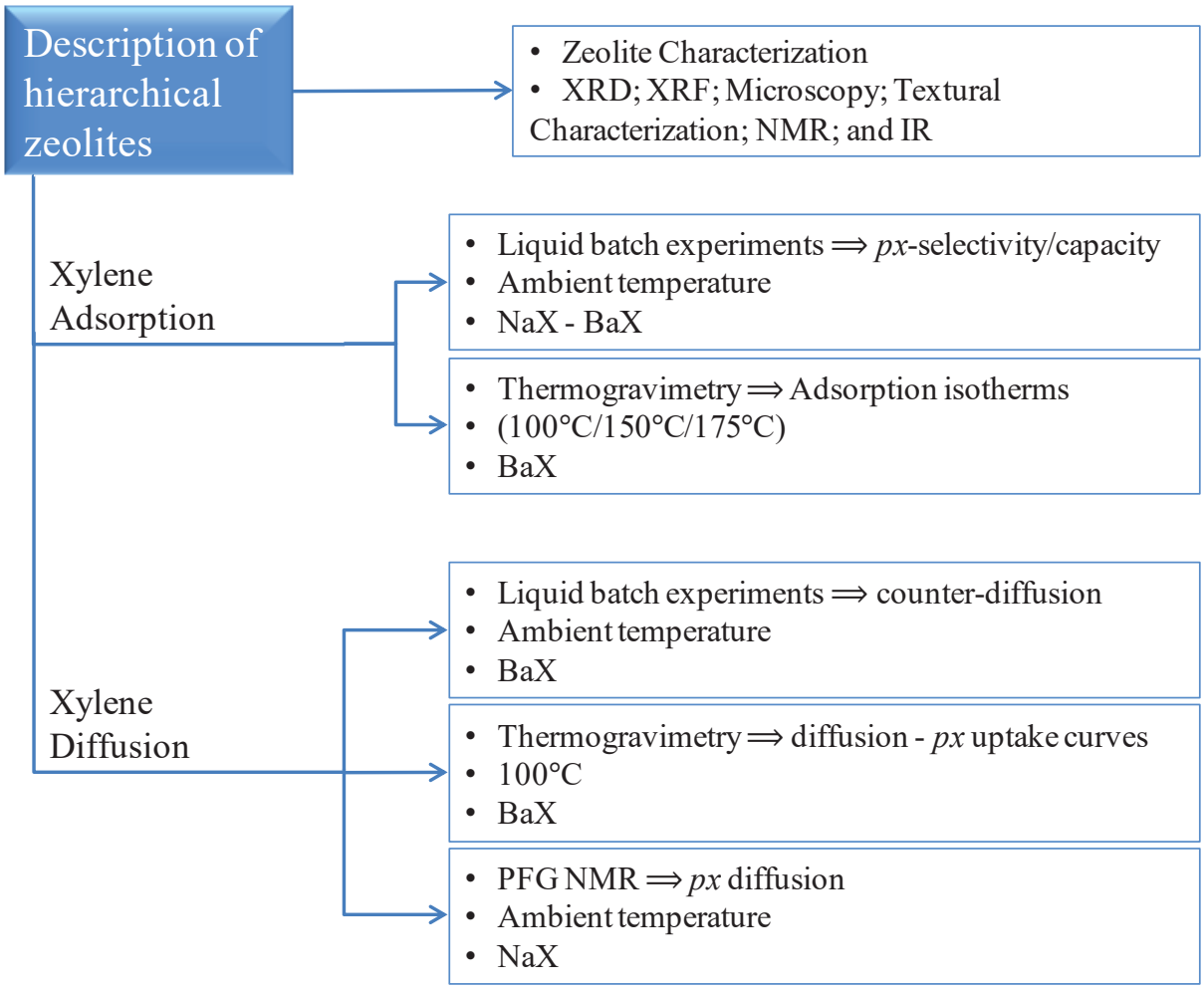

Figure 15. Summary of methods applied in the characterization and application of conventional and hierarchical zeolites.

2.1. *Zeolites*

Along this thesis, the diffusion and adsorption of xylenes in hierarchical and conventional type X zeolites will be studied. Hierarchical zeolites with two structure types are considered: nanoparticles aggregates (NA) and layer-like zeolite (LL) (Figure 16). The synthesis of the NA hierarchical zeolites was performed according to a patent (filing in progress at IFPEN). This synthesis methodology allowed us to obtain three zeolites with different external surface areas and mesoporous volumes. The LL zeolite was obtained from the Materials Engineering department at IFPEN. The synthesis methodology is also part of an IFPEN patent filing in progress. A conventional NaX zeolite was also considered in this study as a reference. This zeolite is a commercial NaX Siliporite G5PC obtained from Ceca-Arkema.

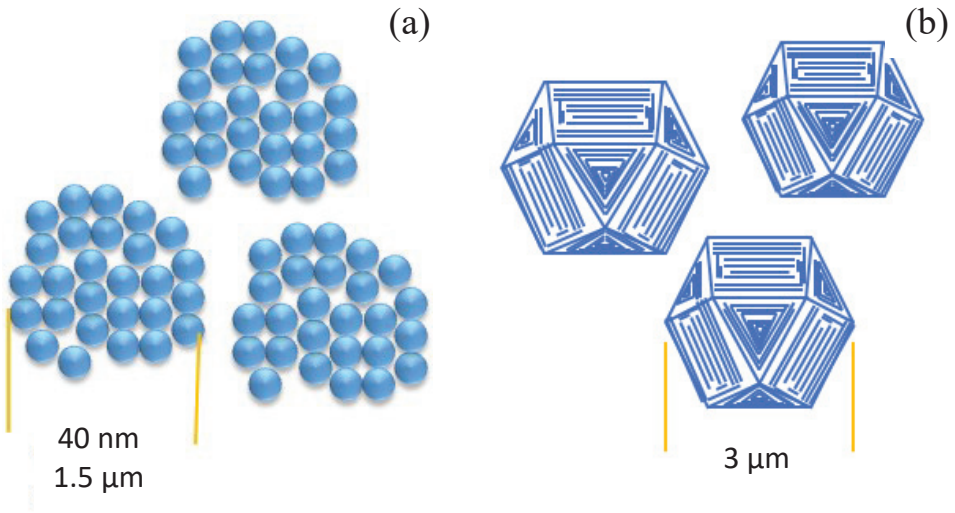

Figure 16. Representation of NA (a) and LL (b) hierarchical zeolites. The zeolite NA is formed by the aggregation of small crystals presenting mesoporosity between them. The zeolite LL is formed by an array of faujasite zeolite layers, which leads to the formation of inter- and intra-layer mesopores.

For the application of hierarchical zeolites to xylene separation, the BaX zeolite is used in industry. Therefore, the ion exchange step is necessary, as the starting material contains Na^+ as cations. The exchange was carried out in batches where the apparatus consists in a balloon coupled to a condenser. The Barium chloride ($BaCl_2$) solution used has a concentration of about $0.25 mol.L^{-1}$; the barium quantity corresponds to 800% of the required stoichiometric amount for a complete exchange. The procedure was performed at 80°C[78] for a period of 16 h and a stirring speed of 350 rpm. Once the exchange period is over, the solution is spontaneously cooled down and filtered under vacuum. Then, the solid is washed four times with 500 cm^3 permuted water. After filtration, the filtrate is left at room temperature for about 1.5 days in

order to evaporate the excess of water which may generate steam and cause damage to the material (when placed directly in the oven). Thereafter, the solid is taken to the oven and dried overnight at 100°C.

2.2. Characterization techniques

The most appropriate techniques selected for the characterization of conventional and hierarchical zeolites will be presented in this section. The characterization proposed here includes the determination of both the quantity and quality of the external surface in the different zeolites. The first part, devoted to characterization techniques for surface area assessment, comprises textural and morphological analysis as well as fundamental analysis such as X-ray diffraction (XRD). In the second part, the surface quality in terms of OH groups is investigated by means of Infrared (IR) and NMR spectroscopies.

2.2.1 *Surface area*

2.2.1.1 *X-ray diffraction*

The principle of X-ray diffraction technique is based on the incidence of X-rays through a crystal. The crystal diffracts the beam at a 2θ angle which is measured by a detector. The diffraction condition is observed when the Bragg law is verified: $\lambda = 2d\sin\theta$ where λ is the wavelength of the incident radiation and d is the distance between two atomic diffraction planes. The X-ray diffraction patterns are considered as the fingerprint of a given material since each crystal with a given symmetry has a unique and specific diffraction pattern[79]. It is therefore possible to identify the type of zeolite in a sample by comparing the obtained diffraction pattern to those available in the literature. The XRD analyses in this thesis were carried out on a diffractometer Bruker AXS D4 Endeavor at IFPEN. The X-ray source is an anticathode with copper-Kα radiation (λ = 1.5418 Å). The data are collected using a "Sol-XE" energy dispersive detector.

2.2.1.2 *X-ray fluorescence*

In the fluorescence analysis, the electrons in the sample are excited to a more energetic level through an incident radiation. Afterwards, these electrons return to their initial energy state and emit X-rays which are characteristic of this transition energy. The wavelength of the emitted radiation and its intensity are characteristic of the type of element and its concentration in the sample, respectively. The quantification of the cationic exchange Na→Ba in the zolites was done by X-ray fluorescence using Axios equipment from Panalytical. Prior to analysis, the zeolites were treated at 550°C for 4h.

2.2.1.3 *N_2 adsorption*

The adsorption of gases such as N_2 and Ar at low temperature is frequently used to determine the textural properties of zeolites and other types of porous materials. From the adsorption isotherms, the textural characteristics of zeolites can be obtained such as their microporous volume, meso/macroporous volume, and specific surface area. The pore size can also be assessed through N_2 adsorption at 77 K. In the literature, there are some widely used physical models for the interpretation of gas sorption isotherms such as the *t*-plot method for the micropore volume and external surface characterization and the BJH method for the mesopore size distribution. The analyses were performed on a Micrometrics ASAP 2420. The NaX samples were pre-treated at 350°C for 6h under vacuum and BaX zeolites at 250°C for 12h under vacuum.

2.2.1.4 *Mercury intrusion*

Mercury intrusion is a technique widely used to probe macropores. This technique consists in applying a controlled mercury pressure to the porous solid while recording the intruded volume[10]. The pore diameter *D* can be deduced from these data using the Washburn-Laplace equation:

$$P_c = \frac{-4\gamma \cos\theta}{D} \qquad \text{(Eq 44)}$$

where P_c is the capillary pressure, θ is the contact angle (~140°) and γ is the gas/liquid surface tension. The mercury intrusion analyses in this thesis were performed using a IV Autopore from Micromeritics. The pre-treatment was carried out at 250°C for 2h in a ventilated oven followed by 30 min in the desiccator.

2.2.1.5 *Electron microscopy and tomography*

The tomography techniques are widely used for the morphological characterization of zeolites. Advanced techniques such as electron tomography also permit the description of pore topology, which is particularly useful in understanding hierarchical zeolitic structures. In this work, scanning and transmission electron microscopies of both the external and internal surfaces of the zeolites will be evaluated. In addition, tomography analysis will be performed for one of the samples. The experimental conditions employed for each technique are described below.

2.2.1.6 *Scanning electron microscopy*

The scanning electron microscopy (SEM) acquisitions were performed in a low vacuum mode on a Nova Nano Sem equipment. The samples are first dispersed in ethanol. Then, a drop of this mixture is directly deposited on the sample holder. For the SEM-internal texture determination, the samples are impregnated with epoxy resin and, then, subjected to ionic polishing (5 kV for about 5 hours).

2.2.1.7 *Transmission electron microscopy*

The transmission electron microscopy (TEM) - internal texture was observed on a JEM 2100F equipment. The sample preparation consists in the impregnation of the zeolite crystals in an epoxy resin which is then cut with a diamond blade. The lamina cuts have a thickness around 70 nm. These nanometric slices are then transferred to a copper grid covered with a holey carbon membrane.

2.2.1.8 *Electron tomography*

The initial preparation consists in the immersion of the zeolite powder in ethanol. The goal of this first step is to disperse the crystals and favor a better visualization during the analysis. A drop of the suspension containing the zeolite crystals is deposited on a copper grid covered with a holey carbon membrane. A 5nm gold colloidal suspension is then deposited on the grid. Analyses were performed on a JEOL 2100F operated at 200 kV, which is equipped with a tomography holder. The angle amplitude was varied between -70° and +70° with an angular step of 1.5°.

2.2.1.9 *^{1}H 2D exchange spectroscopy nuclear magnetic resonance*

A ^{1}H 2D EXSY NMR experiment correlates the frequencies of ^{1}H spins during the evolution (t_1) and detection (t_2) periods[80]. The pulse sequence used in such experiments is described as follows: $\pi/2 - t_1 - \pi/2 - t_m - \pi/2 - t_2$ where t_1 corresponds to the evolution time, t_m to the mixing time and t_2 to the detection period. The chemical displacement of the proton depends on the confinement of the probe molecule in the pore where the proton is adsorbed, *i.e.* it varies with the pore size. In order to visualize proton exchanges in different media, the mixing time must be varied. Changes in NMR frequencies during the mixing time are recognized as leading to a cross-peak. Protons that do not change frequency lead to a diagonal-peak. Thus, a cross-peak indicates an exchange between two porous media (Figure 17).

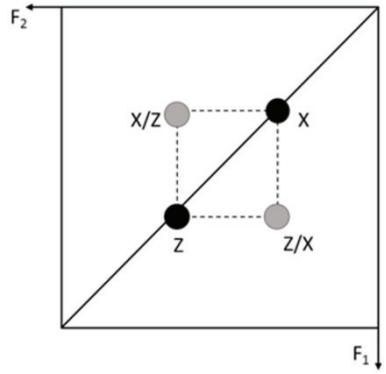

Figure 17. Schematic 2D map for spins (X and Z) in exchange. X/Z and Z/X indicate the presence of cross-peaks. (*Adapted from Ref.* [80])

Prior to NMR analysis, the samples were thermally activated under vacuum at 200°C for 6h in order to remove physisorbed water. Adsorption of a specific amount of xylene molecules (3 molecules/α cage), used as probe molecule, was carried out in a tent under argon atmosphere with the aid of a microsyringe. The transfer into the NMR rotor was done in a glovebox. ^{1}H 2D EXSY NMR experiments were recorded on a Bruker Avance 700 spectrometer operating at 700.03 Hz. The mixing time was varied from 0.5 to 300 ms. A 90° pulse (ca. 10 µs) was used. 8 scans, with a recycle delay of 1s, were recorded. The chemical shifts are referenced to that of adamantane (δ = 1.85 ppm, SR = 32.51 Hz). The 2D experiments were performed under magic angle spinning (MAS) conditions with a spinning rotation of 10 kHz.

2.2.2 *Surface chemistry*

2.2.2.1 *Fourier-transform infrared spectroscopy*

Through infrared spectroscopy, one can identify the composition of groups in a given sample by means of the frequency of the stretching vibration[13]. In the case of zeolites, for example, infrared spectroscopy allows the characterization of OH groups[13]. These groups lead to peaks appearing at wavenumbers between 3200 and 4000 cm^{-1}. The characterization of the OH groups is of great importance for the study proposed in this thesis since it is expected to be a key parameter in the surface effects on adsorption and diffusion of xylenes. The bands indicating the presence of OH groups in faujasite zeolite, especially at the outer surface, are described in the literature and the corresponding IR frequencies are presented in Chapter 3. The Fourier-transform infrared spectroscopy (FTIR) analyses were performed on a Nexus spectrometer with samples undergoing a pre-treatment at 400°C under vacuum for 10h in the case of NaX zeolites and at 250°C under vacuum for 10h in the case of BaX zeolites. The spectra were normalized by the sample mass.

2.2.2.2 *Nuclear magnetic resonance*

The nuclear magnetic resonance (NMR) technique allows studying the environment of nuclei that present an angular momentum[81]. In the case of zeolites, the main isotopes analyzed by means of NMR are ^{1}H, ^{29}Si, ^{27}Al and ^{17}O. Such analysis allows the identification of silanol groups[82] as well as the observation of Al atoms in different environments (tetrahedral or octahedral-extra framework). In the case of zeolites containing Si and Al, ^{29}Si NMR is able to identify the environment of each Si in the structure. In practice, each signal in the ^{29}Si NMR spectrum corresponds to a specific number of Al bound to the Si tetrahedron[81]. In this study the samples were analyzed by magic angle spinning MAS ^{29}Si NMR on an Avance 400 spectrometer from Bruker. The sequence High-power ^{1}H decoupling (HPDEC) was used. The rotation velocity of the samples was set to 7 kHz. The relaxation time was 20 s and the acquisition time of about 0.034 s. In the case of ^{1}H NMR analyses, the samples were activated at 450°C/10h under vacuum and then analyzed by ^{1}H proton MAS NMR, in a 4 mm MQMAS probe in a Bruker Avance 400 spectrometer (9.4 T). The ^{1}H MAS NMR spectra are obtained using the spin echo sequence at a speed of 12 kHz. This sequence consists in applying a pulse of $\pi/2$ (4.75 μs) followed by a π (9.5 μs) pulse at 53 kHz. NMR spectra were normalized by sample mass and number of scans.

2.3. *Xylene adsorption and diffusion*

In this section, the investigation methods for xylene adsorption and diffusion in conventional and hierarchical zeolites will be described. Initially, the procedures performed in the gas phase using a thermobalance and pulsed field gradient NMR are described. In the second part of this section, the methods used in liquid phase batch experiments are presented.

2.3.1 *Thermogravimetric analyses*

The thermogravimetric analysis was used to measure the diffusion and adsorption of xylenes in conventional and hierarchical zeolites in a partially saturated medium (gas phase). The apparatus used for this analysis and the methodology used for diffusion and isothermal adsorption measurements are presented below.

2.3.1.1 *Apparatus*

The thermogravimetric analyses are performed in a thermobalance (SETARAM B 24). A simplified scheme of the thermobalance is represented in Figure 18 (a). It is composed of two symmetrical ovens, each one containing a sample holder: the reference side which contain glass beads used as a reference and the sample side which contains the sample. The unit is also equipped with three lines of gas. The first line goes directly to the top (T) of the balance to protect the electronic components. The second line goes to the reference side (RS) while the third line is connected to the sample side (SS). The latter comes from a saturator where nitrogen gas is saturated with xylene (Figure 18 (b)). In this type of balance the flow of the reference side has to balance the flow on the side of the sample. 100 sccm[†] were then used at each side.

In the saturator, the temperature of the sealed xylene container (Figure 18 (b)) is defined by a heating collar and controlled by a thermocouple in contact with liquid xylene. When the system is at equilibrium, the partial pressure of *px* in the carrier gas is considered to be equal to the vapor pressure of *px* at the measured temperature. The saturator is also equipped with a set of dilution lines that allow mixing the nitrogen gas charged with xylene with more nitrogen gas (indicated by arrows in Figure 18 (b)), being then able to work with different xylene partial pressures. In this way, the variation of the xylene concentration is instantaneous which allows

[†] sccm - standard cubic centimeters per minute – T = 0°C/ P = 1 atm

the study of diffusion and adsorption of xylenes. The system is also equipped with a flowmeter that regulates the gas flow after dilution; this system therefore allows a variation of the xylene partial pressure without changing the total flow that reaches the thermobalance.

(a)

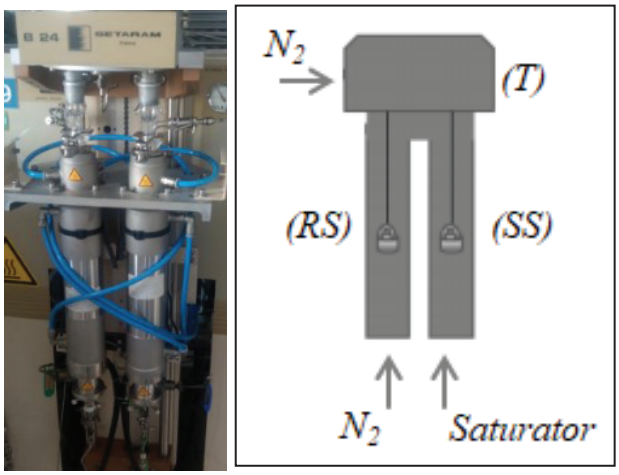

(b)

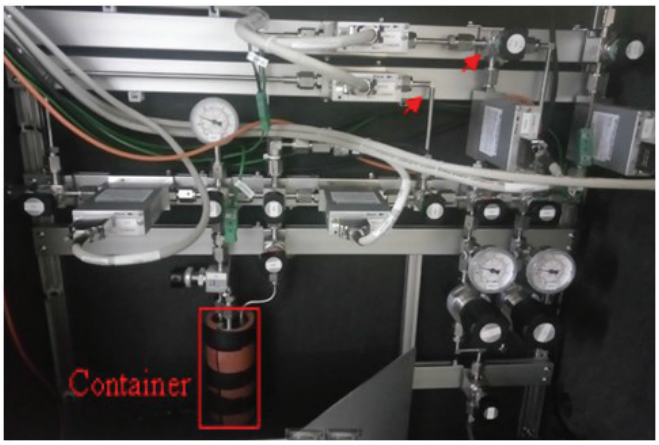

Figure 18. Representation of the thermobalance showing its two parallel ovens and the gas inlet streams (N_2 gas line on the reference side and saturator line on the sample side) (a) and gas saturator showing the xylene container (b). The arrows indicate the two dilution stages in the system (b). The flow diagram of the saturator is shown in Annex 1.

2.3.1.2 *Desorption of samples*

Before carrying out the experiments for diffusion or isotherms measurements, the samples are evacuated at 200°C for 6 h under N_2 flow. To avoid possible degradation of the zeolite structure, a slow temperature ramp to a first dwell at 100°C is carried out, as indicated in the scheme below (Figure 19). After desorption step, the temperature is adjusted to the test temperature.

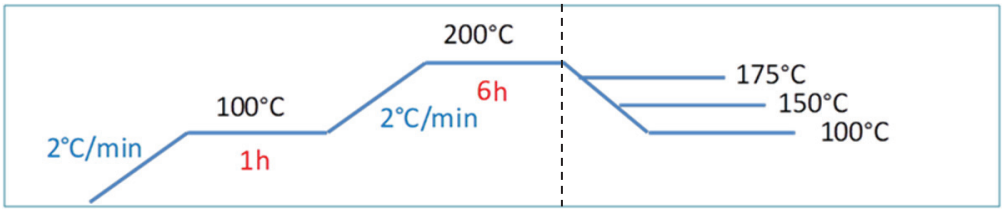

Figure 19. Heat treatment scheme for sample desorption prior to measurements (left side of dashed line). Temperature of xylene adsorption (right side of dashed line).

2.3.1.3 *Diffusion experiments*

The diffusion experiments were performed at 100°C. For the diffusion measurements, an increase in the xylene partial pressure is generated and the response in terms of mass uptake as a function of time is monitored. Based on the uptake rate, the apparent overall diffusion coefficient can be determined according to the diffusion model presented in Chapter 1[64]:

$$\frac{m_t}{m_\infty} = 1 - \frac{6}{\pi^2}\sum_{n=1}^{\infty}\frac{1}{n^2}exp\left(-\frac{\pi^2 D_c t}{r_c^2}\right) \qquad \text{(Eq 45)}$$

where $\frac{m_t}{m_\infty}$ is the fractional filling, D_c is the intracrystalline diffusivity, r_c is the crystal radius and t is the time.

Diffusion measurements were performed starting from an empty zeolite. The uptake curves are measured at 0.03 mbar of *px* after degassing the sample according to the conditions described in Figure 19. All diffusion tests were performed at 100°C.

2.3.1.4 *Adsorption isotherms*

Prior to the adsorption measurements, the samples are degassed as described in Figure 19. The adsorption isotherms are measured by varying the xylene pressure inside the thermobalance. After each pressure change, the system is kept under the same conditions until equilibrium is reached. The construction of the adsorption isotherm is done by determining the correlation between the partial pressure of xylene and the mass measured in the thermobalance under equilibrium conditions for the same xylene partial pressure. The pure *px* and *ox* isotherms were measured at temperatures of 100°C, 150°C and 175°C. The conditions of the tests performed are shown in Table 2.

Table 2. Experimental conditions for the adsorption isotherms measurements, where *px* and *ox* are the adsorbate molecules.

	P (mbar)	T(°C)
px	0.03/ 0.11/ 0.60/ 1.16/ 2.17/ 3.14/ 4.49/ 5.81 and 15.7	100, 150 and 175
ox	0.02/ 0.08/ 0.45/ 0.87/ 1.63/ 2.36/ 3.37/ 4.37 and 11.8	100, 150 and 175

2.3.2 *Pulsed field gradient NMR*

By means of pulsed field gradient NMR (PFG-NMR) techniques one can measure the self diffusivity (D_s) of molecules. The distance traveled by the molecule during PFG NMR analysis is limited by the observation time (diffusion time). The use of field gradients makes it possible to spatially mark the molecules and observe their displacement. The measurement of the NMR diffusion coefficients is based on the fact that the attenuation of the NMR signal (total magnetic moment) depends on the relaxation mechanisms and on the displacements of the spins probed during the time of the experiment. In practice, the PFG-NMR experiment is based on a specific sequence of gradient pulses (Figure 20)[83,84]: A radio frequency ($\pi/2$) is used to turn the spins to the transverse plane, perpendicular to the (z) direction or the direction of the extern magnetic field. A first pulsed field gradient G, for a duration δ, promotes a spin phase shift (information coding): the spins are "marked" according to their position along the z axis by an associated value B_z. The system then evolves during a given time t (diffusion time) and a new pulsed field gradient with the same intensity and duration of the first gradient is applied. If the molecules do not move between the gradient pulses, the total magnetization remains unchanged. On the contrary, if the molecules diffuse, the total magnetization at the end of the experiment is smaller than the initial magnetization. This attenuation is related to the diffusion coefficient (D_s).

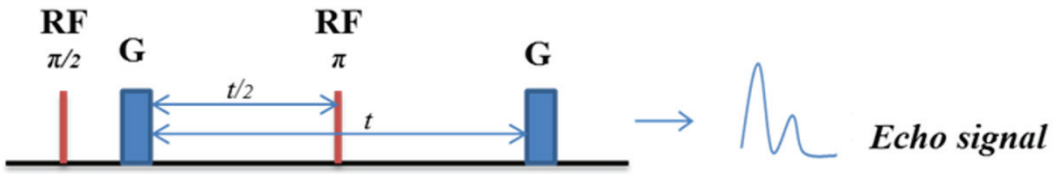

Figure 20. Basic example of sequence for PFG NMR experience showing the location of pulses of radio frequency and gradients field. The diffusion time t between the two gradient fields is also represented. (*Adapted from Ref.* [83])

Prior to PFG NMR analysis, the NaX samples were desorbed at 350°C/10h under vacuum. Adsorption of a specific amount of xylene molecules (3 molecules/α cage) was carried out in a glove box with the aid of a microsyringe. In this work, polarity gradient stimulated echo NMR (PGSTE) sequence was chosen, since it is more adapted to confined media.

2.3.3 *Liquid batch experiments at ambient temperature*

This section describes the methods used to characterize the counter-diffusion and selectivity in conventional and hierarchical zeolites. The batch method has been selected since it can be used with small amount of zeolite, under the form of crystal powder. Moreover, it can provide information on both the selectivity and diffusion properties of confined molecules. On the other hand, zero length column (ZLC) can only provide diffusion information. Breakthrough experiments provide information on both the selectivity and diffusion properties, but it requires a large amount of zeolitic material due to important dead volume in the experimental set-up. Furthermore, in order to avoid preferential path inside the column, the zeolites must be shaped with a binder under the form of a pellet or extrudate. The use of shaped zeolites makes the system more complex including a macroporous resistance inside the pellets, which leads to additional dispersion of the curve and more complex estimation of the diffusion resistance within the zeolite.

In this thesis, the adsorption and diffusion of xylenes in X zeolite was observed through batch experiments in the liquid phase in a closed system without humidity interferences. An amount of zeolite powder is suspended in liquid *normal*-decane (*n*C10) and at time $t = 0$ the xylene is introduced into the system. In the case of tests performed on NaX zeolite, sampling is done at equilibrium only (24 h) in order to check the selectivity. For tests on BaX zeolite, the method consists in performing sampling at different time intervals in order to follow the kinetics of xylene adsorption. The change of xylene concentration in the liquid phase allows determining the amount of xylene adsorbed in the zeolite. Thus, to ensure a precise determination of the xylene concentration, a solvent was used. The use of a solvent allows working with a low adsorbate/adsorbent ratio and, therefore, to observe larger step changes in the xylene concentration in the liquid phase. In the same time, the use of a solvent decreases the heat released during xylene adsorption. The solvent selected for this study was *n*C10 because it is

weakly adsorbed in the zeolite cages compared to xylenes. Therefore, it is not expected to interfere with xylene adsorption for xylene concentrations over 10 wt % [62].

2.3.3.1 *Preliminary tests on NaX zeolite*

Although zeolite NaX is usually not preferred in xylene separation, preliminary tests were carried out with this zeolite in order to observe the effect of surface selectivity. The motivation in using NaX zeolite is because it does not need an ion exchange step. In addition, NaX zeolite is not expected to be selective for any of the isomers, which results in selectivities close to one. This point should make it easier to identify a possible effect on total selectivity arising from the external surface area. The experimental tests on the NaX zeolite were carried out at saturation for the conventional zeolite and for the hierarchical zeolites of the NA type-structure.

Experimental Procedure

The xylene adsorption tests in NaX zeolite were performed by using the apparatus described in Figure 21. The experimental procedure is performed according to three main steps - (A) pretreatment of zeolites and hydrocarbons; (B) Introduction of zeolite, solvent, xylenes and subsequent sampling; (C) Sample analysis.

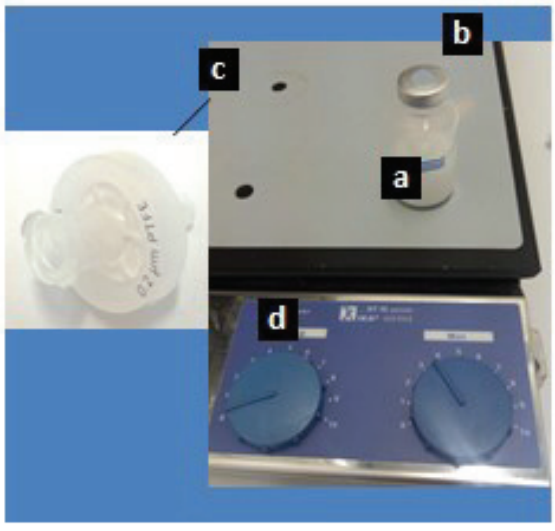

Figure 21. Description of the materials/equipment used for the xylene adsorption tests in NaX zeolites. (a) 30 cc glass vial; (b) Crimp Seal with a rubber septa; (c) Syringe filter; and (d) Magnetic stirring plate.

A. Pretreatment of zeolites and hydrocarbons

Prior to testing the zeolites are degassed. The heat treatment consists of a slow ramp (2°C/min) up to 100°C and a subsequent dwell at 100°C for 3h. This step allows the largest amount of water to be removed from the material at low temperatures in order to avoid possible degradation of the zeolite. Next, a new heating ramp (2°C/min) is carried out up to 350°C. The zeolites are then left at 350°C for 6 h to remove further adsorbed water residues. The whole procedure is done under N_2 flow (20 NL/h).

The hydrocarbons are also dried prior to testing. They are left in contact with a 3A zeolite, under stirring and at room temperature, until the amount of water is less than 15 ppm. The amount of water is measured using a Karl-Fischer titration.

B. Introduction of zeolite, solvent, xylenes and subsequent sampling

After the activation steps, the zeolites are recovered in glass bottles previously filled with argon and transferred to a tent also filled with argon to avoid contact with humidity. The zeolites are then weighed (around 1 g) into the glass flasks, previously containing magnetic stirring bars. Thereafter, a fixed volume of *n*C10 is added into the flask (already containing the zeolite powder) with the aid of an automatic pipette and the mass of *n*C10 is measured (around 7.3 g). The flask in then crimped, transferred out of the tent, and placed on a magnetic stirring plate. The system is stirred for at least 30 minutes and, then, the xylene mixture (50%:50% *px*/*ox* or 50%:50% *px*/*mx*) is injected with the aid of a syringe. The mass of xylene is measured by the difference between the mass of the syringe filled by the xylene and the mass of the empty syringe after the injection (~ 0.73 g).

A sampling is then made after 24 h with the aid of a syringe. At this point, the system is expected to reach equilibrium. During sampling, the stirring is interrupted for about 12 seconds before the liquid suction. In this way the zeolite powder is decanted at the bottom of the flask and only liquid is collected. Subsequently, the aliquots collected are filtered and transferred into crimped vials. The filtration is done using a 200 μm syringe-coupled filter, used once per sample. This step is required in order to avoid the presence of zeolite crystals eventually suspended in the solution (not visible).

C. Sample analysis

The samples are then analyzed by gas phase chromatography. In order to obtain more accurate analysis, each sampling aliquot was used to fill two vials to be analyzed by chromatography.

2.3.3.2 *Adsorption and diffusion on a BaX zeolite*

Two types of studies were carried out for BaX conventional and hierarchical zeolites:

1.Study of counter diffusion of a xylene mixture (50%:50% *px/ox* or 50%:50% *px/mx*) in a zeolite previously saturated with *n*C10. This type of experiment allows observing the competition between the diffusion and adsorption of different isomers at various loadings. With this experiment, it is possible to obtain information on the impact of the presence of other isomers in *px* diffusion. In addition, the *px*-selectivity can be determined throughout all the experiments and at the equilibrium point.

2.Study of counter diffusion of pure *px* in a zeolite previously saturated with *n*C10 and subsequent study of the selectivity after *ox* addition. In this case, the counter-diffusion of pure *px* can be observed. Moreover, the subsequent addition of *ox* allows observing the impact of *px* pre-adsorption on the selectivity.

Experimental Procedure

The xylene adsorption tests in BaX zeolite were performed by using the apparatus described in Figure 22. Like in the tests performed on NaX zeolites, the experimental procedure is performed in three main steps - (A) pretreatment of zeolites and hydrocarbons; (B) Introduction of zeolite, solvent, xylenes and subsequent sampling; (C) Sample analysis. Sections (A) and (C) are essentially the same as those for NaX zeolite, the only consideration is the maximum outgassing temperature in section (A). Here, the BaX zeolites are outgassed at 200°C instead of 350°C for the NaX zeolite. A lower temperature is applied in the case of BaX zeolite since its structure is more fragile. Step B is described in what follows for the tests in the BaX zeolite.

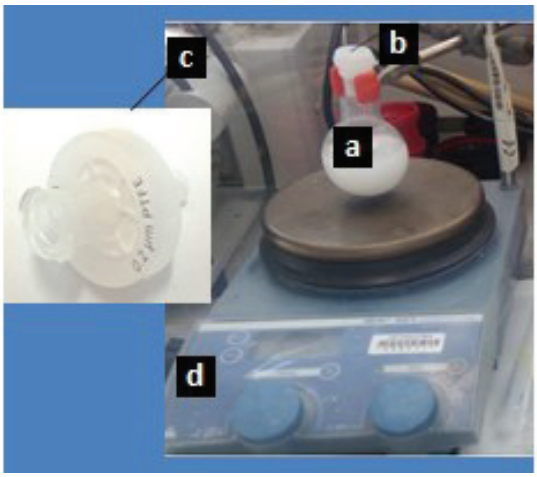

Figure 22. Description of the materials/equipment used for the xylene adsorption tests in BaX zeolites. (a) 50 cc glass Ballon; (b) Rubber stopper; (c) Syringe filter; and (d) Magnetic stirring plate.

A. Introduction of zeolite, solvent, xylenes and subsequent sampling;

After the activation steps, like for NaX zeolites, the zeolites are recovered in glass bottles previously filled with argon and transferred to a tent also filled with argon to avoid contact with humidity. The zeolites are then weighed (around 2.5 g) into the glass balloon (50cc). Thereafter, a fixed volume of *n*C10 measured with the aid of an automatic pipette is added into the balloon (already containing the zeolite powder) and the mass of *n*C10 is measured (~25 g).

The balloon is then covered with a sealed rubber stopper, transferred out of the tent, and placed under a magnetic stirring plate. The balloon containing the mixture is stirred for at least 30 minutes and, then, around 2.5 g of xylene (xylene mixture - Study 1 or pure *px*- Study 2) is injected with the aid of a syringe. The mass of xylene is measured by the difference between the mass of the syringe filled with xylene and the mass of the empty syringe after the injection.

At the time xylene is added, the timer is triggered and sampling is done at certain time intervals. Sampling is done using a syringe and the mass of each aliquot is measured from the difference between the empty syringe and the syringe containing the liquid after sampling. During sampling, the stirring is interrupted for about 12 seconds. In this way the zeolite powder is decanted at the bottom of the balloon and only liquid is collected. After sampling the stirring is immediately restarted. Subsequently, the aliquots collected are filtered and transferred into crimped vials. The filtration is done using a 200 µm syringe-coupled filter, used once per sample. This step is required in order to avoid the presence of zeolite crystals eventually suspended in the solution (not visible).

For Study 1 - In general, the analyses were performed at time intervals between 5 min and 24 h. For the conventional zeolite, the sampling is done by intervals of 20 min until 3h, and then a last sampling is made at 24 h. In the case of hierarchical zeolites, the sampling is more frequent (on average, every 5 min) until the first hour, then a sampling is done at 3 h and another at 24 h.

For Study 2 - The same sampling scheme done for study 1 up to 3 h is performed. However, after the first three hours, about 2.5 g of *ox* is added to the system and a sampling is done after 24 h.

2.3.3.3 *Method to estimate the amount of xylene adsorbed in the zeolite*

The method used to estimate the adsorbed xylene mass consists of estimating the mass of *n*C10 adsorbed from a hypothesis considering the amount of *n*C10 adsorbed in the zeolite with respect to the microporous volume of the zeolite. In the literature this ratio was already estimated for a *n*parafin in faujasite zeolite. About 85% of the microporous volume defined by nitrogen sorption is occupied by the *n*C10 molecules[2]. Then, the remaining adsorbed mass of *n*C10 during xylene adsorption can be estimated as:

$$m_{ads}^{nC10} = (0.85\,.\,V_{N_2}^{micro}.\,d_{nC10}) - \left(\frac{m_{ads}^{px}}{d_{px}} + \frac{m_{ads}^{(m)(o)x}}{d_{(m)(o)x}}\right).\,d_{nC10} \qquad \text{(Eq 46)}$$

where d denotes the density and m_{ads}^{px} and $m_{ads}^{(m)(o)x}$ are, respectively, the mass of *px* and *mx* or *ox* adsorbed.

The mass of the solution is obtained from the following relation:

$$m_{sol} = \frac{\left(m_i^{nC10} - m_{ads}^{nC10}\right)}{C_{nC10}} \qquad \text{(Eq 47)}$$

where m_i^{nC10} is the amount of *n*C10 introduced into the system and C_{nC10} is the concentration of *n*C10 in the solution. m_{ads}^{nC10} is the estimated mass of *n*C10 that remains adsorbed in the zeolite even after the xylene adsorption.

Then, the quantities of *px* and *mx* or *ox* in solution are estimated as follows:

$$m_{sol}^{px} = C_{px} m_{sol} \quad \text{(Eq 48)}$$

$$m_{sol}^{(m)(o)x} = C_{(m)(o)x}\, m_{sol} \quad \text{(Eq 49)}$$

The amount of xylene adsorbed is then calculated by taking into account the total amount of xylene introduced into the system, the mass of sampling and the amount of xylene still present in the solution:

$$m_{ads}^{px} = \left(m_i^{px} - m_{sampling} \,.\, C_{px}\right) - \, m_{sol}^{px} \quad \text{(Eq 50)}$$

$$m_{ads}^{(m)(o)x} = \left(m_i^{(m)(o)x} - m_{sampling} \,.\, C_{(m)(o)x}\right) - \, m_{sol}^{(m)(o)x} \quad \text{(Eq 51)}$$

Then, the adsorbed mass of xylene is expressed in terms of molecules/α cage:

$$n_{molecule/\alpha\ cage} = \frac{\left(m_{ads}^{xyl} \cdot \frac{MM_{zeo}}{MM_{xyl}}\right)}{8\,.\,m_{zeo}} \,.\left(\frac{V_{standard}^{micro}}{V_{N_2}^{micro}}\right) \quad \text{(Eq 52)}$$

where MM_{zeo} and MM_{xyl} are respectively the molar mass of the zeolite unit cell and xylene molecule. The "8" represents the number of α cages per unit cell. $V_{standard}^{micro}$ corresponds to the micropore volume of an ideal crystallized X zeolite, while $V_{N_2}^{micro}$ is the micropore volume measured by N_2 sorption for the tested zeolite.

3. Characterization of conventional and hierarchical X-type zeolites

The surface characterization of the different hierarchical zeolites as well as conventional zeolite (conv.) considered in this work will be presented and discussed in this chapter. The results will be first presented for NaX zeolites followed by those for BaX zeolites. At the end of the chapter, a short conclusion synthesizing the main characteristics of these zeolites will be given.

3.1. NaX zeolite

3.1.1 *Surface area*

Regardless of the interplay between adsorption/diffusion phenomena in the different porosity domains, the external surface area characterizing the different samples is expected to be one of the main descriptors related to the global separation performance of the hierarchical zeolites. As a consequence, different techniques have been employed to quantify the amount of external surface. The techniques employed also allow investigating the characteristics of the different types of porosity in terms of volume and pore size distribution. A morphological characterization was also performed in order to characterize the crystals shape and pores arrangement.

3.1.1.1 *X-Ray diffraction and fluorescence*

X-ray diffraction is a very important tool for the characterization of zeolites. In particular, this technique allows probing the zeolitic phase(s) present in a given sample. Figure 23 shows the X-ray diffractograms for the different hierarchical zeolites and for the conventional NaX zeolite considered in this work. The data for the hierarchical zeolites correspond well to those for the X zeolite structure since the same XRD pattern is observed for all materials. As expected, the zeolite LL also exhibits some EMT phase, as identified from a shoulder seen at low diffraction angles (marked with an asterisk)[31]. In addition, a small contamination of zeolite P can be observed for the sample LL. The arrows in Figure 23 identify

the most intense peaks of phase P. EMT phase is also present in sample NA-3. An estimation of the amount of NaX phase in zeolites NA-3 and LL was made based on the diffraction pattern for zeolite NA-2. The sum of the amplitudes of the first four diffraction peaks for the NA-2 zeolite was used as a reference value for NaX zeolite. This value was compared to those for the NA-3 and LL zeolites to determine their degree of crystallinity. The results indicate NaX phase crystallization of at least 75% in NA-3 and 90% in LL. It is important to note that this result is only indicative of NaX phase crystallization since NA-2 zeolite was not synthesized under the same conditions as NA-3 and LL zeolites

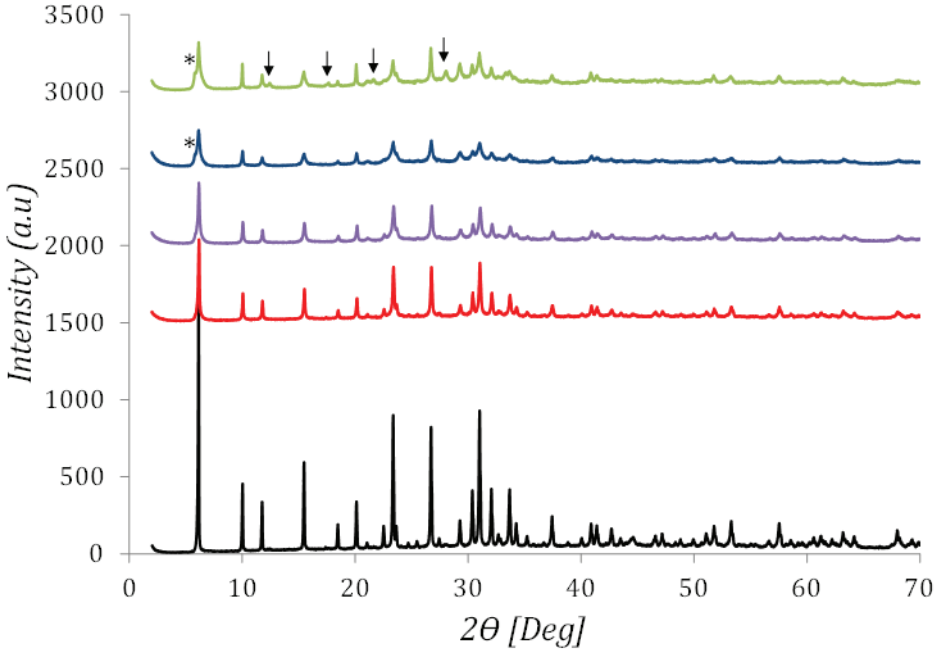

Figure 23. XRD patterns of the conventional NaX zeolite (black line) and NaX hierarchical zeolites: NA-1 (red), NA-2 (purple), NA-3 (blue) and LL (green). The arrows indicate the peaks corresponding to zeolite P.

We also see from the comparison between Figure 23 and Table 3 that there is an effect of the crystallite size on the intensity of the peaks, which makes the comparison above even more uncertain.

Following this reasoning, it should also be noted that the conventional zeolite present some sharp intense peaks while the hierarchical zeolites display broader peaks. This behavior is associated to the fact that hierarchical zeolites present smaller crystallite sizes[85]. Indeed, the XRD data also allow obtaining information such as the crystallite size based on the width of the peaks.

The Scherrer equation correlates the peak width at half height with the crystallite size[86]:

$$C_{size} = \frac{k\lambda}{B(2\theta)cos\theta} \quad \text{(Eq 53)}$$

where $k = 0.9$ is the shape factor for spherical particles, λ is the X-ray wavelength, $B(2\theta)$ is the peak width at half height and θ is the diffraction angle.

The crystallites sizes determined according to the Scherrer equation are presented in Table 3. The size of the hierarchical crystallites is significantly smaller than that of the conventional zeolite. In addition, the size of the crystallites decreases from NA-1 to NA-3 while LL zeolite presents crystallite size similar to NA-3. It is interesting to note that the size of the crystallites does not necessarily correspond to the size of the crystals due mainly to structure defects and aggregation. A proof of this is that the conventional NaX zeolite has well-defined crystals of diameter around 1.5 μm as observed by microscopy (Figure 24) while the size of crystallites is about 0.18 μm. The Si/Al ratio was measured by means of X-ray fluorescence (Table 3). As can be seen, the composition of these zeolites indicates a fairly low silicon content.

Table 3. Crystallite size measured according to the Sherrer equation.

Zeolite	Crystallite Size (nm)	Si/Al
Conv.	180	1.14
NA-1	70	1.09
NA-2	50	1.08
NA-3	30	1.13
LL	30	1.10

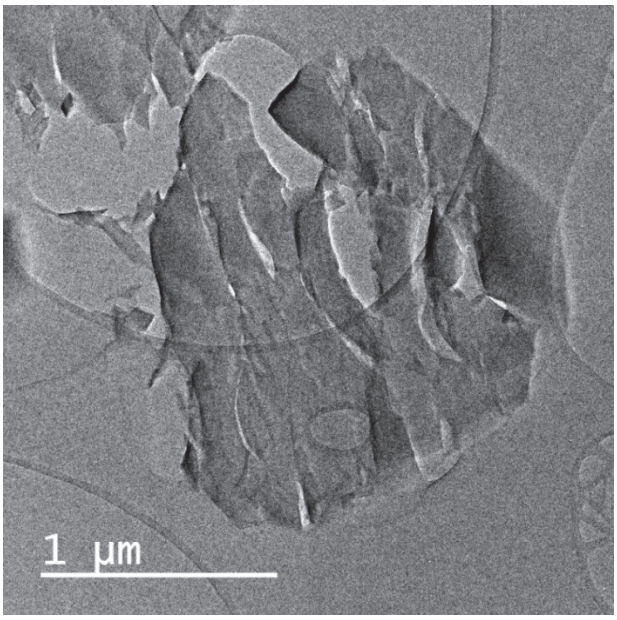

Figure 24. TEM - diamond cutting image for conventional NaX zeolite. The zeolite has the form of well-crystallized crystals of about 1.5 µm size. The crystals are damaged upon cutting.

3.1.1.2 *Microscopy techniques and tomography*

These techniques allow one to directly observe the morphology and topology of a given material. Electron tomography is used to observe the structure of the porous system. Recently, such data allowed to reconstruct a 3D multiscale model, which was used to investigate transport and diffusion features in different domains[87]. In turn, SEM and TEM were satisfactorily employed to study the morphology and the mesopores array in a hierarchical faujasite-type zeolite[30]. These techniques also provide supplementary information about the pore size, the presence of distinct phases[31], as well as the presence of other elements such as cracks and amorphous materials.

In this work, the morphology of the zeolites was explored using microscopy techniques such as SEM, TEM and Electron Tomography. These techniques allowed confirming the presence of meso/macropores as well as their size and arrangement. The crystal size could not be determined for any of the hierarchical zeolites, since they are aggregated or in the form of a house of cards such as in LL zeolite. This makes it impossible to determine boundaries for the crystals. Regarding the NA-type hierarchical zeolites, the size of the NA-1 aggregates was estimated from the measurement of at least 100 units, as observed in the histogram in Figure 25. Aggregates mainly around 0.8 and 1.5 µm were found. On the other hand, the size of NA-2 and NA-3 aggregates could not be measured, although visually NA-2 and NA-3 have smaller

crystals than NA-1 (as can be observed in SEM images in Figure 26). For the zeolite LL, the zeolites layers are grouped forming particles with spherical shape (Figure 27). The size of such particles is also described through a histogram in Figure 25. The size of the particles was found to be mainly between 1.6 and 3.8 µm.

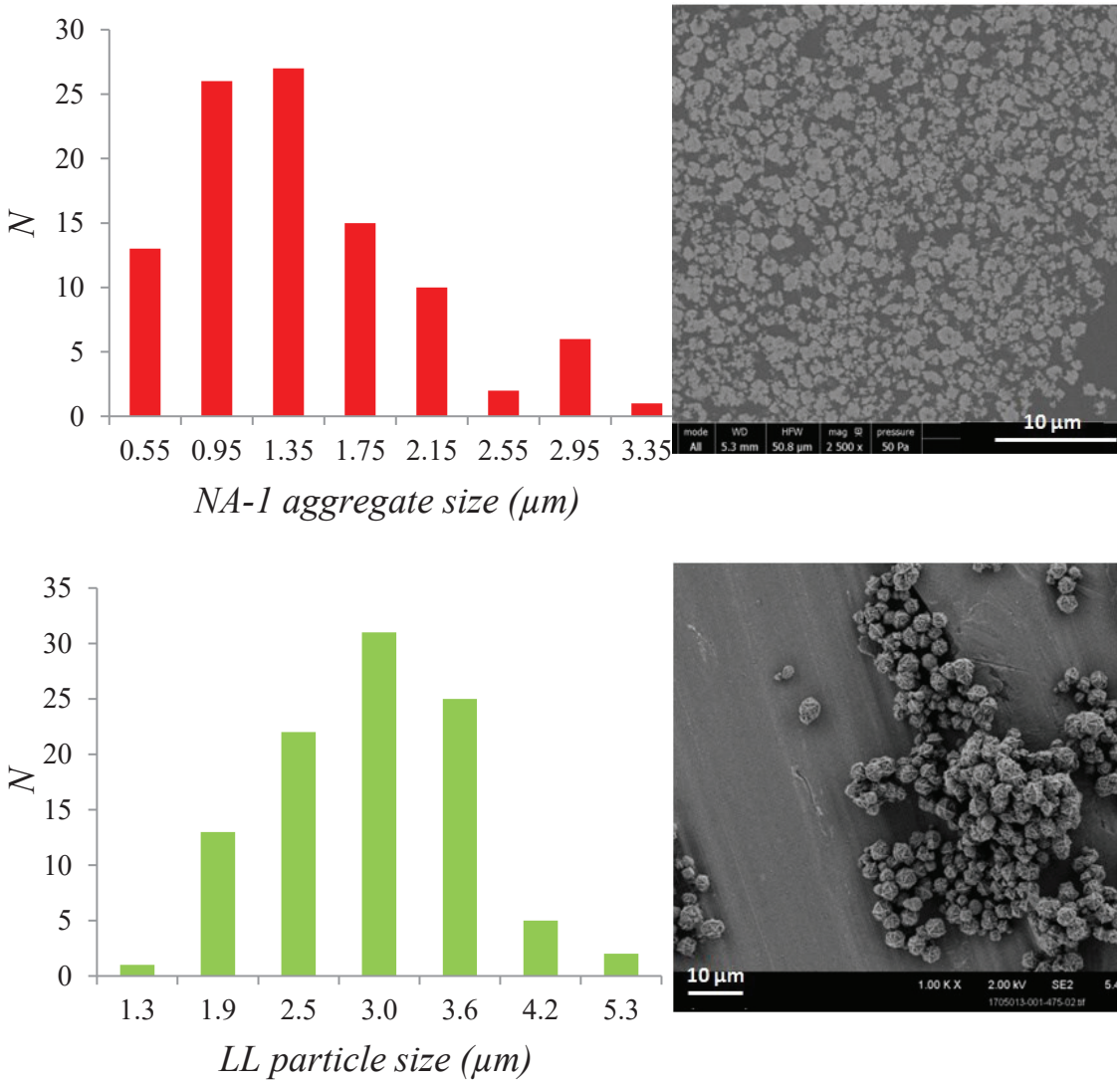

Figure 25. Histogram showing the non normalized size distribution for the NA-1 aggregates (*top*, red) and for the LL zeolite particle size (*bottom*, green). Surface scanning electron microscopy (SEM) images are also shown for each sample on the right side of the corresponding histogram.

The morphology of zeolites can be observed in Figure 26 (1st column) by SEM images. The NA samples exhibit an aggregated particle morphology with most particles having no well-defined shape (even though some of them have a plate-like shape). The particles forming these aggregates appear larger and thicker for NA-1 than for the other NA zeolites. In the case of NA-

1, the particles are aggregated into a sphere-like aggregates. Domain boundaries in the aggregates become less and less identified from NA-1 to NA-3. The LL zeolite is made up of large spherical particles which consist of a house of cards structure of zeolite layers. Regarding the SEM pictures made on cross polished sections (magnification - 2 μm) (Figure 26), it is possible to classify the NA materials in two main groups. A group with lower external surface area, represented by NA-1, presents larger dense microporous domains *per* agglomerate. Some meso and macropores appear to be radially distributed within the agglomerates. It is also possible to observe the presence of larger macropores (*D* ~100-150 nm), which appear to be located in the center of the aggregates. On the other hand, the group with larger external surfaces area, comprising NA-2 and NA-3, has a smaller apparent mean size of crystals/agglomerates and less regular boundaries compared to NA-1. Nevertheless, some large macropores are also present in the center of the agglomerates. Furthermore, we can identify several meso/macropores. In the case of the NA zeolites, the TEM pictures on cross-polished section suggests the presence of channels connecting these macropores with the external surface. In addition, as will be discussed hereafter, the N_2 sorption isotherm for NA zeolites does not provide evidence that these macropores exhibit constrictions.

Figure 27 also shows SEM and TEM images for the LL zeolite. In this case, it can be noted the presence of macropores, connected to the exterior of the structure, formed by the arrangement of zeolite layers. These pores/entries can be seen in more detail in Figure 27. The internal structure of the zeolite was also observed through SEM analysis on cross- polished section (Figure 26). The entries do not look as deep as they appear to be in SEM images (Figure 27 (a)). Moreover, the crystals appear to have dense edges with macropores located at the heart of the particles - which can reach up to 0.5 μm in length. Crystal slices were also observed through TEM. In this case, more details such as the presence of small mesopores can be observed. In an attempt to identify the connectivity of macropores, a TEM image was made with a magnification allowing us to visualize the whole diameter of a sphere shape, created by the array of the zeolites layers (Figure 26 - third column). However, connections between the outside of the particle and the internal macropores could not be visualized - the shadows appearing in the picture are rather cutting defects during sample preparation. In addition, the N_2 adsorption isotherm shape indicates cavitation (as will be detailed later) – which is consistent with macropores being surrounded by a microporous matrix.

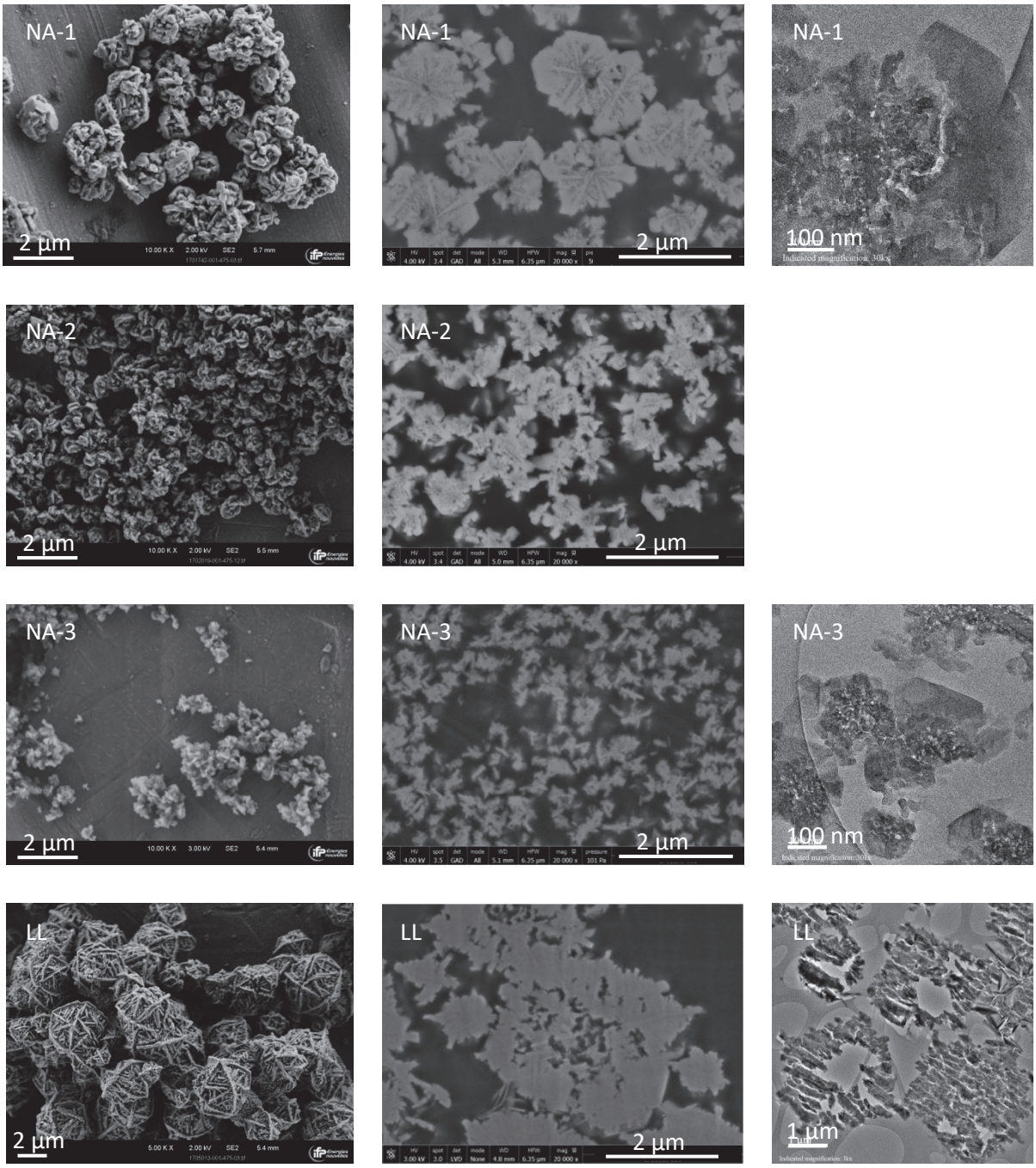

Figure 26. SEM images of the hierarchical zeolites (first column); images of the inner texture of the crystals obtained by SEM-ionic polishing (middle column) and TEM - diamond cutting (third column).

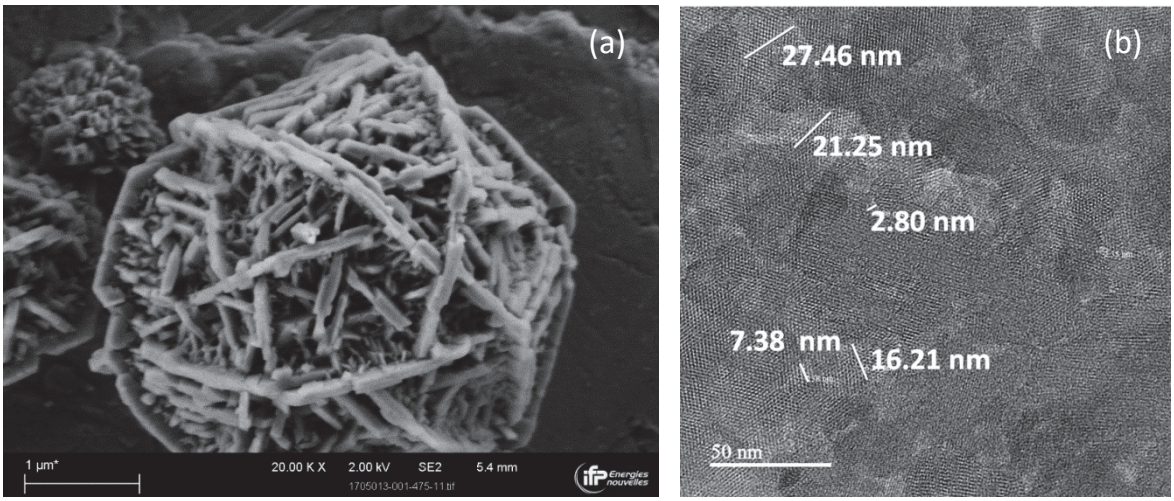

Figure 27. (a) SEM image for the LL zeolite showing the arrangement of the layers and the external pores formed between them; (b) TEM - diamond cutting image for the LL zeolite showing some mesopore size measures.

To get more insights into the topology of the crystals/aggregates, an electron tomography study was performed[88]. NA-1 sample was chosen to be analyzed through electron tomography because it presents the best analysis conditions - aggregates do not have a large size and are well dispersed. Tomography cannot be performed on highly agglomerated samples, since individual crystal viewing cannot be done. Moreover, the analysis of large crystals results in a low resolution tomography[89]. The other samples did not meet the required conditions to be analyzed. NA-2 and NA-3 samples are highly agglomerated and difficult to disperse while LL shows large crystal size. The purpose of the tomography experiments conducted in this thesis is the analysis of the whole topology of the aggregate. The series of images obtained using the 3D tomography reconstruction provides information about the porosity of the agglomerate at different depths. As can be seen in Figure 28, the images confirm that the aggregate edges are dense and made up of micropores. At a depth of 140 nm and deeper, a large porosity in the aggregate is noticed, indicating that these aggregates have a high porous heart. Such meso/macropores appear to be highly accessible from the outer surface along the entire depth where they appear (140-350 nm), as indicated by the arrows in some pictures.

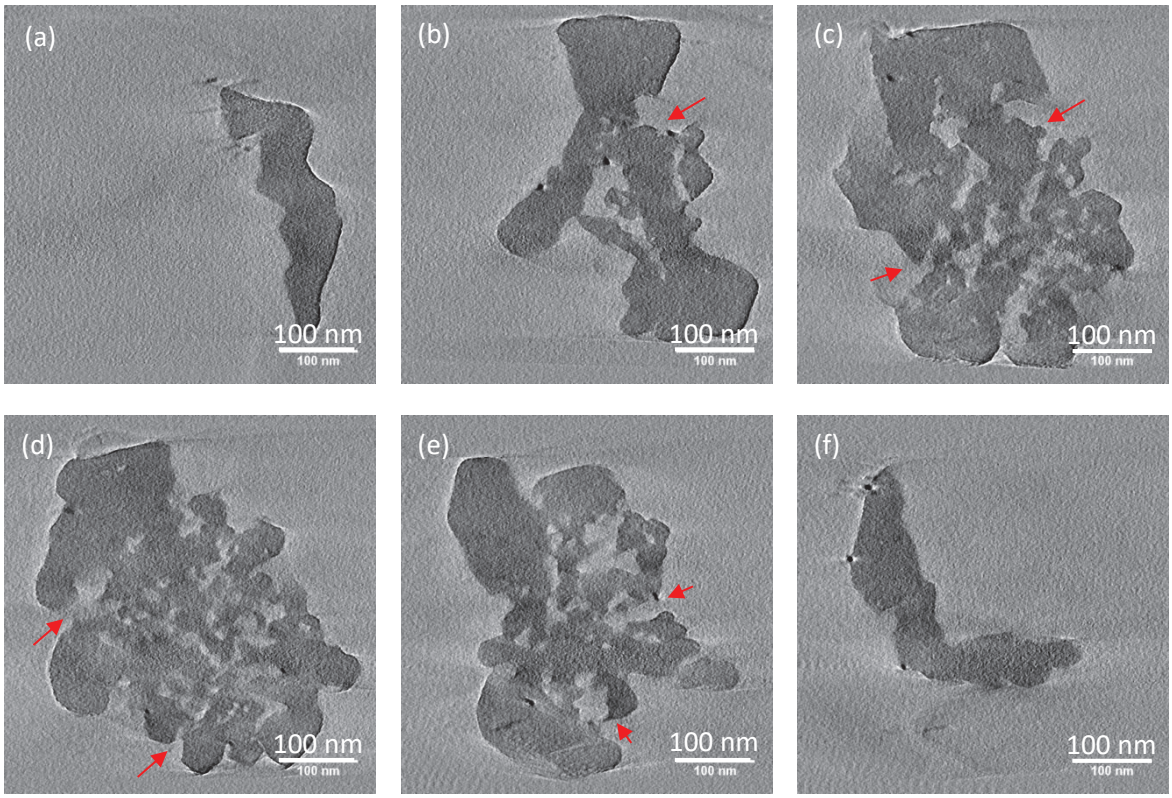

Figure 28. Images obtained from electron tomography reconstruction for NA-1 hierarchical zeolites. Each slice has a 0.8 nm thickness and the images were obtained at different depths: (a) 60 nm, (b) 140 nm, (c) 230 nm, (d) 280 nm, (e) 350 nm and (f) 400 nm.

3.1.1.3 *Textural characterization*

Adsorption isotherms and capillary hysteresis analysis – The N_2 adsorption isotherms are expressed in terms of relative pressure (*x* axis) *versus* adsorbed amount (*y* axis). These adsorptions isotherms were classified by IUPAC[90] in six different types according to their shape. Each adsorption isotherm type is related to the adsorption phenomena relevant to a specific class of materials. Figure 29 shows the classification of some types of adsorption isotherms according to IUPAC[90]: Type I adsorption isotherm is representative of microporous solids having relatively small external surface area. A large amount of adsorbed volume corresponding to the filling of micropores is observed at low relative pressures. In type IV, the adsorption isotherm is characterized by the presence of a hysteresis loop which is associated to capillary condensation taking place in mesopores. The regime before the hysteresis corresponds to monolayer-multilayer adsorption.

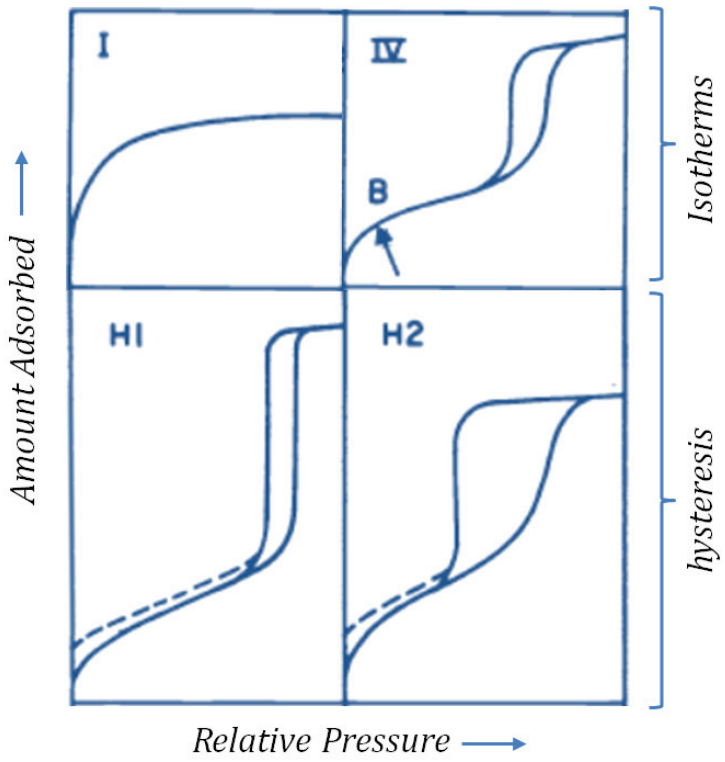

Figure 29. Adsorption isotherms and hysteresis shapes as defined by IUPAC. (*Adapted from Ref.* [90]).

As can be seen in Figure 29, some adsorption isotherms present a hysteresis loop which is caused by capillary condensation. Capillary condensation is the gas/liquid phase transition that occurs in mesopores larger than a critical diameter of about 4 nm when the adsorbate is N_2 at 77 K. The shapes of the hysteresis loop (Figure 29) are also used to characterize the presence of some specific pore structures[91,92,93]. For example, type H1 is representative of materials with uniform and ordered pores[91,94,95]. In contrast, in the case of type H2 hysteresis, materials do not exhibit a well-defined distribution of pore sizes and shapes; it is usually associated to large pores accessible by narrow necks[96,97] .

The observation of the adsorption isotherm shapes and hysteresis loops is also important for the characterization of the arrangement of the pores in hierarchical zeolites. If the adsorption isotherm for a hierarchical zeolite corresponds to the superimposition of the parental adsorption isotherms[58,98], it can be assumed that the mesopores are accessible from the outer surface (Figure 30 (a)). On the other hand, the mesopores access from the outer surface can be limited due to the connected pores/pores entries of smaller diameters (Figure 30 (b) and (c)). When the diameter of the small pores connected to the larger mesopores is less than the critical diameter of 4 nm (~0.42 P/P_0), pore desorption occurs through cavitation (Figure 30 (c)). Cavitation is the phenomenon in which desorption of a large pore occurs through the spontaneous nucleation of a gas bubble that forms in the pore[99]. Desorption occurs while neighboring smaller pores are

still filled, so that the desorption pressure is not related to the diameter of the smaller pores (0.42 P/P_0 - N_2 cavitation pressure at 77 K). An extreme case of the presence of cavitation may be represented by mesopores surrounded by a microporous matrix, although cavitation may also exist when small mesopores (< 4 nm) are the means of access to large pores. Another possible scenario is when the access to large mesopores occurs through smaller mesopores, but this time the latter have a diameter larger than the critical cavitation diameter (D > 4 nm - N_2 at 77 K). In this case, desorption occurs through pore blocking and the hysteresis closing pressure is larger than the cavitation pressure (Figure 30 (b)). In the case of pore blocking, the diameter of the smaller pores can then be deduced from the pressure at which the hysteresis closes[97,100].

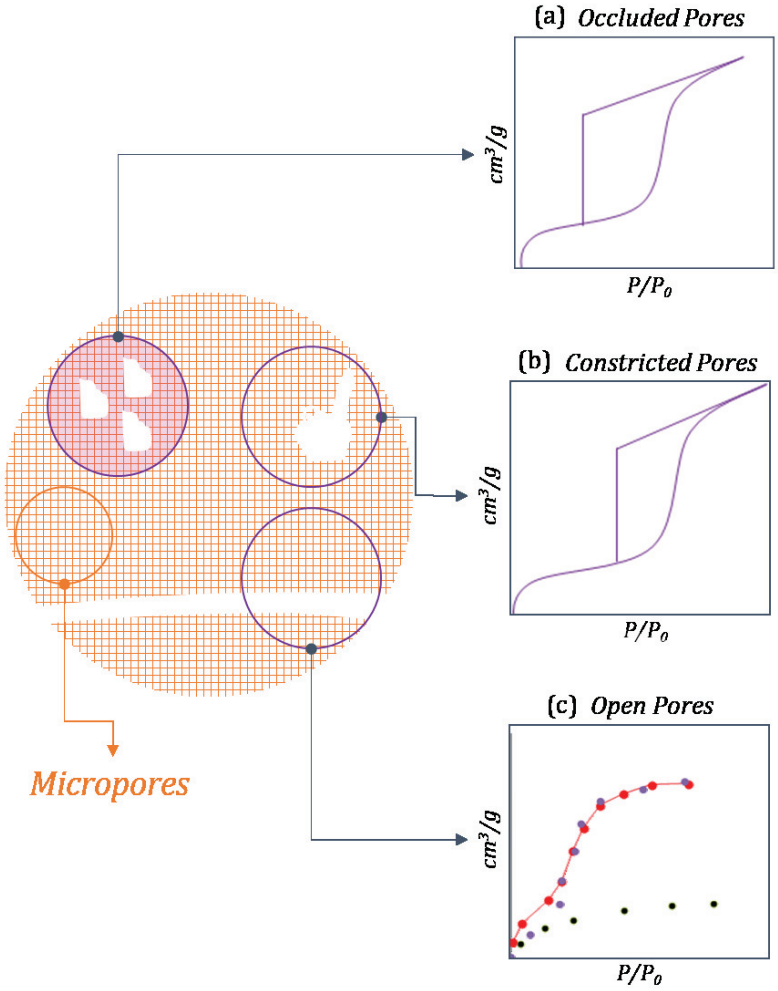

Figure 30. Adsorption isotherm shapes for hierarchical zeolite and the correlation with mesopores array: (a) mesopores accessible to the external surface, (b) mesopores constricted by necks, and (c) mesopores isolated by a microporous matrix. The shaded area shown for occluded pores indicate the state of surrounding micropores during desorption. When a critical partial pressure in the case of occluded pores is reached, the mesopores desorbs while the surrounding micropores remain filled. (*Adapted from Ref.* [100]).

In this thesis, the N_2 adsorption isotherms at 77K were measured for the different zeolites (Figure 31). These adsorption isotherms can be classified as a combination of types I

and IV according to the IUPAC classification. We recall that Type I is characteristic of microporous materials, with strong adsorption in the micropores at low relative pressures. The second part of these adsorption isotherms is similar to type IV, as capillary condensation occurs at higher relative pressures in the mesopores. This phenomenon is supported by the presence of capillary hysteresis loops. The shape of the adsorption isotherms shown in Figure 31 demonstrates the hierarchical nature of these zeolites, as they are representative of materials with both micro and meso/macropores.

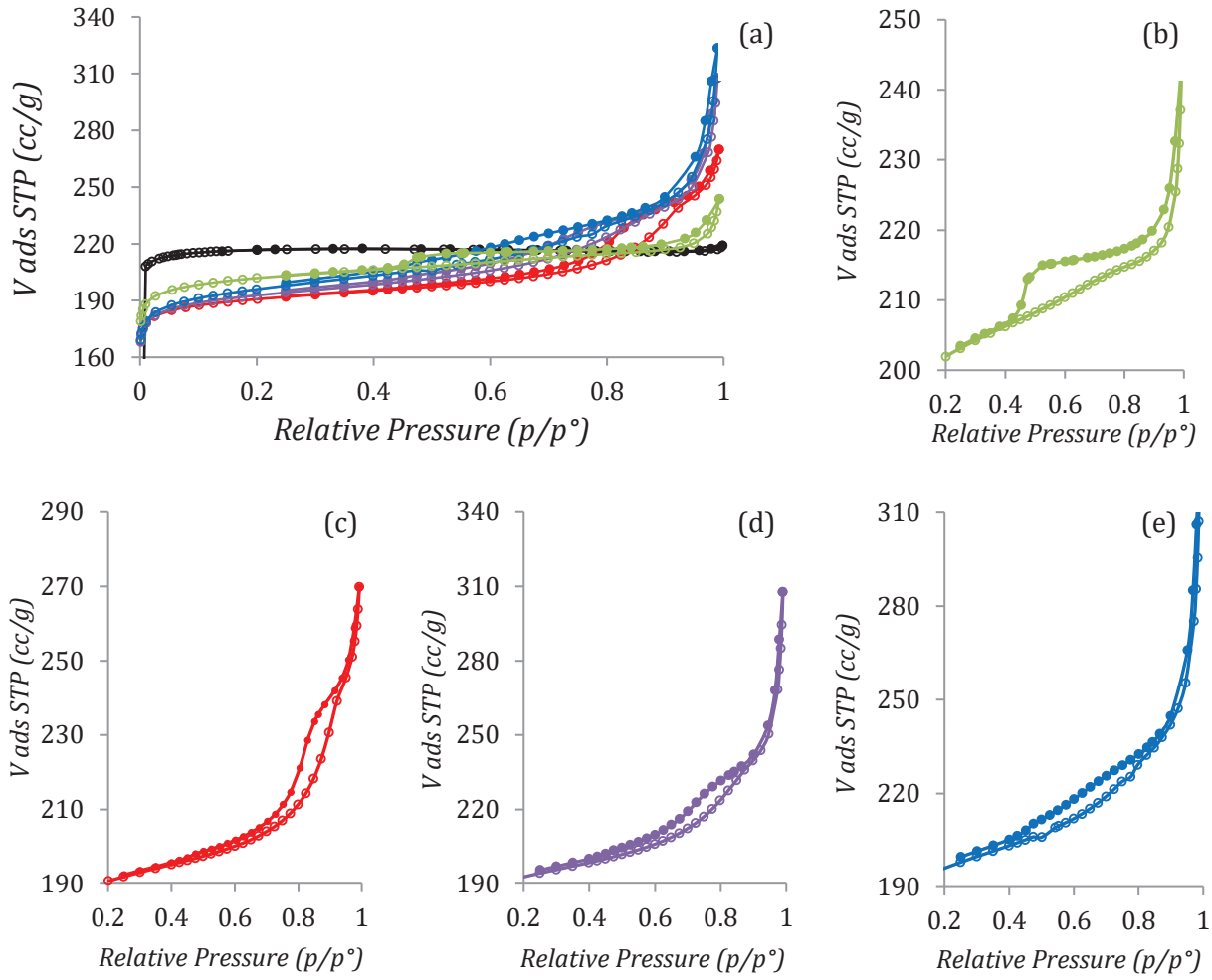

Figure 31. N_2 sorption isotherms at 77 K for the conventional NaX zeolite (black line) and NaX hierarchical zeolites: LL (green), NA-1 (red), NA-2 (purple) and NA-3 (blue) (a); (b-e) are enlargements showing the hysteresis with more detail.

The classification of the hysteresis loops and desorption mechanisms in Figure 31 is not evident in the case of NA hierarchical zeolites. Indeed, the hysteresis loops present neither a parallel adsorption and desorption branches nor an abrupt closure behavior. These adsorption

isotherms rather suggest a combination of different phenomena occurring upon desorption as a result of their complex pore structure. More details will be obtained through the analysis of hysteresis scanning curves presented hereafter. In the case of the Layer-like type (LL), through a simple analysis of the hysteresis, it can be said that desorption occurs predominantly through cavitation. However, other analyses such as mercury intrusion and microscopy will allow us to confirm or invalidate this hypothesis. Throughout this chapter, different information elements will be collected and combined to elucidate the pore arrangement in these materials.

Textural parameters **-** The *t*-plot method is frequently used to determine the microporous/mesoporous volume of porous solids as well as their external surface area. This method consists in plotting the adsorbed volume of N_2 $N_{ads}^0(P)$ as a function of $t(P)$, where $t(P) = N_{ads}^0(P)/\rho_0 S_{ext}$ is the average thickness of an adsorbed film on a reference solid having the same surface chemistry. ρ_0 is the density of the liquid N_2, and S_{ext} is the external surface area of the standard material (reference). Different *t*-methods are described in the literature for the interpretation of *t*-plot in different material types. These models generally employ a *t*-curve as a reference (similar to the adsorbent being analyzed). For example, the Harkins-Jura *t*-plot equation, which is frequently employed to analyze zeolitic materials, is based on the adsorption of N_2 on a nonporous alumina[101]. The *t*-plot method is also used to determine the microporous and total pore volume[101]. The determination of the micropore volume consists in tracing a linear trend based on the linear correspondence between the adsorbed volume and the thickness of an adsorbed layer on a nonporous surface. In general, this correspondence is made for a thickness layer between 0.35 and 0.5 nm. The micropore volume is determined from the *Y*-axis intercept of the extrapolated line.

Despite the importance of the *t*-plot and the ease in applying such method, some studies in the literature have reported that the *t*-plot method may underestimate the micropore volume and overestimate the external surface area[102,103]. As an alternative to the conventional *t*-plot, it was decided to apply an original model, herein denominated *direct identification*. This model is proposed based on a previous work by Remy and Poncelet in 1995[103]. This model describes the adsorption in porous materials by combining the contributions for adsorption in the micropores and at the external surface. This model promotes an accurate identification of the textural parameters and seems to be very promising in the characterization of hierarchical zeolites, considering that such materials present an increased external surface area.

For the *direct identification,* the two mechanisms occurring upon nitrogen adsorption up to a relative pressure about 0.42 are taken into account:

1. Micropore filling (V_{micro}) is determined according to the Dubinin equation[104] as the predominant mechanism at low relative pressure (P/P_0);

$$V_{micro} = V_0 e^{\left(-\frac{RT}{E} ln\left(\frac{P}{P_0}\right)\right)^2} \quad \text{(Eq 54)}$$

where V_0 is the total micropore volume, R is the universal constant of gases, T is the temperature and E is a characteristic energy for a standard adsorbate/solid system.

2. Adsorption at the external surface area which prevails at higher relative pressures. The corresponding adsorbed volume is given by the product of the external surface area S_{ext} and the thickness t at a given partial pressure).

$$V_{Sext} = 0.001 S_{ext} t \quad \text{(Eq 55)}$$

where S_{ext} is the external surface area (m^2/g), t is the thickness of the statistical layer adsorbed on the external surface in nm – according to the Harkins – Jura model. 0.001 is the conversion factor in order to obtain V_{Sext} in cm^3/g.

The total adsorbed volume is given the sum of both contributions:

$$V = V_{micro} + V_{Sext} = V_0 e^{\left(-\frac{RT}{E} ln\left(\frac{P}{P_0}\right)\right)^2} + 0.001 S_{ext} t \quad \text{(Eq 56)}$$

Finally, by the least squares method, the parameters of the Dubinin equation as well as the external surface area can be determined.

The textural parameters obtained using the direct identification method for the conventional and hierarchical zeolites NA and LL are given in Table 4. Note that, although the adsorption isotherms were given in STP (cm^3/g) in Figure 31, the textural parameters in Table 4 are given in cm^3/g. The mesoporous volume, also presented in Table 4, was obtained by the difference between the total adsorbed volume (obtained at relative pressures P/P_0 close to 1) and the microporous volume. In order to compare the results from different methods, the micropore volume and external surface area were determined through the direct identification, Dubinin-Radushkevich (VD) and *t*-plot for different adsorbed film thicknesses. Figure 32 shows the graphical representation of the experimental data and the different models: *t*-plot regressed at different thicknesses and direct identification. It can be seen that the direct identification leads to the best correspondence with the experimental data. Another interesting

point is that the *t*-plot for larger thicknesses (0.45 - 0.6/0.7 nm) better fits the experimental curve compared to the conventional *t*-plot (thickness 0.35 - 0.5 nm).

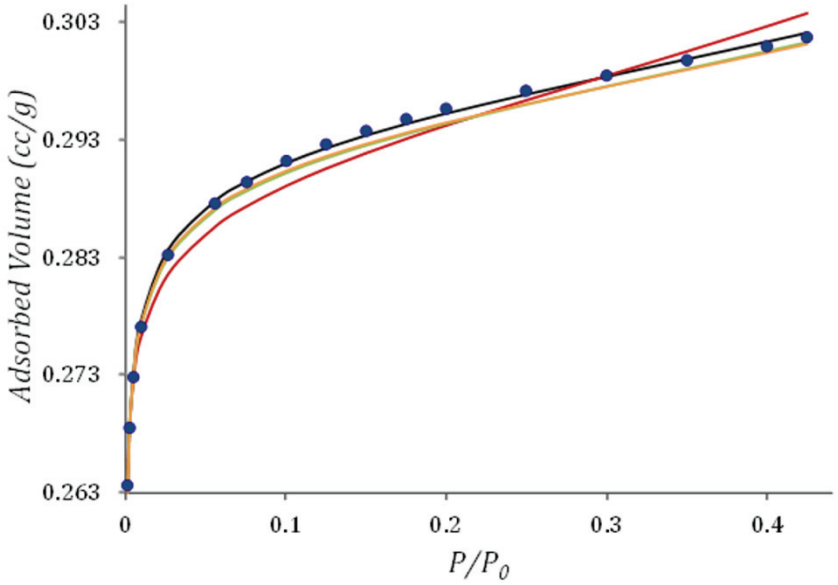

Figure 32. N_2 adsorption isotherm at 77 K for the NA-1 hierarchical zeolite (circles), the direct identification model (black line), and *t*-plot at different thicknesses: 0.35-0.50 nm (red line), 0.45-0.60 (green) and 0.45-0.7 (yellow line).

The results in Table 4 suggest that the Dubinin volume overestimates the micropore volume. Moreover, the larger the external surface area, the larger the overestimation. Concerning the *t*-plot in the commonly considered thickness range (t_1 = 0.35 - 0.5 nm), the micropore contribution is underestimated while the external surface area is clearly overestimated. However, considering larger adsorbed film thicknesses (t_2 and t_3), more realistic micropore volume and external surface area are found (close to those obtained by the direct identification method). Therefore, it is confirmed that the adsorbed film thickness influences the determination of both the micropore volume and the external surface area as already indicated in the literature[103].

Table 4. Textural properties for the conventional and hierarchical zeolites obtained by different methods: Direct identification (D_I), Dubinin (V_D) and *t*-plot for different adsorbed film thicknesses (t_1= 0.35-0.5 nm; t_2=0.45-0.6nm; t_3=0.45-0.7nm).

Zeolite	V_{micro} (cc/g)					S_{ext} (m^2/g)				V_{meso}
	D_I	V_D	t_1	t_2	t_3	D_I	t_1	t_2	t_3	(cc/g)
Conv. NaX	0.34	0.34	0.32	0.33	0.34	-	25	3	-	-
NA-1	0.28	0.30	0.27	0.28	0.28	38	58	39	37	0.12
NA-2	0.27	0.30	0.26	0.27	0.27	64	84	66	66	0.16
NA-3	0.27	0.31	0.26	0.27	0.27	83	103	83	79	0.18
LL	0.29	0.31	0.28	0.29	0.29	45	70	48	43	0.05

Finally, the accuracy of the direct identification method must be highlighted, especially for a refined determination of the textural parameters as in the case of hierarchical zeolites. As can be seen in Table 4, a range of external surface areas between 40 and 80 m^2/g is found by the different samples. In the case of the microporous volume, the conventional zeolite presents the largest micropore volume followed by the Layer-like hierarchical zeolite. Concerning the NA hierarchical zeolites, an almost constant value close to 0.27cc/g is observed.

Pore size distribution and pore accessibility - The pore size distribution (PSD) is often evaluated independently through two different techniques: Probe gases (e.g. N_2, Ar) is used for mesopore analysis while mercury intrusion is used for measuring macropores. Recently, Kenvin et al[105] proposed the combination of these two techniques in order to obtain a consolidated pore size distribution.

In this work, the pore size distribution (PSD) was evaluated through a unified approach as well. For the construction of the consolidated pore size distribution, the model used here takes into account both the N_2 sorption according to the BJH model (1) and mercury intrusion by means of the Washburn-Laplace equation (2).

1. The BJH model[106] is used to calculate the pore size distribution in mesoporous materials. The method is based on the application of the Kelvin equation, through which it is possible to relate the adsorbed/desorbed volume to the pore radius (r_m). The pores are considering as cylindrical and the mesopore radius is equal to the Kelvin radius minus the thickness of the adsorbed monolayer ($r_m = r_k - t$).

Kelvin equation:

$$ln\frac{P}{P_0} = -\left(\frac{2\gamma M cos\theta}{RTr_k}\right) \quad \text{(Eq 57)}$$

where, γ *is the* liquid surface tension, M *is* molar volume of the adsorbate, θ *is* contact angle between the solid and the condensed liquid and $\frac{P}{P_0}$ is the relative pressure of the adsorbate.

2. Mercury intrusion is a technique widely used to probe meso/macropores. The capillary pressure (P_c) is related to the pore diameter (D) through the Washburn-Laplace equation:

$$Pc = \frac{-4\gamma|cos\,\theta|}{D} \quad \text{(Eq 58)}$$

where γ is the liquid surface tension of mercury and θ is the contact angle of the mercury meniscus. For most oxides, such as SiO_2 and Al_2O_3, the contact angle θ is estimated as 140°[107]. This technique is suitable to determine the pore diameter from 4-10 nm up to microns.

The BJH model allows one to calculate the pore size distribution based on the Kelvin equation. The latter equation assumes the existence of a condensed liquid meniscus. The condition that best meets this requirement is the use of the desorption branch for the BJH calculation. However, for disordered materials, the desorption branch rather describes narrower diameters (small pore entries). The limitation in obtaining pore size distribution derived from the desorption curve is related to the tensile strength effect (TSE)[108]. This physical phenomenon, which occurs during the sorption of gases, becomes more pronounce as the diameter of the pore decreases. TSE in the adsorbed phase occurs due to the instability of a hemispherical meniscus during desorption - which, in turn, is caused by the increase in the chemical potential of the confined fluid[108]. TSE effects can be seen during the desorption of large pores connected to small pores – large pores will desorb at lower pressures in comparison to a large pore freely accessible. The desorption pressure of a large pore in a network corresponds to the desorption pressure of the smallest connected pore. The impacts of the TSE may be even more pronounced in the case of cavitation where forced desorption of the pores at a critical relative pressure is observed ~ 0.42 for N_2 at 77 K (d_{TSE} ~ 3.8 nm). In this case, the appearance of an artificial peak in the pore size distribution is observed at diameters close to 4 nm.

Therefore, before determining the unified pore size distribution, the desorption and adsorption curves will be evaluated according to the BJH method (Figure 33). For the NA hierarchical zeolites, both the adsorption/desorption branches lead to a similar distribution of pore diameters, except by the presence of a peak around 4nm in the case of desorption branch for NA-1 and NA-2. The non-appearance of this peak in the adsorption branch leads us to identify it as an artificial peak that does not corresponds to a real pore diameter for these zeolites[109].

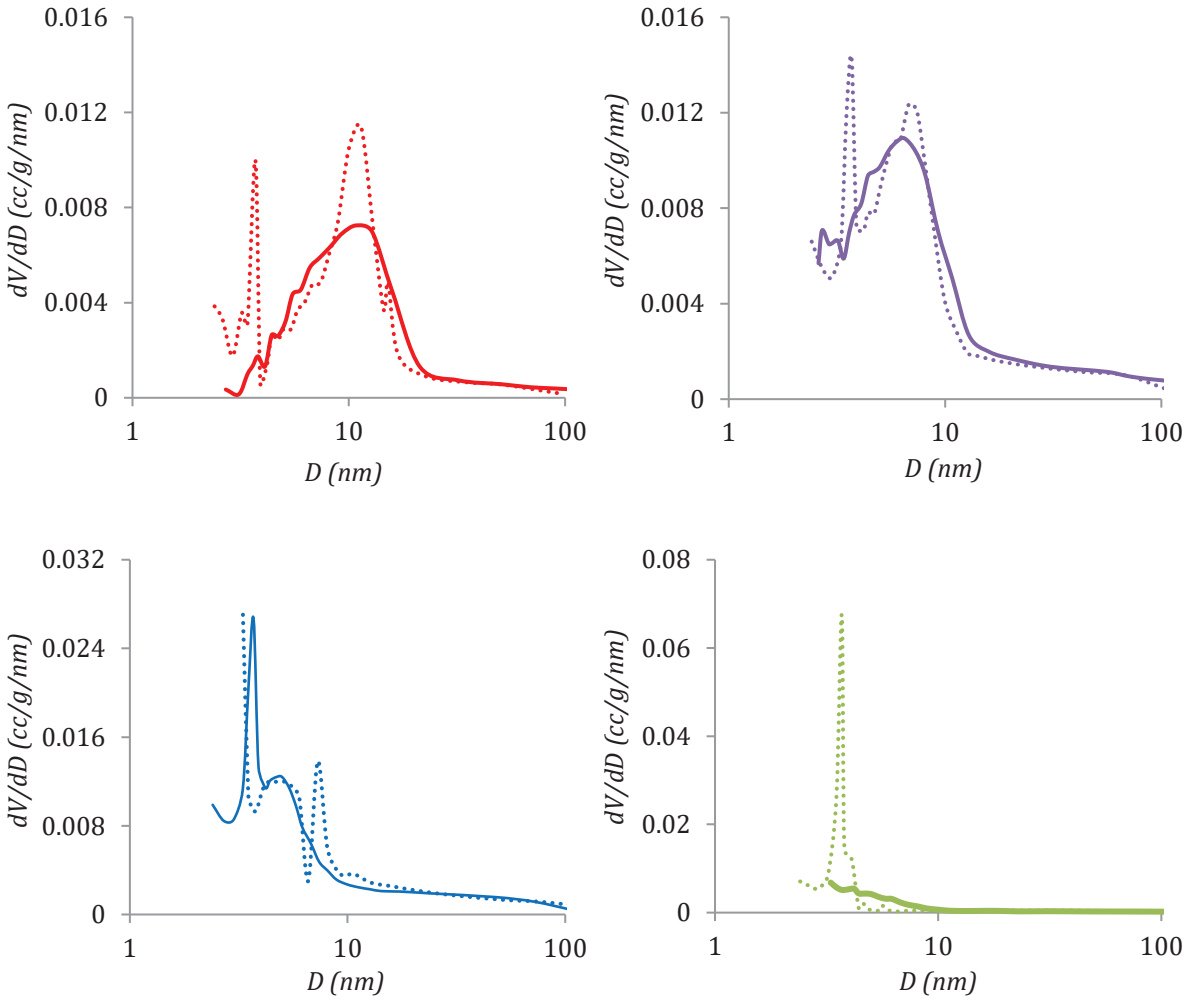

Figure 33. BJH pore size distribution calculated from the adsorption (solid lines) and desorption branches (dotted lines): NA-1 (red), NA-2 (purple), NA-3 (blue) and LL (green).

As can be seeing in Figure 33, there is a shift of the pore size distribution, from NA-1 to NA-3, to a smaller mean diameter as well as a smaller distribution width. Sample NA-3 has an important amount of narrower pores, since, from the adsorption pore size distribution, a large mesopore volume about 4 nm is visible. For the LL-type structure, the pore size distribution is

significantly different between the BJH adsorption and desorption data. While the BJH adsorption curve exhibits a wider pore size distribution, in the BJH desorption all volume appears concentrated in pore diameters around 3.8 - 4 nm. In this case, it is clear that TSE effects are interfering in the pore size distribution.

Based on the results above, the BJH was applied to the desorption branch for the NA samples but to the adsorption branch for the LL zeolite. As already said, the desorption curve is usually preferred for pore size distribution analysis since the kelvin equation takes into account the presence of a hemispherical meniscus. However, as discussed in the case of zeolite LL, the desorption curve does not seem to be representative of the actual pore size distribution (Figure 33). Therefore, the adsorption curve was chosen to be applied in the unified method for this particular sample.

The unified PSD curves are shown in Figure 34 for the hierarchical zeolites: NA and LL. It is interesting to note some overlap between the mercury intrusion and BJH PSD[‡], therefore indicating that both techniques provide the same information about mesopore diameters. However, in some ranges such as in the small mesopore range (< 4 nm), the pores cannot be probed by means of mercury intrusion. In contrast, mercury intrusion is the only technique able to explore macropore domains. In order to obtain the consolidated PSD in Figure 34, the N_2 sorption and mercury intrusion data were combined according to the following relation: If $PV_{N_{2(D_x)}} > PV_{Hg_{(D_x)}}$, $PV_{uni} = PV_{N_{2(D_x)}}$, otherwise $PV_{Uni} = PV_{Hg_{(D_x)}}$, where D_x is a given pore diameter and PV is the corresponding pore volume.

For the mesopore range (the zone of intersection between the two techniques - porosimetry and N_2 sorption) a criterion should be established in order to define which value is the most correct. If the volume corresponding to a mesopore diameter, measured through intrusion, is lower than that obtained by N_2 sorption, this measure should not be accurate. This must indicate that mercury access is hindered. Such behavior is evident for pore diameters smaller than 4 nm, where mercury cannot enter. On the other hand, if mercury is able to probe a volume larger than N_2 in relatively small mesopores, it should be the closest to the correct volume. For macropores, it is already clear that mercury intrusion is the most reliable answer.

[‡] The BJH and intrusion PSD analysis curves were obtained respectively by means of Microactive and Autopore softwares from Micromeritics.

This is why we have always chosen to use the largest volume value (either from N_2 sorption or from mercury intrusion) for the characterization of a given pore diameter.

The consolidated pore size distribution for the NA zeolites in Figure 34 reveals the presence of two populations of pores for the NA samples: Mesopores (between 3.5 - 30 nm) - which can be identified as those between the crystals within the same crystal agglomerate; and macropores (greater than 50 nm) – mostly present between the agglomerates. It is also known that part of these macropores is located in the center of the agglomerates, as observed through SEM on cross-polished section (Figure 27). However, it is not possible to separate the macropores within the aggregates from those which appear between the aggregates. In the case of LL zeolite, some macropores have also been identified in the particle centers by means of microscopy (Figure 27). However, such macropores are not observed here, probably because smaller connected pores (possibly micropores) hinders the access to mercury.

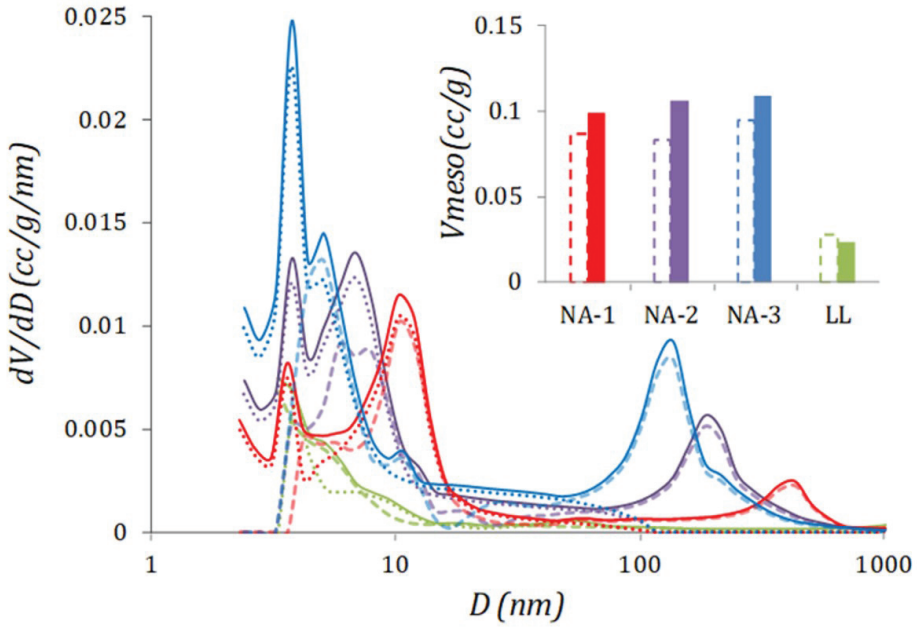

Figure 34. Consolidated pore size distribution for the NaX hierarchical zeolites: NA-1 (red), NA-2 (purple), NA-3 (blue) and LL (green). Dotted lines correspond to BJH (N_2 desorption data for NA zeolites and adsorption for LL). Dashed lines correspond to mercury intrusion. The solid line represented by the unified distribution was slightly shifted upwards to ensure a better visualization. The inset shows the mercury intrusion (dashed contour line) and N_2 desorption volumes (solid color column) for pore diameters between 4 and 50 nm.

Concerning the pore sizes observed in Figure 34 the characteristic mesopore diameter for the NA-hierarchical zeolites decreases from NA-1 (12nm) to NA-3 (5nm). The same is true for the macropores. This behavior is related to the decrease of the crystal size - small crystals as in NA-3 tend to lead to smaller pores. In contrast, the Layer-like zeolite presents a different

structure from the NA series, a smaller mesopore volume, and external surface area. Nevertheless, this zeolite presents mesopores with diameters comprised between those of the hierarchical zeolites NA.

The insert of Figure 34 highlights another advantage arising from the comparison between nitrogen sorption and mercury intrusion. By comparing these two techniques, valuable information regarding the accessibility of the mesopores can be obtained[110,111]. It is known that mercury cannot access pores with diameters below 4 nm. Thus, if we compare the mesopore volume of pore diameters between 4 and 50 nm obtained by N_2 sorption and mercury intrusion, it is possible to identify if these mesopores are accessible from the crystal surface or if they are constricted such as through micropores or small mesopores.

For the NA series, the volumes obtained using both techniques are quite close. Mercury intrusion volumes for pore diameters between 4-50 nm correspond to 87%, 78% and 87% of the N_2 desorption volumes for NA-1, NA-2 and NA-3 respectively. These values indicate that most pores are accessible from the exterior of the crystal and that a small percentage is subject to constrictions.

Another feature concerning the NA zeolite series is that all materials have very similar pore volumes between 4 and 50 nanometers. The volume of these mesopores observed by nitrogen sorption is around 0.1cc/g (Table 5): the volume difference for the hierarchical zeolites in the range of pores $4 < D < 50$ nm is limited to 2-10%. However, when the comparison is made for pores with diameters smaller than 4 nm, more significant differences are observed especially between NA-1 and the other zeolites. For small mesopores with diameters below 4 nm, the volume difference can reach a value around 200% when comparing NA-1 and NA-3.

Table 5. Volume difference for the NA hierarchical zeolites based on the BJH desorption branch. Each value in the table represents the volume increment for the zeolites in the rows with respect to the zeolites in the columns.

	V meso<4nm *Increment (%)*			Vmeso (4<d<50 nm) *Increment (%)*	
	NA-2	NA-3		NA-2	NA-3
NA-1	84	211	NA-1	7	10
NA-2		69	NA-2		2

This information is important when understanding the performance of these zeolites in a given application. If the small mesopores represent a limiting factor to *px* diffusion, NA-2 and NA-3 zeolites would perform worse than NA-1. However, if the presence of such small mesopores are not a limiting factor and if only the presence of mesopores between 4 and 50 nm are important, the performance of all hierarchical zeolites in this group should be similar. Another possible scenario, where the size of small mesopores is not a limiting factor and the most important characteristic is the total volume of mesopores, would lead to a better performance of NA-2 and NA-3 zeolites.

Hysteresis Scanning curves - The scanning curves consist of repeating several adsorption/desorption cycles within the limits of the capillary hysteresis. Initially, the total adsorption and desorption curves are measured to draw the hysteresis limits. These data are referred to as the boundary adsorption isotherm (black curve in Figure 35). Then, several cycles of partial adsorption curves are measured at various relative pressure ranges within the hysteresis. The idea is that, during the adsorption scans, only a part of the porous network (whose pore size is associated with a given relative pressure) is partially filled, so that desorption mechanisms can be identified for different populations of pores. This provides information on connectivity of such domains.

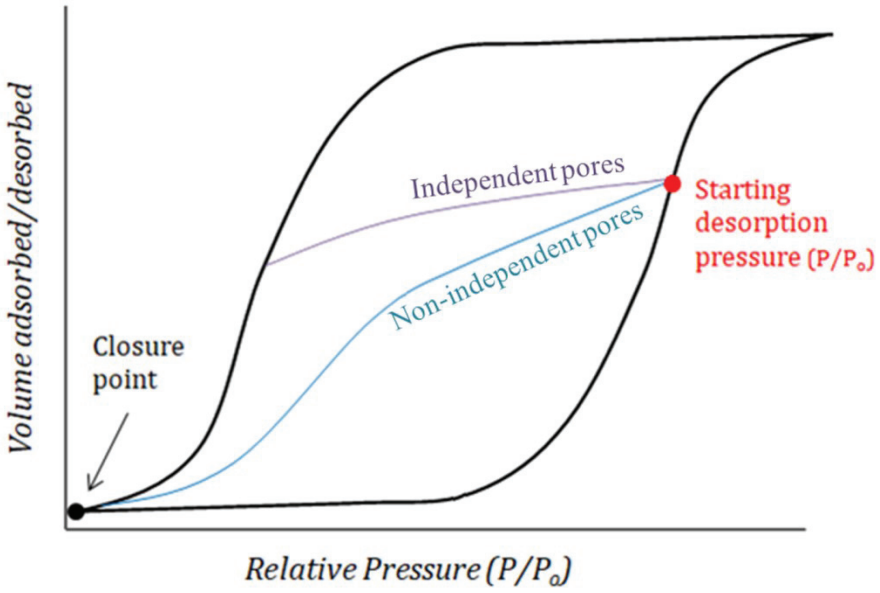

Figure 35. Different types of scanning curves observed for materials with independent pores - reach the boundary isotherm above its closure point; and typical scanning curves for connected pores - meet the boundary adsorption isotherm only at its closure point. (*Adapted from Refs.*[112,113,114]).

For the interpretation of the curves and the characterization of the pores, some theories regarding the origin of the capillary hystereses must be considered. For example, in the case of independent pores, the origin of the hysteresis is related to the fact that adsorption is not at thermodynamic equilibrium while desorption is at equilibrium[115]. Meanwhile, for interconnected pores, the existence of a capillary hysteresis is related to the fact that the desorption of a pore is controlled by the state of its neighboring pores (such as when pore blocking occurs)[115]. The shape of the scanning curves therefore allows identifying the type of desorption mechanism at play (Figure 35). In the case of independent pores, the desorption scan is not affected by the partial filling of the pore network[97]. In this case, scanning curves are meeting the boundary isotherm above its closure point, such as those described in Figure 35[112,113]. On the other hand, taking as an example a pore freely accessible to the external surface, it would empty before a pore presenting constrictions (non – independent pore). In the latter case, pores can only desorb after the smaller pores are emptied. In this way, a large pore presenting constrictions will have its desorption pressure conditioned to the state of the small neighboring pores - a typical pore blocking example. A representation of such connected pores can be seen in Figure 35[112].

As already mentioned, these scanning curves are obtained by partially filling and emptying the pores of the material. In this work, for the NA hierarchical zeolites, three scans were made by starting desorption from relative pressures of 0.7, 0.8 and 0.9 P/P_0. For the LL hierarchical zeolites, the scans were made from 0.6, 0.8 and 0.9 P/P_0. In all cases, a main complete adsorption isotherm – boundary isotherm - was measured up to the relative pressure of $P/P_0 = 1$. The maximum relative pressure for a given scan will be representative of the largest diameter of saturated pores[116]. The scanning curves are presented in Figure 36 for the different hierarchical zeolites.

As shown in Figure 36, converging scanning curves are observed for the NA hierarchical zeolites. In the case of NA-1, the converging curve indicating the presence of constricted pores starts at $P/P_0 = 0.9$ (maximum diameter calculated by the BJH model is around 15 nm). However, the other scanning curves ($P/P_0 = 0.7$ and 0.8) that are representative of pores with diameters up to 8.8 nm are reversible, which indicates the absence of pore blocking or cavitation effects. Therefore, one can assume that pores smaller than8.8 nm are independent and accessible from the outer surface. On the other hand, the gap between pores above 8.8 nm (exact diameter not known) to a diameter which may be equal or greater than 15 nm desorbs through pore blocking. A better resolution concerning the pore structure, constricted or not, would be

established from the measurement of scanning curves at smaller relative pressures intervals. In the case of the hierarchical zeolites NA-2 and NA-3, mesopores of intermediate diameters (NA-2 (8.8 nm) and NA-3 (9.9 nm)) seem to be constricted, since converging-type desorption scans starting at 0.8 P/P_0 are observed.

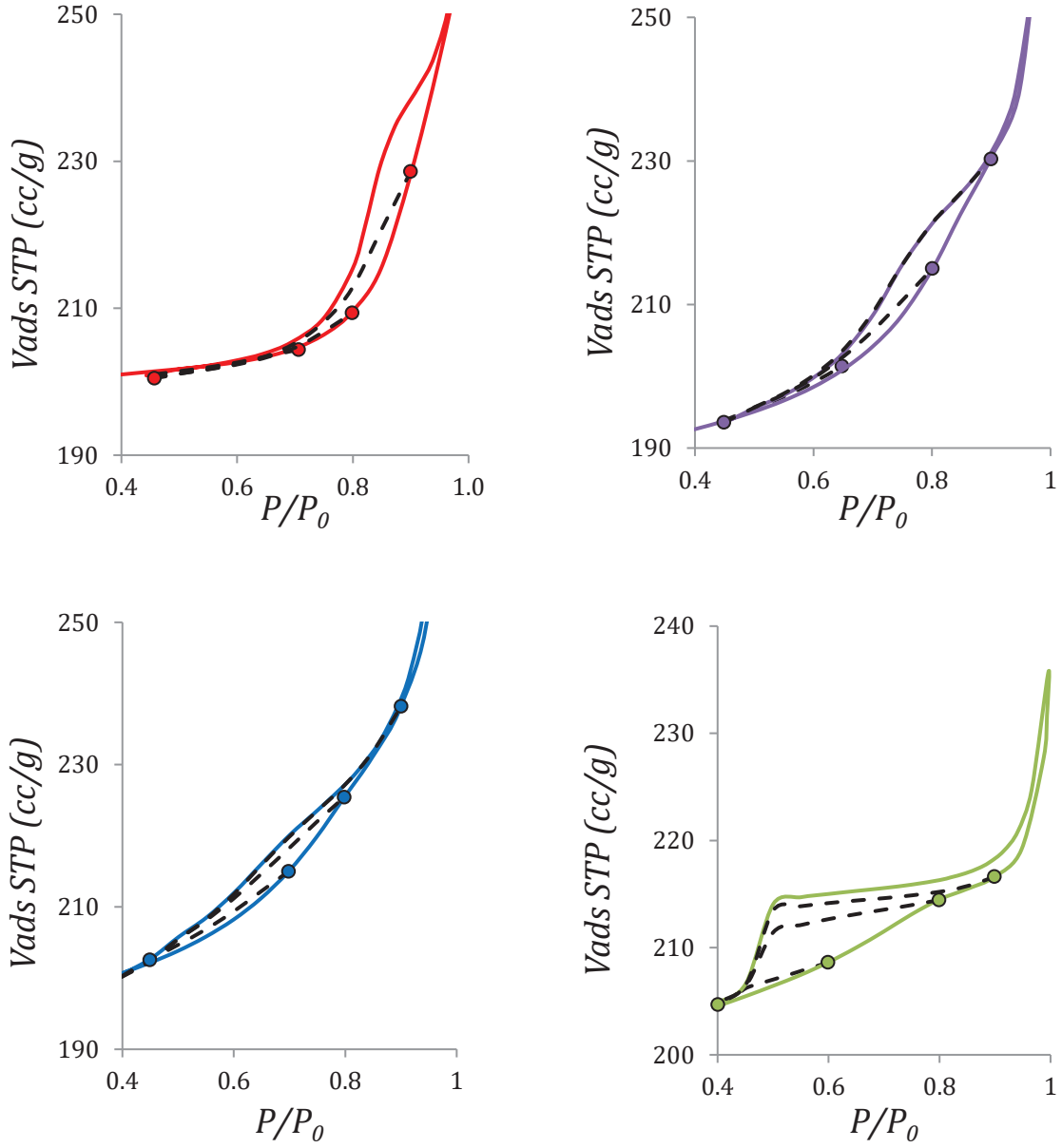

Figure 36. Desorption scanning curves (dashed lines) and adsorption/desorption complete adsorption isotherm (solid lines) for the NA hierarchical zeolites: NA-1 (red), NA-2 (purple) and NA-3 (blue); and for the LL zeolite (green).

For the NaX-LL zeolite, all descending scanning curves, including the boundary adsorption isotherm, close abruptly at the cavitation pressure. This shows that the mesopores in the NaX-LL zeolite are isolated from the external surface of the particles through small pores (i.e. smaller than the critical diameter D_C ~ 3.8 nm for cavitation for N_2 at 77 K) [97,117].

3.1.2 *Surface chemistry*

Once the external surface area is characterized, it is important to assess its nature. In what follows, IR and NMR results will be presented in order to get insights into the chemical features of the external surface of the different samples.

3.1.2.1 *Nuclear magnetic resonance (NMR)*

Figure 37 shows the ^{29}Si NMR spectra of conventional and hierarchical zeolites. Each of the five peaks presented in the spectra corresponds to the number of aluminum tetrahedra-bonded to a central silicon tetrahedron. The Si atom is characterised by five different environments, denoted as Si(nAl) with n = 0, 1, 2, 3 and 4 (Figure 37)[118]. The Si(2Al) and Si(1Al) bands may include the contributions of surface/defect silanol groups such as $Si(OH)_2$ and Si(OH)[119,120], respectively. Moreover, the band Si(4Al) is representative of silicon groups present in the bulk-crystal.

An estimate of the amount of bulk Si atoms with respect to Si atoms that are more likely to be present at the surface can be obtained from the ratio between the sum of the amplitudes of Si(4Al) and Si(3Al) peaks and the sum of those of the Si(2Al) and Si(1Al) peaks. The following ratios were found for the different zeolites: conventional (5.8), NA-1 (5.9), NA-2 (4.1), NA-3 (4.0) and LL (4.5). As can be seen from Figure 37, the zeolite NA-1 and the conventional zeolite has a larger bulk-crystal contribution. This result was expected since they are made of bigger crystals. Concerning the hierarchical zeolites NA-2, NA-3 and LL, the results in Figure 37 suggests that the LL zeolite has the same amount of crystal terminations and eventually silanol groups relative to bulk-crystal species as NA zeolites with greater external surface areas. However, this correlation remains qualitative and only allows distinguishing crystals with important characteristics differences.

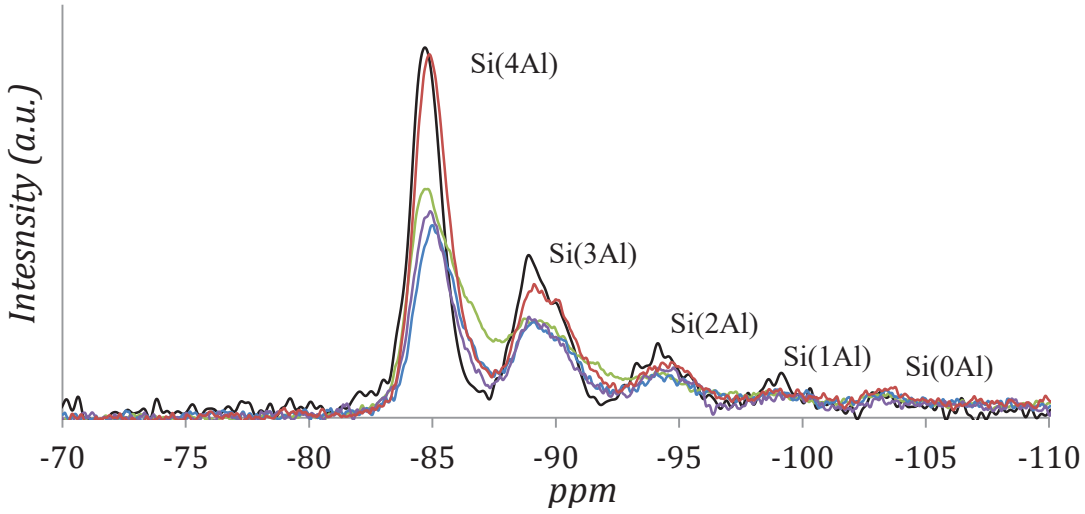

Figure 37. ^{29}Si NMR spectra of conventional (black) and hierarchical zeolites - NA-1 (red), NA-2(purple), NA-3 (blue) and LL (green). Each peak in the spectra corresponds to a number n of alumina tetrahedrally-bonded to a central silicon Si(nAl) tetrahedron.

The ^{1}H NMR can provide us with more detailed information on the OH groups present in the zeolites. The ^{1}H NMR spectra in Figure 38 shows the three major contributions of OH groups (from the left to the right)[82]: OH located in the supercages, SiOH at external surface or defects and OH interacting with cations in the supercages/external surface. The presence of SiOH groups at external surface or defects, with respect to the other OH groups, is the major contribution in the hierarchical zeolites. Furhtermore, the contribution of this peak is farther larger in the case of hierarchical zeolites when compared to the conventional zeolite. The spectra were deconvoluted and the areas of each peak, obtained (Annex 2). This is, in general, logical, since the hierarchical zeolites present larger external surface area. However, as shown in Figure 38 (b), by calculating the relative peak area for each of the contributions of OH groups, it is not possible to observe a relation between the amount of SiOH and the external surface of the hierarchical zeolites. Instead, we observe a nearly constant contribution of SiOH to the NA-type zeolites and a much larger contribution to the LL zeolite. In turn, the amount of OH groups in the supercavities is much higher in conventional zeolites, when compared to the hierarchical zeolites. In this case, the contribution of this peak in the hierarchical zeolites appears to decrease with the increase of the external surface area in NA zeolites and this is especially small in the case of LL zeolite. This may be an indication that the supercavities are incomplete at the surface level. In addition, the structure type LL seems to affect even more these supercavities. Finally, the presence of OH interacting with cations also increases by increasing the external surface area of zeolites, suggesting that we should have some of these groups that are certainly located

at the external surface. The LL zeolite, although having a smaller external surface area than NA-3 zeolite, exhibits relative amount of OH interacting with cations similar to zeolite NA-3, which again indicates a particularity of the LL structure.

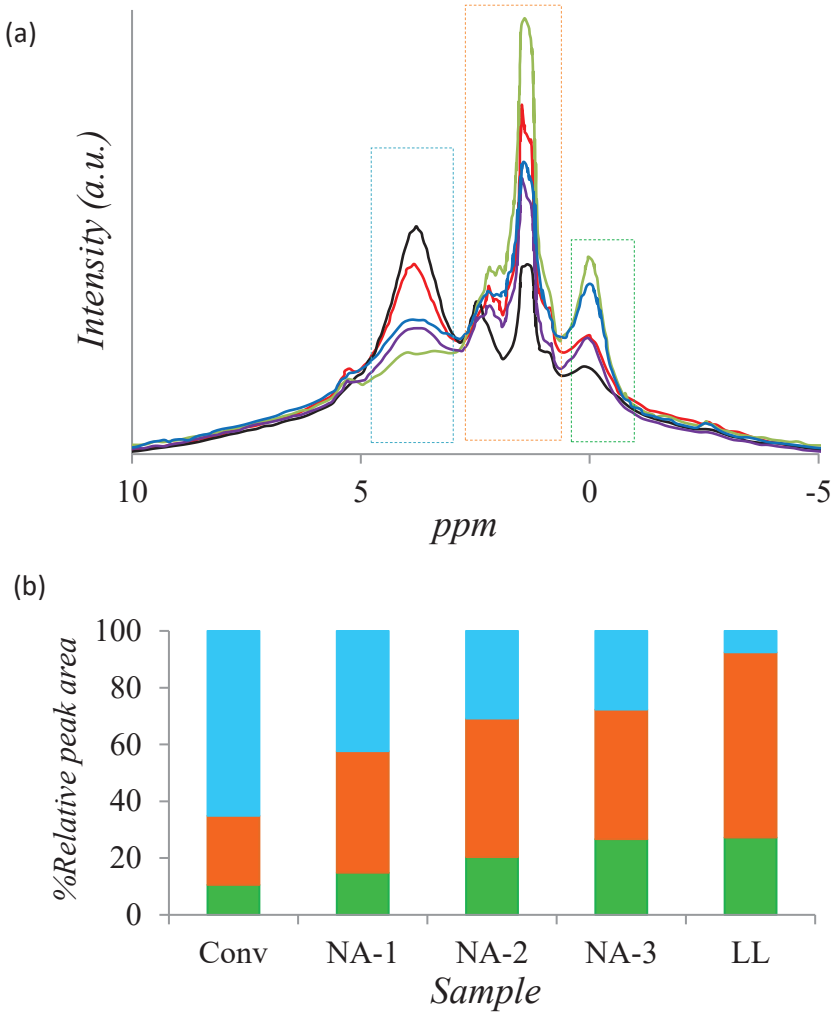

Figure 38. (a) ^{1}H NMR spectra for conventional and hierarchical zeolites, Conventional (black) NA-1 (red), NA-2 (purple), NA-3(blue) and LL (green). The areas marked with the dashes in the ^{1}H NMR spectra indicate OH groups at different environment. (b) Relative peak area for the main contributions in the ^{1}H NMR MAS spectra measured for conventional and hierarchical NaX zeolites. OH located in the supercages (blue), SiOH at external surface/defects (orange) and OH interacting with cations (green).

3.1.2.2 *Fourier-transform infrared spectroscopy (FTIR)*

The external and structural hydroxyl groups were already characterized for faujasite zeolite in the literature by means of IR. A study performed for a mesoporous faujasite zeolite (obtained by acid treatment) has identified the band around 3730 cm^{-1} as free silanol groups at the outer surface[121]. The same study showed that, by increasing the temperature, some silanol groups located in hydroxy nests suffer dehydroxylation forming siloxane. However, those

silanol groups located at the external surface are not affected by the change in temperature, since the distance between such groups located at the outer surface is relatively large (which prevents silanol condensation)[121,122].

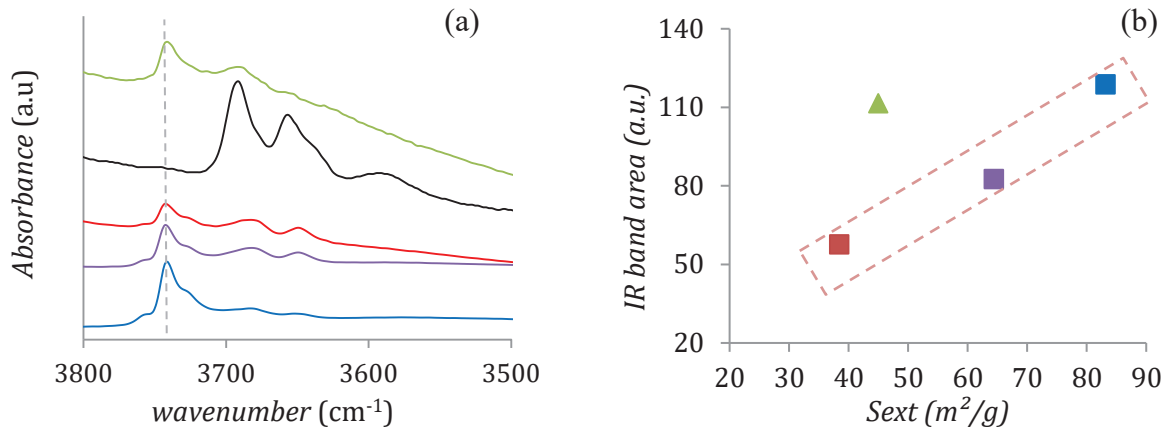

Figure 39. (a) Infrared spectra showing the OH zone for the conventional and hierarchical NaX zeolites; (b) Correlation between the bands area of the IR spectra (*i.e.* OH groups amount) and the external surface area for hierarchical and conventional NaX zeolite. Conventional NaX (black), NA-1 (red), NA-2 (purple), NA-3 (blue) and LL (green).

In order to investigate the chemical nature of the zeolites surface, infrared analyses were performed in the hydroxyl zone, between 3500 and 4000 cm^{-1} (Figure 39). The band appearing in the spectra at 3740 cm^{-1} (marked with the dashed line) corresponds to the OH groups located at the external surface of the crystals[121]. Since this last band indicates the presence of OH groups in the surface, it is expected that its contribution is larger for hierarchical zeolites with larger external surface area. Structural OH bands are also identified. A small shoulder at 3720 cm^{-1} is related to OH groups at defect sites[123]. The band appearing around 3700 cm^{-1} results from the interaction of water molecules with cations and the band at 3650 $cm^{-1}$is related to OH groups located at the supercages[124]. The band corresponding to the interaction between water and cations is especially developed in the conventional zeolites, which may be indicative of incomplete desorption during pretreatment. A larger presence of OH groups in the supercages observed for the conventional zeolite is also confirmed by ^{1}HNMR (Figure 38). Bands at 3600 cm^{-1} are assigned as OH groups attached to extra framework alumina debris (EFAL)[125].

In an attempt to obtain quantitative information about the amount of OH groups at the external surface, the band at 3740 cm^{-1} described above was integrated. By plotting the external surface area of NA zeolites versus the area of the IR bands, it is possible to notice a fairly linear correlation between both parameters: the amount of OH groups increases proportionally to the external surface of the zeolites (Figure 39 (b)). From this observation, it can be said that the

hierarchical zeolites of the NA series present the same density of OH groups at their external surface. In contrast, the hierarchical zeolite LL does not follow the same linear trend and exhibits a higher density of OH groups, which suggests that different synthesis routes induce modifications in terms of surface chemistry. Prior to integration of band 3740 cm^{-1}, a deconvolution of the spectra bands was performed by means of Indigo software (Annex 3).

3.2. BaX zeolite

BaX zeolite is the most widely used zeolite for xylene separation. As a result, ion exchange for the conventional and hierarchical zeolites considered in this work has been performed. The exchange rate for each zeolite was evaluated by means of X-ray fluorescence. In addition, since there is a step subsequent to the ion exchange where the zeolites are subjected to heat treatment, a new textural characterization was performed with the objective of obtaining real information on micropore capacity and external surface area after the ionic exchange. Besides, the characterization of surface quality by IR was also made. The main results will be briefly presented below.

3.2.1 *Surface area*

3.2.1.1 *X-Ray diffraction and fluorescense*

Figure 40 shows the X-ray diffractograms for the zeolites after cation exchange. By comparison with the diffractogram of the conventional zeolite, it can be seen that the structure BaX is present in all hierarchical zeolites. It is also noted that the intensity of the peaks decreases and width increases as the degree of hierarchy of the NA (Na-1 to NA-3) zeolites increases. For the BaX zeolite, peaks are more intense in the region between 10° and 45° with respect to the low angle peak around 6°. This behavior is not observed in NaX zeolite and must be related to the rearrangement of the cationic sites[126]. Despite the presence of EMT (marked with an asterisk), the P phase is not easily identified in the BaX zeolite spectrum (probably due to sharp BaX peaks in proximity of those of the zeolite P).

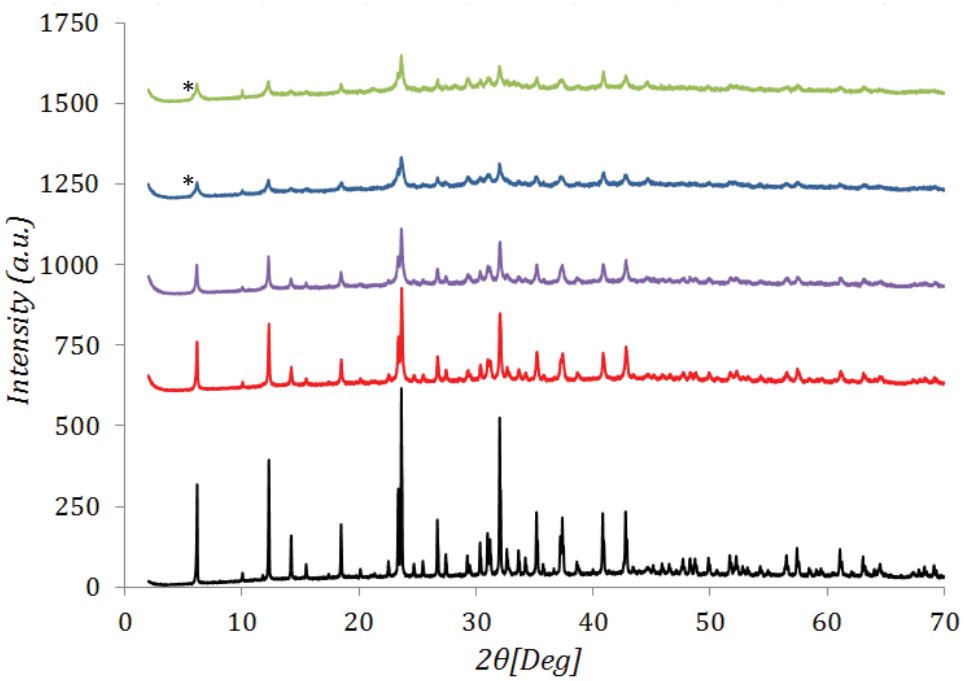

Figure 40. X-Ray diffraction of the conventional BaX zeolite (black line) and BaX hierarchical zeolites: NA-1 (red), NA-2 (purple), NA-3 (blue) and LL (green).

The Na → Ba exchange rate of the zeolites reached values around 80% as presented in Table 6. For the sake of simplicity, zeolites exchanged with Ba cations will commonly be referred to as Ba-type zeolites even if the exchange is not complete. In addition, Si/Al ratio was evaluated for Ba-exchanged zeolites through X-ray fluorescence, but no significant changes were found with respect to NaX zeolites.

Table 6. Exchange rates and composition of the different zeolites measured by X-ray fluorescence.

Zeolite	Exchange Rate (%)	Err(+/-)	Composition
Conv.	82.6	1.6	$Ba_{37.1}Na_{15.6}(Si_{102.3}Al_{89.7}O_{384})$
NA-1	81.5	1.6	$Ba_{37.4}Na_{17.0}(Si_{100.1}Al_{91.9}O_{384})$
NA-2	78.2	1.5	$Ba_{36.1}Na_{20.1}(Si_{99.7}Al_{92.3}O_{384})$
NA-3	85.2	1.6	$Ba_{38.4}Na_{13.3}(Si_{101.9}Al_{90.1}O_{384})$
LL	82.4	1.6	$Ba_{38}Na_{16}(Si_{102.3}Al_{89.7}O_{384})$

3.2.1.2 *Textural characterization*

N2 sorption Isotherms - The BaX adsorption isotherms, such as NaX, are composed of types I and IV adsorption isotherms, therefore indicating the presence of both micro and mesopore. These adsorption isotherms therefore confirm that the hierarchization of the zeolites was maintained after the cation exchange. With respect to the hysteresis, a profile similar to the NaX zeolite hysteresis can be seen, which probably corresponds to desorption through pore blocking for NA1, NA2 and NA3 zeolites and cavitation for zeolite LL.

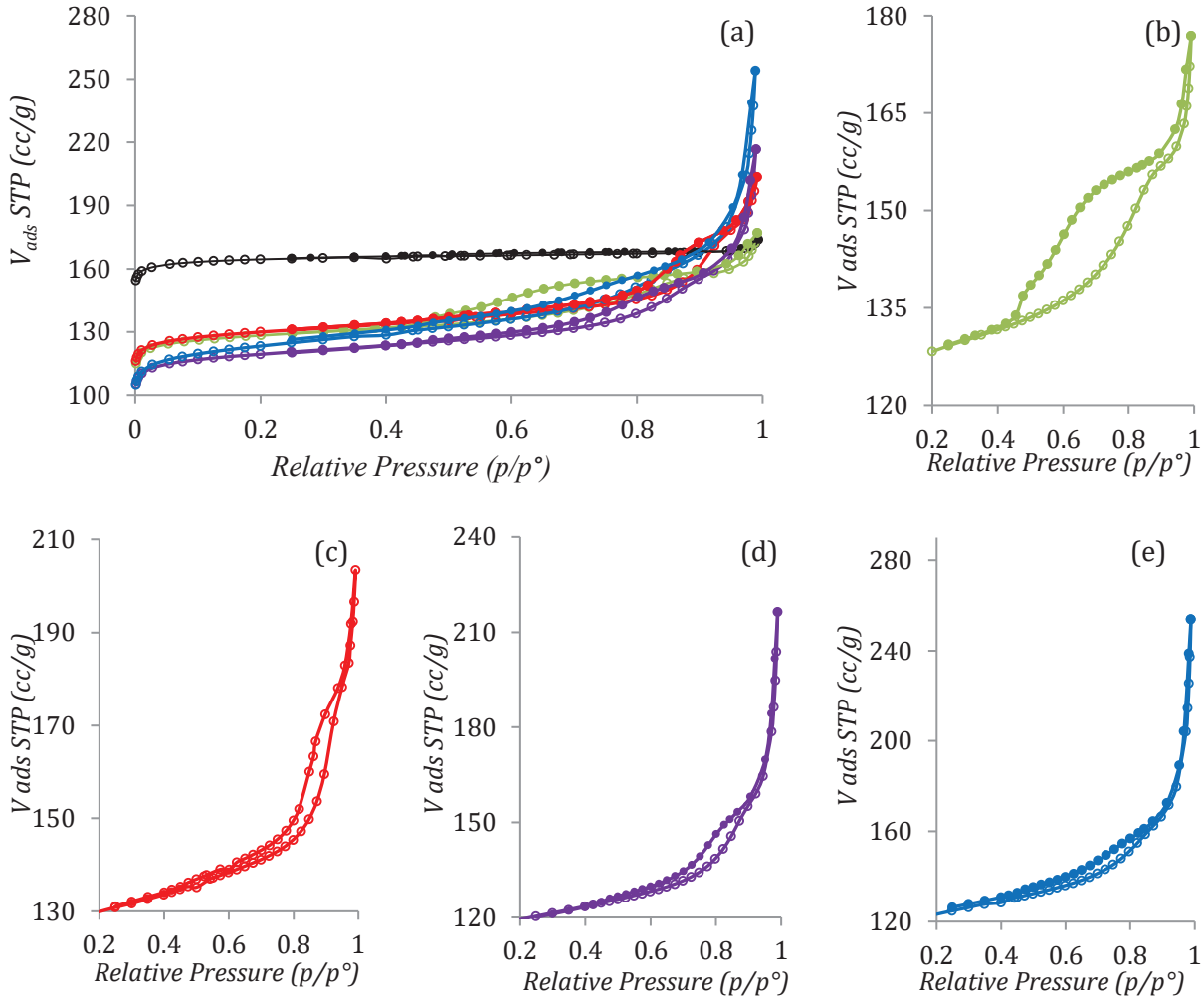

Figure 41. N_2 sorption isotherms at 77 K for the conventional BaX zeolite (black line) and the BaX hierarchical zeolites: LL (green), NA-1 (red), NA-2 (purple) and NA-3 (blue) (a); enlargements showing the hysteresis with more detail are available in (b-e).

Textural Parameters **-** Table 7 shows the textural parameters of BaX zeolites after cation exchange. The method used for characterization was the direct identification (D_I), which was discussed previously. Moreover, theoretical values based on the starting NaX zeolites are also shown. A drop in the microporous volume can be observed with respect to the expected values.

This may be an indication of zeolite structure damage during the exchange procedure and the subsequent heat treatment, which result in loss of crystallinity. As can be seen, the hierarchical zeolites suffered larger microporous volume drop than the conventional zeolite, which is explained by their structure being more fragile. Variations between the theoretical values and those experimentally obtained are also observed for the other textural parameters. An increase in the external surface area of the conventional and NA-1 zeolites is observed, as well as an increase in the mesoporous volume of samples NA-3 and LL.

Table 7. Textural parameters calculated according to direct identification model for the Ba-exchanged zeolites. An estimation considering no damage of zeolites during cation exchange is also presented.

Zeolite	V_{micro} (cc/g)		S_{ext} (m^2/g)		V_{meso} (cc/g)	
	D_I	$*V_{t-\mu}$	D_I	$*S_t$	D_I	$*V_{t-meso}$
BaX-Conv.	0.25	0.27	11	0	0.01	0.00
Ba-NA-1	0.18	0.22	43	30	0.11	0.10
Ba-NA-2	0.16	0.22	48	51	0.13	0.13
Ba-NA-3	0.16	0.21	68	66	0.18	0.14
Ba-LL	0.18	0.23	38	36	0.08	0.04

**Theoretical values estimated based on the molar mass of the zeolites before and after the cation exchange and also on the textural data of the NaX zeolites, prior to exchange.*

For the zeolite NA series, we still observe an increase in the external surface area and mesoporous volume from NA-1 through NA-3. Although the outer surfaces of NA-1 and NA-2 are closer after the exchange, the mesoporous volume remains significantly different for these two zeolites. The zeolite LL continues to present an external surface close to that of the zeolite NA-1, but its mesoporous volume has increased.

Pore size distribution - Figure 42 shows the consolidated pore size distribution for the BaX zeolites. As can be seen, the pore size decreases in the order NA-1> NA-2> NA-3 and LL zeolite has a pore size similar to NA-3 (as in the case of NaX zeolite). The pore diameter measured for BaX zeolites is similar to that observed for NaX zeolites. A slight variation can be observed for zeolite NA-1, whose mesopore diameters were centered on 12 nm for NaX while a maximum of pores at 14 nm is observed for BaX. This effect must be related to the increases of mesoporous volume and outer surface observed during the textural analysis. Likewise, LL zeolite shows a significant increase in mesoporous volume.

As we can see from the comparison between the volumes of Hg porosimetry and N_2 sorption, the mesopores appear less accessible than those of NaX. For NA - BaX zeolites, about 60-75% of the N_2 volume between 4-50 nm is accessible. In the case of NaX, this accessible volume was about 80-90% for NA zeolites. The LL zeolite, however, presents full accessibility to Hg, therefore indicating that the mesopores in this material are accessible by up to 4 nm entrances.

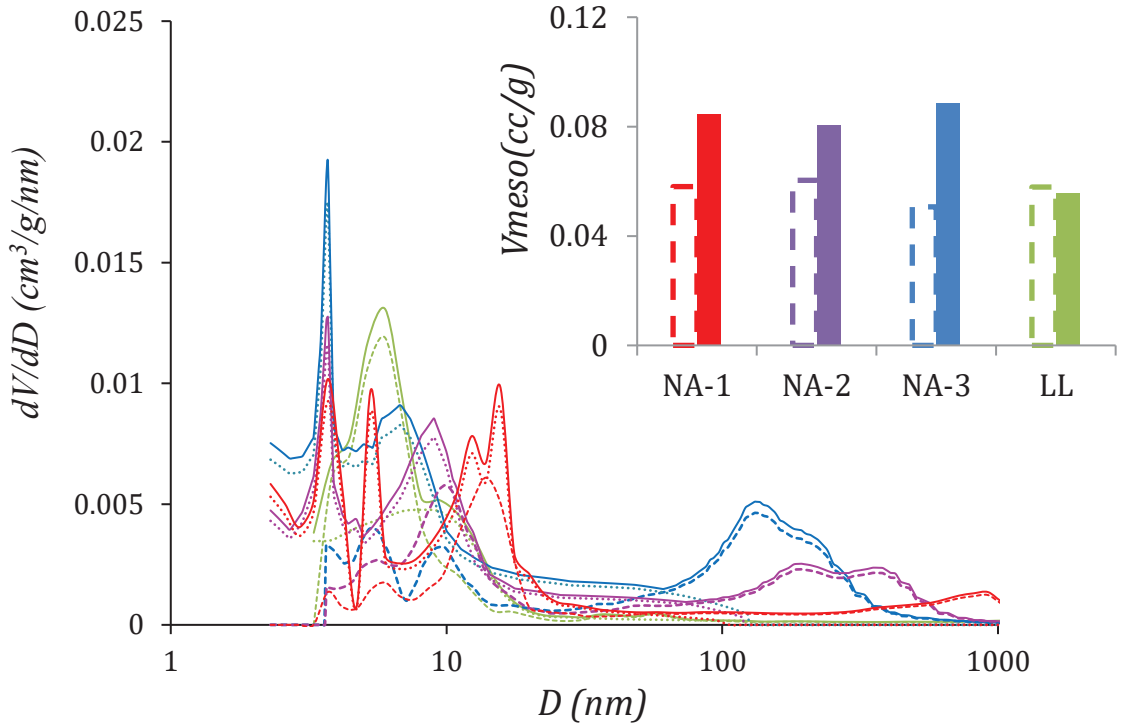

Figure 42. Consolidated pore size distribution for the BaX hierarchical zeolites: NA-1 (red), NA-2 (purple), NA-3 (blue) and LL (green). Dotted lines correspond to BJH (N_2 desorption data for NA zeolites and adsorption for LL). Dashed lines correspond to mercury intrusion. The solid line represented by the unified distribution was slightly shifted upwards to ensure a better visualization. The inset shows the mercury intrusion (dashed contour line) and N_2 desorption volumes (solid color column) for pore diameters between 4 and 50 nm.

^{1}H 2D exchange (EXSY) NMR experiments - A study by means of NMR techniques was also performed in order to evaluate pore connectivity in the hierarchical zeolites (using *px* as probe molecule). The aim of this work is to give new insights about the description of the porosity of zeolites, by highlighting the connectivity between pore domains of different sizes, (which is characterized by different proton chemical shifts). This is made possible by observing the transition of proton from one domain to another one. The present study can complete the description of the textural properties of zeolites and be a link with the study of diffusion properties[80].

The ^{1}H NMR spectra obtained for each zeolite with previously adsorbed *px* are shown in Figure 43. For conventional BaX zeolite, which has a monomodal porous distribution (microporous), the ^{1}H NMR spectrum shows only one large signal (noted A) characteristic of this porosity. In contrast, for NA-1 zeolite, one can additionally distinguish a narrow signal (noted C), which can be attributed to *px* in the fluid phase. Indeed, in addition to microporosity, NA-1 also presents some mesoporosity (D_p ~14 nm) and some macroporosity, which could explain the presence of *px* in fluid phase. For NA-3, the ^{1}H NMR spectrum shows three signals: A and B are characteristic of the two porosities, respectively, micro and mesoporosity (D_p ~5 nm), while C corresponds to *px* in fluid phase within the macroporosity. As the mesopore diameter is smaller than in the case of NA-3, *px* may remain confined in this porosity which explains the appearance of this signal B.

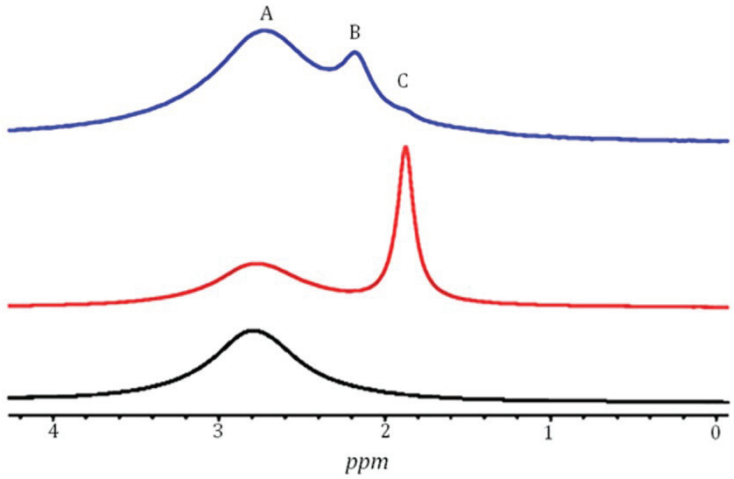

Figure 43. 1D ^{1}H NMR spectrum of *px* adsorbed in different zeolites: conventional (black), NA-1 (red) and NA-3 (blue). Spectra are not normalized to their mass; the intensity of spectrum of NA-3 was multiplied by a factor of 4.

For conventional BaX, the ^{1}H 2D NMR spectrum shows only one signal of *px* confined in the porosity. The one-dimensional spectrum is then found on the diagonal of the 2D spectrum. An example is given in Figure 44 for a mixing time of 200 ms.

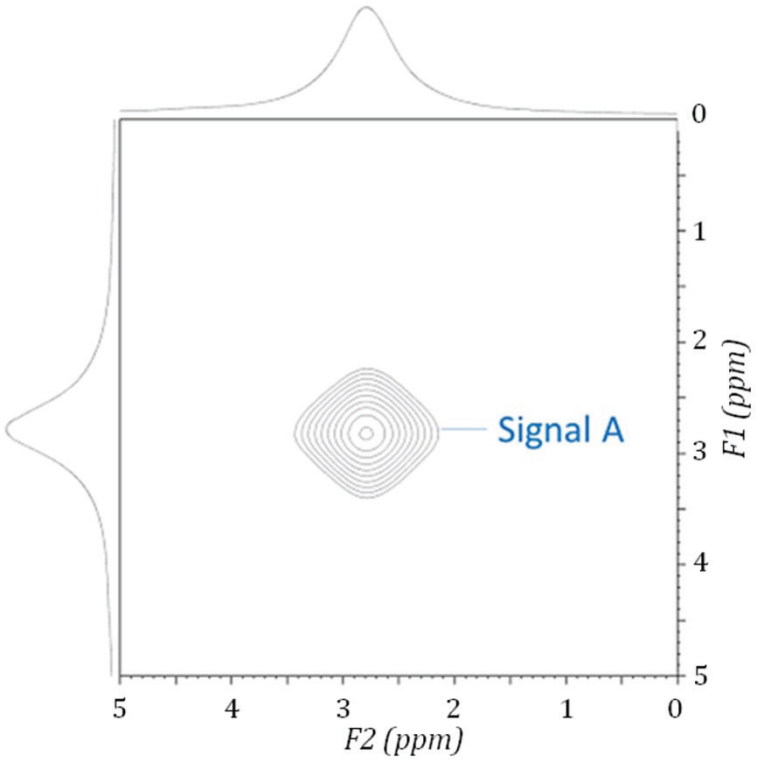

Figure 44. ^{1}H 2D EXSY NMR spectrum of *px* adsorbed in conventional BaX zeolite for mixing time of 200 ms. The number of contour lines is related to the signal intensity. Signal A correspond to the presence of *px* adsorbed in the micropores.

Figure 45 shows the ^{1}H 2D EXSY NMR spectra of *px* adsorbed in NA-1 zeolites for different mixing times. The absence of cross peaks at a mixing time of 0.5 ms indicates that no exchange between *px* confined in the microporosity (signal A) and *px* in the fluid phase (signal C) occurs during this short period. Yet, cross peaks become visible at 50 ms (which corresponds to the minimum time needed to *px* diffuse between the microporosity and macroporosity) and their intensity increases until 200 ms, above which it stays constant and then can eventually decrease due to relaxation phenomena.

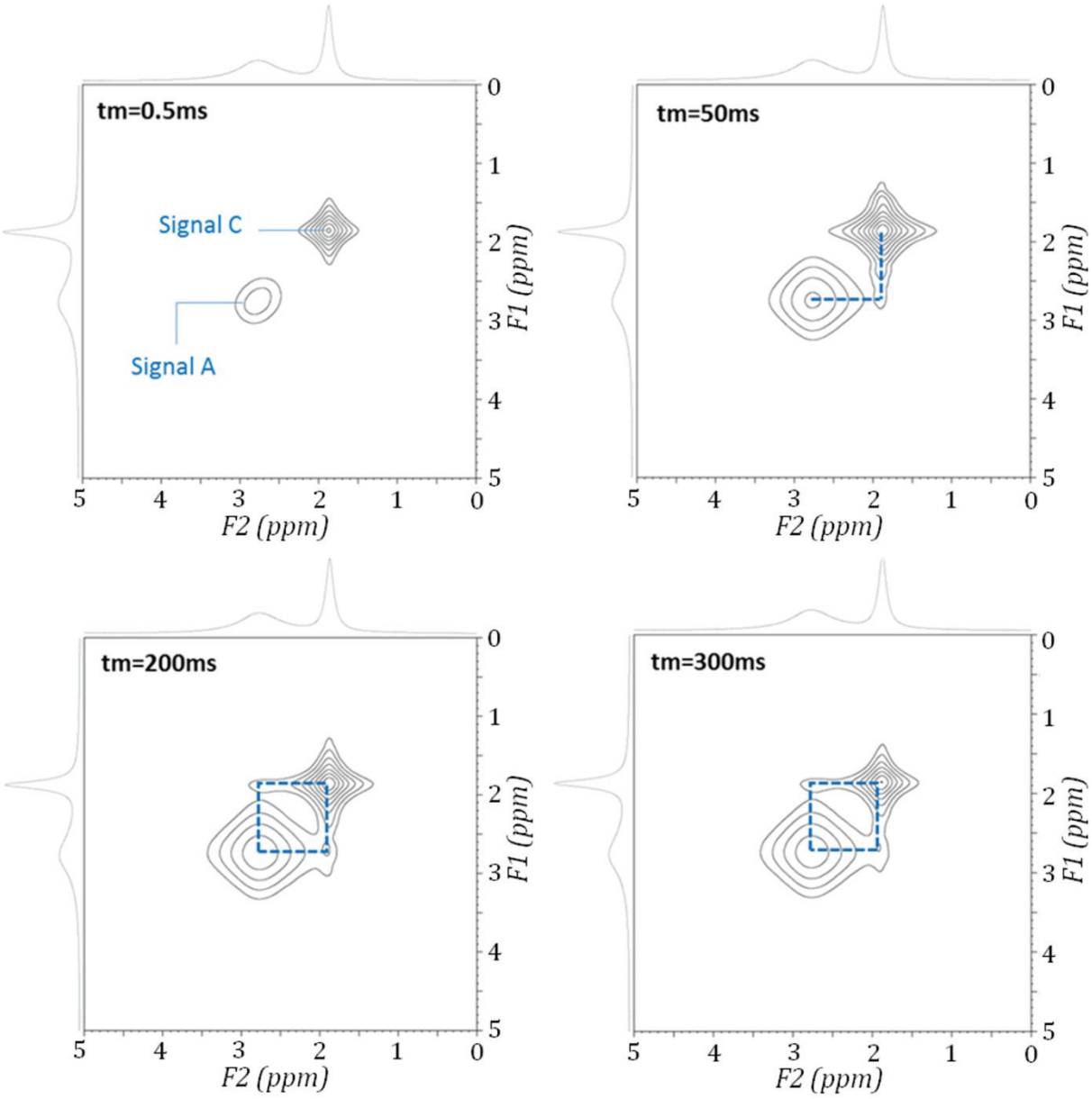

Figure 45. ^{1}H 2D EXSY NMR spectra of *px* adsorbed in NA-1 zeolite. The experimental mixing times are shown above the spectra. At initial times (0.5 ms) two separate signals, A and C, are observed, indicating no exchange between molecules in the fluid phase and molecules adsorbed in the micropores. Proton exchange is observed from 50 ms, evidenced by the crossing scans.

^{1}H 2D EXSY NMR spectra of *px* adsorbed in NA-3 zeolite are shown in Figure 46 for different mixing times. Even for a short mixing time (0.5 ms), an off-diagonal peak is observed between A and B signals. For a mixing time of 50 ms, a cross-peak between porosity B and *px* in the fluid phase (signal C) is observed. For longer mixing times (200 ms), one can also observe an off-diagonal peak between porosity A and *px* in the fluid phase. These results indicate that the two porous domains A and B are connected and that the *px* in the fluid phase can migrate between the two porosities.

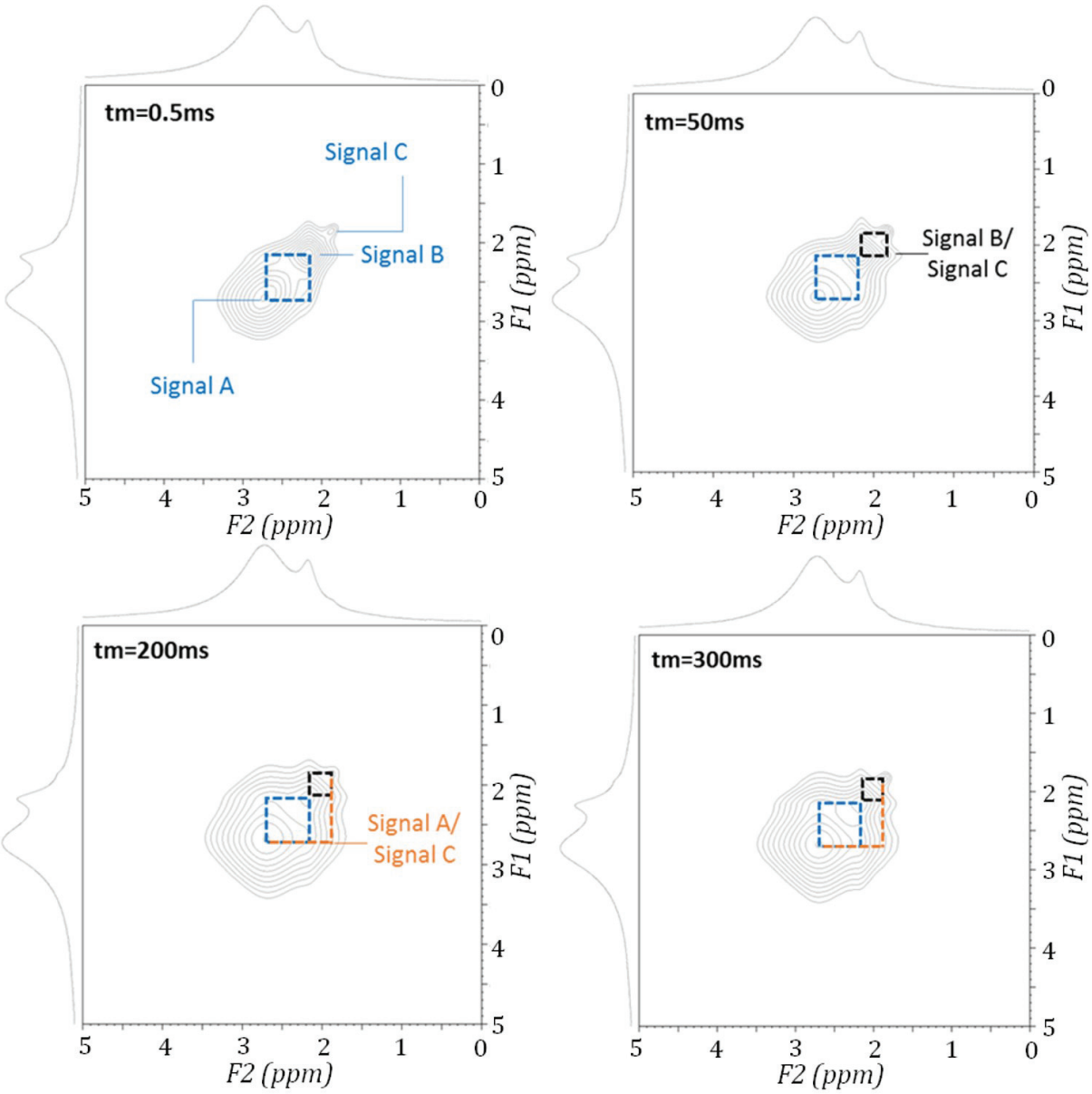

Figure 46. ^{1}H 2D EXSY NMR spectra of *px* adsorbed on NA-3 zeolite. The experimental mixing times are shown above the spectra. The presence of crossed signals at all times indicates strong exchange of *px* molecules between different pose domains.

3.2.2 *Surface chemistry*

3.2.2.1 *Fourier-transform infrared spectroscopy (FTIR)*

The IR analyses allow observing the OH groups in zeolites. The band at 3740 cm^{-1}, marked with a dashed line in Figure 47 (a), was already addressed here as representative of SiOH groups on the external surface of faujasite zeolites. The band at 3600cm^{-1} is present in the conventional zeolites and for the hierarchical zeolites. This confirms that the thermal treatment used during the ion exchange caused a slight amorfization of the structure of hierarchical zeolites, which may have generated EFAL species. The integral of the band indicating silanol groups at the external surface was plotted against the external surface area of the zeolites (Figure 47 (a)). As can be seen, a very similar density of OH groups on the external surface is observed for all BaX zeolites, in contrast to what has been observed for NaX zeolites (which present higher OH density for LL zeolite). In the case of conventional BaX zeolite, a small amount of SiOH groups could be identified due to the discrete enhancement of its external surface area after ion exchange. The SiOH density at the external surface for conventional BaX is the same as for hierarchical BaX zeolites. The integral of the bands of the infrared spectra was made after previous deconvolution of the bands (Annex 4), using Indigo software.

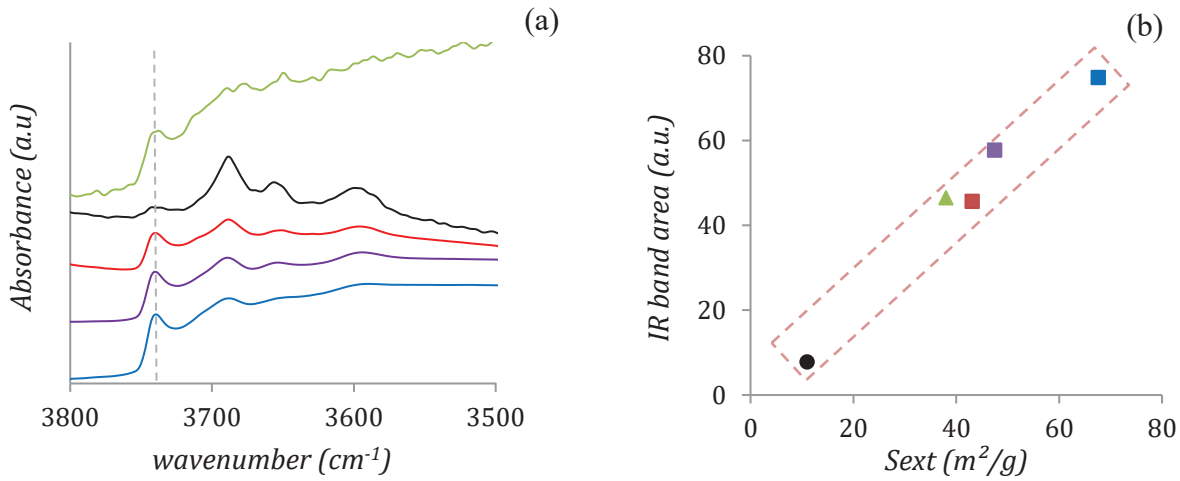

Figure 47. (a) Infrared spectra showing the OH zone for the conventional (black) and hierarchical BaX zeolites; (b) Correlation between the bands area of the IR spectra (*i.e.* OH groups amount) and the external surface area for hierarchical and conventional BaX zeolite. Conv. BaX (black), NA-1 (red), NA-2 (purple), NA-3 (blue) and LL (green).

3.3. Conclusions on characterization

This chapter presented the characterization of the conventional and hierarchical zeolites studied in this thesis. The characterization is of great importance for the understanding of their performance for xylene separation. Special attention was given to the characterization of the external surface of these zeolites and their pore network in order to further observe the impact of these parameters on xylene diffusion and selectivity.

First, the direct identification model was successfully applied to nitrogen adsorption isotherm and provided accurate information on the texture of zeolites. Problems linked to the classical methods such as *t*-plot and Dubinin equation were also observed and discussed. The series of NA hierarchical zeolites was found to have an external surface area between 38 and 83m²/g. A similar micropore volume (~0.27cc/g) was observed in the case of these samples. The conventional NaX zeolite and the Layer-like structure (LL) present higher micropore volume, 0.34 and 0.30cc/g respectively. The external surface area of LL zeolite is 45m²/g (intermediate between the NA samples). The BaX hierarchical zeolites showed a small loss of microporous volume which should be associated with some degradation during the ion exchange procedure and its subsequent thermal treatment. Conventional BaX zeolite exhibits 0.25cc/g while the hierarchical zeolites NA-2 and NA-3 (higher external surface area) present around 0.16cc/g. The BaX-LL and NA-1 zeolites have a microporous volume of 0.18cc/g.

Pore size distribution was analyzed for NaX zeolites through a unified method. In this method, the meso and macropore size distributions were determined by combining N_2 sorption and Hg intrusion. Some attention was paid to the differences found between the applications of BJH model for adsorption and desorption branches. The results showed that the materials present mesopore sizes around 3.5 and 30nm. The mesopore size decreases progressively from NA-1 to NA-3, (LL pore sizes are close to those for NA-3). The accessibility of these mesopores was tested by comparing the nitrogen sorption and mercury intrusion data. Through this analysis, it can be concluded that the mesopores of zeolite LL appear more accessible than those of the series NA. NA zeolites also have good accessibility, but a small percentage of the pores appear to be constricted by bottlenecks below 4 nm. The scanning curves analyses were carried out and allowed to have information about the range of pore diameters constricted in zeolites NA. In general, the analysis of pore size distribution for BaX zeolite indicated pores with diameters similar to those of the NaX zeolites. However, the volume accessible to the mercury was lower with respect to the NaX zeolites.

The electron microscopy analysis suggests the appearance of an internal macroporosity in all samples, which appears to be more accessible in the NA hierarchical zeolites. This observation can be made thanks to SEM/TEM images and the analysis of the N_2 adsorption isotherm. In the case of LL zeolite, the complete N_2 desorption hysteresis closes at relative pressures about 0.42 P/P_0, which indicates the occurence of cavitation. In addition, the SEM images obtained in the cross-polished section show that these pores are mainly surrounded by micropores and, thus, confirm desorption through cavitation mechanism. SEM and TEM analyses also confirm the presence of mesopores in all materials and, furthermore, some channels connecting the outer surface and the heart of the aggregates can be observed.

Last but not least, the presence of OH groups at the zeolites surface was investigated by IR analysis. There is a linear correlation between the amount of OH groups and the external surface area in the hierarchical zeolites. In addition, LL zeolite appears to exhibit a higher density of these OH groups at its surface when compared to NA zeolites. Furthermore, the presence of these groups, which is probably a measure of surface polarity, will be used in order to better understand the effects on surface selectivity. In the case of BaX zeolite, the OH density at the external surface was found to be very similar among all zeolites.

4. Xylene adsorption in conventional and hierarchical zeolites

As already discussed, the separation of xylenes is done by means of adsorption on a conventional BaX type zeolite. In order to improve the diffusional properties of the system, the use of hierarchical zeolites with different external surfaces and different meso/macropore volumes was proposed in this thesis. However, special attention should be paid to other zeolite properties with respect to xylene separation - such as adsorption capacity and selectivity. In order to evaluate such characteristics, thermogravimetry will be used to measure the adsorption capacities of conventional and hierarchical zeolites and derive isoteric adsorption enthalpies. These parameters are indicative of the interaction between the different xylene isomers and the external surface of the zeolites. Next, the results obtained for liquid phase adsorption through batch experiments will be presented. This will allow accessing information about the selectivity of xylenes in conventional and hierarchical zeolites.

4.1. Adsorption in partially saturated medium

Adsorption isotherms of pure *px* and *ox* were measured in order to evaluate the adsorption capacity of conventional and hierarchical zeolites. The choice between these two xylenes was motivated by the polarity difference between them - *px* is a non-polar molecule while *ox* is the most polar molecule among xylene isomers. As pointed out by Bellat et al.[12], the external surface of a conventional faujasite zeolite should adsorb more polar molecules than apolar – which means that between *px* and *ox*, the surface of a faujasite zeolite would present greater affinity for the *ox* molecules. In the case of hierarchical zeolites, such as the zeolites used in this thesis, it is important to investigate whether the increased external surface area entails significant adsorption differences between *px* and *ox*.

As mentioned in Chapter 2 (2.3.1 Thermogravimetric analyses), the gas adsorption isotherms were measured using a thermobalance which is connected to a saturator. N_2 gas is used as the carrying gas through the saturator, where it is enriched with xylene molecules. The pressure of xylene within the thermobalance can be varied as shown in Chapter 2 (paragraphe 2.3.1.4). For each xylene pressure surrounding the zeolite sample within the thermobalance, the

zeolite adsorbs a specific amount of xylene. As the xylene pressure increases, the adsorbed amount at equilibrium in the zeolite increases. So doing, the adsorption isotherms are measured by varying the pressure of xylene while the temperature is maintained constant. Thermogravimetry is a widely used technique in studies related to xylene adsorption[47–53]. By varying the temperature, the number of adsorbed molecules varies as well. The higher the temperature, the lower the adsorbed amount of xylene.

The adsorption isotherms of pure xylenes in the hierarchical and conventional zeolites are presented in Figure 48. Significant adsorption can be observed already at low pressures of xylene. The adsorption of *px* in conventional BaX zeolite was compared to values reported in the literature. According to Moise's thesis[11], the adsorption of *px* at 150°C shows a saturation equivalent to 3.4 molecules/α cage. Meanwhile, in this work the adsorption of *px* at 150°C is about 3.6 molecules/α cage. The difference between the two measurements is probably due to the error inherent to the differences in the analysis, or to an improved cristallinity of the zeolite or to possible additional adsorption that would occur at the surface (crystals used here are relatively small - 1.5 μm). In addition, the BaX zeolite studied in this thesis exhibits some small mesoporosity, due to the cation exchange treatment and the subsequent thermal treatment, which may also contribute to the increased adsorption.

With respect to the adsorption capacity of the zeolites, the zeolite NA-3 has a larger adsorption capacity than LL and the conventional zeolite. This enhanced adsorption seems to be directly associated with the presence of a greater mesoporous volume/external surface area. Indeed, this is the textural feature that differentiates the NA-3 zeolite from the other zeolites considered here. Therefore, in the case of NA-3 zeolite, adsorption probably corresponds to the filling of the micropores (~3.9 molecules/α cage at 100°C which matches adsorption in conventional zeolite) and to the adsorbed amount in the mesopores/external surface. Therefore, the amount adsorbed in the mesopores/external surface must correspond to the difference between the adsorbed amount at saturation and the adsorbed amount corresponding to micropore filling (~3.9 molecules/α cage). At 175°C – the temperature at which xylene separation is performed, the excess amount corresponding to adsorption in mesopores/external surface in NA-3 zeolite is about 0.4 molecules/α cage. LL zeolite exhibits an adsorbed amount of *ox* which is close to the adsorbed amount for the conventional zeolite. On the other hand, the adsorption of *px* in the LL zeolite is lower than that for the conventional zeolite. Two explanations are possible for these differences: (1) the mesopore volume of LL zeolite is not

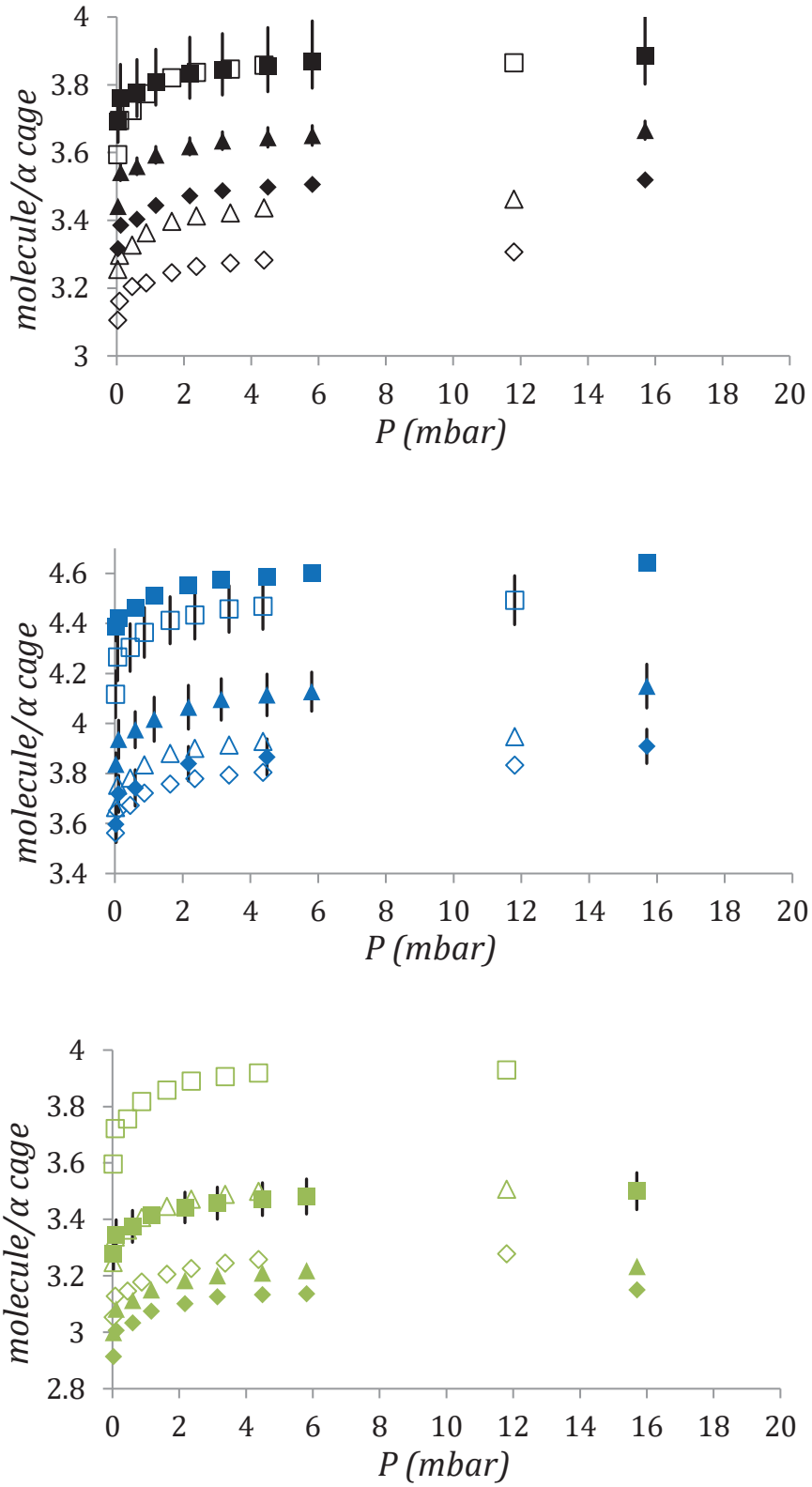

Figure 48. Adsorption isotherms of pure *px* and *ox* in conventional and hierarchical BaX zeolites: Conventional BaX zeolite (black), LL BaX zeolite (green) and NA-3 BaX zeolite (blue). Filled symbols indicate the adsorption of *px* and empty symbols refer to the adsorption of *ox*. The different temperatures can be identified by the symbols: squares (100°C), triangles (150°C) and lozenges (175°C).

large enough to observe significant difference in the total adsorbed volume or (2) the morphology of the zeolite, made up of layers, exhibits many cavities open towards the exterior. This may decrease the stability, *i.e.* energy, of the adsorbed molecules in such cavities. In the literature, the presence of an adsorption site, referred to as window site, that is observed at high filling rates, has been identified at the entrance of the supercavities[17,20]. The adsorption of xylene in such a site may not be possible due to lack of stability in the morphology of the zeolite LL.

Thermodynamic properties such as the isosteric enthalpy of adsorption ΔH_{ads} can be derived from adsorption isotherms measured at different temperatures[128]. The adsorption isotherms presented in Figure 48 were measured at different temperatures in order to obtain such enthalpy of adsorption at different loadings for conventional and hierarchical BaX zeolites. The isosteric adsorption enthalpies are calculated based on the Clausius-Clayperon equation (Eq 59). This equation states that, for a given loading θ of adsorbed molecules, the temperature and pressure provide a measurement of ΔH_{ads}. The slope of the curve of $ln\ p$ versus $1/T$, described by Eq 59, therefore provides the isosteric enthalpy of adsorption (ΔH_{ads}).

$$\frac{\Delta H_{ads}}{R} = \left[dln(p)/d\left(\frac{1}{T}\right)\right]_{\theta} \qquad \text{Eq 59}$$

4.1.1 *Modeling of adsorption isotherms*

Prior to the calculation of the isosteric adsorption enthalpy, the adsorption isotherms at different temperatures were compared with each other according to the Polanyi characteristic curve $A = f(W)$. The adsorbed amount W is a function of the adsorption potential defined as $A = RT \ln p_{sat}/p$. The characteristic curve was plotted in order to observe the temperature invariance of the adsorption in conventional and hierarchical zeolites. The Polanyi theory states that the adsorption potential is the work of adsorption forces which are temperature independent[129]. In other words, Polanyi theory proposes that each adsorbent/adsorbate system can be represented by a characteristic distribution curve of adsorbed amount, which is independent of temperature.

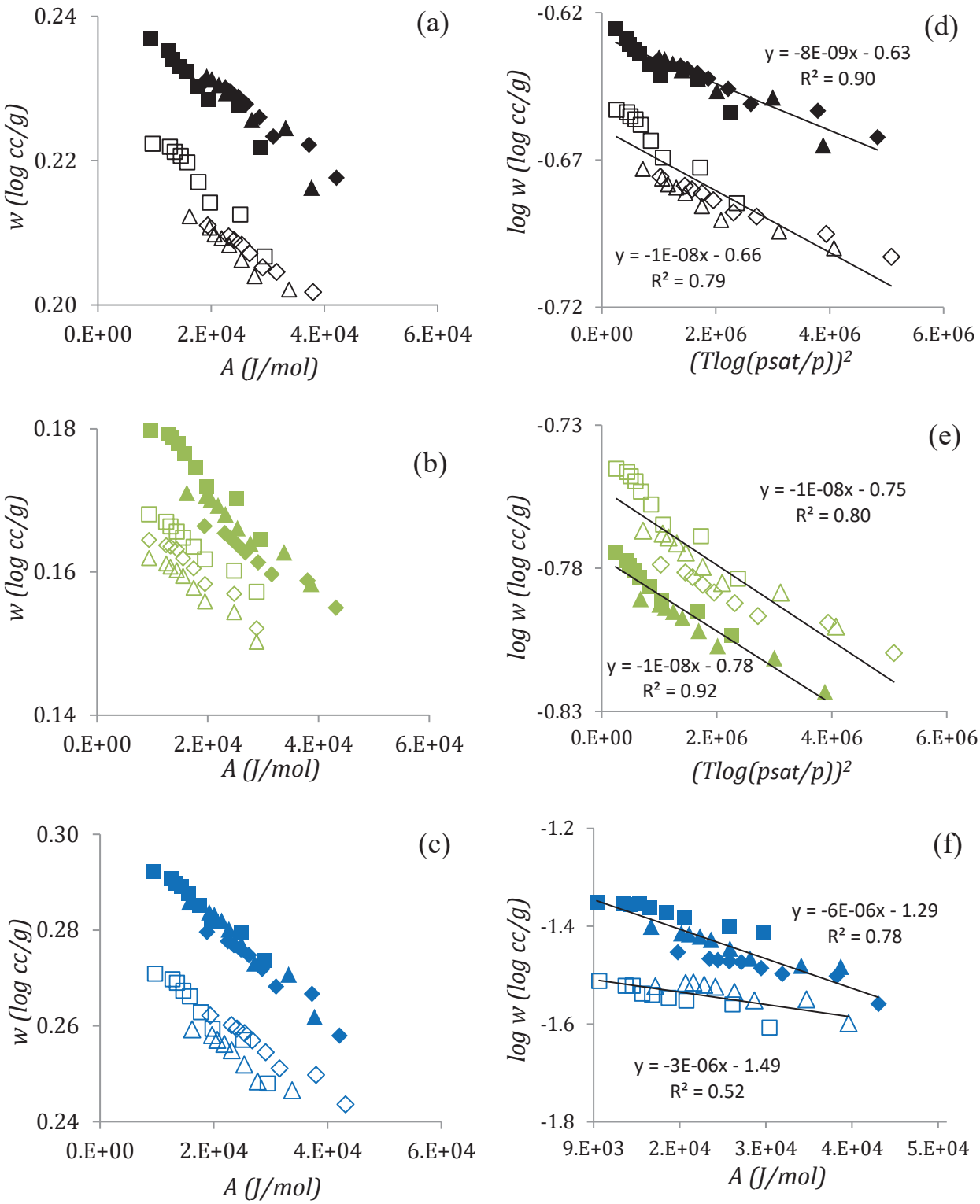

Figure 49. Characteristic adsorption curves of *px* and *ox* in conventional and hierarchical zeolites: (a) conventional, (b) LL and (c) NA-3. Linear plot of Dubinin-Radushkevich equation of *px* and *ox* in the conventional and hierarchical zeolites: (d) conventional and (e) LL. Linear plot of the characteristic curve equation for nonporous materials of *px* and *ox* on the surface of hierarchical NA-3 zeolite (f). Filled symbols indicate the adsorption of *px* and empty symbols refer to the adsorption of *ox*. The different temperatures can be identified by symbols: squares (100°C), triangles (150°C) and lozenges (175°C).

As can be seen in Figure 49 (a), (b) and (c), adsorption for each xylene measured at different temperatures satisfies the condition given by Polanyi for both conventional and hierarchical zeolites. This condition is important since it shows that the measures carried out with the thermobalance are coherent from a thermodynamic point of view.

Later, Polanyi theory was used by Dubinin and Radushkevich to describe adsorption in microporous materials and also on nonporous surfaces. In both cases, the adsorbed volume distribution was treated as a Gaussian distribution[38]. The well-known Dubinin-Radushkevich model for adsorption in micropores in its linear form is therefore expressed by the following relation: $\log W = \log W_0 - \frac{B}{\beta^2}\left(T \log\left(\frac{p_{sat}}{p}\right)\right)^2$. By plotting $\left(T \log\left(\frac{p_{sat}}{p}\right)\right)^2$ as a function of the logarithm of the adsorbed volume *log W*, the parameter $\frac{B}{\beta^2}$ can be obtained from the slope of the curve. Similarly, the logarithm of micropore volume capacity (W_0) is obtained from the intersection with the Y axis. Such information allows tracing new adsorption isotherms at different temperatures.

The linear plot of the DR equation in Figure 49 (d) and (e) shows a good correspondence with the experimental data for the conventional and LL BaX zeolites. The DR model was chosen to describe the adsorption in these zeolites due to the microporous characteristics of these materials. The zeolite NA-3 could not be accurately represented by the DR equation, due to adsorption in its mesopores/external surface. Based on the parameters extracted through the curves in Figure 49 (d) and (e), the model for adsorption of *px* and *ox* isotherms in conventional and LL BaX zeolites can be used satisfactorily (Figure 50). The adsorption model better fits the conventional zeolite than the LL type zeolite, which is probably due to the mesoporosity present in LL.

As already mentioned, the zeolite NA-3 is made up of micro and mesopores. As a result, enhanced adsorption of *px* and *ox* molecules in NA-3 zeolite is observed compared to conventional zeolite. Therefore, the adsorption in the micropores (i) and adsorption in the mesopores/external surface (ii) were both considered in the adsorption model of xylene in zeolite NA-3. For this, the contribution of micropores in zeolite NA-3 was considered to be the same as that in the conventional zeolite. With respect to adsorption in the mesopores/external surface, this adsorbed volume was assumed to be the difference between the total adsorbed volume in the zeolite NA-3 at a given pressure and the total adsorbed volume at the same pressure for the conventional zeolite.

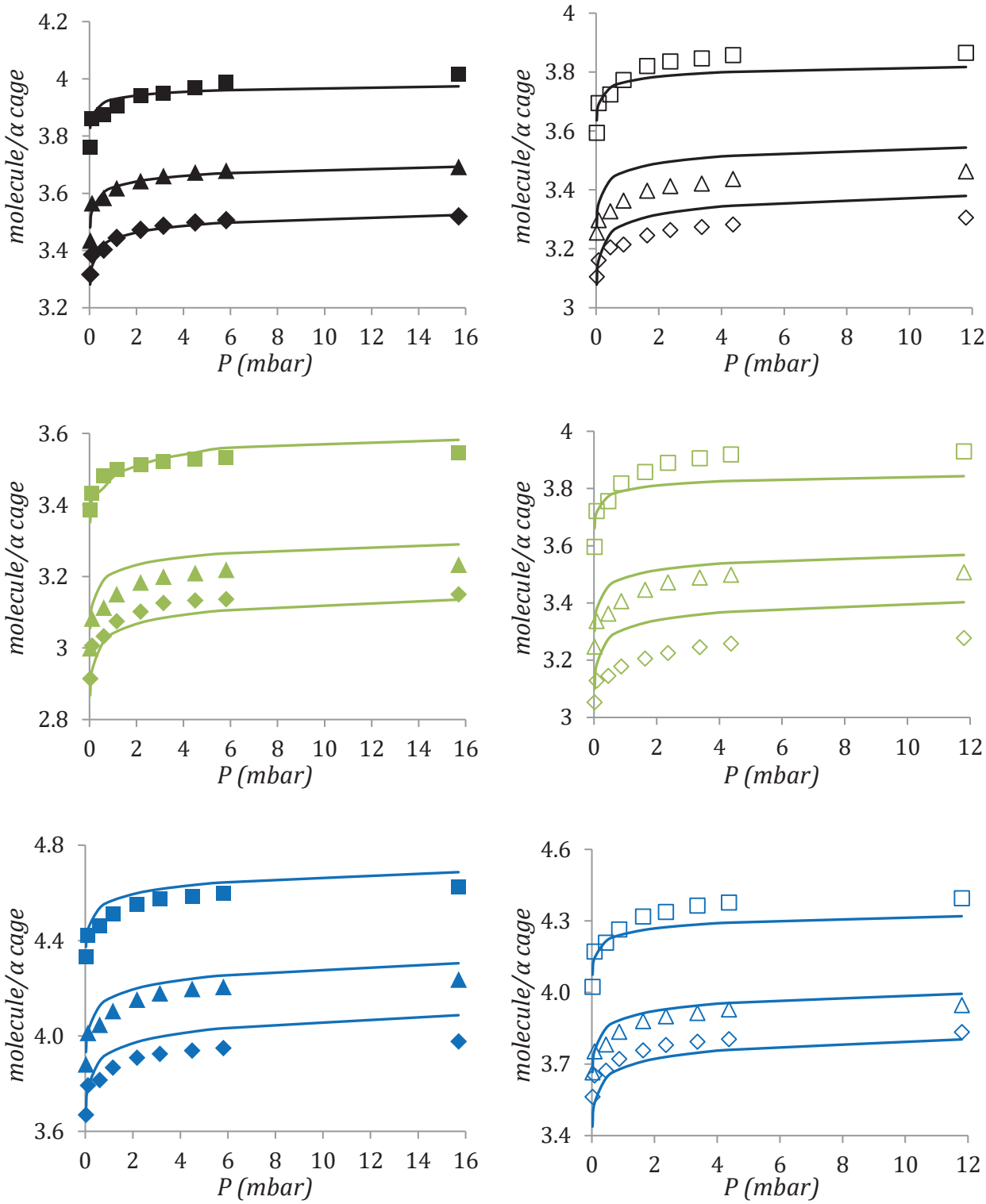

Figure 50. Comparison between experimental data and model for adsorption isotherms of *px* and *ox* on conventional and hierarchical BaX zeolites: conventional BaX zeolite (black), LL BaX zeolite (green) and NA-3 BaX zeolite (blue). Filled symbols indicate the adsorption of *px* and empty symbols refer to the adsorption of *ox*. The different temperatures can be identified by symbols: squares (100°C), triangles (150°C) and lozenges (175°C).

Once the adsorption volume in the mesopores/external surface was estimated, it was described by the characteristic curve for nonporous materials proposed by Radushkevich[36] ($\log W = \log W_0 - \frac{m}{\beta^2} A$). These curves, for adsorption in NA-3 zeolites are shown in Figure 49 (f) for the different xylene isomers and at different temperatures. These data allow one to obtain the parameters of the equation to modeladsorption isotherms at different temperatures in the mesopores/external surface. The adsorption isotherms for the NA-3 hierarchical zeolite could then be expressed as the sum of the model described by the adsorption in the micropores in the conventional zeolite and by the adsorption model in the mesopores/external surface. The final model for adsorption on NA-3 zeolite is presented in Figure 50, showing a good agreement with the experimental data at different temperatures for different xylene isomers.

4.1.2 *Isosteric adsorption enthalpies* ΔH_{ads}

Once the adsorption models of *px* and *ox* are obtained for the conventional and hierarchical zeolites, the thermodynamic properties such as enthalpy can be obtained according to the Clapeyron-Clausius equation (Eq. 59). The isosteric enthalpies of adsorption calculated for the conventional and hierarchical LL and NA-3 BaX zeolites are shown in Figure 51. In order to compare the enthalpies of adsorption obtained here with those already available in the literature, the enthalpies of adsorption for *px* and *mx* at 150°C on a conventional BaX zeolite are also shown in Figure 51 (dark and light orange lines for *mx* and *px*, respectively**)**. From the literature data, we can see that the adsorption enthalpies are constant and larger at low loadings compared to adsorption heats at high loadings. In addition, the enthalpies of adsorption for both *px* and *mx* are similar from low to intermediate loadings. However, at high loadings, a drop in the adsorption heats is observed. Moreover, at high loadings, the adsorption enthalpies for *px* and *mx* are different: a more pronounced decrease in the adsorption enthalpy for *px* is observed compared to *mx*, which suggests that, near saturation, *px* molecule is adsorbed in different, less energetic adsorption sites[16].

In the case of the zeolites studied here, the adsorption enthalpies were measured at high loadings from values of about 3.3 molecules/α cage. In Figure 51 (a), it can be observed that the zeolites with the largest adsorption capacity present an offset in the adsorption enthalpies towards higher values (NA-3 > Conv. > LL). The same is true for the adsorption enthalpies of the different isomers. For example, the most obvious case is the adsorption of the zeolite LL where more *ox* molecules are adsorbed compared to *px*, so that a higher adsorption heat is

observed for the adsorption of *ox*. This can be interpreted as a stronger adsorption of *ox* on the surface of LL zeolite.

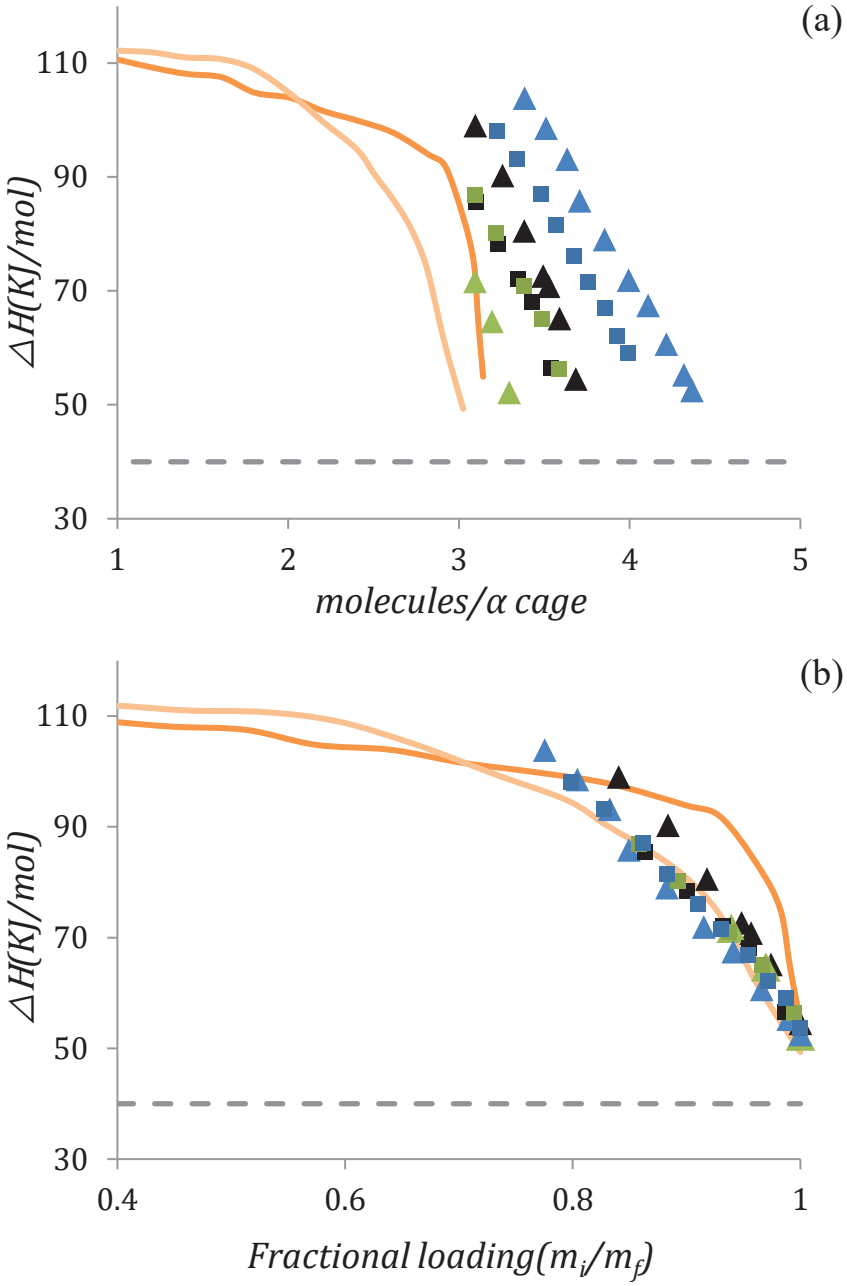

Figure 51. Isosteric enthalpy of adsorption for xylene in zeolite BaX at 150°C represented as a function of molecules per cage (a) or fractional loading (b). Triangles represent the enthalpy of adsorption measured for pure *px* and the squares are the enthalpy of adsorption for pure *ox*. The black color represents the conventional BaX zeolite and the green and blue colors correspond to the BaX-LL and BaX-NA-3 zeolites, respectively. The dark and light orange lines represent the enthalpy of adsorption for *mx* and *px*, respectively. The latter data were obtained from the literature and also correspond to BaX zeolite adsorption at 150°C[16]. The dashed gray line corresponds to the enthalpy of vaporization at the same temperature.

It is interesting to observe how the adsorption enthalpies vary according to the adsorption loading in Figure 51 (b). Almost independent enthalpies of adsorption with respect to the type of isomer analyzed are observed. Furthermore, for the zeolites analyzed here, the adsorption enthalpies are more important for the conventional zeolite followed by the zeolite LL and zeolite NA-3. This seems logical since, at high loadings, a larger contribution of molecules adsorbed at the external surface of NA-3 zeolite is observed compared to the conventional zeolite. As surface adsorption is less energetic than adsorption in micropores, this justifies the smallest values for the adsorption enthalpies of NA-3 zeolite.

4.2. Adsorption in saturated zeolites

In this section, the results of xylene selectivities for conventional and hierarchical zeolites, obtained from liquid batch experiment, as described in Chapter 3 (2.3.3 Liquid batch experiments at ambient temperature), will be presented. The selectivity was evaluated for NA and conventional NaX zeolites so that the effect of an increased external surface on *px*-selectivity could be observed. The xylene selectivities for different BaX zeolites were also measured, which allowed evaluating the effects on selectivity of different structure types (NA, LL and conventional BaX zeolite). Through this last study, it was also possible to determine the role of the external surface in the selectivity of a para-selective zeolite (BaX) and to identify differences with respect to a non-selective zeolite (NaX).

4.2.1 *Selectivity with NaX zeolites*

From the preliminary tests performed in liquid phase for NaX zeolite, it is possible to observe that, for both isomer mixtures (*px*/*ox* and *px*/*mx*), the *px*-selectivity decreases as the external surface area of the zeolites increases. In Figure 52, the values in bold show the average *px*-selectivity found for the different zeolites. The minimum and maximum selectivity values obtained in each experiment are also reported. Some results show a lower accuracy, *i.e.* large error bars, than that desired in view of the difference of selectivities for the different zeolites - as is the case of the *px*/*ox* selectivity for the conventional zeolite. Nevertheless, we can note a clear trend in the *px*-selectivity which decreases for zeolites with larger external surface areas. In addition, *px*-selectivity in the presence of *mx* is greater in comparison to a *px*/*ox* mixture.

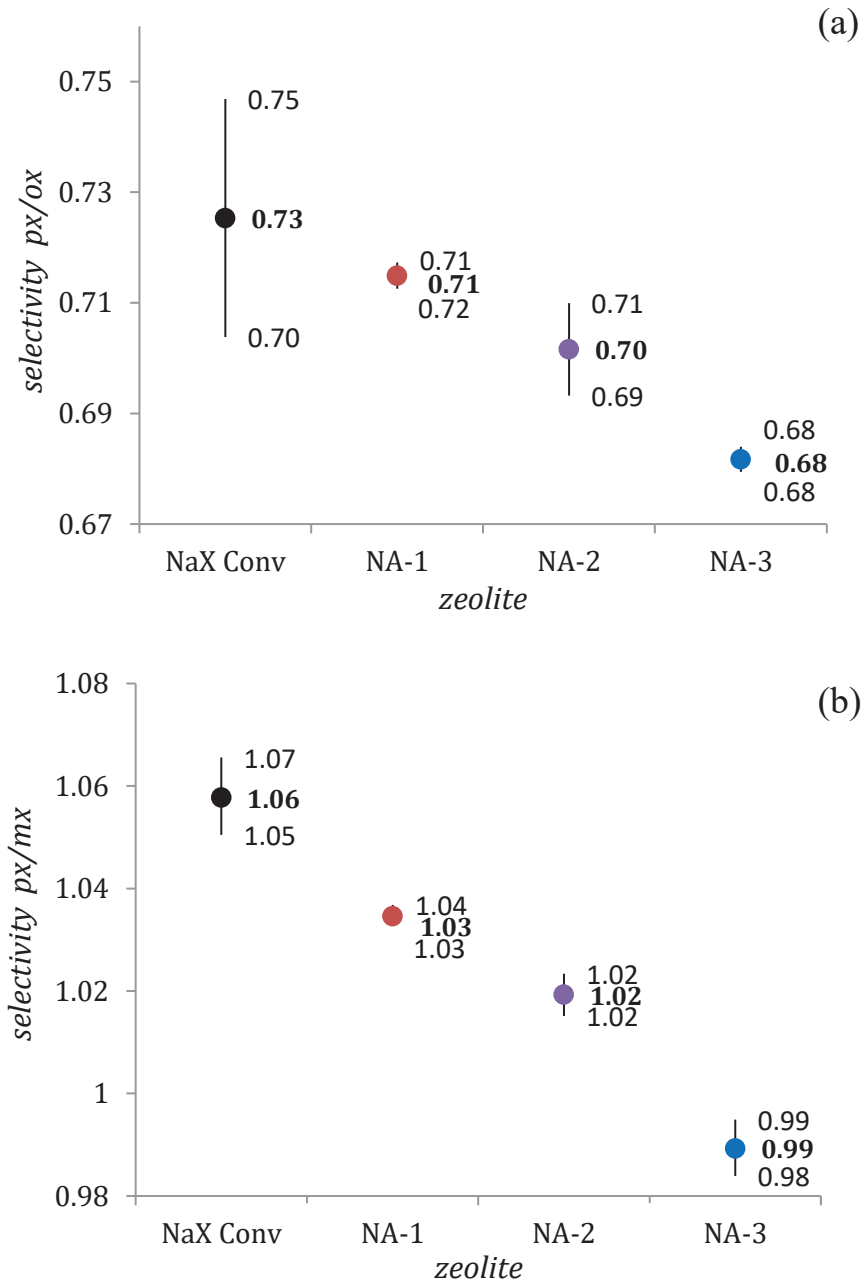

Figure 52. *px*-selectivity at saturation measured in liquid phase for different mixtures: (a) *px*/*ox* (50%:50%) and (b) *px*/*mx* (50%:50%). The conventional and hierarchical NaX zeolites correspond to the different colors: conventional (black) and hierarchical zeolites - NA-1 (red), NA-2 (purple), NA-3 (blue) and LL (green). The tests were performed at room temperature.

In an attempt to identify the external surface selectivity for hierarchical zeolites, three hypotheses were made: (1) at saturation, a layer of xylenes is adsorbed at the external surface of the hierarchical zeolite; (2) the selectivity measured for the hierarchical zeolites is an effective selectivity, corresponding to the combination between the selectivity in the micropores and external surface selectivity; (3) the selectivity in the microporous phase in hierarchical zeolites is given by the selectivity in the conventional NaX zeolite.

The volume of xylene adsorbed at the external surface of the hierarchical zeolites is given by the product of the external surface area of each zeolite (obtained through N_2 sorption measurements - m^2/g) and the thickness of the adsorbed film which is assumed to be equal to the size of the xylene molecule (0.42 nm).

$$V_{ads}^{surf} = 0.001 S_{ext}\ 0.42 \qquad \text{Eq 60}$$

the factor 0.001 is used in order to obtain the adsorbed volume in the surface V_{ads}^{surf} in cc/g.

To estimate the surface selectivity of the zeolites, the selectivity measured during the experiment for the hierarchical zeolites was assumed to be an effective selectivity determined from a correlation between the surface and micropore selectivities and the respective amounts of xylene adsorbed in each domain (surface or micropores).

In the selectivity tests performed for a mixture of two components, $C_{px} and\ C_{(n)x}$ are the concentrations of both isomers in the liquid phase and the selectivity $(\alpha_{px/(n)x})$ is given by:

$$\alpha_{px/(n)x} = \frac{q_{px}}{q_{(n)x}} \frac{C_{(n)x}}{C_{px}} = \frac{q_{px}}{q_{tot} - q_{px}} \qquad \text{Eq 61}$$

where q_{px} and $q_{(n)x}$ are the adsorbed amounts of each isomer. In the case where adsorption at the external surface takes place, the surface selectivity $(\alpha_{px/(n)x}^{S})$ can be expressed as:

$$\alpha_{px/(n)x}^{S} = \frac{q_{px}^{s}}{q_{(n)x}^{s}} \frac{C_{(n)x}}{C_{px}} = \frac{q_{px}^{s}}{q_{tot} - q_{px}^{s}} \frac{C_{(n)x}}{C_{px}} = \frac{q_{px}^{s}}{\sigma\ q_{tot} - q_{px}^{s}} \frac{C_{(n)x}}{C_{px}} \qquad \text{Eq 62}$$

where σ is the ratio corresponding to surface adsorption with respect to total adsorption. The amount of *px* adsorbed at the external surface (q_{px}^{s}) can be then written as follows:

$$q_{px}^{s} = \frac{\alpha_{px/(n)x}^{S}}{\frac{C_{(n)x}}{C_{px}} + \alpha_{px/(n)x}^{S}} \sigma\ q_{tot} \qquad \text{Eq 63}$$

The selectivity in the microporous phase $(\alpha_{px/(n)x}^{\circ})$ is then given by

$$\alpha^{\circ}_{px/(n)x} = \frac{q^{\mu}_{px}}{q^{\mu}_{(n)x}} \frac{C_{(n)x}}{C_{px}} = \frac{q^{\mu}_{px}}{q_{tot} - q_s - q^{\mu}_{px}} \frac{C_{(n)x}}{C_{px}} = \frac{q^{\mu}_{px}}{q_{tot}\,(1-\sigma) - q^{\mu}_{px}} \frac{C_{(n)x}}{C_{px}} \qquad \text{Eq 64}$$

and,

$$q^{\mu}_{px} = \frac{\frac{\alpha^{\circ}_{px}}{(n)x}}{\frac{C_{(n)x}}{C_{px}} + \alpha^{\circ}_{\frac{px}{(n)x}}} q_{tot}\,(1-\sigma) \qquad \text{Eq 65}$$

The effective selectivity therefore includes the surface and micropore adsorption contributions:

$$\alpha^{*}_{px/(n)x} = \frac{q^{\mu}_{px} + q^{s}_{px}}{q_{tot} - q^{\mu}_{px} - q^{s}_{px}} \qquad \text{Eq 66}$$

which results in an equation for the effective selectivity:

$$\alpha^{*}_{px/(n)x} = \frac{\frac{\alpha^{\circ}_{px/(n)x}}{\frac{C_{(n)x}}{C_{px}} + \alpha^{\circ}_{px/(n)x}}(1-\sigma) + \frac{\alpha^{S}_{px/(n)x}}{\frac{C_{(n)x}}{C_{px}} + \alpha^{S}_{px/(n)x}}\sigma}{\left(1 - \frac{\alpha^{S}_{px/(n)x}}{\frac{C_{(n)x}}{C_{px}} + \alpha^{S}_{px/(n)x}}\sigma\right) - \frac{\alpha^{\circ}_{px/(n)x}}{\frac{C_{(n)x}}{C_{px}} + \alpha^{\circ}_{px/(n)x}}(1-\sigma)} \frac{C_{(n)x}}{C_{px}} \qquad \text{Eq 67}$$

where $\alpha^{*}_{px/(n)x}$ is the effective selectivity measured for hierarchical zeolites, $\alpha^{\circ}_{px/(n)x}$ is the selectivity in micropores (measured for the conventional zeolite) and $\alpha^{S}_{px/(n)x}$ is the surface selectivity to be estimated. σ corresponds to the percentage of xylene adsorbed at the external surface of the hierarchical zeolites with respect to the total adsorbed amount. $C_{(n)x}$ and C_{px} are the concentration of the respective isomers in the liquid phase.

Table 8 and Table 9 show the estimated *px*-selectivity at the external surface of hierarchical zeolites in the presence of *ox* and *mx* respectively. It is interesting to note that the surface selectivity significantly differs between the hierarchical zeolites. However, it represents only a slight difference in the effective selectivities. This is due to the fact that the effective selectivity is mainly influenced by the selectivity in the microporous phase since the largest part of the molecules is adsorbed in the micropores.

Table 8. *px/ox* surface selectivities for hierarchical zeolites type NA. Vμ and $\mathbf{V_{ads}^{surf}}$ represent the volume adsorbed in micropores and at the external surface area, respectively.

Zeolite (Sext - m²/g)	Vμ (cc/g)	V_{ads}^{surf}(cc/g)	σ	$\alpha_{px/ox}^{*}$	$\alpha_{px/ox}^{\circ}$	$\alpha_{px/ox}^{S}$
Conv. NaX (0)	0.27	-	-	0.73	0.73	-
NA-1 (38)	0.23	0.016	7%	0.71	0.73	1.40
NA-2 (64)	0.23	0.026	11%	0.70	0.73	1.08
NA-3 (83)	0.21	0.034	16%	0.68	0.73	0.57

Table 9. *px/mx* surface selectivities for hierarchical zeolites type NA. Vμ and $\mathbf{V_{ads}^{surf}}$ represent the volume adsorbed in micropores and at the external surface area, respectively.

Zeolite (Sext - m²/g)	Vμ (cc/g)	V_{ads}^{surf}(cc/g)	σ	$\alpha_{px/\mathrm{m}x}^{*}$	$\alpha_{px/mx}^{\circ}$	$\alpha_{px/mx}^{S}$
Conv. NaX (0)	0.28	-	-	1.06	1.06	-
NA-1 (38)	0.23	0.016	7%	1.03	1.06	2.10
NA-2 (64)	0.23	0.026	11%	1.02	1.06	1.60
NA-3 (83)	0.23	0.034	15%	0.99	1.06	0.85

As shown in Table 8 and Table 9, the *px*-selectivity at the external surface decreases as the external surface of the zeolites increases. It is also possible to observe that the *px*/*ox* selectivity at the surface is smaller than the *px*/*mx* selectivity. In zeolites with small external surfaces, the difference between *px*/*ox* and *px*/*mx* is larger with respect to zeolites with larger external surfaces.

In order to better understand the origin of the selectivity effect at the surface of the hierarchical zeolites, surface selectivities were plotted versus the amount of silanol groups present at the outer surface (Figure 53). The estimation of the amount of silanol groups was made from the integral of the IR band appearing at 3740 cm^{-1} assigned in the literature to silanols at the external surface (Chapter 3, in 3.1.2.2 Fourier-transform infrared spectroscopy (FTIR)). As can be observed, the amount of silanol groups correlates well with the selectivity data and may, therefore, be the cause of the selectivity variations occurring at the surface of the hierarchical zeolites. The selectivity at the surface is therefore thought to be linked to the interaction between the silanol groups and the xylene molecules. However, the silanol groups cannot explain the small selectivity differences between *px*/*mx* and *px*/*ox* (since this difference is also observed for the conventional zeolite, which has an external surface area close to zero). Nevertheless, when comparing the differences between *px*/*ox* and *px*/*mx*

selectivities with respect to the amounts of silanol, it is noticed that the larger the amount of silanol groups the smaller the difference between both selectivities. This suggests that, for a larger surface polarity (greater number of OH groups), *mx* and *ox* are adsorbed at the surface in a similar way.

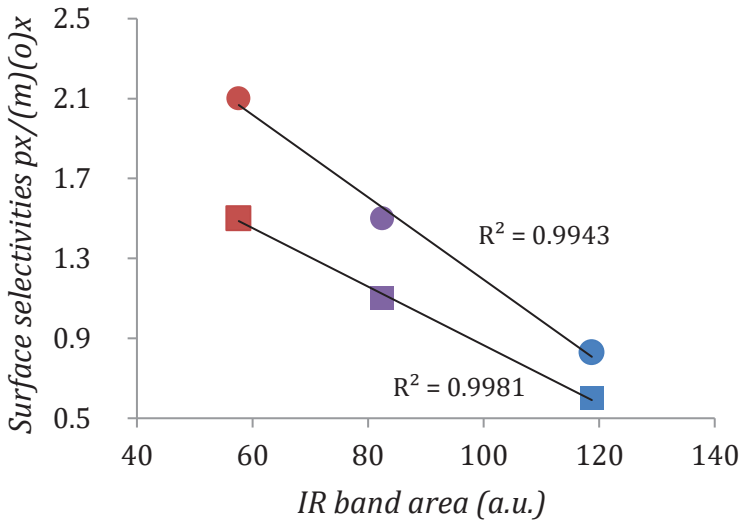

Figure 53. Correlation between the surface selectivity and the amount of OH groups present at the external surface. The hierarchical NaX zeolites correspond to the different colors: NA-1 (red), NA-2 (purple) and NA-3 (blue). Circles correspond to px/mx selectivity and squares correspond to px/ox selectivity.

Since the outer surface of the hierarchical zeolites appears to induce preferential adsorption of *ox*, and to a lesser extent of *mx*, immersion calorimetry experiments were performed. The immersion calorimetry measures the enthalpy of adsorption released when the zeolite is brought into contact with a liquid. In fact, the hierarchical zeolite surface presents an impact on the immersion enthalpies for the different isomers. For hierarchical zeolites, the immersion enthalpies are larger for zeolites with larger external surface areas (Figure 54). The decrease in *px*/*mx* selectivity as the external surface area of the zeolites increases seems to be partially explained when comparing the immersion enthalpies for *px* and *mx*. The immersion enthalpies of *mx* for the hierarchical zeolites are always larger than those for *px*, which suggests a large affinity of the external surface of the zeolites with *px* molecules. However, it does not explain the fact that NA-1 and NA-2 are still *px*-selective. When comparing the immersion enthalpies of *px* and *mx* for the conventional zeolite, very similar values are found which is consistent with the fact that the microporosity of the NaX zeolite is not selective between *px* or *mx*.

However, the immersion enthalpies do not allow explaining the preferential *ox*-selectivity of the zeolites. While for the zeolites NA-1 and NA-2 the immersion enthalpies of *ox* are larger than those for *px*, the magnitude of immersion enthalpies of *mx* are always larger, which is in disagreement with the selectivities previously obtained from batch experiment (*px*/*mx* selectivity always larger than *px*/*ox* selectivity). Moreover, in the case of the conventional zeolite, the immersion enthalpy of *px* is larger than that of *ox*. This suggests that, in the case of *px*/*ox,* the selectivity is not a purely enthalpic factor in NaX zeolites.

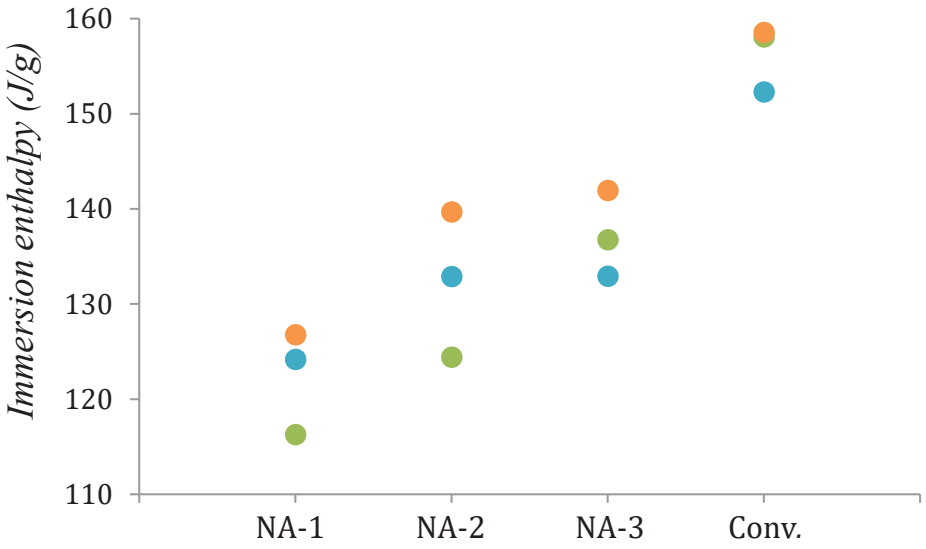

Figure 54. Immersion enthalpies of *px* (green), *mx* (orange) and *ox* (blue) at room temperature for the different NaX zeolites (along *x* axis).

Although the immersion enthalpies explain, in part, the selectivity for the NaX zeolites, these data should be evaluated with caution. At the end of the analyses, it was observed that the hierarchical zeolite samples acquired a yellowish coloration, which suggests that a chemical reaction occurred and that it may have consumed part of the energy released during the immersion. The absence of yellowish coloration in the conventional zeolite sample indicates that this reaction is only occurring at the external surface. We believe this reaction results from the oxidation of aromatic molecules and further condensation of benzenic nuclei that are deposited at the surface. This kind of reaction occurring at the surface of faujasite zeolites has already been reported[130]. However, in the case of the zeolites studied here, the origin of the reactivity is not well understood. Nevertheless, the occurrence of the reaction seems to be linked to the heating of the system during xylene adsorption, *i.e.* in the breakthrough column and in the case of immersion calorimetry, the system is heated during xylene adsorption but this heat is not instantaneously released.

The fact that a reaction takes place at the external surface of the hierarchical zeolites is also supported by results obtained through breakthrough curves (Annex 5). In summary, a significant drop in the microporous volume is observed after the measurements. In this case, the microporous volume is evaluated from the adsorption of xylene molecules. Thus, deposition of coke at the surface during the supposed reaction could block the porosity, therefore preventing the access and adsorption of xylenes in the micropores. This would result in a decrease in the microporous volume, as seen in the breakthrough measurement.

4.2.2 *Selectivity on BaX zeolites*

The adsorption characteristics of xylene isomers for the conventional and hierarchical zeolites, obtained from liquid batch experiment after a time of 3 h and a time of 24 h, are shown in Table 10 and Table 11. After 3h, the hierarchical zeolites already present quite significant xylene adsorption, with an adsorbed amount larger than the adsorbed amount for the conventional zeolite. Up to this stage, the selectivity in the hierarchical zeolites NA-1 and NA-2 are similar and, in some cases, even larger than for the conventional zeolite. However, a loss of selectivity is already observed for zeolite NA-3 (greater external surface) and for zeolite LL.

After 24 h, the xylene adsorption capacity for the NA-type hierarchical zeolites remains larger than in the case of LL and conventional zeolites (the mean values are 3.13 molecules/α cage in NA zeolites, 2.77 molecules/α cage for conventional zeolite, and 2.57 molecules/α cage for LL). It is important to note that the adsorption capacity measured in the liquid phase is significantly reduced with respect to the adsorption capacity previously measured from the gas phase (even if the gas phase measurements have been made at higher temperatures). This difference in adsorption capacities probed from the gas and liquid phases should be understood as the result of diffusional limitations experienced by the system in the liquid phase at low temperatures, which prevents the zeolites from reaching the adsorption equilibrium even after 24 h. In addition, in the liquid phase adsorption for the hierarchical zeolites, which contain macropores, the adsorbed molecules are supposed to be in equilibrium with the bulk liquid phase. Therefore, the amount adsorbed in the macropores is not taken into account since the estimation of the adsorbed amounts are made from the analysis of molecules left in the liquid phase.

Table 10. Xylene (*px* + *ox*) adsorption characteristics for the conventional and hierarchical zeolites after a time of 3h and 24h at ambient temperature.

px/ox		*3h*			*24h*		
Sample (BaX)	zeo (g)	Molecule/ α Cage	**n*C10 (g)	Selectivity (*px*/*ox*)	Molecule/ α Cage	**n*C10 (g)	Selectivity (*px*/*ox*)
NA-1	2.53	2.75	0.09	1.75	3.14	0.06	1.89
NA-2	2.54	2.92	0.06	1.87	3.16	0.05	2.35
NA-3	2.54	3.10	0.06	1.49	3.21	0.05	1.62
LL	2.60	2.33	0.12	1.37	2.56	0.10	1.54
Conv.	2.57	1.92	0.20	1.5	2.66	0.13	3.71

* Remaining adsorbed mass of *n*C10 after xylene adsorption.

Table 11. Xylene (*px* + *mx*) adsorption characteristics for the conventional and hierarchical zeolites after a time of 3h and 24 h at ambient temperature.

px/mx		*3h*			*24h*		
Sample (BaX)	zeo (g)	Molecule/ α Cage	**n*C10 (g)	Selectivity (*px*/*mx*)	Molecule/ α Cage	**n*C10 (g)	Selectivity (*px*/*mx*)
NA-1	2.58	2.51	0.11	1.61	3.32	0.05	1.79
NA-2	2.59	2.65	0.09	1.85	2.87	0.07	2.17
NA-3	2.45	2.89	0.07	1.34	3.07	0.06	1.36
LL	2.61	2.41	0.12	1.23	2.57	0.10	1.31
Conv.	2.47	1.85	0.21	1.72	2.87	0.11	2.67

* Remaining adsorbed mass of *n*C10 after xylene adsorption.

In all cases, *px* adsorption is favored over *mx* and *ox* adsorption. In addition, the *px*-selectivity is not the same among the different samples. Highest para-selectivity is obtained for the conventional zeolite. As can also be seen in Table 10 and Table 11, the adsorbed amounts and selectivity are quite close when comparing *px/ox* and *px/mx* adsorption for the same types of zeolites, *i.e.* NA-3 presents 3.21 molecule/α cage and *px*-selectivity of 1.62 for *px/ox* adsorption and 3.07 molecule/α and *px*-selectivity of 1.36 for *px/mx* adsorption. The most different values of selectivity are found for the conventional zeolite which exhibits lower *px*/*mx* selectivity relative to *px*/*ox* selectivity. Nevertheless, such a selectivity difference is at the limit of reproducibility that can be found in this type of analysis. Annex 6 contains a graph showing two batch analyses under the same temperature and apparatus conditions used to obtain the results presented here. Several samplings were taken at different time intervals. Most of the

data indicate a good reproducibility of the method. However, for the last point, a variation in the adsorbed amount of *ox* up to 15% can be observed for the 24-hour sampling.

px-selectivity was evaluated for all the sampling intervals and, consequently, for different loadings (Figure 55). In general, selectivities are roughly similar for conventional and hierarchical zeolites, except for the last point close to saturation. In the latter case, the selectivity of the conventional zeolite was found to be larger than the selectivity in hierarchical zeolites. Likewise, the evaluation of *px*/*ox* selectivity from the addition of *ox* in a zeolite previously saturated with *px* (inset Figure 55) indicates a surface effect on selectivity. As the outer surface is increased in NA-type zeolites, a decrease in selectivity is observed. The selectivities are generally larger in this case than when xylenes are added at the same time. This may be justified by the fact that in the case of an initial *px* adsorption, the system has a preference for not changing the already adsorbed *px* molecules in the structure by *ox* molecules. It should also be noted that when investigating selectivity on a previously *px* saturated zeolite, the *px*-selectivity of the zeolite LL is the lowest and is even lower than when measuring selectivity through the conventional method. This observation suggests that the LL morphology does not stabilize *px* molecules like the other zeolites.

A possible explanation for the selectivity loss in hierarchical zeolites is the fact that the increase of the external surface area induces a preferential adsorption of more polar isomers (*mx* and *ox*) compared to *px*. One of the hypotheses suggests that an increased external surface area generates more sites for xylene adsorption - directly at the external surface. Such molecules are adsorbed at the outer surface, the driving force for the selectivity in this region would be enthalpy (which was expected to be larger for the most polar molecules). However, such a hypothesis seems questionable since the adsorption enthalpies observed in the previous section do not appear to be significantly different between *px* and *ox* at high loadings (Figure 51). The other hypothesis concerning the loss in selectivity for hierarchical zeolites is related to entropic differences between xylene adsorption in conventional and hierarchical zeolites. As already discussed, it is known that *px*-selectivity in a conventional BaX zeolite is promoted by the presence of an adsorption site (window site) at high loadings[17,18,131]. This site only allows *px* adsorption, due to the aligned position of the methyl groups. Thus, *px* presents a larger number of possible adsorption configurations in comparison to the other isomers. In other words, *px* adsorption is entropically favored. However, the effect that the hierarchization of the zeolitic structure may have on the stability of adsorption in the window sites (selective to *px*) is not known. This site is located in the windows that may be exposed to the exterior at the crystal

edges. Hierarchical zeolites with large external surface areas display more crystal edges compared to a conventional zeolite. So far, it is not known whether open window sites at the outer surface have the same ability to stabilize the adsorption of *px* molecules as a window site within the crystal. Considering the significant difference between *px*-selectivity in conventional and hierarchical BaX zeolites, the hypothesis relating the loss of selectivity to a destabilization of the window site seems to be the most coherent. However, we do not ignore the first hypothesis where surface adsorption may exert some influence on the loss of selectivity, but it is not able to explain itself all the selectivity changes observed.

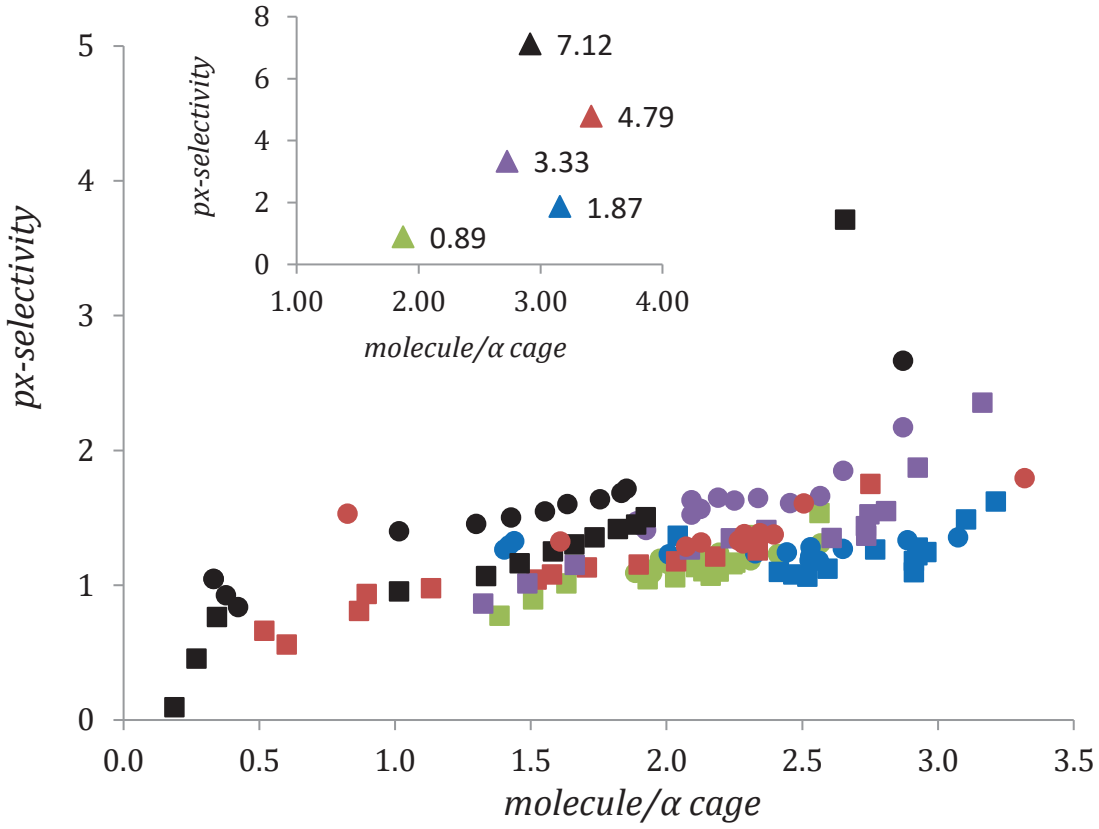

Figure 55. *px*-selectivity at different loadings for conventional (black) and hierarchical zeolites: NA-1 (red), NA-2 (purple), NA-3 (blue) and LL (green). Square symbols represent *px*/*ox* selectivities for a test done in excess of *n*C10 and subsequent addition of *px*/*ox* (50%:50%). Circles represent *px*/*mx* selectivities for a test done in excess of *n*C10 and subsequent addition of *px*/*mx* (50%:50%). The inset shows the *px*/*ox* selectivities for a zeolite pre-saturated with *px* (fluid phase with excess of *n*C10) and subsequent addition of *ox*. All tests were performed at room temperature.

4.3. Conclusions on adsorption properties

The adsorption capacity of the hierarchical zeolites was first investigated in gas phase. The amounts of xylene adsorbed in NA type hierarchical zeolites were found to be larger than in the conventional zeolite. On the other hand, the zeolite LL exhibits an adsorption capacity equal or smaller than the conventional zeolite. The adsorption of pure xylene isomers in the conventional zeolites and NA-3, observed by means of thermogravimetry, as well as the adsorption heats are very similar for the *px* and *ox* isomers. This does not allow us to conclude about surface selectivity. For zeolite LL, larger adsorption can be observed in the case of *ox* in comparison to the adsorption of pure *px*. This may therefore be an indication of preferential adsorption of *ox* at the outer surface.

In order to evaluate xylene selectivites, liquid batch experiments were performed. The hierarchical zeolites are found to be less selective to *px* compared to conventional zeolites (for both Na and Ba type). In the case of the NaX hierarchical zeolites, the low selectivity seems to be related to the fact that a part of the molecules is adsorbed at the external surface, which contributes to reducing the effective *px*-selectivity. In the case of hierarchical zeolites with the largest external surface area (NA-3), the *px*-selectivity estimated at the surface is much lower than the *px*-selectivity measured in the micropores.

Meanwhile, for BaX zeolites, the *px*-selectivity loss is more pronounced than in NaX zeolites, which may indicate other causes besides surface adsorption. The selectivity loss in BaX zeolites may for instance be related to the decrease in stability of the *px*-selective window sites. The decrease in the window site adsorption would therefore be due to the increase of the outer surface in the hierarchical zeolites. In addition, the larger the surface, the greater the number of window sites affected, which explains a decrease in the selectivity as the specific surface of the NA hierarchical zeolites increases. The zeolite LL exhibits a larger *px*-selectivity loss compared to NA zeolites, which can be interpreted as coming from the LL-type structure made up of edges.

5. Xylene diffusion in conventional and hierarchical zeolites

The study of diffusion is an important step for the evaluation of hierarchical zeolites and their applicability to xylene separation. In this chapter, the different hierarchical and conventional zeolites will be tested with respect to the transport of xylenes. In view of the final application, the different structure types were tested in their barium form (obtained by ionic exchange as described in section 2.1). In a first part, we will investigate the transport of xylenes in the zeolitic structures in the liquid phase, *i.e* in the saturated medium by means of counter-diffusion. In a second part, the transport of xylenes in the zeolitic structures is studied in the gas phase, *i.e.* in the partially saturated medium using different techniques. This second part aims at investigating important effects such as the impact of the surface in the diffusion of xylenes. In the literature, the presence of external surface barriers, which were identified in hierarchical zeolites, lead to a reduced use of their diffusive efficiency[56].

5.1. Counter-diffusion in saturated medium.

In this section, results for xylene counter-diffusion in liquid phase for conventional and hierarchical zeolites will be presented. The counter-diffusion experiments were performed for the conventional BaX and for the different BaX hierarchical zeolites (NA/LL). This study allows observing the influence of the external surface area as well as the influence of an additional meso/macroporosity network of the different structures types (NA, LL and conventional BaX zeolite) on xylene diffusion.

5.1.1 *Counter-diffusion of px in the presence of mx or ox*

The counter-diffusion tests were performed according to the methodology described in section 2.3.3.2. For that, *n*C10 is initially mixed with the zeolite for about 30 min. The use of *n*C10 as solvent allows observing larger step changes in the xylene concentration in the liquid phase and reduce heat of adsorption released upon xylene adsorption. Then, the *px/ox* or *px/mx* (50%:50%) mixture is added. After addition of the xylenes, liquid samples are taken at different time intervals. The uptake curves for the *px/ox* and *px/mx* mixtures obtained at ambient temperature for the different samples are shown in Figure 56 and Figure 57.

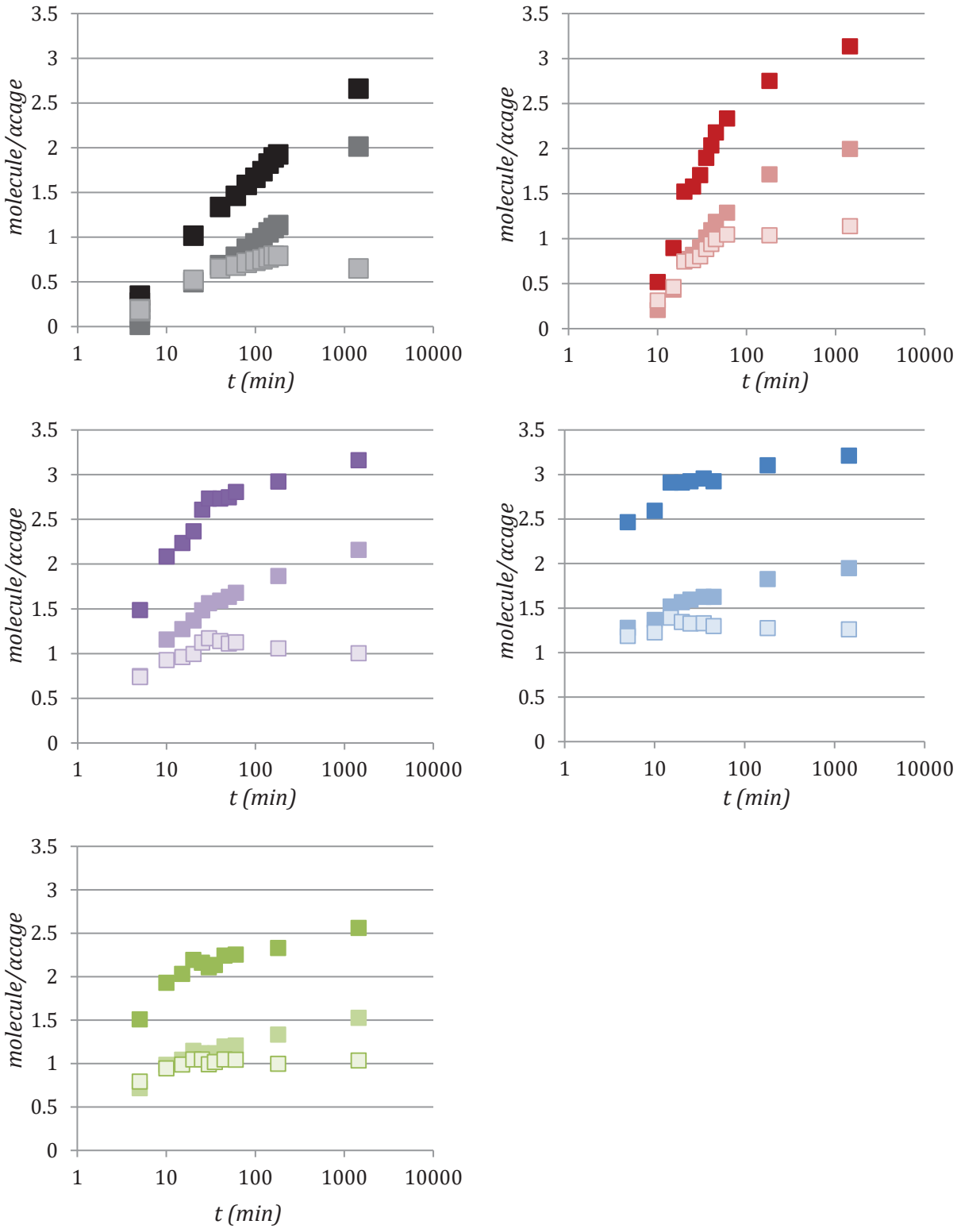

Figure 56. Uptake curves for *px* and *ox* in a mixture (50%:50%) at ambient temperature. The type of zeolite is represented by the different colors: conventional (black) and hierarchical zeolites - NA-1 (red), NA-2 (purple), NA-3 (blue) and LL (green). The type of adsorbed molecule is represented by the intensity of the color: dark color - *px*/*ox*, intermediate color – pure *px* and lighter color – pure *ox*.

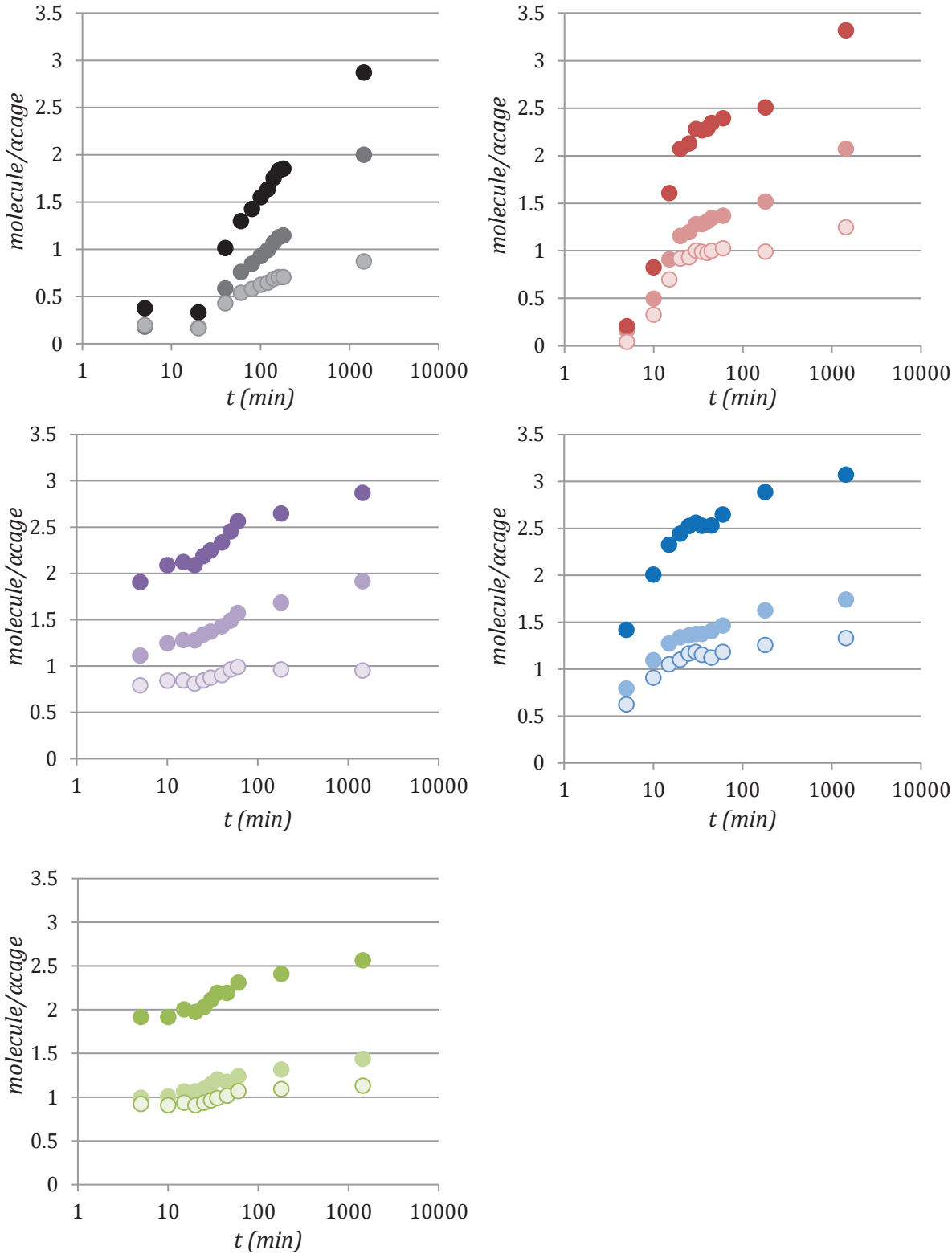

Figure 57. Uptake curves for *px* and *mx* in a mixture (50%:50%) at ambient temperature. The type of zeolite is represented by the different colors: conventional (black) and hierarchical zeolites - NA-1 (red), NA-2 (purple), NA-3 (blue) and LL (green). The type of adsorbed molecule is represented by the intensity of the color: dark color - *px*/*mx*, intermediate color – pure *px* and lighter color – pure *mx*.

The curves resulting from the adsorption of both mixtures show similar trends for each structure type. It is also interesting to note that the uptake curves for the hierarchical zeolites

display two distinct regimes. By observing separately the contributions of each isomer, it can be postulated that the first regime (time range is about 0 - 60 min for NA-1 zeolite and about 0 - 20 min for other hierarchical zeolites in the case of *px*/*ox* adsorption) is representative of the direct access of *ox*, *mx* and *px* molecules all together to the micropores. On the other hand, the second regime (time range about 60 - 1440 min for NA-1 zeolite and about 20 - 1440 min for other hierarchical zeolites in the case of *px/ox* adsorption) seems to correspond to the diffusion of *px* to wards its preferential adsorption site.

Indeed, during the second regime, it can be noted that the amount of *px* continues to increase while there may be only a slight change of *ox* or *mx* adsorbed amount. In the case of the conventional zeolite, only one regime is observed over the duration of the experiment. Interestingly this regime is characterized not only by the diffusion of the different molecules, but also by the preferential adsorption of *px* (which is observed as early as the first hour). As previously discussed in Chapter 4 the amount of xylene adsorbed after 24 hours in the conventional zeolite is low (~ 2.7 molecules/α cage in the case of *px/ox* adsorption). The reason is that xylene adsorption on the conventional zeolite is still far from equilibrium, which also indicates a very slow diffusion, which is expected since the experiment are carried out at ambient temperature. In a faujasite exchanged with Ba the diffusion coefficient of xylenes at 25°C in liquid phase is about $8x10^{-19}$ m²/s [63]. While in the case of a faujasite exchanged with Na it is around $1x10^{-16}$ m²/s at 25°C[59], *i.e.* 2 orders of magnitude compared to BaX, and increases to $2x10^{-13}$ m²/s at 80°C[60].

The counter-diffusion time of *px* in the presence of *mx* and *ox*, with *n*C10 as a solvent, was determined from the data presented in Figure 56 and Figure 57. The effective counter-diffusion time was obtained using the finite system volume model[10] considering a non-constant concentration in the fluid phase:

$$\frac{m_t}{m_\infty} = 1 - 6\sum_{n=1}^{\infty} \frac{\exp\left(\frac{-D_c p_n^2 t}{r_c^2}\right)}{\frac{9\Lambda}{(1-\Lambda)+(1-\Lambda)p_n^2}} \qquad \text{(Eq 68)}$$

where p_n are given by the non-zero roots of

$$\tan p_n = \frac{3p_n}{3 + (\frac{1}{\Lambda - 1})p_n^2} \qquad \text{(Eq 69)}$$

The first one hundred "n" terms of the Eq 68 were taken into account[§]. Since the crystals radius is not known, the term D_c/r_c^2 was replaced by the inverse of the effective counter-diffusion time constant,$1/t_c$. The latter is then determined by the least square method.

As already mentioned, in the case of the conventional zeolite, the diffusion process is so slow at ambient temperature that equilibrium conditions could not be observed even after 24 h. Therefore, the maximum adsorbed amount for the conventional zeolite to be used in the diffusion model was assumed to be equal to the maximum adsorbed amount on the hierarchical zeolites ~3.2 molecule/α cage. Then, since we are measuring *px* diffusion in the presence of *ox* or *mx*, it was necessary to distinguish the amount of adsorbed *px* from the total adsorption. To do so, the *px*/*ox* and *px/mx* selectivities of the last points experimentally measured for the conventional zeolite were taken into account and the *px* adsorbed amount was estimated. For instance, in the case of *px/ox* mixture, the *px* adsorbed amount was 2.34 molecule/α cage out of 3.2 molecules/α cage, and the diffusivity of *px* in the presence of *ox* measured for the conventional BaX zeolite at ambient temperature is $1x10^{-18}m^2/s$, which is close to the values found in the literature for a Ba-faujasite at same temperature[63].

As can be seen in Figure 58, the finite system volume model from (Eq 68 well describes the uptake curve for the conventional zeolite and for the zeolite NA-1. Those curves show a more restricted accessibility for these two samples compared to the other hierarchical zeolites (in agreement with data in Chapter 3). Concerning the other hierarchical zeolites, it can be observed that the adsorption of *px* reaches a condition close to equilibrium at times much shorter than the conventional zeolite. This indicates that the diffusion is much faster. For the hierarchical zeolites NA-2, NA-3 and LL, the finite system volume model is not able to fit accurately the uptake curve. However, we clearly observe a much faster diffusion for these zeolites. This indicates that addition of new meso/macropores positively impact the access of the xylene molecules to the micropores. In the case of the conventional zeolite the xylene molecules must travel through a longer diffusion pathway within the micropores in order to access all micropore volume. On the other hand, the hierarchical zeolites exhibit those meso/macroporous network that facilitate access to the micropores, making it faster to fill total adsorbable volume.

[§] p_n roots were determined between 1 and 350. No significant changes are observed in the summation for values greater than 350.

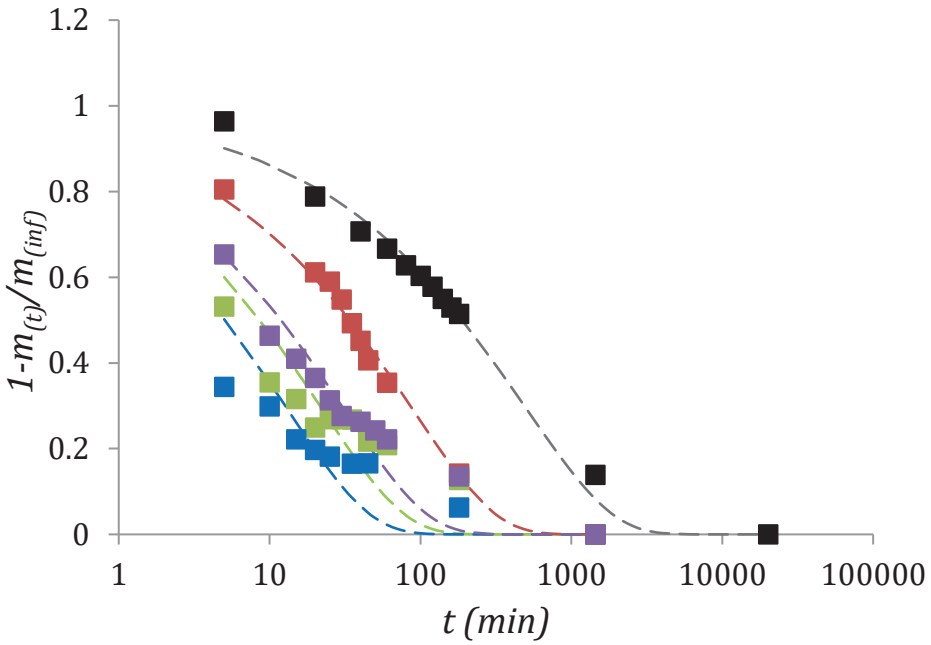

Figure 58. Normalized uptake curves of the different zeolites for *px* in a (50%:50%) *px/ox* mixture and finite system volume model (dashed lines). *n*C10 is the solvent being displaced. The zeolite sample is represented by the different colors: conventional (black) and hierarchical zeolites - NA-1 (red), NA-2 (purple), NA-3 (blue) and LL (green).

Table 12 shows the counter-diffusion times for *px* in the presence of *mx* and *ox*. Although the coefficients are comparable, they are in general smaller for *px* in the presence of *mx* compared to *px* in the presence of *ox*. This difference in *px* diffusion in the presence of the different isomers is probably related to the kinetic diameter of these molecules. Indeed the *ox* (6.86 Å), being larger than *mx* (6.66 Å), generates more resistance to the diffusion of *px*. The largest differences between the time constants for *px* in the different mixtures are observed for the zeolites with smaller external surface areas and/or meso/macropore volumes. As can be seen, the time constants also point out to faster counter-diffusion for hierarchical zeolites - a reduction of the counter-diffusion time around 85% can be observed by comparing the conventional zeolite and zeolite NA-1 for *px* in the presence of *ox*. The reduction in counter-diffusion times may reach values greater than 95% for NA-3 compared to the conventional zeolite. However, this last estimation should be considered with caution, since the counter-diffusion in NA-3 is not ideally described by the model. The absence of a good correlation between experimental data and the diffusion model for the zeolites mentioned above is thought to be related to the existence of the two adsorption regimes described earlier in this section. In the case of the most accessible hierarchical zeolites (NA-2, NA-3 and LL), the first adsorption regime corresponds to a fast diffusion regime. On the other hand, diffusion during the second

regime is slower. This should be the explanation by which the first regime cannot be well represented along with the second regime by means of the finite system volume model.

Table 12. Effective counter-diffusion time constant for the *px* in the presence of *ox* and *mx* for the different zeolites.

Sample Characteristics			Effective Counter-Diffusion Time Constant (h)	
Sample (BaX)	Sext(m^2/g)	Vmeso/macro (cc/g)	*px* (*px/ox* mix)	*px* (*px/mx* mix)
NA-1	43	0.11	23	17
NA-2	48	0.13	8	6
NA-3	68	0.18	3	5
LL	38	0.08	5	4
Conv.	11	0	146	117

For that reason, the counter-diffusion model was applied again, but this time for each regime separately (Figure 59). The boundaries between the first and second regimes were determined with the aid of the uptake curves in Figure 56 and a description is given in Table 13 and Table 14.

The boundaries were determined in terms of molecules/α cage and fractional loading. In general, the last point of the first regime corresponds to larger loadings for the most accessible zeolites (NA-1<NA-2<NA-3). The first point of the second regime is assumed to be equal to the last point in the first regime. As can be seen in Figure 59 (a), the diffusion model for the first regime shows a good correlation with the experimental points for all zeolites. Moreover, the increase of the external surface area, as in the case of zeolite NA-3, does not appear to negatively impact diffusion. This means that diffusion barriers at the external surface level are not significant or are overcome by the positive effect from the presence of meso/macropores.

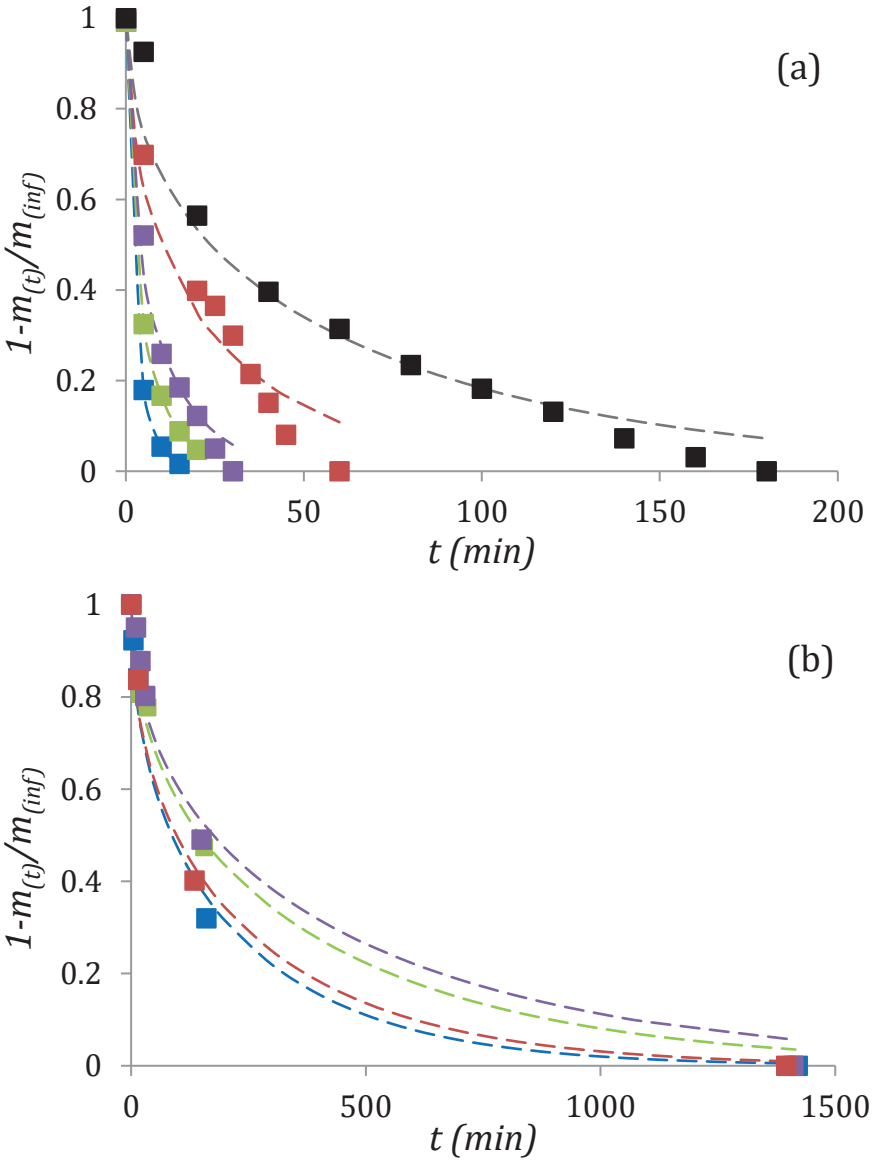

Figure 59. Normalized uptake curves of hierarchical zeolites for *px* in a mixture (50%:50%) and finite system volume model (dashed lines) for first (a) and second regimes (b). *n*C10 is the solvent being displaced. The type of zeolite is represented by the different colors - NA-1 (red), NA-2 (purple), NA-3 (blue) and LL (green).

Furthermore, the diffusion time in the NA-type hierarchical zeolites was found to decrease as the meso/macroporous volume increases. Thus, NA-3 zeolite has optimal diffusional properties among NA zeolites. Nevertheless, the LL zeolite, despites its low meso/macroporous volume compared to other hierarchical zeolites, presents diffusion time similar to the NA-3 zeolite. This demonstrates that the layered structure of the zeolite is more accessible than that of nano-aggregate zeolites. Moreover, as observed in Table 13, the end of the first regime and the beginning of the second regime occur at higher loading for zeolites presenting optimal accessibility (NA-3 and LL). This observation suggests that the greater the

accessibility of the zeolite, the greater the number of xylene molecules that are adsorbed during the fast diffusional regime. As shown in Figure 59 (b), when the concentration in the adsorbed phase becomes significant, the diffusion of *px* behaves according to another diffusional regime (herein designated as second regime). In this case, we are evaluating the *p*-xylene diffusion at high loadings, which slow down the diffusion process.

Table 13. Number of molecules per cage and loadings delimiting the boundaries for the first regime in hierarchical zeolites.

1st Regime					Effective Counter-Diffusion Time Constant (h)
Sample (BaX)	Molecule/α Cage		Loading (%)		
	px	*px/ox*	*px*	*px/ox*	
NA-1	(0 – 1.29)	(0 – 2.34)	(0 – 75)	(0 – 85)	6
NA-2	(0 – 1.56)	(0 – 2.73)	(0 – 72)	(0 – 87)	2
NA-3	(0 – 1.52)	(0 – 2.91)	(0 – 83)	(0 – 91)	0.7
LL	(0 – 1.15)	(0 – 2.19)	(0 – 86)	(0 – 94)	1.4

Table 14. Number of molecules per cage and loadings delimiting the boundaries for the second regime in hierarchical zeolites.

2nd Regime					Effective Counter-Diffusion Time Constant (h)
Sample (BaX)	Molecule/α Cage		Loading (%)		
	px	*px/ox*	*px*	*px/ox*	
NA-1	(1.29 – 2.00)	(2.34 – 3.14)	(75 – 100)	(85 – 100)	44
NA-2	(1.56 – 2.16)	(2.73 – 3.16)	(72 – 100)	(87 – 100)	101
NA-3	(1.52 – 1.95)	(2.91 – 3.21)	(83 – 100)	(91 – 100)	49
LL	(1.15 – 1.53)	(2.19 – 2.56)	(86 – 100)	(94 – 100)	84

Table 14 shows the counter-diffusion time for the second regime, which confirms a much slower diffusion compared to the first regime. It is interesting to note that the counter-diffusion for the second regime is considerably slower for the NA-2 and LL zeolites. This fact is quite peculiar, since these zeolites do not have the same type of structure. Moreover, they do not have the same accessibility characteristics either. Taking a look at the surface chemistry characteristics, we are able to identify that both zeolites have a larger OH density (Figure 60) which seems to justify the long diffusion times. The difference in OH density among all the

samples is very subtle, being perceived only in the second order. The density of OH is designated as the ratio of the integral of the IR band (a.u) (corresponding to OH in the outer surface area) divided by the external surface area of the zeolites. Thus, the density of OH for the LL and NA-2 zeolites are estimated as 1.22 (a.u) m^{-2}, while for NA-1 and NA-3 this density is about 1.10 (a.u) m^{-2}. The fact that a higher density of OH groups reduces *px* counter-diffusion can be explained by a greater interaction with the xylene molecules. Indeed, this causes a slower surface diffusion and possible hindrance of the access to the internal cavities in the zeolite. It can also be suggested that the diffusion at high loadings is more related to the quality (surface chemistry) than to the external surface area.

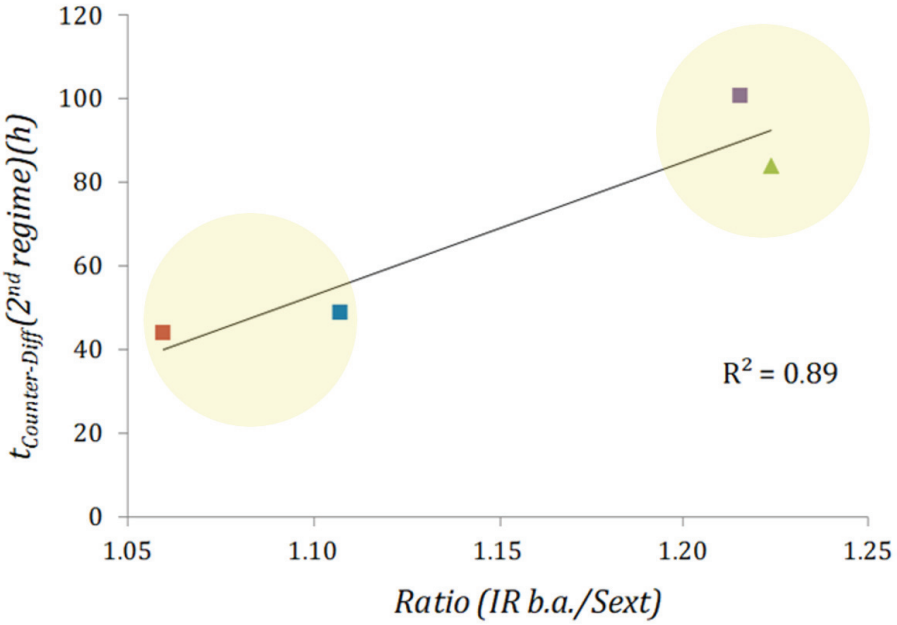

Figure 60. Correlation between OH density at the external surface of hierarchical zeolites and counter-diffusion time constant in the second regime. Squares: NA-1 (red), NA-2 (purple), NA-3 (blue). LL zeolite is represented by the green triangle.

5.1.2 *Comparison with pure px*

The uptake curve of counter-diffusion between *n*C10 and pure *px* was also determined. For this analysis, the samples were taken between 5 and 180 min. The uptake curves for pure *px* do not appear to show different regimes, in contrast to the *px* uptake curve in the presence of other isomers. This may be due to the fact that, at high loadings, the presence of other isomers can hinder *px* diffusion. Moreover, the counter-diffusion of *px* up to 180 min was compared to

the counter-diffusion of *px* in the presence of *ox* and *mx* for the same period of time. Table 15 presents the effective counter-diffusion time constant for pure *px* and for *px* in the presence of *ox* and *mx*. The difference between both time constants is also reported for each zeolite. Figure 61 shows the uptake curves and the fits against the diffusion model for the different systems.

Table 15. Counter-diffusion time constant for pure *px* and for *px* in a mixture (50%:50%). In both cases, *n*C10 is the solvent being displaced. The value of effective counter-diffusion constant in parentheses represents the difference between the counter-diffusion of *px* in the presence of a given isomer and the counter-diffusion of pure *px*.

Sample Characteristics			Effective Counter-Diffusion Time Constant (h)		
Sample (BaX)	Sext (m^2/g)	Vmeso/macro (cc/g)	*px* (pure)	*px* → *px/ox* mix	*px* → *px/mx* mix
Conv.	11	0	11	15 (4)	16 (5)
NA-1	43	0.11	4	14 (10)	6 (2)
NA-2	48	0.13	3	5 (2)	3 (0)
NA-3	68	0.18	1	2 (1)	3 (2)
LL	38	0.08	1	3 (2)	2 (1)

From the data presented in Table 15 and the curves shown in Figure 61, it is seen that, in general, pure *px* diffusion is faster than *px* diffusion in presence of *ox* and *mx*. The difference between the effective counter-diffusion time constant observed for these systems is significantly larger for zeolites with smaller external surfaces (such as conventional zeolite and NA-1). This seems to suggest that *mx* and *ox* isomers get adsorbed at the external surface, which causes some delay during the adsorption/diffusion of the *px* molecules. The hierarchical zeolites with larger meso/macropore volumes and larger external surfaces are probably less impacted by the adsorption of *mx* and *ox* at the surface because *px* has better access in these zeolites.

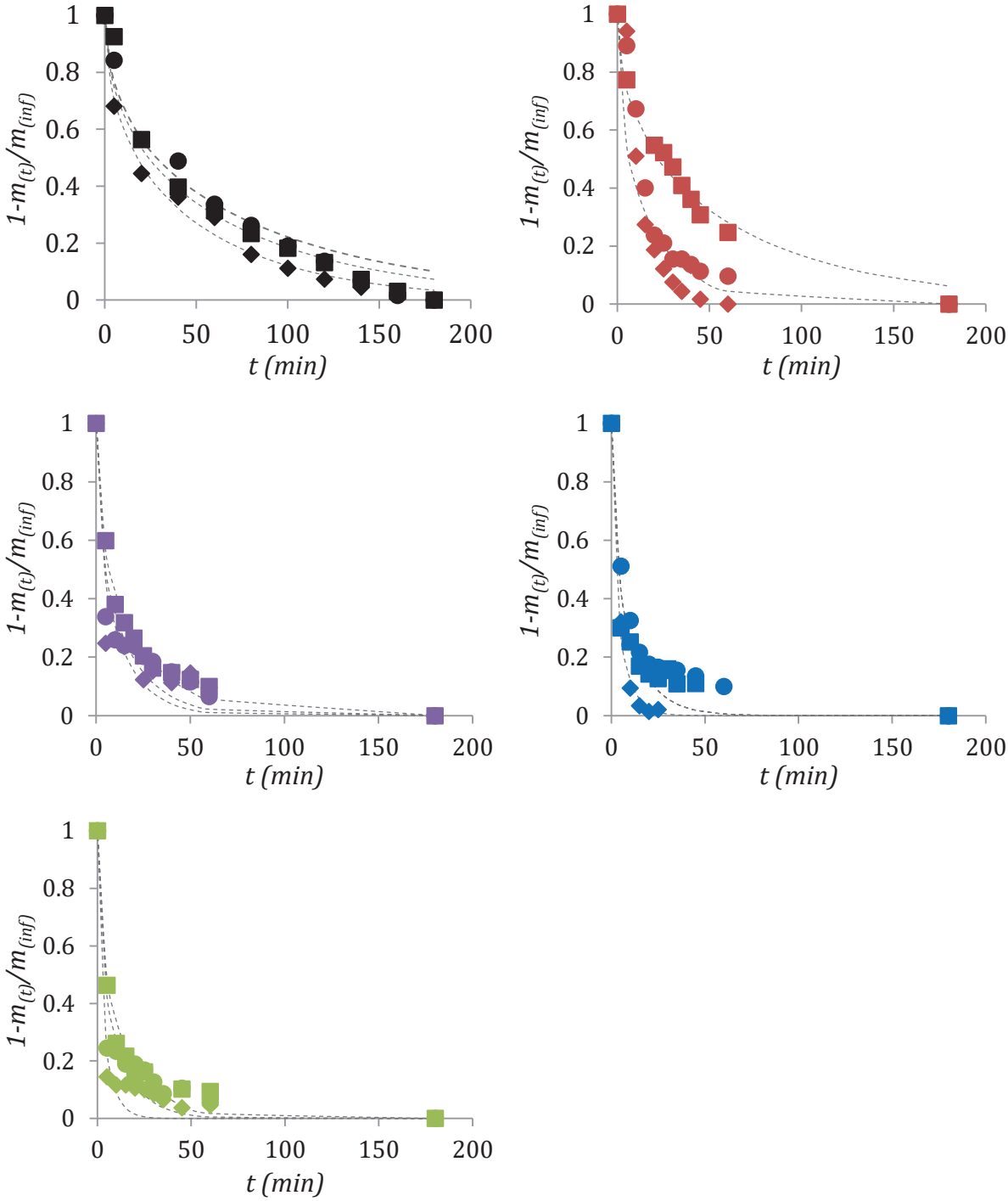

Figure 61. Normalized uptake curves (symbols) and finite system volume model (dashed lines) for pure *px* (diamonds) and for pure *px* in presence of other isomers - 50%:50% *px/ox* (squares) and 50%:50% *px/mx* (circles). In all cases *n*C10 is the solvent being displaced. The zeolite type is represented by the different colors: conventional (black) and hierarchical zeolites - NA-1 (red), NA-2 (purple), NA-3 (blue) and LL (green).

5.2. *Diffusion in partially saturated medium*

As previously explained, the study of diffusion is an important step in the evaluation of an adsorbent for xylene separation. So far, in this work, the diffusion has been studied in the liquid phase and at low temperatures. The results indicate a favorable behavior regarding the use of the hierarchical zeolites. However, with the increase of the external surface, as in the case of hierarchical zeolites, some novel phenomena such as surface resistance may arise. Although surface barriers seem negligible based on the results obtained so far, it is a factor that can hinder the use of a hierarchical zeolite. Thus, in this section, techniques allowing a better understanding of surface barriers and determination of intercrystalline diffusion in gas phase will be addressed.

5.2.1 *Thermogravimetric technique*

Thermogravimetry is a technique that has been widely used for the characterization of diffusion in porous media. This includes the evaluation of diffusion in hierarchical zeolites, where it was able to identify the presence of surface barriers[56]. The diffusion of xylenes in zeolite NaX has already been studied by Ruthven in the 80's[54]. In this seminal study, the use of large crystals of NaX zeolite (250 μm) was used and an accurate estimation of intracrystalline diffusion of about 6 x 10^{-13} m²/s was possible. However, already at this time, Ruthven warned about the fact that finding favorable conditions for the measurement of diffusion in NaX crystals of around 1 μm by the thermogravimetric method is quite complicated[54]. This is due to extracrystalline resistances such as heat effects and bed diffusion, which are usually aggravated upon decreasing the crystal size. The presence of external resistances can be identified by comparing the uptake curves made for two different sample masses. In the absence of external effects, the curves for the same sample, but with different mass must overlap. The absence of thermal effects can also be evaluated by the equation of intracrystalline diffusion (Eq 71). In general, for fractional fillings greater than 70%, $\ln(1-\frac{m_t}{m_{eq}})$ versus *t*-axis should have a Y-axis intercept of about $\ln(-6/\pi^2)$. Otherwise, thermal effects occur.

The uptake curves obtained from thermogravimetric experiments performed at 100°C for hierarchical and conventional BaX zeolites are presented in Figure 62. The curves were obtained from an "empty" zeolite previously desorbed at a temperature of 200°C. Then, the clean zeolite is brought into contact with a *px* pressure of 0.03 mbar.

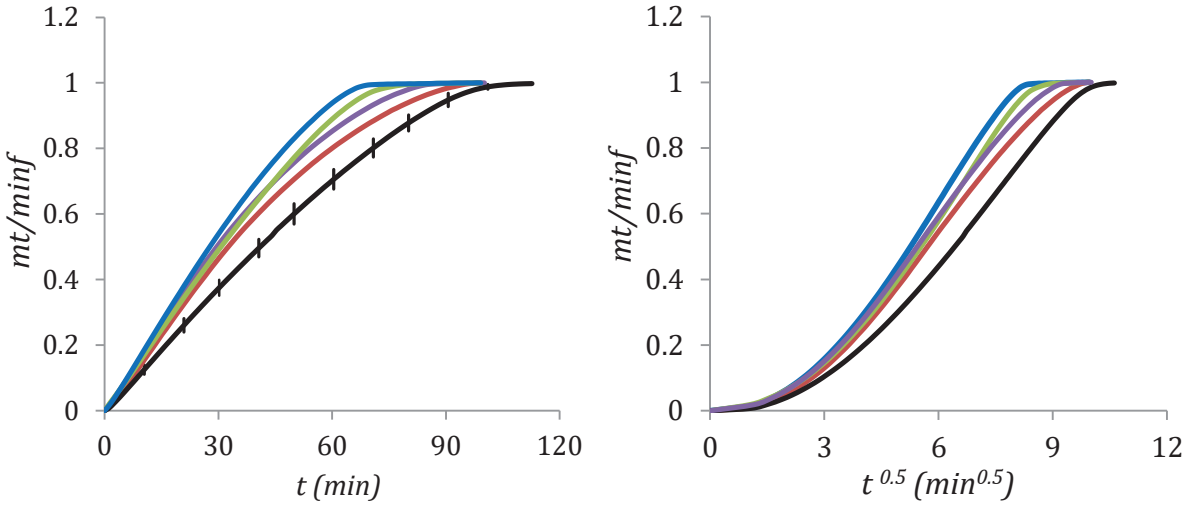

Figure 62. Normalized uptake curves as a function of time (a) and as a function of square root of time (b) for conventional and hierarchical BaX zeolites. The BaX zeolite type is represented by the different colors: conventional (black) and hierarchical zeolites - NA-1 (red), NA-2 (purple), NA-3 (blue) and LL (green). The error bars for the conventional zeolite represent the measures made for two different zeolite masses (upper points correspond to m_{zeo} =8.5 mg and bottom points m_{zeo} =11 mg)

As shown in Figure 62, the time to reach adsorption equilibrium is different among the samples. The conventional zeolite exhibits the slowest diffusion time, which was already expected due to its purely microporous character. The hierarchical zeolites, in all cases, show improved diffusion time compared to the conventional zeolite. It can also be observed that, in the NA zeolites, the greater the mesoporous volume, the shorter the time needed to reach equilibrium. In the case of the LL-type hierarchical zeolite, it presents a diffusion time between those for the NA-2 and NA-3 zeolites (which is not directly linked to the mesoporous volume, as it has even lower mesopore volume than the NA-1 zeolite).

The shape of the curve when plotted as a function of the square root of time (Figure 62 (b)) indicates that the limiting diffusional regime is not intracrystalline diffusion, since a linear relationship is not observed. However, these curves are somewhat different from the sigmoidal curves presented in the literature for diffusion controlled by surface resistance[132]. Furthermore, the initial part of the curve in Figure 62 (a) shows a discrete linear evolution with time for all zeolites, which may also be interpreted as a limitation of the molecule supply during the first few minutes.

In order to get better insight into possible external transport resistance, different samples of conventional BaX zeolite were analyzed by varying the mass of the sample (~ 8.5 and 11 mg). As can be seen in Figure 62 (a), the data difference between the two curves is rather small. In any case, the fact that neither curves overlap indicates that the data difference may be a result

of heat transfer effects[10]. However, the difference between the two curves obtained with conventional BaX upon varying the sample mass is not significant compared to the difference with the other curves for the hierarchical zeolites. Therefore, the comparison to the other curves remains valid, since the mass of the hierarchical zeolites used during the analyses (~10 mg) lies in the range of the masses used for measurements with the conventional zeolite (~ 9 and 11 mg).

All the zeolites were analyzed in terms of microporous (Eq 70) and surface resistance (Eq 72) diffusion models[132]. The experimental data are compared with both models in Figure 63. As can be seen, none of the models is able to accurately represent the experimental data, which may be another indication that heat transfer effect occurs (especially at short time). However, the plots corresponding to the surface resistance model seem more suitable. As an alternative, the intracrystalline diffusion coefficient was obtained from the diffusion model in a linear range found between 0.4 and 0.7 fractional loadings, according to the long time diffusion approach (Eq 71). Although the regime chosen is not commonly used in the literature, one should mention that the intermediate loading intervals are interesting for the description of the diffusion coefficients[10]. Especially because at the beginning of the curve (low loadings) the adsorption of xylenes (due to its exothermicity) generates a non-isothermal condition to the system.

$$\frac{m_t}{m_{eq}} = 1 - 6/\pi^2 \sum_{n=1}^{\infty} \frac{1}{n^2} \exp\left(\frac{-n^2\pi^2 D_{intra} t}{r^2}\right) \quad \text{Eq 70}$$

$$\frac{m_t}{m_{eq}} = 1 - 6/\pi^2 \exp\left(\frac{\pi^2 D_{intra} t}{r^2}\right) \quad \text{Eq 71}$$

$$\frac{m_t}{m_{eq}} = 1 - \exp\left(-\alpha \frac{3}{r} t\right) \quad \text{Eq 72}$$

$$\frac{1}{D_{app}} = \frac{1}{D_{intra}} + \frac{5}{\alpha r} \quad \text{Eq 73}$$

where D_{intra} and D_{app} are, respectively, the apparent and intracrystalline diffusivity (both in m²/s). r is the crystal radius in m and α is the surface permeability (m/s).

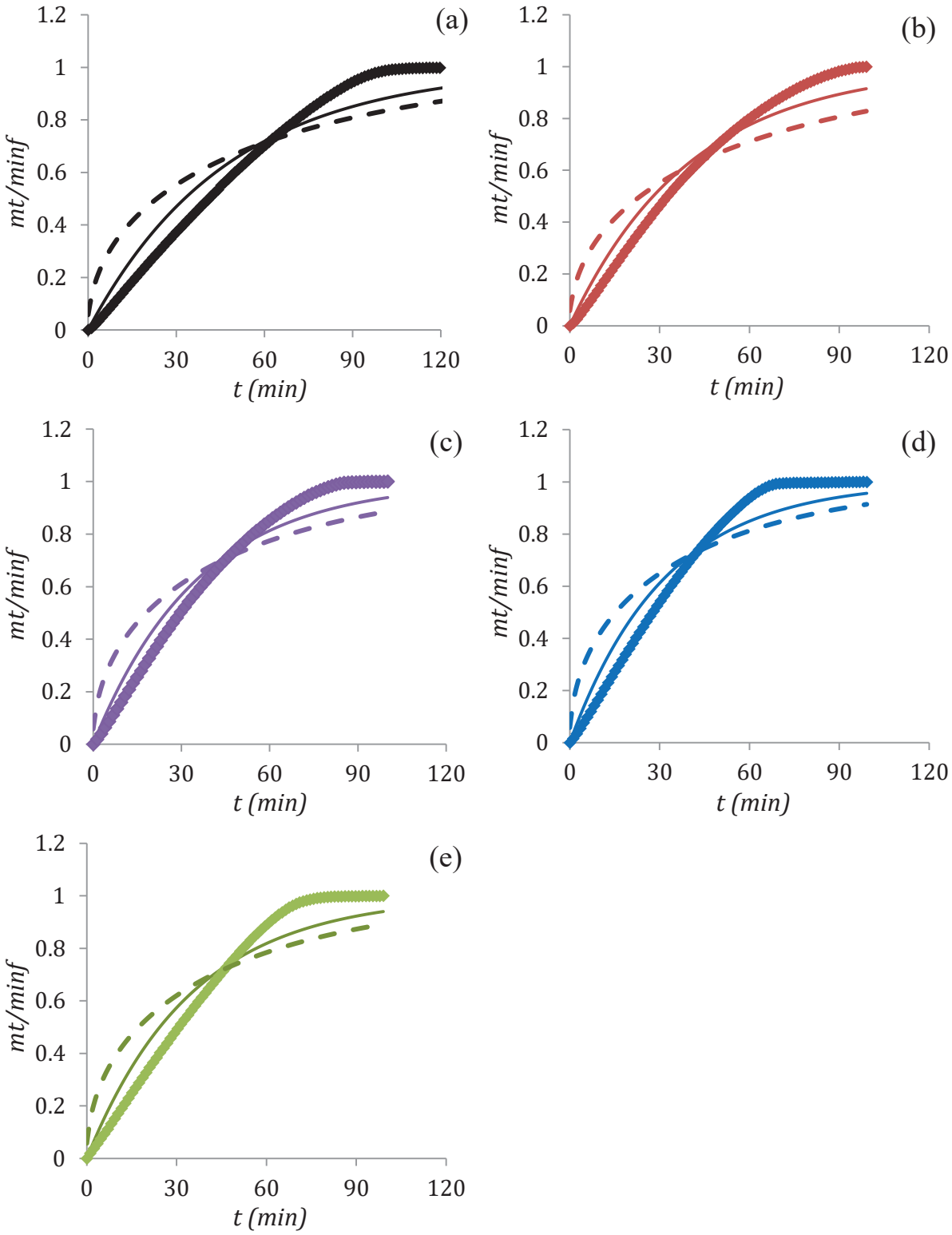

Figure 63. Normalized uptake curves (thick line) as a function of time and respective models for measurement of intracrystalline diffusion (dashed line) and surface resistance (solid line) (a-e). The BaX zeolite type is represented by the different colors: conventional (black) and hierarchical zeolites - NA-1 (red), NA-2 (purple), NA-3 (blue) and LL (green).

After obtaining the diffusion and surface permeability coefficients, a comparison between the hierarchical and conventional zeolites was made. The diffusion time decreases by 30% between the conventional and the hierarchical zeolite NA-3. The NA-2 and LL zeolite have shown quite similar diffusion properties, while NA-1 zeolite displays about 20% of diffusional time reduction with respect to the conventional zeolite. The diffusion times are plotted against the equivalent crystal radius calculated from XRD analysis in Figure 65 (b) (filled symbols). Moreover, as similarly proposed by Tanaka et al.[132], an estimate of the apparent diffusivity based on the diffusivity of a conventional zeolite was performed. To do so, the intracrystalline diffusion coefficient for the conventional zeolite was calculated from the slope of the corresponding curve as plotted in Figure 64 and from its crystal radius.

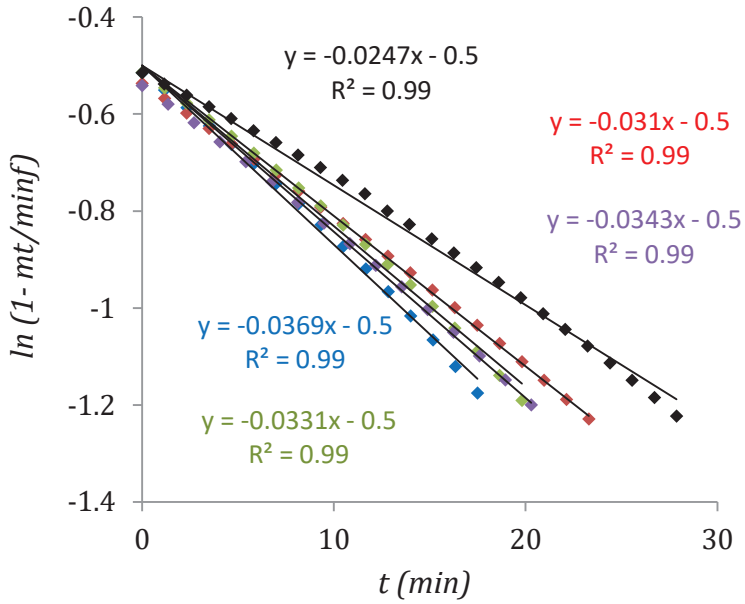

Figure 64. Diffusion model at long times for all zeolites and for fractional filling between 0.4 and 0.7. The BaX zeolite type is represented by the different colors: conventional (black) and hierarchical zeolites - NA-1 (red), NA-2 (purple), NA-3 (blue) and LL (green). The curve slope presented in the equations correspond to $\left(\frac{\pi^2 D_{intra} t}{r^2}\right)$.

As the crystal size of the hierarchical zeolites could not be obtained due to the high agglomeration rate, we will use, for comparison purposes only, the radius of the size of the crystallites calculated by the Scherrer equation (from the XRD measurement as presented in chapter 3). As the size of the crystallites does not necessarily reflect the size of the crystals but rather the size of periodic domains without defects, the diffusion coefficients extracted from this approximation have to be considered with caution. Proof of this is that the intracrystalline diffusion coefficient found for the conventional zeolite is $2.3 \times 10^{-17} m^2/s$, considering the real

crystal radius (0.75 μm), while the diffusion coefficient calculated based on the Scherrer crystallite radius (90 nm) is $3.4x10^{-19}$ m²/s. Nevertheless, the estimation of the diffusion coefficients from the Scherrer crystallites size is relevant for comparison purposes. Through this measure a ranking of crystallite sizes is consistent with the characteristics of the hierarchical zeolites (NA-1<NA-2<NA-3~LL). Therefore, for the estimation of apparent diffusion coefficients of the hierarchical zeolites (empty symbols in Figure 65 (a)), Eq 73 was used. D_{intra} was considered as the diffusion coefficient obtained for the conventional zeolite and the surface permeability was considered as the average of all zeolites. The crystal radius was assumed to be the respective Scherrer crystallite radius measured for each zeolite.

The graph obtained for the apparent diffusivities (Figure 65 (a)) indicates that the effect of the surface resistance is the limiting effect in the case of the diffusion in the hierarchical zeolites. Indeed, using the intracrystalline diffusion of the conventional zeolite to estimate the apparent diffusions in the hierarchical zeolites has almost no effect in the apparent diffusivities. The same can be concluded by observing the expected apparent diffusion for the conventional zeolite if it had surface permeability similar to a hierarchical zeolite.

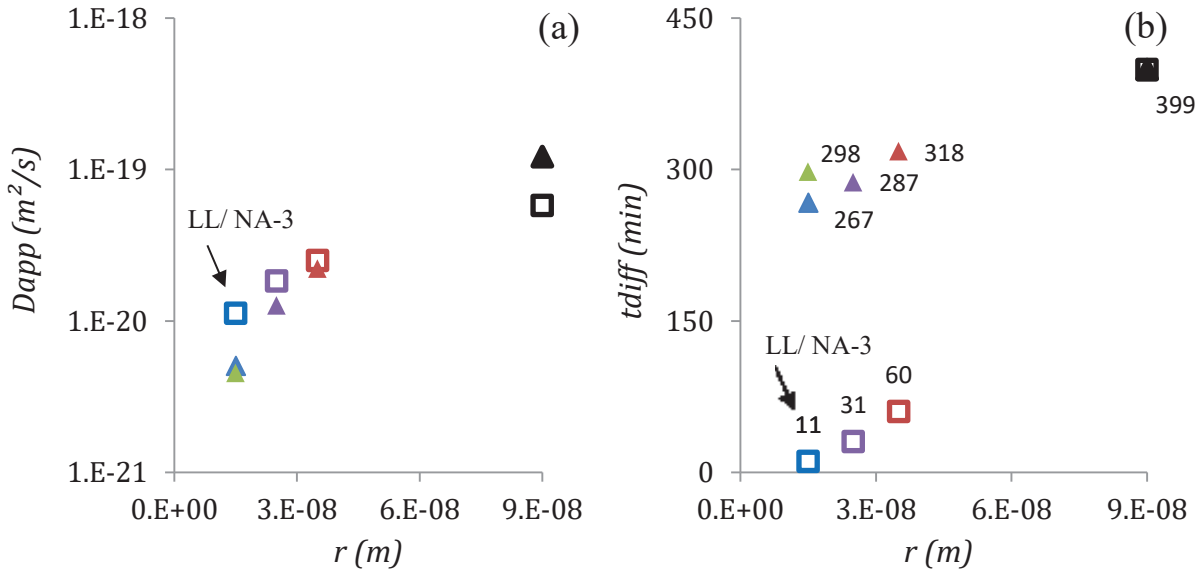

Figure 65. (a) Experimental apparent diffusivity (filled symbols) and estimated apparent diffusivities based on the diffusivity of the conventional zeolite (open symbols); (b) Experimental diffusion times (filled symbols) and estimated diffusion times based on the diffusivity of the conventional zeolite and crystallite radius of hierarchical zeolites (open symbols). The BaX zeolite type is represented by the different colors: conventional (black) and hierarchical zeolites - NA-1 (red), NA-2 (purple), NA-3 (blue) and LL (green).

The diffusion time constant for the hierarchical zeolites were estimated based on the diffusivity of the conventional zeolite. The diffusion time constant was given by the product of diffusivity for a conventional zeolite and square of the Scherrer crystallite radius of the respective hierarchical zeolites (empty symbols in Figure 65 (b)). This approach allows to evaluate the ideal diffusion time constant in the hierarchical zeolites, as a function of their crystallites radius, if these zeolites had the same intracrystalline diffusion than the conventional zeolite.

The results above indicate that the theoretical diffusion time should lead to an improvement of about 97% of the diffusion time. In contrast, only a 30% diffusion increase is observed according to the experiments, which implies that there is a strong surface resistance hindering the diffusion time. In the literature, surface resistance was identified in different works that linked the origin of this effect to: (1) partial blockage of pores on the surface[43]; (2) distortion of the crystal structure at the external surface[44,45]. Contrary to what is observed in the gas phase, batch experiments performed in liquid phase have shown a reduction of the diffusion time in hierarchical zeolite NA-3 by about 95% compared to the conventional BaX (see section 5.1). This suggests that in hierarchical zeolites, liquid phase diffusion is surface barriers free, as opposed to gas phase diffusion. One can explain this by the larger concentration of molecules surrounding the particles surface in liquid phase, which yields higher probability for the molecules to enter then zeolites cavities[46]. In contrast, in the gas phase, there are fewer molecules surrounding the surface and, therefore, when they hit the surface, they have a higher probability to stick to the surface rather than entering the cavities.

5.2.2 *Pulsed field gradient nuclear magnetic resonance (PFG - NMR)*

The PFG - NMR is a technique that allows the investigation of microscopic diffusion pathways. Therefore, this technique is efficient for the determination of intracrystalline diffusion in small crystals as in the case of hierarchical zeolites. A work using this technique to determine diffusion coefficients in hierarchical zeolites is already available in the literature [57]. However, as it will be demonstrated below, in order to achieve accurate measurements of intracrystalline diffusion coefficients in small crystal zeolites, it is necessary to fulfill some requirements regarding the magnetic field gradient intensities and pulse duration.

Stimulated echo sequences PGSTE (see section 2.3.2) were performed at ambient temperature on as synthesized zeolites, *i.e.* NaX forms, by varying the diffusion time Δ (10 ms, 50 ms, 100 ms, 150 ms and 200 ms) with a pulsed field gradient intensity G for a duration δ of 1ms. Figure 66 presents the attenuation curves obtained with conventional NaX zeolite. These data show the evolution of the attenuation signal Ψ as a function of $(\gamma\delta G)^2\Delta'$ for the different diffusion times ($\Delta' = 4\Delta + 6\tau - \frac{2}{3}\delta$ is the effective diffusion time, where τ is the time interval between two pulses). These data were obtained for a system where the zeolite is loaded with 3 *px* molecules/α cage. It is possible to observe that each curve presents two linear regimes. The first decay corresponds to the long-range diffusion ($D_{long\text{-}range}$) (small $(\gamma\delta G)^2\Delta'$), which is associated with the large displacements during the NMR experiment time. The second decay, obtained for large $(\gamma\delta G)^2\Delta'$ is associated with intracrystalline diffusion (D_{intra}), which corresponds to small displacements. It is possible to calculate the intracrystalline and long-range diffusion coefficients using a bi-exponential fitting (Eq 74) to determine $D_{long\text{-}range}$, D_{intra} and β (probability of finding molecules out of the crystal).

$$\Psi(\Delta', q) = \left(1 - \beta(\Delta')\right)\exp\left(-q^2\Delta' D_{intra}\right) + \beta(\Delta')\exp\left(-q^2\Delta' D_{long-range}\right) \qquad \text{Eq 74}$$

where $\Psi(\Delta', q)$ is the signal attenuation and $q = \gamma\delta G$ is the intensity of the wave vector.

This model was applied to the data in Figure 66. The results of D_{intra} and $D_{long\text{-}range}$ are shown in Table 16. The intracrystalline diffusion values are in good agreement with those observed for cyclohexane in NaX zeolite at ambient temperature (1.2 x10^{-12}m²/s). It is possible to observe that the contribution of the intracrystalline diffusion differs according to the diffusion time. Furthermore, the decrease of D_{intra} observed with the increase of the diffusion time can be taken as an evidence of the presence of activation barriers to intra-crystal diffusion. This conclusion can be observed from the evaluation of the displacement Z^2 (~0.2-0.3 μm), obtained through the values of diffusivity and diffusion time. This displacement is inferior to the size of the crystals (~ 1.5 μm), which justifies the presence of intracrystalline diffusion barriers rather than surface barriers. However, even though the tests were performed at room temperature, PFG NMR (NaX) results still indicate a faster diffusivity than those evaluated by thermogravimetry (BaX at 100°C) (section 5.2.1). The difference is from 4 to 6 orders of magnitude between BaX and NaX (a 2 order of magnitude was already reported in the case of liquid phase diffusion): such a huge difference is at least partially explained by the nature of

the cation (probably related to the ionic radius, 0.95Å and 1.35Å for Barium and Sodium, respectively).

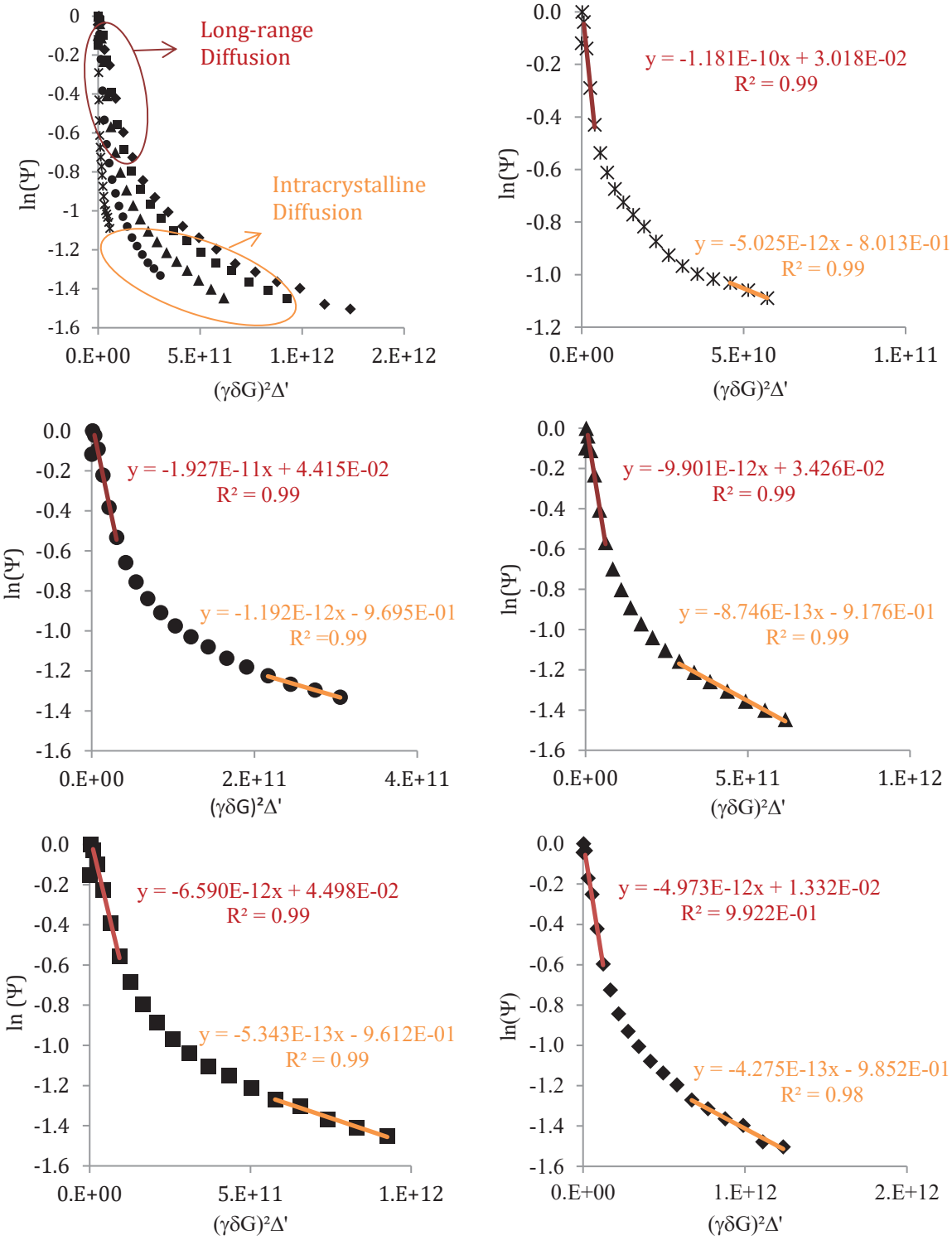

Figure 66. Variation of lnΨ as a function of $(\gamma\delta G)^2\Delta'$ using the sequence PGSTE with a gradient pulse duration δ of 1 ms and a diffusion time Δ of: 10 ms (asterisks), 50 ms (circles), 100 ms (triangles), 150 ms (squares) and 200 ms (lozenges). The system is *px* in conventional NaX zeolite at a loading of 3 molecules/α cage.

Table 16. Long-range and intracrystalline diffusion coefficients of *p*x in conventional NaX zeolite.

	Δ (ms)	$D_{long-range}$ (m^2/s)	Error (m^2/s)	D_{intra} (m^2/s)	Error (m^2/s)	α	Z^2 (μm)
px/ Conv. NaX	10	$1.2x10^{-10}$	$6.2x10^{-12}$	$5.0x10^{-12}$	$1.4x10^{-13}$	55%	0.22
	50	$1.9x10^{-11}$	$6.6x10^{-13}$	$1.2x10^{-12}$	$7.3x10^{-14}$	62%	0.24
	100	$9.9x10^{-12}$	$2.9x10^{-13}$	$8.7x10^{-13}$	$3.0x10^{-14}$	60%	0.29
	150	$6.6x10^{-12}$	$1.6x10^{-13}$	$5.3x10^{-13}$	$2.8x10^{-14}$	62%	0.28
	200	$5.0x10^{-12}$	$2.5x10^{-13}$	$4.3x10^{-13}$	$2.6x10^{-14}$	63%	0.29

The PGSTE sequence was applied to the system *px*/LL NaX zeolite with a gradient pulse duration δ of 1 ms and varying the diffusion time Δ from 10 ms to 15 ms (to observe the intracrystalline diffusion). The purpose of applying different diffusion times is to highlight the existence of energy barriers on intracrystalline diffusion. However, in contrast to what has been observed for the conventional NaX zeolite, in this case, we cannot measure the coefficient of intracrystalline diffusion because the linear trend at the end of the curve could not be observed.

In the case of NA-3 NaX zeolite, another attempt to obtain a signal for intracrystalline diffusion was done. This time, the measurements were performed by increasing the gradient pulse duration δ to 1.2 ms and for diffusion times Δ of 5 ms, 15 ms, 50 ms, 100 ms, 150 ms and 200 ms. In Figure 67, it can be noticed that the attenuation of the NMR signal evolves linearly with $(\gamma\delta G)^2\Delta'$ (the last experimental points of the curve are irrelevant due to the noise of the NMR spectrum). Therefore, no signals of intracrystalline diffusion were obtained for times between 50 - 200 ms. For shorter diffusion times, the NMR signal disappears so that it does not allow the measurement of the attenuation curves.

Therefore, in conclusion, a very short observation times (Δ) is needed to measure diffusion in hierarchical zeolites. This conclusion, although only qualitative, means that the diffusion pathway in the hierarchical zeolites is strongly reduced compared to the one in the conventional zeolite. In order to have a quantitative estimate of the intracrystalline diffusion in hierarchical zeolites, very strong intensity gradients (G) and/or longer gradient pulses (δ) are needed to obtain a signal sufficiently attenuated in the region of small displacements. However,

the limit of the equipment used for these analyses does not allow to go further in relation to these parameters.

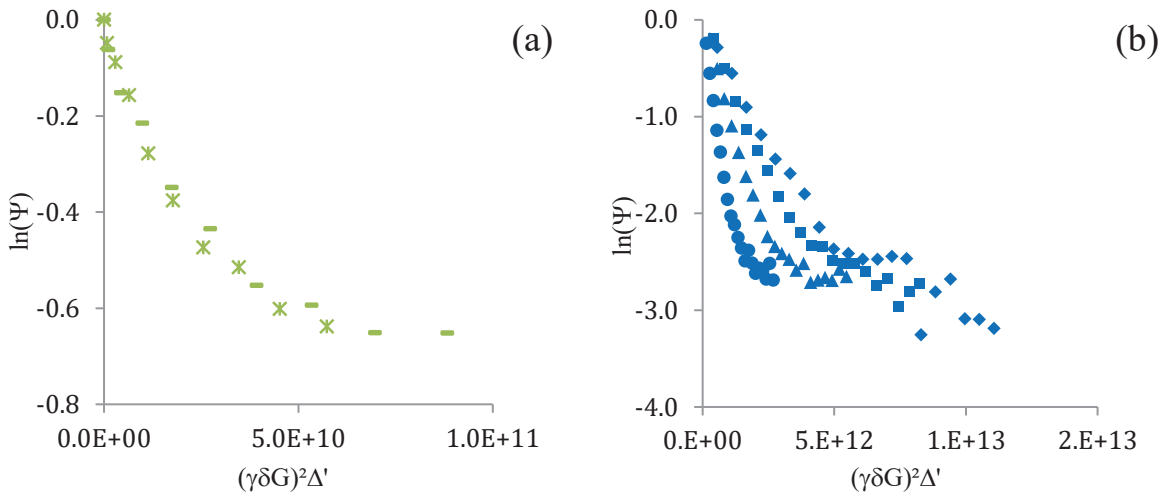

Figure 67. Variation of lnΨ as a function of $(\gamma\delta G)^2\Delta'$ using the sequence PGSTE (a) with a gradient pulse duration δ of 1 ms and a diffusion time Δ of: 10 ms (asterisks), 15 ms (dashes) – System - *px*/ LL NaX – zeolite (green); (b) with a gradient pulse duration δ of 1.2 ms and a diffusion time Δ of: 50 ms (circles), 100 ms (triangles), 150 ms (squares) and 200 ms (lozenges) – System - *px*/ NA-3 NaX – zeolite (blue).

5.3. Conclusions on diffusion properties

Throughout this chapter, the diffusion of xylenes in the conventional and hierarchical zeolites with different structures (NA and LL) was studied. Diffusion in saturated medium was investigated through counter diffusion in liquid phase of xylenes and *n*C10 solvent. The uptake curves indicate the presence of two different diffusion regimes. The first regime corresponds to direct access of the xylene molecules to the micropores while the second regime is slower and corresponds to the diffusion at high loadings within the microporosity. The second regime features a slow diffusion of *px* towards its preferential adsorption site, accompanied in some cases with slight desorption of the other isomers. The model for the study of counter-diffusion was applied to the total uptake curve and also to the first and second regime regions. In all cases, it is clearly observed that the hierarchical zeolites display faster diffusional properties compared to the conventional zeolite.

In the case of NA zeolites, it was observed that the larger the meso/macroporous volume, the faster the diffusion. In addition, surface diffusion barriers were not observed in

the case of zeolite NA-3 (which has the largest external surface area). It could still be seen that the LL-type structure shows diffusion characteristics superior to NA zeolites with similar external surface characteristics. This is also in agreement with Hg intrusion and N_2 sorption analysis in Chapter 3, which showed total mesopore accessibility in the LL structure, while NA zeolites presented a small portion of restricted mesopores. Similarly, the scanning curves also indicated fully mesopore accessibility for LL zeolite. As shown in this chapter, the diffusional benefit between a conventional zeolite and the hierarchical zeolite NA-1 is about 85%, as observed through the comparison of time constants for counter-diffusion. This gain is even larger when dealing with the other hierarchical zeolites. Values of around 95% were suggested for the NA-3 zeolite, although the low correspondence between the model and the experimental data in the latter case does not allow an accurate determination.

The study of xylene diffusion in partially saturated medium in hierarchical and conventional zeolites proved to be a difficult task. The used techniques, have shown to be very sensitive to experimental conditions, which makes it difficult to obtain clear answers. Thermogravimetry, for example, appears to be impacted by external resistance. For PFG NMR, the limitation appears to be due to the equipment and its ability to provide sufficiently intense and long magnetic gradient fields. Despite these difficulties, the study of xylene diffusion in the gas phase at 100°C using thermobalance allowed to demonstrate the existence of surface barriers that had not been identified during the liquid phase experiments. It could be interesting to investigate this difference in more detail, for instance using molecular dynamics. However, it seems that the large concentration of molecules surrounding the particles reduces the surface resistance barriers in liquid phase adsorption. Such observations confirm the interest of the xylene separation in liquid phase in the case of the use of hierarchical zeolites, since in these conditions the surface barriers seem negligible.

6. *Study of the surface adsorption by molecular simulation*

In the previous chapters, efforts were dedicated to characterize the external surface of zeolites by means of different techniques. In the same direction, several experimental techniques were implemented in order to study both the adsorptive and diffusive behavior of hierarchical systems. Although the information obtained is significantly rich, the main difficulty is linking the surface features to the adsorption/diffusion properties. In the present chapter, molecular simulation techniques are proposed in order to try to get more insights on the relationship between the two previous mentioned items. In first attempt in the frame of this work, Monte Carlo (MC) simulations are performed in order to study the surface influence in the adsorption properties.

Although different molecular simulation techniques are eligible to study the surface effects (Quantum chemistry, Molecular Dynamics), a choice must be done among them due to the limited amount of time available for such work, as this thesis is mainly experimental. MC techniques were selected due to different factors. On the one hand, the xylene separation applications are mainly based on equilibrium adsorption phenomena. Despite some minor differences can exist between the diffusive behaviors of the different isomers, the separation selectivity arises from thermodynamic affinity (entropic) of the adsorbent for the *px* molecule. Therefore, the use of the MC method is justified by its ability to describe the adsorption equilibrium. On the other hand, Monte Carlo techniques present a main advantage when compared to *ab initio* quantum chemistry calculations: it allows considering a much larger amount of system particles. In this way, the use of the MC technique can account for the cooperative ensemble effects associated to the adsorption in liquid phase.

In the next paragraphs, a short description of the methodology will be presented. First, a short introduction of the theoretical aspects of MC technique will be presented along with the parameterization of the system (performed in the frame of previous studies to this work). Then, the methodology adopted in this thesis to create the surface will be introduced. The validation of the model will be done over the bulk-crystal adsorption (adsorption in a system comprising only the microporous domain) of both pure compounds (*px* and *mx*) and their equimolar mixture in two different faujasitic adsorbents: NaLSX and BaLSX. Finally, the adsorption behavior on the surface will be investigated on the systems incorporating a surface.

6.1. Grand canonical Monte Carlo (GCMC) methodology

Along with Molecular Dynamics (MD), the Monte Carlo molecular simulation methodology allows the application of Molecular (or Classical) Mechanics to large size particle systems as is the case of liquid adsorption in zeolites. Both methodologies, based on the use of intermolecular potentials (also known as Force fields), allow calculating the forces/energies acting on each particle of the system. Contrary to *ab initio* quantum chemistry calculations, the notion of electronic density distribution is not considered and the potential energy of the particle system (or ensemble) is considered to be only a function of the mass centre coordinates of the different particles. This approximation holds particularly well for the case of the physisorption of xylene molecules in zeolites, characterized by the absence of chemical bonding. In addition, the use of Molecular Mechanics allows to significantly reducing the computational cost of the calculation. As an example, the computational time scales is about N^2 (being N the total number of particles) for the case of MC molecular simulation. In the case of *ab initio* quantum chemistry calculations, the computational time scales has an exponent between four and seven (N^4 to N^7).

GCMC (Grand Canonical Monte Carlo) simulations combined with a bias scheme[133] for the insertion of the centre of mass of the guest molecules were performed to calculate the adsorption isotherms with the GIBBS code v.9.3. Systems were allowed to equilibrate for at least five million MC steps followed by production runs of at least 10 million MC steps. The atomic positions of the solid were frozen during the simulations. This allowed the construction of a guest-host interaction energy grid prior to the MC simulations. While bulk-crystal simulations were performed in a simulation box incorporating a single unit cell, for the study of the surface larger systems were used. The total number of atoms corresponds at least to the equivalent of three elementary unit cells. Lenard-Jones interactions were calculated using a cutoff radius of 12.50 Å. No Lennard-Jones tail corrections were considered. In order to account for the long-range nature of the electrostatic contribution, the standard Ewald summation technique was employed. The crystallographic positions of the different atoms were taken from the data available in the Materials Studio software[134].

6.2. *Force field implementation*

6.2.1 *Xylene adsorption in NaLSX and BaLSX for bulk-crystal systems*

The bulk-crystal systems take into account only adsorption in the micropores. Both the adsorbent and the adsorbates are considered as rigid molecules. This assumption has been shown to be valid in previous works considering the adsorption of xylene isomers in zeolitic systems[17]. Since the Si/Al ratio of the X zeolites considered in this work is relatively close to that of their analogous LSX (Low Silica X) forms, in what follows the latter forms will be considered. Thanks to this approximation, a simplification is performed, interesting from both the point of view of the extra-framework cationic distribution and the Silicon/Aluminium distribution. Thanks to these assumptions, the general form of the force field is reduced to a simplified expression only based on the summation of two different contributions accounting for the dispersion-repulsion and the electrostatic interaction forces:

$$U_{TOT} = U_{LJ} + U_{elec} \quad \text{(Eq 75)}$$

Although it is well known that the origin of the adsorption *px*-selectivity in some zeolitic forms arises from an entropic contribution[53], it is worth mentioning the importance of the electrostatic contribution when dealing with counter-cationic species and aromatic hydrocarbons.While the first contribution, corresponding to the dispersion-repulsion energy is described *via* a Lennard-Jones potential, the second contribution (electrostatic) is treated by means of a coulombic term:

$$U_{LJ}^{ij}(r) = 4\,\varepsilon_{ij}\left[\left(\frac{\sigma_{ij}}{r_{ij}}\right)^{12} - \left(\frac{\sigma_{ij}}{r_{ij}}\right)^{6}\right] \quad \text{(Eq 76)}$$

$$U_{elec}^{ij}(r) = \frac{q_i q_j}{4\pi\varepsilon_0 r_{ij}^2} \quad \text{(Eq 77)}$$

where ε_{ij} is the depth potential energy, $r_{ij}$is the distance between two particles, σ_{ij} is the distance between two particles where the potential energy is zero. The first term $\left(\frac{\sigma_{ij}}{r_{ij}}\right)^{12}$ describes repulsive interaction and the second one $\left(\frac{\sigma_{ij}}{r_{ij}}\right)^{6}$ attractive interaction. ε_0 is the electrostatic vacuum permittivity, q_n is the electric charge and *r* is the distance between the charges.

In what follows, a brief description of the implementation of the force field is done for the different species of the system.

6.2.2 *Xylenes force field*

The adsorbate molecules are described according to the electrostatic version of the anisotropic united atom (AUA) for aromatics[135]. Inspired from the work of Peralta et al.[136] and to avoid charges collapse between the ring-centered quadrupole and the counter-cations, slight modifications were introduced in order to distribute the electrostatic interaction around the totality of the aromatic ring. A schematic representation of the implementation of the model is shown in Figure 68. The different parameters used in the calculations are compiled in Table 17.

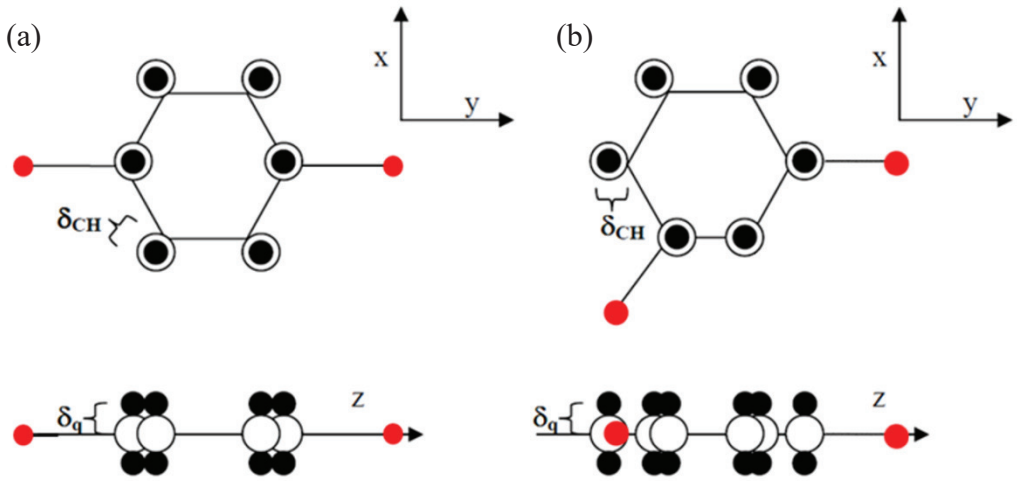

Figure 68. Schematic representation of the implementation of the electrostatic version of the AUA potential for *px* (a) and *mx* (b). (*Adapted from Ref.* [136])

Table 17. Lennard-Jones parameters and electrostatic punctual charges of the adsorbate molecules.

Force center	$\sigma^{\dagger}$ [Å]	$\varepsilon^{\dagger}$ [K]	$\delta^{\dagger\dagger}$ [Å]	$\delta_q{}^{\dagger\dagger\dagger}$ [Å]	q [e]
CH3-AUA	3.6072	120.15	0.21584	---	0.025
CH-arom-AUA_elec	3.361	75.6	0.315	0.4	1.355/-0.68167
C-arom-AUA_elec	3.361	35.43	---	0.4	1.355/-0.68167

† Lorentz-Berthelot mixing rules were employed to determine the interactions between different force center types. †† δ is the anisotropic distance used in the AUA (Anisotropic United Atoms) potential. ††† δ_q corresponds to the shift between the positive and negative electrostatic charges of the aromatic ring.

6.2.3 *NaLSX and BaLSX force field*

As previously mentioned and for the sake of simplicity, the low silica LSX analogous forms of the NaX and BaX adsorbents are considered. In the same way, the general assumption of considering rigid the zeolite framework is adopted. The description of the dispersion-repulsion interactions of the framework is considered *via* a *Kiselev* type potential[137]. This type of potential assumes that the *T* atoms (either Silicon or Aluminium) of the different tetrahedra constituting the zeolite framework are screened by their respective four surrounding oxygen atoms. Concerning the sodium counter-cations, the parameters are borrowed from the work of Smith and Dang[138]. The barium parameters are calculated following the strategy derived by Maurin *et al.*[139] The crystallographic positions of the cations were obtained from Pichon et al.[19] In order to account for the electrostatic interactions, electrostatic punctual charges were determined from Density Functional Theory (DFT) calculations performed in the scope of previous works. The different parameters used in the calculations are compiled in the following tables:

Table 18. Lennard-Jones parameters and punctual electrostatic charges of the adsorbents.

Force center	$\sigma^{\dagger}$ [Å]	$\varepsilon^{\dagger}$ [K]	$q^{\dagger\dagger}$ [e] NaLSX	$q^{\dagger\dagger}$ [e] BaLSX
O-zeolite	3.00	112.236	-1.2529	-1.2447
Si-zeolite	0.00	0.00	1.9751	2.1439
Al-zeolite	0.00	0.00	2.0728	1.9931
Na	2.584	50.34	0.9770	---
Ba	3.3191	141.789	---	1.6834

† Lorentz-Berthelot mixing rules were employed to determine the interactions between different force center types.
†† Average values.

6.2.4 *Xylene adsorption in NaLSX and BaLSX systems bearing an interface*

Through the following sections the choice of the types of surfaces is justified and the methodology used to cleave the solids is described. Then, the extension of the general force field is presented.

6.2.4.1 *Surface selection and preparation*

As far as known, no evidence of preferential growth direction in faujasite zeolites is established. Therefore, the surface direction {0 1 1} was chosen since the cleavage is performed at the level of the *α* cages. Figure 69 shows an example of surface cleavage {0 1 1}, where the open *α* cages can be seen at the surface level. As previously discussed in Chapter 4, it is possible that such open cavities at the surface level induce an impact on *px*-selectivity. At high loadings, *px* is selectively adsorbed in a site at the center of the dodecagonal window. In the case of the surface {0 1 1}, the incomplete dodecagonal window at the surface level can affect *px*-selectivity. The surface direction {0 1 1} cleavage was performed using the Materials Studio software[134]. The parameters used were as follows: Cleavage plane {h k 1} is equal to {0 1 1} with origin (a b c) at (0 0 1).

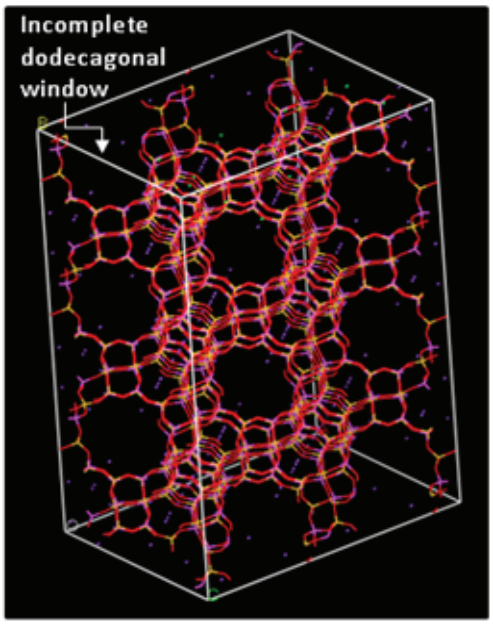

Figure 69. Structure of the cleaved surface {0 1 1} for a LSX zeolite. The surface {0 1 1} cut the α cages leading to incomplete dodecaconal windows at the surface level.

The chemical reconstruction of the surface was based on IR analyses reported in Chapter 3, through which silanol groups are observed on the outer surface. Since the zeolites also exhibit aluminum tetrahedra at the surface level, all bonds missing in the Si or Al tetrahedra were saturated with OH groups after surface cleavage. A similar approach has been reported in the literature[140]. After generating the surfaces by cleaving the bulk-crystal zeolites and modifying their surface chemistry, the positions of the atoms in the surface were optimized in order to

obtain systems not bearing any dipole moment contribution. The surfaces have been positioned sufficiently far from each other, so that there is no interaction between them.

6.2.4.2 *Surface force field*

In order to simulate the systems including the interface between the adsorbent and the fluid in equilibrium, the surface atoms need to be parameterized. Since the main impact caused by the introduction of the surface is expected to mainly present an electrostatic nature, the adopted strategy consisted in 1) keep for the surface atoms the same parameterization as in the case of the bulky atoms, and 2) borrow the electrostatic charges from the CLAYFF potential as recently done by Crabtree et al.[141] Finally in the case of the dispersion-repulsion parameters lacking, they were obtained from the generic Universal Force Field (UFF) potential[142]. A compilation of the different parameters used for the surface oxygen and hydrogen atoms is presented in Table 19:

Table 19. Lennard-Jones parameters and electrostatic punctual charges of the zeolite surface.

Force Center	$\sigma^{\dagger}$[Å]	$\varepsilon^{\dagger}$[K]	q[e]
O-zeolite_surf	3.0000	112.236	-1.0984
H-zeolite_surf	2.5711	22.1418	0.4250

† Lorentz-Berthelot mixing rules were employed to determine the interactions between different force center types.

6.3. Xylene adsorption in NaLSX and BaLSX

In a first step, the adsorption of xylenes in bulk-crystal sodium and barium LSX exchanged faujasites is considered for two main goals. On the one hand, the consideration of such systems allow the comparison with experimental data of both xylene pure isomers (adsorption isotherms and enthalpies of adsorption) and mixtures (adsorption selectivities). On the other hand, the obtained results and observed behaviors will serve as a reference when considering the surface adsorption. In this way, the deviations from the bulk-crystal behavior can be identified.

6.3.1 *Xylene adsorption in NaLSX and BaLSX bulk-crystal systems*

The computed isotherms obtained for pure xylenes in the NaLSX and BaLSX systems are shown in Figure 70. The amount of adsorbed molecules/α cages is in agreement with the experiments carried out here in gas phase for the conventional zeolite at 175°C. When *px* is the adsorbate, the adsorbed amount is about 3.5 molecules/α cage, against 3.4 molecules/α cage obtained through simulation at the same temperature. The obtained results allow validating the force field on the basis of capacity of adsorption. The adsorption isotherms obtained from an equimolar xylene mixture are also shown in Figure 70. The adsorption of mixtures is considered in order to further validate the system force field. These binary simulations are firstly aimed to check the validity of the model to reproduce the different ratios between isomer affinities for a given adsorbent.

The amounts adsorbed between NaLSX and BaLSX are close. However, in general, a slight increase in the adsorbed amounts is observed for BaLSX zeolite. The amount of *px* (from *px/mx* mixture) adsorbed in the zeolite BaLSX (dashed line) is also more significant, which is an indication of the *px*-selectivity in zeolite BaLSX.

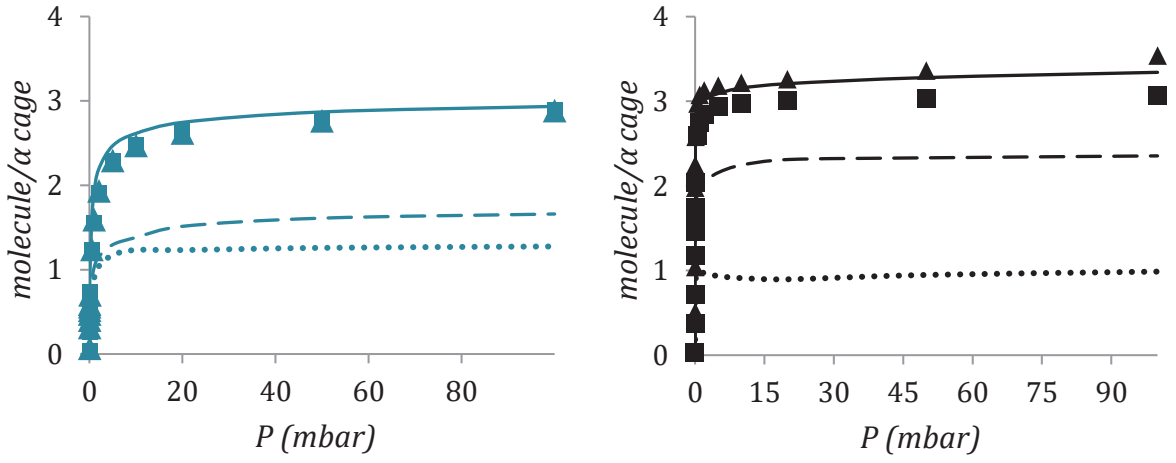

Figure 70. Calculated xylene adsorption isotherms in bulk-crystal NaLSX (blue) and in bulk-crystal BaLSX (black) zeolites at 175°C. The adsorption of pure xylenes is represented by symbols: pure *px* (triangles) and pure *mx* (squares). The mixture (*px/mx*) adsorption is represented by the solid line. The amount of each constituent in the mixture is then identified by the dashed (*px*) and dotted line (*mx*).

The *px/mx* selectivity of zeolites NaLSX and BaLSX as a function of the loading is presented in Figure 71. As expected, the selectivity of zeolite BaLSX is higher than that of NaLSX. This behavior corresponds to that observed in the literature. The maximum *px*-

selectivity in BaLSX zeolite occurs after the introduction of the third xylene molecule. As previously discussed, this selectivity arises from the higher volume of Ba cations, which at high loadings induces the adsorption of *px* on a non-cationic site (only accessible to *px*) in the center of the dodecagonal window. Also, it is found that *px* and *mx* have similar adsorption sites in NaLSX zeolite (selectivity around 1).

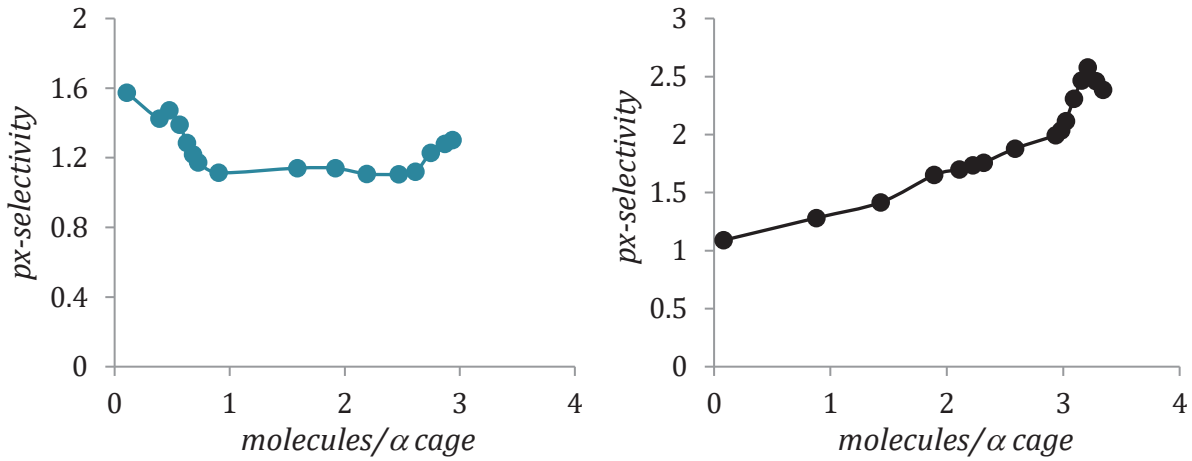

Figure 71. *px*-selectivity in bulk-crystal NaLSX (blue) and in bulk-crystal BaLSX (black) zeolites as function of loading in molecules/α cage. The *px*-selectivities were calculated at 175°C according the adsorption isotherms of the mixture *px*/*mx*, shown in Figure 70.

The isosteric enthalpies of adsorption were computed according to the fluctuations method. The obtained results are presented in Figure 72 as a function of the loading. The enthalpies of adsorption in BaLSX zeolite are, in general, larger than those for zeolite NaLSX. At low and intermediate loadings, the higher enthalpies of adsorption in BaLSX could result from stronger interactions of xylene molecules with Ba cations. The enthalpies of adsorption described herein are not far from those reported in the literature (~120 KJ/mol in the case of BaX). Contrary to the experimental adsorption enthalpy curves of zeolite X, showing a strong decrease at high loadings, such a phenomenon is not observed here through simulation[19]. The absence of this behavior, typical from the capillary condensation, is attributed to the absence of external surface in the simulations, as will be seen in the next results on systems bearing an interface.

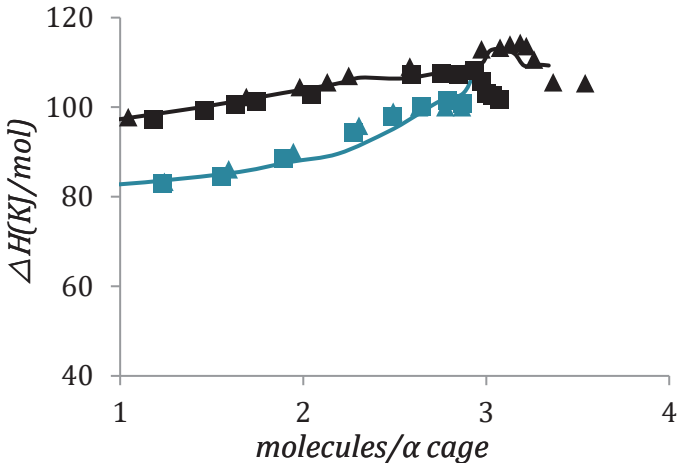

Figure 72. Isosteric enthalpies of adsorption for xylene isomers in bulk-crystal NaLSX (blue) and in bulk-crystal BaLSX (black) zeolites at 175°C. The adsorption of pure xylenes is represented by symbols: pure *px* (triangles) and pure *mx* (squares). The 50%:50% *px/mx* mixture adsorption is represented by the solid line.

6.3.2 *Xylene adsorption in NaLSX and BaLSX systems bearing an interface*

The adsorption isotherms of binary mixtures, as well as of pure compounds are studied at different loadings with the modified NaLSX and BaLSX zeolites systems comprising a surface (Figure 73). It is possible to observe that the adsorbed quantities in the zeolites presenting external surface is larger than the bulk-crystal adsorption. This increase in adsorption must be related to additional surface adsorption. Another interesting behavior is observed in adsorption isotherms for the cleaved zeolites. At high pressures a sharp increase in adsorbed amount is observed. This should be the result of capillary condensation. Before capillary condensation, two regions can be distinguished in the adsorption isotherms, especially evident in the case of BaX zeolite when looking at the adsorption of each component in the mixture (dashed and dotted lines). In the first part of the curve an increasing adsorption of *px* is observed with respect to *mx*. From a certain point, a decrease in the adsorbed amount of *px* is observed. The region of decrease in *px* adsorption is probably the one where surface adsorption is most important.

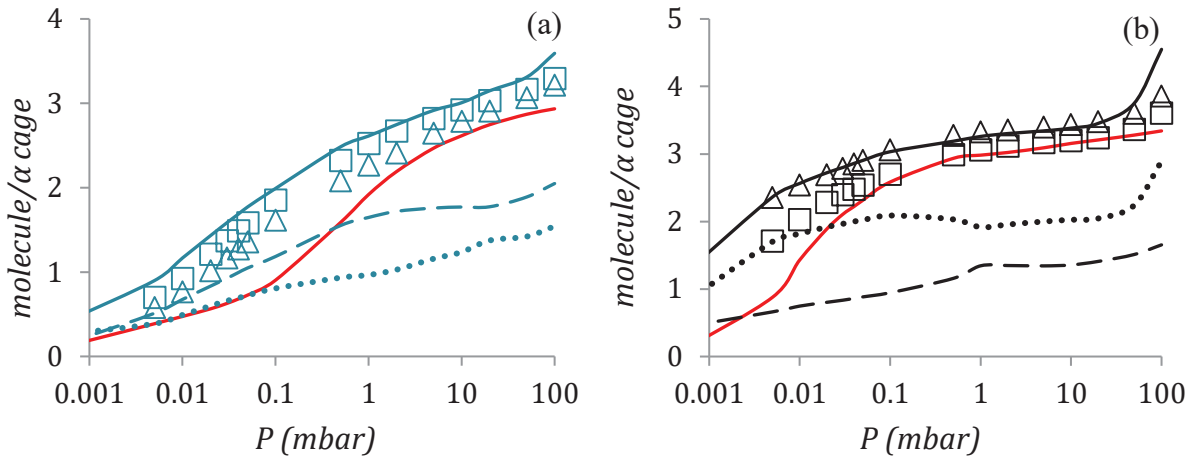

Figure 73. Calculated adsorption isotherms of xylenes in a NaLSX system bearing an interface (blue) (a) and in a BaLSX system bearing an interface (black) (b) at 175°C. The adsorption of pure xylenes is represented by symbols: pure *px* (triangles) and pure *mx* (squares). The mixture (*px/mx*) adsorption is represented by the solid line. The amounts of each constituent in the mixture are then identified by the dashed (*px*) and dotted lines (*mx*). The red solid lines in the graphs show the amount of (*px/mx*) adsorbed in the respective bulk-crystal zeolite: NaLSX bulk-crystal (a) and BaLSX bulk-crystal (b).

From the indication of surface adsorption seen above for cleaved zeolite systems, a comparison of selective properties and enthalpies of adsorption may be useful for the understanding of the surface effects. In Figure 74 the adsorption selectivities are represented as a function of the loading, with a comparison between the selectivities in the bulk-crystal systems and in the systems bearing an interface. In the case of NaLSX zeolites, the curve indicating the selectivities has a very similar profile along the adsorption until saturation. However the selectivity in the case of the system including a surface is relatively smaller. This may indicate that the surface selectivity in NaLSX zeolites is less than 1, which contributes to the decrease in total selectivity. This is in agreement with our experimental results in Chapter 4 and with the studies on Y zeolite made by Bellat et al.[12] In the case of *px*-selectivities in BaLSX type zeolites a maximum of selectivity (about 3) can be observed in both cases (with or without surface). This suggests that during xylene adsorption a selectivity maximum is reached close to saturation. However, after this maximum, a specially marked reduction in selectivities is observed for the system considering surface adsorption. Then, by comparing both curves, it can be suggested that after the selectivity maximum, the adsorption enters the zone of surface selectivity in zeolite BaLSX, as indicated by the arrow in Figure 74.

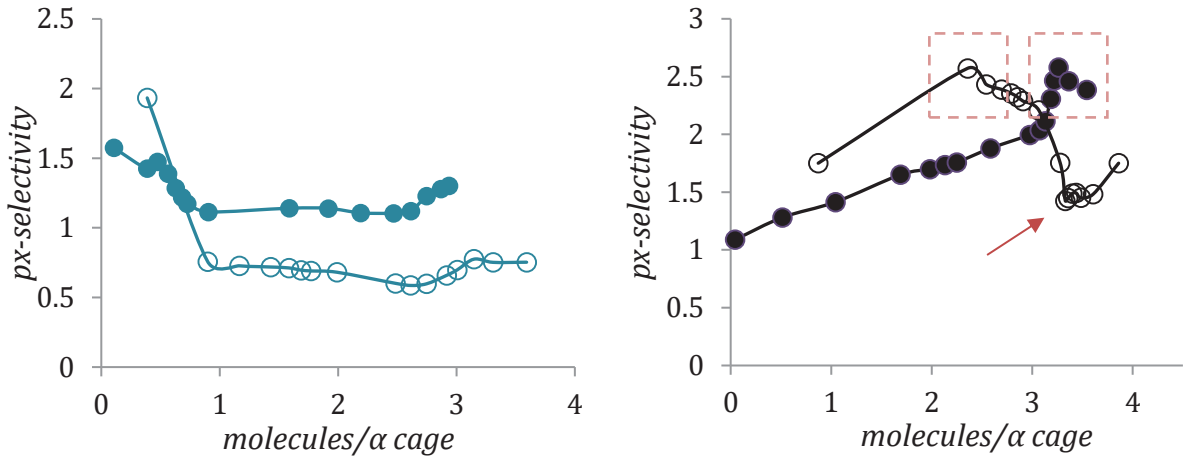

Figure 74. *px*-selectivity in bulk-crystal systems (full symbols) and systems bearing an interface (open symbols) for NaLSX (blue) and BaLSX (black) zeolites forms as function of loading in molecules/α cages. The *px*-selectivities were calculated at 175°C according the adsorption isotherms of the mixture *px/mx*, shown in Figure 70.

The isosteric enthalpies of adsorption are shown in Figure 75 for BaLSX and NaLSX, for both systems including a surface. Contrary to what is seen in the bulk-crystal systems (Figure 72), the enthalpies of adsorption curves for the zeolite systems including a surface are close to those described in the literature[19]. In such curves, as already mentioned, enthalpies of adsorption drastically decrease at high loadings. It is still interesting to note the differences in the enthalpies of adsorption curves for the different zeolites form. While the decrease in enthalpies of adsorption is more gradual in the case of NaLSX, an abrupt drop is observed in the case of the BaLSX zeolite. Such a change in adsorption values seems to be associated with selectivity changes observed throughout the loading (Figure 74). In general, in the case of zeolite NaLSX including surface, small changes in selectivity are perceived which would be in agreement with a slower decrease of enthalpies of adsorption. On the other hand, in the case of the BaLSX zeolite including surface, the drastic reduction of adsorption heats at high loadings seems to be directly linked to the "bulk-crystal selectivity/surface selectivity" transition (significantly different in the case of BaLSX).

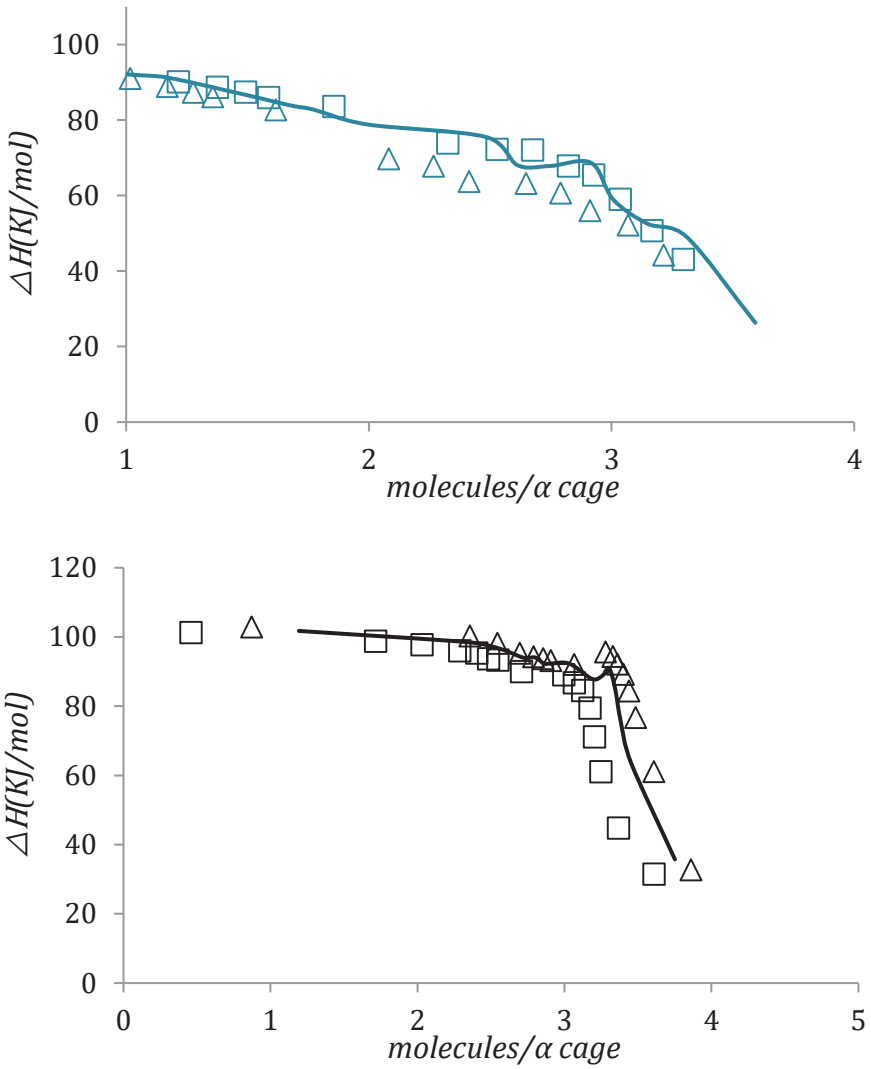

Figure 75. Isosterics enthalpies of adsorption for xylene isomers in surface model NaLSX (blue) and surface model BaLSX (black) zeolites at 175°C. The adsorption of pure xylenes is represented by symbols: pure *px* (triangles) and pure *mx* (squares). The enthalpy of adsorption for a 50%:50% *px/mx* mixture is represented by the solid line.

6.3.3 *Configurational analysis of the adsorption in the interface*

In order to better understand the behavior of the adsorption in the surface, a configurational analysis of the systems bearing an interface has been performed. In this way, distribution profiles of the adsorbed isomers along the bulk-crystal, surface and bulk-fluid have been determined. The boundaries for such regions as well as the density distribution profiles are described in Figure 76 and Figure 77. Based on the calculated profiles, the selectivity of the different regions of the system can be dissociated.

The density distribution profiles are in practice built from an histogram of the adsorption frequency of each isomer in the direction normal to that of the surface cleavage. Such histogram is then normalized by the total number of adsorption events in order to obtain the adsorption probability at a given position. The obtained profiles are shown in Figure 76 and Figure 77 for the adsorption of an equimolar binary mixture of *px*/*mx* in both NaLSX and BaLSX at different total pressures.

As can be seen from the comparison between Figure 76 and Figure 77, the profile in the region of the adsorption in the bulk-crystal phase of BaLSX system is characterized by a more regular adsorption pattern compared to that of NaLSX. This is a consequence of the more regular countercation distribution of BaLSX due to the absence of cations in site III. In the case of the NaLSX, the cations in site III are randomly distributed due to the degenerated nature of this site. The degree of symmetry obtained for BaLSX allows better observation of the impact of the surface at low loadings (and low pressures). As can be seen for the adsorption at lower pressures (P = 5x10^{-4} and P = 2x10^{-2} mbar) the loading in the region closer to the surface of BaLSX is lower than that of the bulk-crystal region. However, especially in the case of BaLSX zeolite, the amounts adsorbed on the surface at high pressures increases. The simulation was then able to confirm that the concentration of molecules adsorbed on the surface changes considerably in between gas (low pressure) and liquid phase (high pressure~100 mbar). Such higher adsorption on the surface in the liquid phase approach was found to be responsible for the elimination of diffusional surface barriers (Chapter 5).

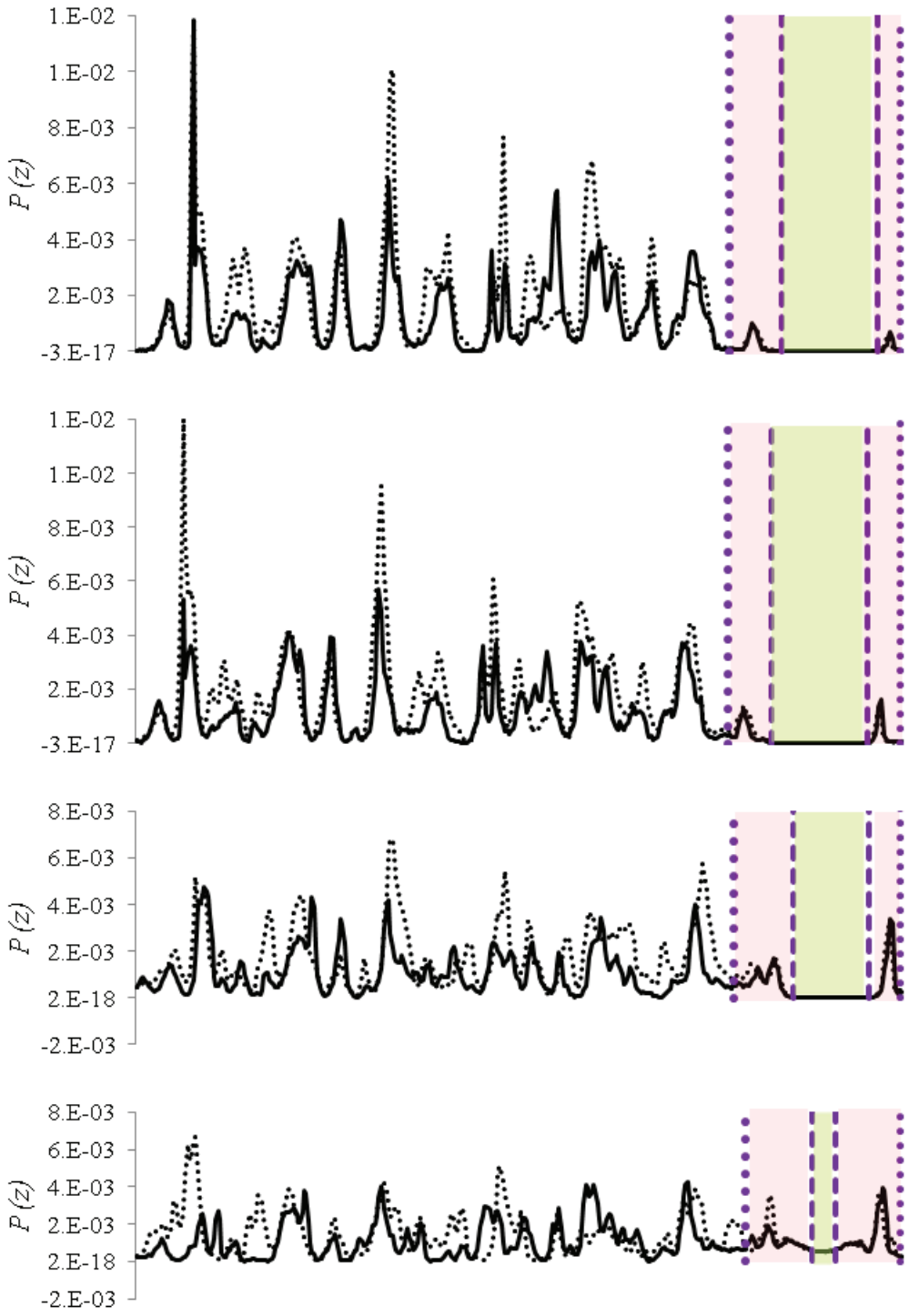

Figure 76. Probability density distribution profiles for *px* (solid line) and *mx* (dotted line) obtained for the adsorption at 175°C of an equimolar binary mixture in a NaLSX system bearing an interface. The different total pressures considered are from top to bottom to $P= 2x10^{-2}$, *0.1, 5 and 100 mbar.* The corresponding loadings are respectively 1.4, 2.0, 2.8 and 3.3 molecules per α cage. Pink and green zones represents the surface and bulk-fluid phases. The dotted and dashed purple lines account respectively for the bulk-crystal/surface and surface/bulk-fluid interface.

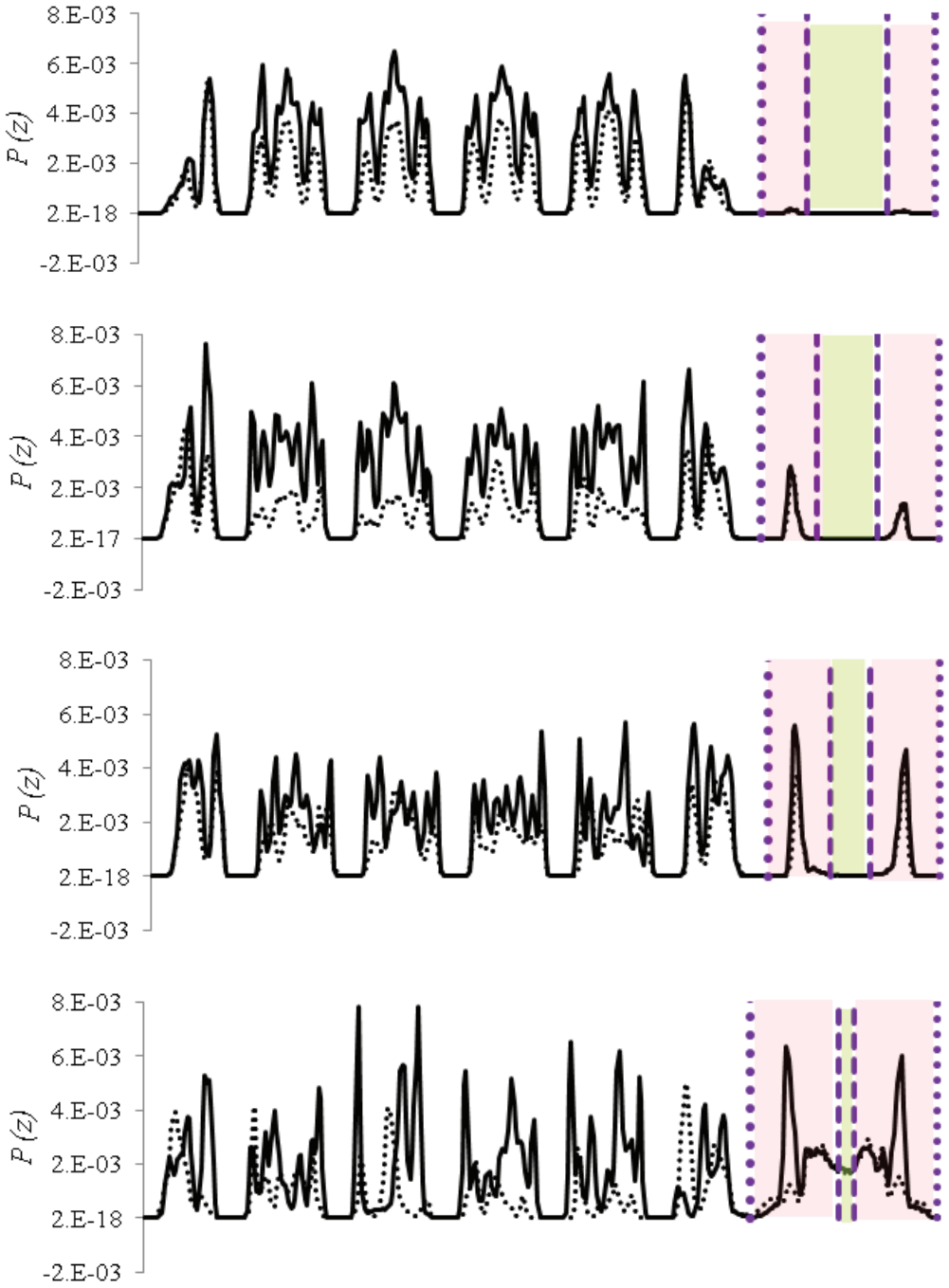

Figure 77. Probability density distribution profiles for *px* (solid line) and *mx* (dotted line) obtained for the adsorption at 175°C of an equimolar binary mixture in a BaLSX system bearing an interface. The different total pressures considered are from top to bottom to $P=5x10^{-4}$, $2x10^{-2}$, *5 and 100 mbar.* The corresponding loadings are respectively 1.3, 2.7, 3.3 and 3.9 molecules per α cage. Pink and green zones represents the surface and bulk-fluid phases. The dotted and dashed purple lines respectively account for the bulk-crystal/surface and surface/bulk-fluid interfaces.

The selectivity is another property that can vary with the pressure range and consequently with the loading. In this way, the observation of the BaLSX system at a higher pressure (P=100 mbar) display the impact of the loading on the *px/mx* selectivity. As can be seen, when the capillary condensation occurs, the bulk-crystal region closer to the interface recovers the *px*-selectivity which characterizes the bulk-crystal. In order to better understand the effect of the loading over the surface adsorption, the selectivities associated to the different regions (bulk-crystal, surface and bulk-fluid) are extracted from the profiles and presented in Figure 78 and Figure 79 for NaLSX and BaLSX systems respectively.

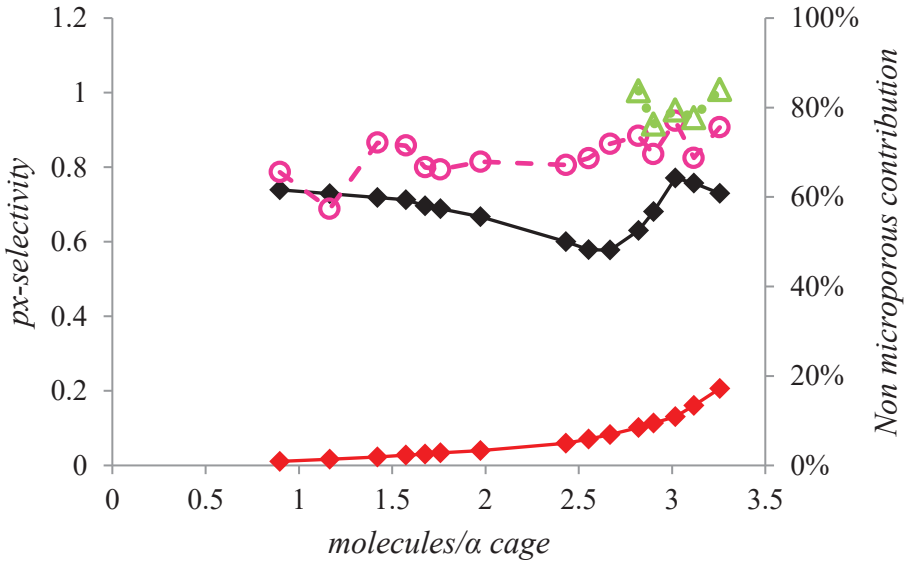

Figure 78. Dissociated *px*-selectivities of the bulk-crystal (black), surface (pink) and bulk-fluid (green) for the adsorption at 175°C of 50%:50% *px/mx* mixture in a NaLSX system bearing an interface (*px*-selectivity values on vertical axis on the left). Contribution of the sum of the surface and bulk-fluid to the total adsorption (Red curve with values on vertical axis on the right).

As can be observed from Figure 78 and Figure 79, the surface selectivities are relatively similar for both systems. Nevertheless, slightly higher values (between 1 and 1.4) are obtained in the case of BaLSX when compared to those of NaLSX (between 0.6 and 0.8). This trend is in agreement with the order of selectivy obtained for the bulk-crystal (larger selectivity for BaX zeolites). In other words, although the cleavage of the solid causes a significant impact on the adsorbent concerning the loss of *px*-selectivity in the surface, the nature of the cation seems to maintain a relative effect in this region. On the other hand, the difference between crystal selectivity and surface selectivity is much higher in the case of BaLSX zeolite. The same behavior could be observed experimentally in Chapter 4. As expected, the bulk-fluid

selectivities calculated when the non-microporous contribution becomes relevant enough, present values close to one.

When looking to the trend of the bulk-crystal and the surface selectivities, in both systems their values tend to converge when the non microporous contribution increases. From Figure 77 (profile corresponding to 3.3 molecules per α cage), this fact seems be explained by the propagation of the surface effect to the immediately closer microporous regions. Also, for BaLSX system, the *px*-selectivity nature of the bulk-crystal seems to be recovered when capillary condensation occurs. Nevertheless, the obtained values do not reach the maximum values obtained for intermediate-high loadings. Such a phenomenon is less evident in the case of the NaLSX system due to the absence of complete capillary condensation.

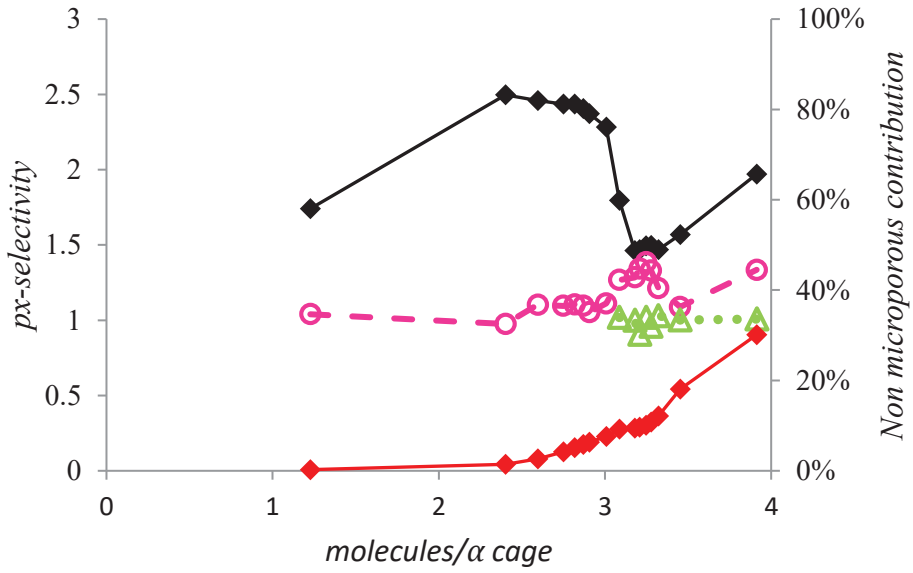

Figure 79. Dissociated *px*-selectivities of the bulk-crystal (black), surface (pink) and bulk-fluid (green) for the adsorption at 175°C of 50%:50% *px/mx* mixture in a BaLSX system bearing an interface (*px*-selectivity values on vertical axis on the left). Contribution of the sum of the surface and bulk-fluid to the total adsorption (Red curve with values on vertical axis on the right).

6.4. Conclusions on molecular simulation

In this chapter the results of molecular simulation by means of Monte Carlo method were presented. This method allowed describing the adsorption of xylenes on NaLSX and BaLSX type zeolites. Adsorption in bulk-crystal phase and adsorption in a model taking into account the presence of a surface were investigated. The implementation of the force field was validated through the adsorption of mixture/pure xylenes in the bulk-crystal phase. The validation was conducted through the comparison with experimental data (either adsorption capacit, enthalpy or selectivity), observed both in this thesis and in the literature. Despite a simplified approach has been implemented in this work to minimize the energetic impact of the surface reconstruction (by minimizing the total dipole of the system), it is worth mentioning that the use of *ab initio* methodology would allow for a more accurate minimization of the surface energy. Nevertheless, the implemented methodology remains valid for the comprehension of the surface adsorption phenomena.

The comparison between adsorption in both systems (bulk-crystal and surface) allowed us to identify an adsorption zone, on the surface, where there is a reduction of the *px*-selectivity, especially evident in BaLSX zeolites. The transition between the adsorption in the micropores and adsorption in the surface is observed mainly in the xylene mixture adsorption isotherms (*px/mx*). When surface adsorption becomes important, a decrease in the adsorbed amount of *px* is observed and therefore a decrease in selectivity as well. The loss of *px*-selectivity on the surface, for a BaLSX, was evaluated around 40% (from 2.57 in the bulk-crystal to 1.4 on the surface). Thanks to the probability density distribution profiles it was possible to identify the contributions of each region of the system separately *i.e.* crystal-bulk, surface and fluid-bulk. It was possible to observe that px-selectivity on the surface was almost constant all along the loading. When the contribution of adsorption in non microporous phase becomes more important it seems to cause a decrease of selectivity in the bulk-crystal phase. Specifically in the case of BaLSX zeolite, capillary condensation appears to have a regenerative effect on px-selectivity, although partial.

Conclusions and perspectives

Different faujasite samples exhibiting a hierarchical nature, i.e. a secondary porous network (meso and/or macro) have been characterized with the main goal of rationalizing the impact of this feature on their properties for the separation of xylene isomers. In order to get insight into the mechanisms associated to the interface generated by the introduction of additional porosity, i.e. the external surface area, different characterization techniques have been employed. The selected characterization techniques have been chosen to provide detailed information about both the quantity and quality (chemical nature) of the external surface. Besides, different experimental and theoretical methodologies have been employed to acquire information about both adsorption and diffusion behaviors arising due to the introduction of this surface area.

When compared to the conventional zeolite, the quantitative characterization of the surface allowed to identify increasing external surface areas and mesoporous volume for the hierarchical zeolites type NA (NA-1<NA-2 <NA-3). On the other hand, the LL zeolite, presents an external surface area similar to that of NA-1 and the lowest mesoporous volume among all the hierarchical zeolites. X-ray diffraction, through the Scherrer equation, allowed determining crystallite (nanometric) sizes for all zeolites. The following order was obtained: conventional zeolite > NA-1> NA2> NA-3 ≈ LL. Textural data including external surface areas, microporous volumes and pore size distributions were obtained from N_2 sorption and mercury porosimetry. The BaX-NA type zeolites present external surface areas between 43 m^2/g and 68 m^2/g while the mesopore volumes range between 0.11cc/g and 0.18 cc/g. The micropore volume of such zeolites lies in between 0.16 cc/g – 0.18cc/g. Concerning the BaX- LL type zeolite, the microporous volume is larger than that of NA materials - about 0.2 cc/g while the external surface area and the mesopore volume are respectively 38 m^2/g and 0.08 cc/g. The pore size distribution was established according to a consolidated model integrating both the adsorption data of N_2 and mercury intrusion. The pore sizes observed for the hierarchical zeolites were between 3.5 and 30 nm. Particularly, the characteristic mesopore sizes lie in the range of small mesopores: about 5 nm (NA-3 and LL), 8 nm (NA-2) and 10 nm (NA-3). The internal and external morphology of crystals was analyzed by means of microscopy (SEM and TEM). For the NA-1, NA-2 and LL materials, some macropores presenting a size about hundreds of nanometers were identified. In general, the agglomerates present a very porous core with dense

borders. However, in all cases, connections between the external surface and the inner part of the agglomerates were visualized. Electron tomography was also performed to allow the visualization of the depth and distribution of pores in the crystal. Along with the morphological features of the hierarchical adsorbents, getting insight about the surface composition of these samples is also relevant as it allows the study of its impact on surface selectivities. Therefore, the quality of the surface in terms of the presence of OH groups was investigated through infrared analysis. The amount of these polar groups such as Si-OH was found to considerably increase upon increasing the external surface area. The density of OH groups in the external surface was found to be nearly constant for all zeolites. The connection between the different porosities was observed by means of 1H 2D exchange spectroscopy nuclear magnetic resonance (1H EXSY NMR) using px as probe molecule. In the case of zeolite NA-1, the exchange between fluid-phase molecules and molecules adsorbed in the micropores was observed. In the case of zeolite NA-3, the exchange of px molecules was further observed in micropores, small mesopores and fluid-phase.

Once the characterization of the quantity and quality of the zeolites surface was carried out, the study of the adsorption and diffusion properties of xylenes was performed. At this stage, the characterization of the materials performed in the third chapter of this work proved to be essential in the understanding of the phenomena occurring during the adsorption and diffusion of xylenes in the hierarchical zeolites. The xylene adsorption capacity of the hierarchical zeolites, obtained by means of thermogravimetry, pointed out larger amounts of xylene adsorbed in NA hierarchical zeolites with respect to the conventional zeolite. The xylene adsorption in the zeolite LL was found to be equal or smaller than in the case of the conventional zeolite. In order to study the adsorption behaviour close to saturation conditions, the isosteric enthalpies of adsorption were calculated from the adsorption isotherms for pure xylene isomers in the conventional and hierarchical zeolites at high loadings. Due to the fact that the enthalpies of adsorption were found to be very similar between the px and ox isomers, it was not possible to extract a clear conclusion about a possible enthalpic effect on surface selectivity.

In general, hierarchical zeolites exhibited a loss of px-selectivity with respect to the conventional zeolite. The evaluation of a non-selective NaX zeolite and a px-selective BaX allowed the understanding of the phenomena responsible for the loss of selectivity in hierarchical zeolites. As could be seen in Chapter 4, the loss of effective selectivity in the NaX-type hierarchical zeolites was very subtle, whereas the loss of selectivity in the BaX-type hierarchical zeolites was quite significant. The reason why the loss of selectivity is more marked

for BaX zeolite than for NaX zeolite must therefore be related to the intrinsic characteristics of each zeolite with respect to selectivity. In the case of adsorption in NaX zeolite, the mx and px isomers have the same affinity since they share the same preferential adsorption sites. In the case of the BaX zeolite, there is a specific site for the adsorption of px that appears at high loadings. This site is located at the center of the 12-member window and has already been identified by different authors as responsible for the px-selectivity in the BaX zeolite. The fact of observing a loss of selectivity more marked in BaX than in NaX suggests that the presence of an increased external surface area, as in the case of hierarchical zeolites, can decrease the stability of px adsorption in the window site. In addition, by increasing the external surface area, the effect on selectivity loss becomes reinforced. The selectivity of the NA-3 zeolite is smaller than the others. The layer-like morphology of crystals in the zeolite LL also seems to further favor the selectivity loss. Despite a smaller external surface area, compared to the zeolite NA-3, the selectivity found for zeolite LL is similar to that found for zeolite NA-3 (highest external surface area). The obtained results show an increase of the selectivity loss when increasing the external surface area of the zeolites. The effect of the silanol groups on the selectivity was not easy to evidence due to the fact that all zeolites presented close densities of silanol groups on their external surface. Since the OH amount increases proportionally to the external surface area, dissociating both potential impacts were not evident.

In the case of liquid phase adsorption conditions, the use of hierarchical zeolites proved to be highly satisfactory with respect to the px diffusion in conventional zeolites. The diffusion ability of zeolites NA-2, NA-3 and LL showed increases greater than 94% (expressed in terms of reduction of the px characteristic diffusion time) as compared to the conventional zeolite. The px diffusion time in the NA-1 zeolite was about 85% lower than that observed for the conventional zeolite. In the case of NA zeolites, diffusion was faster for zeolites with larger mesopore volumes. In the particular case of the LL zeolite, the diffusion time enhancement seems to be related to the zeolite lamellar morphology. As a matter of fact this zeolite presents smaller volume of mesopores compared to the other hierarchical zeolites. The evaluation of diffusion in the gas phase indicated the presence of diffusion barrier phenomena in the case of hierarchical zeolites. The improvement of the diffusion time was never higher than 30% for the ensemble of tested zeolites and was reduced to only 20% in the case of NA-1. Compared to the diffusivity measured for the conventional zeolite, the theoretically estimated diffusion times were expected to decrease by values between 85% and 95% according to the size of the respective crystallites. It is worth mentioning that the theoretical decrease in the diffusion time

calculated for the gas phase corresponds to that observed experimentally in the liquid phase. These results suggest that diffusion barriers are not significant in the case of the liquid phase: the access time to the interior of the crystal is significantly reduced due to the high concentration in the fluid film (liquid phase) surrounding the surface. Such observations confirm the interest of the xylene separation in liquid phase in the case of the use of hierarchical zeolites, since in these conditions the surface barriers seem negligible.

The measured properties of the zeolites associated to adsorption and diffusion of xylene allow us to identity, among the zeolites studied, those exbiting the best overall separation performance. Such performance is related to the notion of productivity, which is directly proportional to both selectivity and adsorption capacity, and inversely proportional to the diffusion time. When the estimation of productivity is established in liquid phase conditions, NA-type zeolites presenting enhanced accessibilities also present the best productivities (NA-1<NA-2<NA-3). In the case of the LL zeolite, despite a reasonable accessibility, the obtained productivity is smaller than that of zeolite NA-2. The productivity ratio between the NA-3 zeolite and the conventional one is expected to be about 25. Contrary to the observations in liquid phase conditions, the evaluation of gas phase productivity (considering the same selectivity measured in liquid phase) indicates that the conventional zeolite would present a productivity value superior to those of other zeolites. In the case of the gas phase, the ratio between the productivities of the conventional zeolite and NA-3 is around 1.3. The low productivity observed for hierarchical zeolites in the gas phase is attributed to the presence of surface barriers.

The theoretical study, performed by means of Monte Carlo methods confirmed that an increase in adsorption can take place due to the presence of an external surface area. The loss of px-selectivity at the surface level could also be proved through MC simulations. This phenomenon was particularly significant in the case of the BaLSX zeolite, whereas in the case of the NaLSX zeolite, the loss of selectivity is difficult to highlight due to closer selectivity values between the micropores and the surface. For BaLSX zeolite, the loss of selectivity due to the presence of surface with respect to micropore selectivity is about 40%. As hypothesized In Chapter 4, the loss of px-selectivity observed should be related to the presence of α cages exposed to the outer surface. In order to verify this hypothesis, the theoretically studied systems were generated by cleaving the bulk adsorbent in the {0 1 1} direction. In this way, the cleavage plane crosses the α cages and generates incomplete dodecagonal windows at the surface level. The results obtained from the simulations seem to confirm the emitted hypothesys since a

reduction of the px-selectivity was observed. In perspectives and in order to consolidate the observation about the decrease in adsorption on the surface, the study of systems cleaved in the direction {1 1 1} would be interesting as long as the α cages could be mantained intact.

As general perspectives for future work, the theoretical study could be expanded. The observation of different surface directions and different OH densities at the surface would bring more insightful explanations to the surface phenomena observed throughout this thesis. Moreover, the study of diffusion through molecular dynamics (MD) in zeolite models containing different pore sizes would contribute to a better understanding of the diffusion barrier phenomena observed in the case of gas phase conditions. In the same direction, the effect of the surface concentration on the dissapearance of the surface barriers could be verified by molecular simulation. Another interesting aspect of the theoretical study to be investigated is the study of diffusion from different concentration rates, in order to investigate if the diffusion in this type of materials is always described by Fick's diffusion law. With regard to the experimental work, studying the extrusion of the materials with different binders would allow to test them under industrial separation conditions by means of xylene breakthrough tests. The study of different binders would allow for the identification of conditions where no condensation reaction of xylenes would occur at the surface level (phenomenon potentially expected to block the pore entries). Therefore, the test of hierarchical zeolites for xylenes separation under real conditions could be studied in future works.

.

References

(1) Guillon, E.; Leflaive, P. Traitement des essences aromatiques pour la pétrochimie. *Techniques de l'Ingénieur* 2011.

(2) *Zeolite molecular sieves: structure, chemistry and use;* Breck, D. W., Ed.; John Wiley & Sons, Inc, 1974.

(3) Coombs, D. S. Recommended Nomenclature for Zeolite Minerals: Report of the Committee on zeolites of the international mineralogical association on new minerals and minerals names. *The Canadian Mineralogist* 1997, *35*, 1571–1606.

(4) Lowenstein, W. The distribution of aluminum in the tetrahedra of silicates and aluminates. *Am. Mineral* 1954, *39*, 92-96.

(5) Inglezakis, V. J. The concept of "capacity" in zeolite ion-exchange systems. *Journal of Colloid and Interface Science* 2005, *281*, 68–79.

(6) Rasouli, M.; Yaghobi, N.; Chitsazan, S.; Sayyar, M. H. Adsorptive separation of meta-xylene from C8 aromatics. *Chemical Engineering Research and Design* 2012, *90*, 1407–1415.

(7) Lee, J. M.; Seo, S. M.; Suh, J. M.; Lim, W. T. Synthesis and single-crystal structures of fully dehydrated fully Sr^{2}+exchanged zeolite Y (FAU) and its benzene sorption complex. *J. Porous Mater.* 2011, *18*, 523–534.

(8) Thomas, J. M. Uniform Heterogeneous Catalysts: The Role of Solid-State Chemistry in their Development and Design. *Angew. Chem. Int. Ed.* 1988, *27*, 1673–1691.

(9) Frising, T.; Leflaive, P. Extraframework cation distributions in X and Y faujasite zeolites: A review. *Microporous and Mesoporous Materials* 2008, *114*, 27–63.

(10) *Principles of adsorption and adsorption processes;* Ruthven, D. M., Ed.; John Wiley & Sons, Inc: USA, 1984.

(11) Moïse, J.-C. Equilibres de coadsorption du p-xylène et du m-xylène par les zéolithes X et Y. Effet du cation compensateur, de la température et du taux d'hydratation de la zéolithe sur la sélectivité d'adsorption, IFPEN, 1999.

(12) Bellat, J.-P.; Pilverdier, E.; Simonot-Grange, M.-H.; Jullian, S. Microporous volume and external surface of Y zeolites accessible to p-xylene and m-xylene. *Microporous Materials* 1997, *9*, 213–220.

(13) Hadjiivanov, K. Identification and Characterization of Surface Hydroxyl Groups by Infrared Spectroscopy. *Advances in Catalysis* 2014*, 57,* 99-318.

(14) Kawai, T.; Tsutsumi, K. A Study on the Surface Silanol Groups Developed by Hydrothermal and Acid Treatment of Faujasite Type Zeolites. *Journal of Colloid and Interface Science* 1999, *212*, 310–316.

(15) *Zeolites and Clay Minerals as Sorbents and Molecular Sieves;* Barrer, R. M., Ed., 1st; Academic Press: London, 1978.

(16) Mellot, C.; Simonot-Grange, M. H.; Pilverdier, E.; Bellat, J.P.; Espinat, D. Adsorption of Gaseous p- or m-Xylene in BaX Zeolite: Correlation between Thermodynamic and Crystallographic Studies. *Langmuir* 1995, *11*, 1726–1730.

(17) Lachet, V. Simulation moléculaire de l'adsorption sélective des isomères du xylène dans les faujasites, IFPEN, 1998.

(18) Pichon, C. Etude Structural et énergétique de l'adsorption des isomères para- et meta- du xylene dans la zéolithe BaX préhydratée, Université de Bourgogne et IFPEN, 1999.

(19) Pichon, C.; Méthivier, A.; Simonot-Grange, M.-H.; Baerlocher, C. Location of Water and Xylene Molecules Adsorbed on Prehydrated Zeolite BaX. A Low-Temperature Neutron Powder Diffraction Study. *J. Phys. Chem. B* 1999, *103*, 10197–10203.

(20) Descours, A. Adsorption des isomères para- et méta - du xylene dans les zéolithes NaX et BaX: Etude des relations propriétés-structure, IFPEN, 1997.

(21) Mellot, C.; Simonot-Grange, M. H.; Pilverdier, E.; Bellat, J.P; Espinat, D. Adsorption of Gaseous p- or m-Xylene in BaX Zeolite: Correlation between Thermodynamic and Crystallographic Studies 1995, *11*, 1726–1730.
(22) Serrano, D. P.; Escola, J. M.; Pizarro, P. Synthesis strategies in the search for hierarchical zeolites. *Chem. Soc. Rev.* 2013, *42*, 4004–4035.
(23) Musilová, Z.; Žilková, N.; Park, S.-E.; Čejka, J. Aromatic Transformations Over Mesoporous ZSM-5: Advantages and Disadvantages. *Top Catal* 2010, *53*, 1457–1469.
(24) Chen, L.-H.; Li, X.-Y.; Rooke, J. C.; Zhang, Y.-H.; Yang, X.-Y.; Tang, Y.; Xiao, F.-S.; Su, B.-L. Hierarchically structured zeolites: Synthesis, mass transport properties and applications. *J. Mater. Chem.* 2012, *22*, 17381.
(25) Koohsaryan, E.; Anbia, M. Nanosized and hierarchical zeolites: A short review. *Chinese Journal of Catalysis* 2016, *37*, 447–467.
(26) Liu, Z.; Hua, Y.; Wang, J.; Dong, X.; Tian, Q.; Han, Y. Recent progress in the direct synthesis of hierarchical zeolites: Synthetic strategies and characterization methods. *Mater. Chem. Front.* 2017, *1*, 2195–2212.
(27) Mintova, S.; Gilson, J.-P.; Valtchev, V. Advances in nanosized zeolites. *Nanoscale* 2013*, 5*, 6693–6703.
(28) Valtchev, V. P.; Bozhilov, K. N. Transmission Electron Microscopy Study of the Formation of FAU-Type Zeolite at Room Temperature. *J. Phys. Chem. B* 2004, *108*, 15587–15598.
(29) Wang, K. et al. Agregates of small particles of synthetic faujasite zeolite. US2012/0227584.
(30) Inayat, A.; Knoke, I.; Spiecker, E.; Schwieger, W. Assemblies of Mesoporous FAU-Type Zeolite Nanosheets. *Angew. Chem. Int. Ed.* 2012, *51*, 1962–1965.
(31) Khaleel, M.; Wagner, A. J.; Mkhoyan, K. A.; Tsapatsis, M. On the Rotational Intergrowth of Hierarchical FAU/EMT Zeolites. *Angew. Chem. Int. Ed.* 2014, *53*, 9456–9461.
(32) Dougnier, F.; Patarin, J.; Guth, J. L.; Anglerot, D. Synthesis, characterization, and catalytic properties of silica-rich faujasite-type zeolite (FAU) and its hexagonal analog (EMT) prepared by using crown-ethers as templates. *Zeolites* 1992, *12*, 160–166.
(33) Inayat, A.; Schneider, C.; Schwieger, W. Organic-free synthesis of layer-like FAU-type zeolites. *Chemical communications (Cambridge, England)* 2015, *51*, 279–281.
(34) Sing, K. S. W.; Everett, D. H.; Haul, R. A. W.; Perotti, R. A.; Rouquerol, J.; Siemieniewska, T. Reporting physisorption data for gas/solid systems: with Special Reference to the Determination of Surface Area and Porosity. *Pure & App. Chem.* 1985, *57*, 603–619.
(35) *Adsorption: By Powders & Porous Solids;* Rouquerol, F.; Rouquerol, J.; Sing, K., Ed., 1st ed.; Academic Press: Great Britain, 1999.
(36) Hutson, N. D.; Yang, R. T. Theoretical basis for the Dubinin-Radushkevitch (D-R) adsorption isotherm equation. *Adsorption* 1997, *3*, 189–195.
(37) Dubinin, M. M. The Potential Theory of Adsorption of Gases and Vapors for Adsorbents with Energetically Nonuniform Surfaces. *Chem. Rev.,* 1960, 235–241.
(38) *Adsorption, surface area and porosity;* Gregg, S. J.; Sing, K. S. W., Ed., 2nd ed.; Academic Press: Great Britain, 1995.
(39) Myers, A. L. Thermodynamics of adsorption in porous materials. *AIChE J.* 2002, *48*, 145–160.
(40) Bourrelly, S.; Moulin, B.; Rivera, A.; Maurin, G.; Devautour-Vinot, S.; Serre, C.; Devic, T.; Horcajada, P.; Vimont, A.; Clet, G. *et al.* Explanation of the adsorption of polar vapors in the highly flexible metal organic framework MIL-53(Cr). *Journal of the American Chemical Society* 2010, *132*, 9488–9498.
(41) *Diffusion in nanoporous materials;* Kärger, J.; Ruthven, D. M.; Theodorou, D. N., Eds.; Wiley-VCH: Weinheim Germany, 2012.

(42) Ruthven, D. M.; Post, M.F. Diffusion in Zeolite Molecular Sieves: Studies in Surface Science and Catalysis. *Elsevier Science* 2001, *137,* 525–577.
(43) *Diffusion in Zeolites and Other Microporous Solids.* Karger, J.; Ruthven, D. M., Eds.; John Wiley & Sons, Inc: USA, 1992.
(44) Gueudré, L.; Jolimaître, E.; Bats, N.; Dong, W. Diffusion in zeolites: Is surface resistance a critical parameter? *Adsorption* 2010, *16*, 17–27.
(45) Wloch, J. Effect of surface etching of ZSM-5 zeolite crystals on the rate of n-hexane sorption. *Microporous and Mesoporous Materials* 2003, *62*, 81–86.
(46) Gueudré, L. Diffusion du cyclohexane dans la silicalite-1: Origine et caractérisation de la résistance de surface. Thesis, ENS, Lyon - France, 2010.
(47) Bellat, J.-P.; Simonot-Grange, M. H. Adsorption of gaseous p-xylene and m-xylene on NaY, KY, and BaY zeolites. Part 2: Modeling. Enthalpies and entropies of adsorption. *Zeolites,* 1995*, 15*, 219–227.
(48) Bellat, J.P; Simonot-Grange, M. H.; Jullian, S. Adsorption of gaseous p-xylene andm-xylene on NaY, KY, and BaY zeolites: Part 1, Adsorption equilibria of pure xylenes. *Zeolites,* 1995*, 15*, 124–130.
(49) Cottier, V.; Bellat, J.-P.; Simonot-Grange, M.-H.; Méthivier, A. Adsorption of p-Xylene/ m-Xylene Gas Mixtures on BaY and NaY Zeolites. Coadsorption Equilibria and Selectivities. *J. Phys. Chem. B* 1997*, 101,* 4798–4802.
(50) Pichon, C.; Méthivier, A.; Simonot-Grange, M.-H. Adsorption of m-Xylene on Prehydrated Zeolite BaX: Correlation between Temperature-Programmed Desorption and Low-Temperature Neutron Powder Diffraction Studies. *Langmuir* 2000*, 16,* 1931–1936.
(51) Ruthven, D. M.; Goddard, M. Sorption and diffusion of C8 aromatic hydrocarbons in faujasite type zeolites. I. Equilibrium isotherms and separation factors. *Zeolites* 1986*, 6*, 275–282.
(52) Simonot-Grange, M.-H.; Bertrand, O.; Pilverdier, E.; Bellat, J.-P.; Paulin, C. Differential calorimetric enthalpies of adsorption of p-xylene and m-xylene on y faujasites at 25°C. *Journal of Thermal Analysis* 1997*, 48*, 741–754.
(53) Tournier, H.; Barreau, A.; Tavitian, B.; Le Roux, D.; Moïse, J.-C.; Bellat, J.-P.; Paulin, C. Adsorption Equilibrium of Xylene Isomers and p-Diethylbenzene on a Prehydrated BaX Zeolite. *Ind. Eng. Chem. Res.* 2001, *40*, 5983–5990.
(54) Goddard, M.; Ruthven, D. M. Sorption and diffusion of C8 aromatic hydrocarbons in faujasite type zeolites. II. Sorption kinetics and intracrystalline diffusivities. *Zeolites* 1986, *6*, 283–289.
(55) Germanus, A.; Kärger, J.; Pfeifer, H. Intracrystalline self-diffusion of benzene, toluene and xylene isomers in zeolites Na-X. *Zeolites,* 1985, *5*, 91–95.
(56) Gueudré, L.; Milina, M.; Mitchell, S.; Pérez-Ramírez, J. Superior Mass Transfer Properties of Technical Zeolite Bodies with Hierarchical Porosity. *Adv. Funct. Mater.* 2014, *24*, 209–219.
(57) Mehlhorn, D.; Inayat, A.; Schwieger, W.; Valiullin, R.; Karger, J. Probing mass transfer in mesoporous faujasite-type zeolite nanosheet assemblies. *Chemphyschem : a European journal of chemical physics and physical chemistry* 2014, *15*, 1681–1686.
(58) Galarneau, A.; Guenneau, F.; Gedeon, A.; Mereib, D.; Rodriguez, J.; Fajula, F.; Coasne, B. Probing Interconnectivity in Hierarchical Microporous/Mesoporous Materials Using Adsorption and Nuclear Magnetic Resonance Diffusion. *J. Phys. Chem. C* 2016, *120*, 1562–1569.
(59) Moore, R. M.; Katzer, J. R. Counterdiffusion of liquid hydrocarbons in type Y zeolite: Effect of molecular size, molecular type, and direction of diffusion. *AIChE J.,* 1972, *18,* 816–824.
(60) Awum, F.; Narayan, S.; Ruthven, D. Measurement of intracrystalline diffusivities in NaX zeolite by liquid chromatography. *Ind. Eng. Chem. Res,* 1988, *28*, 1510–1515.
(61) Eic, M.; Goddard, M.; Ruthven, D. M. Diffusion of benzene in NaX and natural faujasite. *Zeolites,* 1988, *8,* 327–331.

(62) Moya-Korchi, V. Etude de la contre-diffusion des xylenes dans les adsorbants zéolitiques de type Y, Université Piere et Marie Curie, 1995.
(63) Minceva, M.; Rodrigues, A. E. Adsorption of Xylenes on Faujasite-Type Zeolite. *Chemical Engineering Research and Design,* 2004, *82,* 667–681.
(64) The mathematics of diffusion; Crank, J., Ed., 2nd ed.; Oxford University Press: Bristol, 1975.
(65) Silva, M. S. P.; Moreira, M. A.; Ferreira, A. F. P.; Santos, J. C.; Silva, V. M. T. M.; Sá Gomes, P.; Minceva, M.; Mota, J. P. B.; Rodrigues, A. E. Adsorbent Evaluation Based on Experimental Breakthrough Curves: Separation of p-Xylene from C8 Isomers. *Chem. Eng. Technol.,* 2012, *35*, 1777–1785.
(66) Silva, M. S.P.; Mota, J. P.B.; Rodrigues, A. E. Fixed-bed adsorption of aromatic C8 isomers: Breakthrough experiments, modeling and simulation. *Separation and Purification Technology,* 2012, *90*, 246–256.
(67) Khabzina, Y.; Laroche, C.; Perez-Pellitero, J.; Farrusseng, D. Xylene separation on a diverse library of exchanged faujasite zeolites. *Microporous and Mesoporous Materials* 2017, *247,* 52–59.
(68) Khabzina, Y. Influence des cations d'échange dans les zéolithes type faujasites sur la selectivité d'adsorption des isomères du xylène. Doctoral thesis, Université Lyon 1, 2015.
(69) Eic, M.; Ruthven, D. M. A new experimental technique for measurement of intracrystalline diffusivity. *Zeolites,* 1988, *8*, 40–45.
(70) Ruthven, D. M.; Stapleton, P. Measurement of liquid phase counter-diffusion in zeolite crystals by the ZLC method. *Chemical Engineering Science,* 1993, *48*, 89–98.
(71) Brandani, S.; Ruthven, D. M. Analysis of ZLC desorption curves for liquid systems. *Chemical Engineering Science,* 1995, *50*, 2055–2059.
(72) Huang, Q.; Eić, M.; Xiao, H.; Kaliaguine, S. Characterization of the diffusion path in micro- and meso-porous materials from ZLC analysis. *Adsorption,* 2010, *16*, 531–539.
(73) Vattipalli, V.; Qi, X.; Dauenhauer, P. J.; Fan, W. Long Walks in Hierarchical Porous Materials due to Combined Surface and Configurational Diffusion. *Chem. Mater.,* 2016, *28*, 7852–7863.
(74) Magalhães, F. D.; Laurence, R. L.; Conner, W. C. Diffusion of Cyclohexane and Alkylcyclohexanes in Silicalite. *J. Phys. Chem. B,* 1998, *102*, 2317–2324.
(75) Hoang, V.-T.; Huang, Q.; Eić, M.; Do, T.-O.; Kaliaguine, S. Structure and diffusion characterization of SBA-15 materials. *Langmuir: the ACS journal of surfaces and colloids,* 2005, *21*, 2051–2057.
(76) Chang, C.-C.; Teixeira, A. R.; Li, C.; Dauenhauer, P. J.; Fan, W. Enhanced molecular transport in hierarchical silicalite-1. *Langmuir : the ACS journal of surfaces and colloids,* 2013, *29*, 13943–13950.
(77) Song, A.; Ma, J.; Xu, D.; Li, R. Adsorption and Diffusion of Xylene Isomers on Mesoporous Beta Zeolite. *Catalysts,* 2015, *5*, 2098–2114.
(78) Sherry, H. S. Ion-exchange properties of zeolites. IV. Alkaline earth ion exchange in the synthetic zeolites Linde X and Y. *J. Phys. Chem* 1968, *72,* 4086-4094.
(79) *Introduction to X-ray powder diffractometry;* Jenkins, R.; Snyder, R. L., Eds. 138; John Wiley & Sons, Inc, 1996.
(80) Weiland, E.; Springuel-Huet, M.-A.; Nossov, A.; Guenneau, F.; Quoineaud, A.-A.; Gédéon, A. Transport properties of catalyst supports studied by pulsed field gradient (PFG) and 2D exchange (EXSY) NMR spectroscopy. *New J. Chem.* 2016*, 40*, 4447–4454.
(81) Hunger, M.; Wang, W. Solid State NMR spectroscopy. In Handbook of Heterogeneous Catalysis. John Wiley and Sons, Inc, 2008. 912–932.
(82) Hunger, M. NMR Spectroscopy for the Characterization of Surface Acidity and Basicity. In Handbook of Heterogeneous Catalysis. John Wiley and Sons, Inc, 2008. 1163–1178.

(83) Kärger, J.; Valiullin, R. Mass transfer in mesoporous materials: The benefit of microscopic diffusion measurement. *Chem. Soc. Rev.* 2013, *42*, 4172.
(84) Quoineaud, A.-A. Rapport interne IFP: Etude de la diffusion d'hydrocarbures dans des solides poreux, 2005.
(85) Ngoc, D. T.; Pham, T. H.; Hong Nguyen, K. D. Synthesis, characterization and application of nanozeolite NaX from Vietnamese kaolin. *Adv. Nat. Sci: Nanosci. Nanotechnol.* 2013*, 4*, 45018.
(86) Langford, J. I.; Wilson, A.J.C. Scherrer after Sixty Years: A Survey and Some New Results in the Determination of Crystallite Size. *J. appl. Cryst.* 1978, *11*, 102–113.
(87) Botan, A.; Ulm, F.-J.; Pellenq, R. J.-M.; Coasne, B. Bottom-up model of adsorption and transport in multiscale porous media. *Physical review. E, Statistical, nonlinear, and soft matter physics* 2015, *91*, 32133.
(88) Mendes, P. S. F.; Taleb, A.-L.; Gay, A.-S.; Daudin, A.; Bouchy, C.; Silva, J. M.; Ribeiro, M. F. Nanoscale insights into Pt-impregnated mixtures of zeolites. *J. Mater. Chem. A* 2017, *5*, 16822–16833.
(89) Weyland, M.; Midgley, P. A. Electron tomography. *Materials Today* 2004, *7*, 32–40.
(90) Sing, K. S. W.; Everett, D. H.; Haul, R. A. W.; Moscou, L.; Perotti, R. A.; Rouquerol, J.; Siemieniewska,T. Reporting physisorption data for gas/solid systems. *Pure & App. Chem.* 1985, *57*, 603–619.
(91) Benamor, T.; Vidal, L.; Lebeau, B.; Marichal, C. Influence of synthesis parameters on the physico-chemical characteristics of SBA-15 type ordered mesoporous silica. *Microporous and Mesoporous Materials* 2012*, 153*, 100–114.
(92) Garcia-Martinez, J.; Xiao, C.; Cychosz, K. A.; Li, K.; Wan, W.; Zou, X.; Thommes, M. Evidence of Intracrystalline Mesostructured Porosity in Zeolites by Advanced Gas Sorption, Electron Tomography and Rotation Electron Diffraction. *Chem. Cat. Chem.* 2014, *6*, 3110–3115.
(93) Thommes, M.; Mitchell, S.; Pérez-Ramírez, J. Surface and Pore Structure Assessment of Hierarchical MFI Zeolites by Advanced Water and Argon Sorption Studies. *J. Phys. Chem. C,* 2012, *116*, 18816–18823.
(94) Galarneau, A.; Cambon, H.; Di Renzo, F.; Fajula, F. True Microporosity and Surface Area of Mesoporous SBA-15 Silicas as a Function of Synthesis Temperature. *Langmuir* 2001, *17*, 8328–8335.
(95) Ravikovitch, P. I.; Neimark, A. V. Characterization of Micro- and Mesoporosity in SBA-15 Materials from Adsorption Data by the NLDFT Method. *J. Phys. Chem. B,* 2001*, 105*, 6817–6823.
(96) Thommes, M. Physical Adsorption Characterization of Nanoporous Materials. *Chemie Ingenieur Technik,* 2010, *82*, 1059–1073.
(97) Cychosz, K. A.; Guillet-Nicolas, R.; García-Martínez, J.; Thommes, M. Recent advances in the textural characterization of hierarchically structured nanoporous materials. *Chemical Society reviews,* 2017*, 46*, 389–414.
(98) Coasne, B.; Galarneau, A.; Gerardin, C.; Fajula, F.; Villemot, F. Molecular Simulation of Adsorption and Transport in Hierarchical Porous Materials. *Langmuir* 2013, *29*, 7864–7875.
(99) Monson, P. A. Understanding adsorption/desorption hysteresis for fluids in mesoporous materials using simple molecular models and classical density functional theory. *Microporous and Mesoporous Materials* 2012*, 160*, 47–66.
(100) Coasne, B. Multiscale adsorption and transport in hierarchical porous materials. *New J. Chem.* 2016, *40*, 4078–4094.
(101) Harkins, W. D.; Jura, G. An Absolute Method for the Determination of the Area of a Finely Divided Crystalline Solid. *J. Am. Chem. Soc.* 1944, *66*, 1366–1368.
(102) Galarneau, A.; Villemot, F.; Rodriguez, J.; Fajula, F.; Coasne, B. Validity of the t-plot Method to Assess Microporosity in Hierarchical Micro/Mesoporous Materials. *Langmuir* 2014, *30*, 13266–13274.

(103) Remy, M. J.; Poncelet, G. A New Approach to the Determination of the External Surface and Micropore Volume of Zeolites from the Nitrogen Adsorption Isotherm at 77 K. *J. Phys. Chem.* 1995, *99*, 773–779.
(104) Dubinin, M. M. The Potential Theory of Adsorption of Gases and Vapors for Adsorbents with Energetically Nonuniform Surfaces. *Chemical Society reviews* 1960, *60,* 235-241.
(105) Kenvin, J.; Jagiello, J.; Mitchell, S.; Pérez-Ramírez, J. Unified method for the total pore volume and pore size distribution of hierarchical zeolites from argon adsorption and mercury intrusion. *Langmuir : the ACS journal of surfaces and colloids* 2015, *31*, 1242–1247.
(106) Barrett, E. P.; Leslie G. Joyner, L. G.; Halenda, P. P. The Determination of Pore Volume and Area Distributions in Porous Substances. I. Computations from Nitrogen Isotherms. *J. Am. Chem. Soc.* 1951, *73*, 373–380.
(107) Groen, J. C.; Peffer, L.A.A.; Pérez-Ramírez, J. Incorporation of appropriate contact angles in textural characterization by mercury porosimetry. *Studies in Surface Science and Catalysis* 2002, *144*, 91–98.
(108) Groen, J. C.; Peffer, L. A.A.; Pérez-Ramírez, J. Pore size determination in modified micro- and mesoporous materials. Pitfalls and limitations in gas adsorption data analysis. *Microporous and Mesoporous Materials* 2003, *60*, 1–17.
(109) Zečević, J.; Gommes, C. J.; Friedrich, H.; de Jongh, P. E.; de Jong, K. P. Mesoporosity of zeolite Y: quantitative three-dimensional study by image analysis of electron tomograms. *Angewandte Chemie (International ed. in English)* 2012, *51*, 4213–4217.
(110) Milina, M.; Mitchell, S.; Crivelli, P.; Cooke, D.; Pérez-Ramírez, J. Mesopore quality determines the lifetime of hierarchically structured zeolite catalysts. *Nat Commun* 2014, *5*, 17.
(111) Mitchell, S.; Pinar, A. B.; Kenvin, J.; Crivelli, P.; Kärger, J.; Pérez-Ramírez, J. Structural analysis of hierarchically organized zeolites. *Nature communications* 2015, *6*, 8633.
(112) Tompsett, G. A.; Krogh, L.; Griffin, D. W.; Conner, W. C. Hysteresis and scanning behavior of mesoporous molecular sieves. *Langmuir: the ACS journal of surfaces and colloids* 2005, *21*, 8214–8225.
(113) Coasne, B.; Galarneau, A.; Pellenq, R. J. M.; Di Renzo, F. Adsorption, intrusion and freezing in porous silica: the view from the nanoscale. *Chemical Society reviews* 2013, *42*, 4141–4171.
(114) Coasne, B.; Gubbins, K. E.; Pellenq, R. J.-M. Domain theory for capillary condensation hysteresis. *Phys. Rev. B* 2005, *72*, 1726.
(115) *Characterization of Porous Solids and Powders: surface area, pore size and density*; Lowell S.; Shields J. E.; Thomas M. A.; Thommes M., Eds., 4 th; Kluwer Academic Publishers, 2004.
(116) Kenvin, J.; Mitchell, S.; Sterling, M.; Warringham, R.; Keller, T. C.; Crivelli, P.; Jagiello, J.; Pérez-Ramírez, J. Quantifying the Complex Pore Architecture of Hierarchical Faujasite Zeolites and the Impact on Diffusion. *Adv. Funct. Mater.* 2016, *26*, 5621–5630.
(117) Rasmussen, C. J.; Vishnyakov, A.; Thommes, M.; Smarsly, B. M.; Kleitz, F.; Neimark, A. V. Cavitation in metastable liquid nitrogen confined to nanoscale pores. *Langmuir : the ACS journal of surfaces and colloids* 2010*, 26*, 10147–10157.
(118) Lippmaa, E.; Magi, M.; Samoson, A.; Tarmak, M.; Engelbardt, G. Investigation of the Structure of Zeolites by Solid-state High-Resolution 29Si NMR Spectroscopy. *J. Am. Chem. Soc.* 1981, *103*, 4992–4996.
(119) Korányi, T. I. Distribution of Aluminum in the Periodical Building Units of Faujasites. *J. Phys. Chem. C* 2007*, 111*, 2520–2524.
(120) Yan, Z.; Ma, D.; Zhuang, J.; Liu, X.; Han, X.; Bao, X.; Chang, F.; Xu, L.; Liu, Z. On the acid-dealumination of USY zeolite: a solid state NMR investigation. *Journal of Molecular Catalysis A: Chemical* 2003, *194*, 153–167.

(121) Kawai, T.; Tsutsumi, K. A Study on the Surface Silanol Groups Developed by Hydrothermal and Acid Treatment of Faujasite Type Zeolites. *Journal of Colloid and Interface Science* 1999, *212*, 310–316.
(122) Jentys, A.; Tanaka, H.; Lercher, J. A. Surface Processes during Sorption of Aromatic Molecules on Medium Pore Zeolites. *J. Phys. Chem. B* 2005, *109*, 2254–2261.
(123) Karge, H. G. Characterization by infrared spectroscopy. *Microporous and Mesoporous Materials* 1998, *22*, 547–549
(124) Fritz, P. The effect of sodium poisoning on dealuminated Y-type zeolites. *Journal of Catalysis* 1989, *118*, 85–98.
(125) Khabtou, S.; Chevreau, T.; Lavalley, J. C. Quantitative infrared study of the distinct acidic hydroxyl groups contained in modified Y zeolites. *Microporous Materials* 1994, *3*, 133–148.
(126) Mfoumou, C. M.; Mignard, S.; Belin, T. The preferential adsorption sites of H2O on adsorption sites of CO2 at low temperature onto NaX and BaX zeolites. *Adsorption Science & Technology,* 2018, *36,* 1246–1259.
(127) Murray, D. K. Differentiating and characterizing geminal silanols in silicas by 29Si NMR spectroscopy. *Journal of Colloid and Interface Science* 2010, *352*, 163–170.
(128) Yan, X.; Komarneni, S.; Yan, Z. CO2 adsorption on Santa Barbara Amorphous-15 (SBA-15) and amine-modified Santa Barbara Amorphous-15 (SBA-15) with and without controlled microporosity. *Journal of Colloid and Interface Science* 2013, *390*, 217–224.
(129) Polanyi, M. Theories of the adsorption of gases. A general survey and some additional remarks. *Trans. Faraday Soc.,* 1932, *28*, 316–333.
(130) Jeong, H.; Kim, Y.; Lee, Y.; Kang, M. Control of acidity on the external surface of zeolite Y for m-xylene isomerization using a mechanochemical neutralization method. *Korean J. Chem. Eng.* 2009, *26,* 371–376.
(131) Mellot, C. Caracterisation structurale de l'adsorption des isomeres para- et meta- du xylene dans des zeolithes de type X., ENS ULM-SEVRES, Universite Pierre et Marie Curie- Paris VI et IFPEN, 1993.
(132) Tanaka, S.; Fujita, K.; Miyake, Y.; Miyamoto, M.; Hasegawa, Y.; Makino, T.; van der Perre, S.; Cousin Saint Remi, J.; van Assche, T.; Baron, G. V.; Denayer, J.F.M.Adsorption and Diffusion Phenomena in Crystal Size Engineered ZIF-8 MOF. *J. Phys. Chem. C,* 2015*, 119*, 28430–28439.
(133) Bourasseau, E.; Ungerer, P.; Boutin, A. Prediction of Equilibrium Properties of Cyclic Alkanes by Monte Carlo SimulationNew Anisotropic United Atoms Intermolecular PotentialNew Transfer Bias Method. *J. Phys. Chem. B*, 5483–5491.
(134) Dassault Systèmes. *Materials Studio*; Dassault Systèmes BIOVIA: San Diego.
(135) Nieto-Draghi, C.; Bonnaud, P.; Ungerer, P. Anisotropic United Atom Model Including the Electrostatic Interactions of Methylbenzenes. I. Thermodynamic and Structural Properties. *J. Phys. Chem. C* 2007, *111*, 15686–15699.
(136) Peralta, D.; Barthelet, K.; Pérez-Pellitero, J.; Chizallet, C.; Chaplais, G.; Simon-Masseron, A.; Pirngruber, G. D. Adsorption and Separation of Xylene Isomers: CPO-27-Ni vs HKUST-1 vs NaY. *J. Phys. Chem. C* 2012, *116*, 21844–21855.
(137) Pascual, P.; Ungerer, P.; Tavitian, B.; Pernot, P.; Boutin, A. Development of a transferable guest–host force field for adsorption of hydrocarbons in zeolites: I. Reinvestigation of alkane adsorption in silicalite by grand canonical Monte Carlo simulation. *Phys. Chem. Chem. Phys.* 2003, *5*, 3684–3693.
(138) Smith, D. E.; Dang, L. X. Computer simulations of NaCl association in polarizable water. *The Journal of Chemical Physics* 1994, *100*, 3757–3766.

(139) Maurin, G.; Llewellyn, P.; Poyet, T.; Kuchta, B. Influence of extra-framework cations on the adsorption properties of X-faujasite systems: Microcalorimetry and molecular simulations. *The journal of physical chemistry. B* 2005, *109*, 125–129.
(140) Crabtree, J. C.; Molinari, M.; Parker, S. C.; Purton, J. A. Simulation of the Adsorption and Transport of CO2 on Faujasite Surfaces. *J. Phys. Chem. C* 2013, *117*, 21778–21787.
(141) Purton, J. A.; Crabtree, J. C.; Parker, S. C. DL_MONTE: A general purpose program for parallel Monte Carlo simulation. *Molecular Simulation* 2013, *39*, 1240–1252.
(142) Rappe, A. K.; Casewit, C. J.; Colwell, K. S.; Goddard, W. A.; Skiff, W. M. UFF, a full periodic table force field for molecular mechanics and molecular dynamics simulations. *J. Am. Chem. Soc.* 1992, *114*, 10024–10035.

Annex 1

Flow diagram of the saturator coupled to the thermobalance.

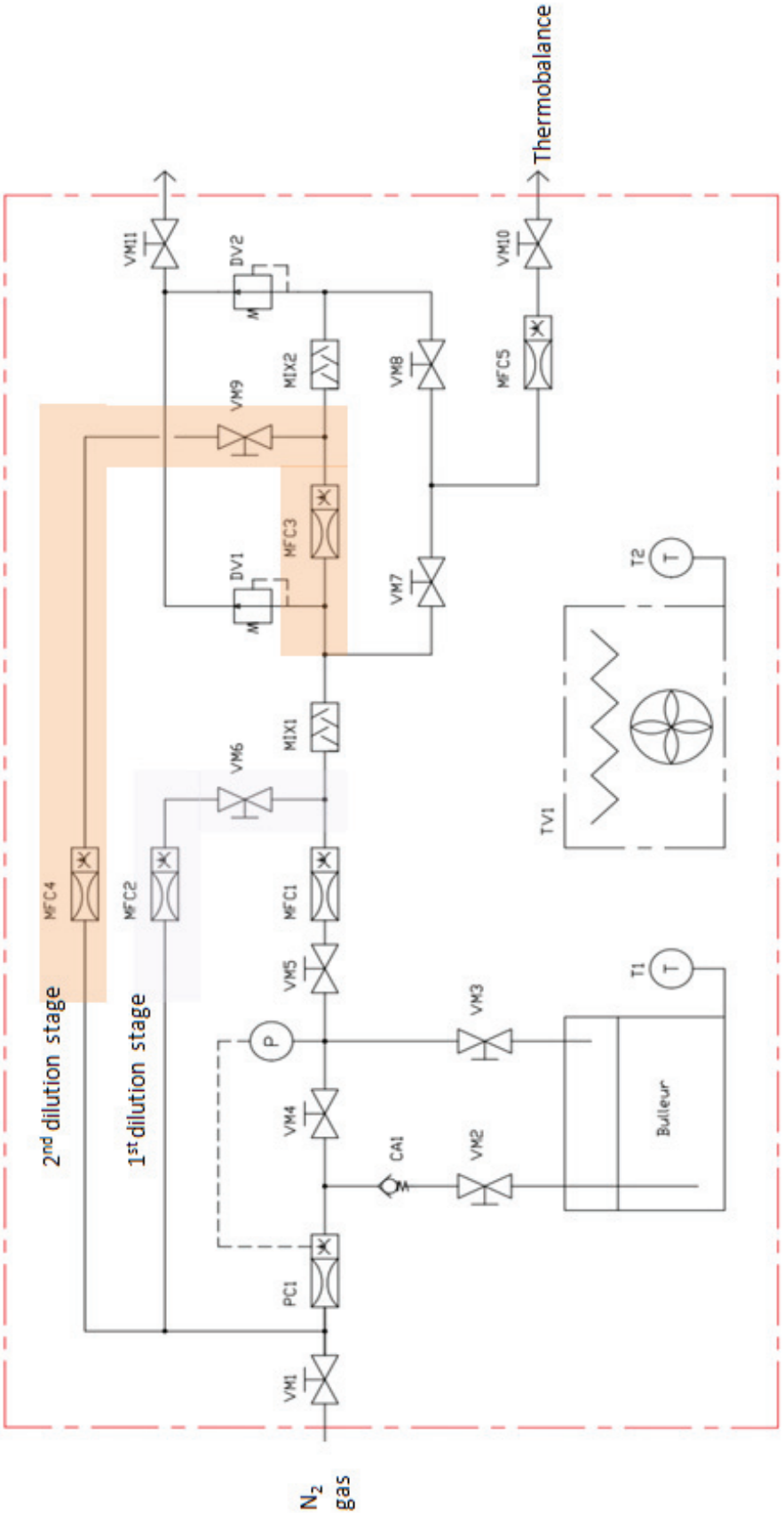

Annex 2

The decomposition of the ^{1}H MAS spectra, using the *dmfit* software, gives direct access to the quantity of the different species. Since the sequence used is not a quantitative, the different percentages are only for comparison purposes. The presence of a very broad signal in all spectra, which corresponds to the background, was observed. This signal was not considered for the calculations of the relative intensities of each signal. Nevertheless, its presence can impact the results obtained. (a) Conventional, (b) NA-1, (c) NA-2, (d) NA-3 and (e) LL.

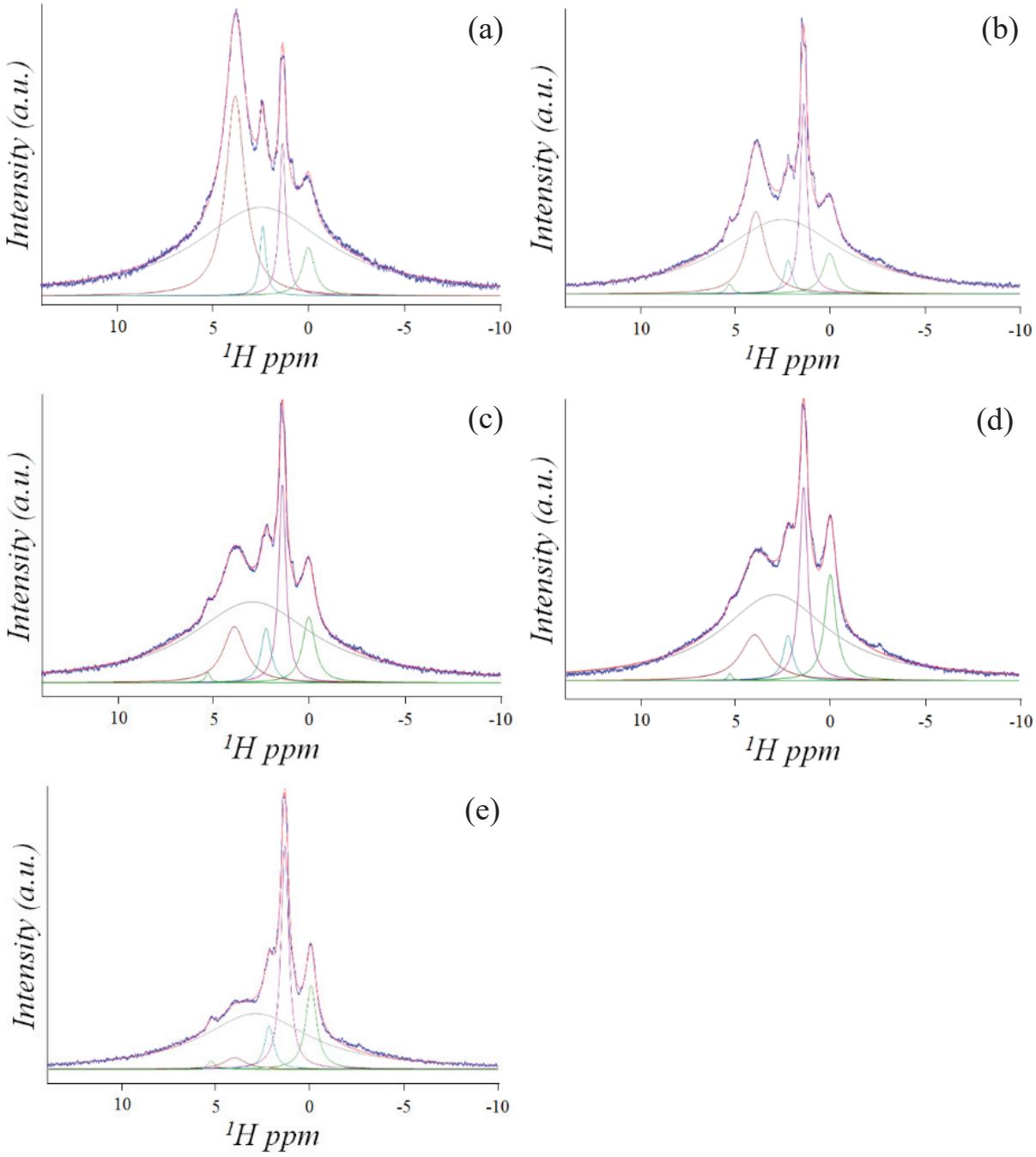

Annex 3

Deconvolution of the IR spectra bands for NaX zeolites. The deconvoluted peaks are represented in green and the sum of the contributions in red that fits well the experimental curve (black). The deconvolution was done by using Indigo software « plug im! » an open access and customizable software for signal and image processing. https://www.plugim.fr.

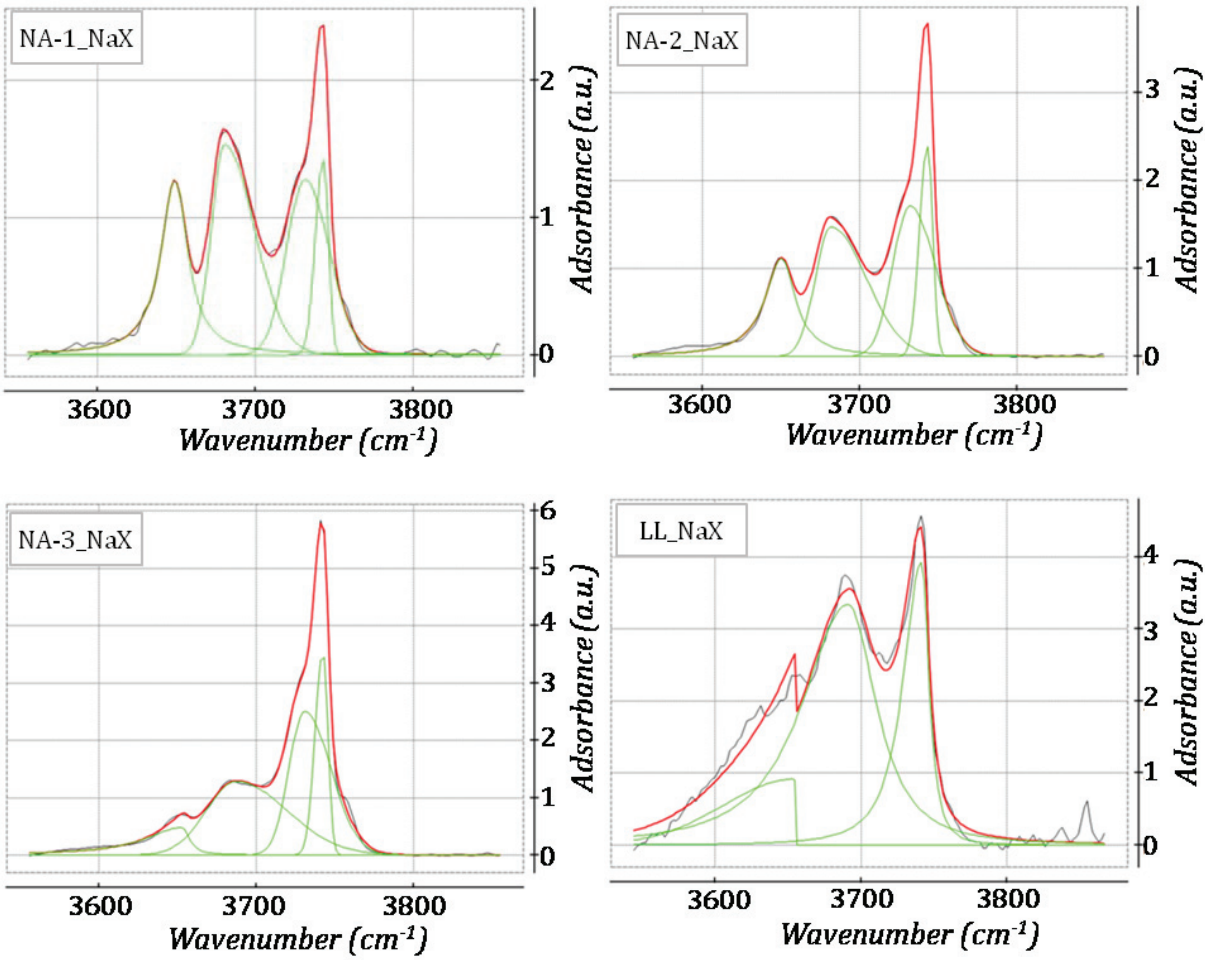

Annex 4

Deconvolution of the IR spectra bands for BaX zeolites. The deconvoluted peaks are represented in green and the sum of the contributions in red that fits well the experimental curve (black). The deconvolution was done by using Indigo software « plug im! » an open access and customizable software for signal and image processing. https://www.plugim.fr.

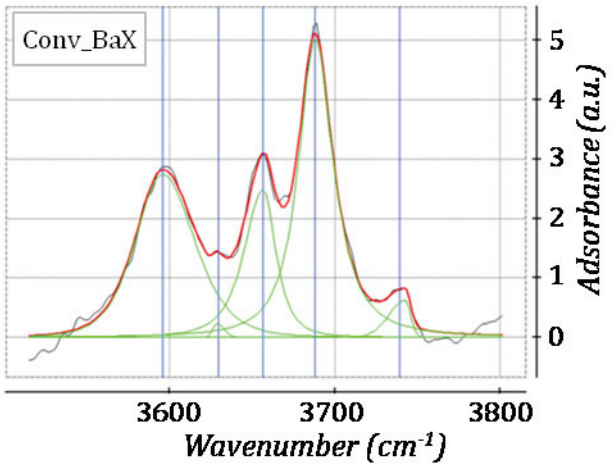

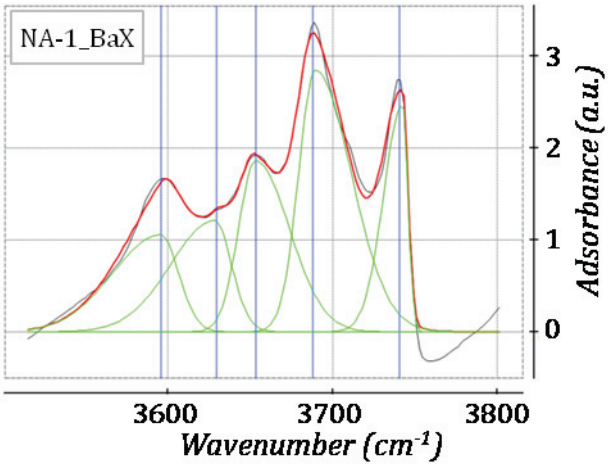

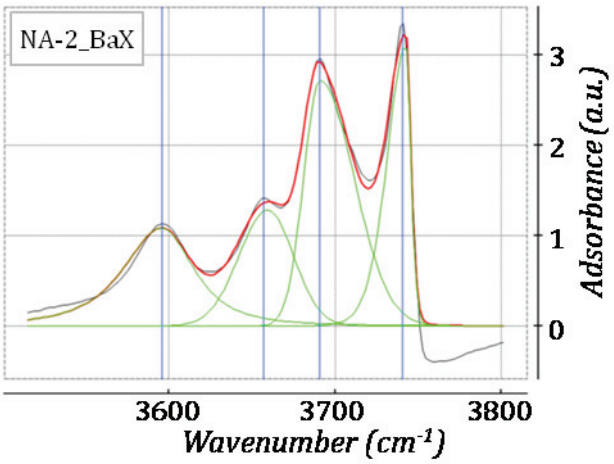

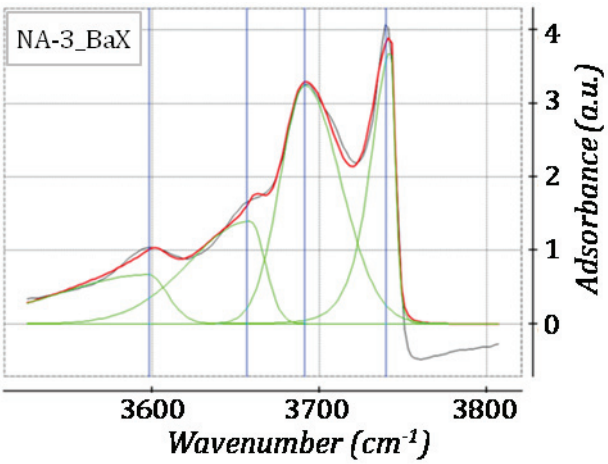

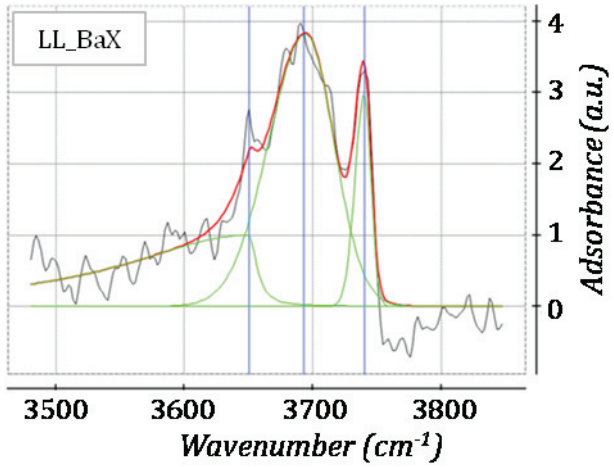

Annex 5

The following curves are the result of successive breakthrough tests (*x axis*). The analyzed solids are the conventional hierarchical zeolites NA-2 (purple) and NA-3 (blue). All zeolites were shaped with kaolin and sieved to a size between 375 and 500 µm. Analyses were performed at 50°C and the solvent used was *paradiethylbenzene*. The feed used was *px/ox/nC10* or *px/mx/nC10* (45%/45%/10%). As can be observed, the volume of micropores in the hierarchical zeolites is reduced after the second test. The micropore volume probed by xylene reaches a minimum of 0.03cm^3/g for NA-3 zeolite and 0.04cm^3/g for NA-2 zeolite. Such a decrease appears to be caused by blocking of the pore entries of the adsorbent. Taking into account the immersion calorimetry analyses (where hierarchical samples acquired a yellow color after test), it may be suggested that pore blocking is being caused by a surface reaction. Such a reaction generates the deposition of condensed aromatic compounds on the surface and causes the blockage of pores entries.

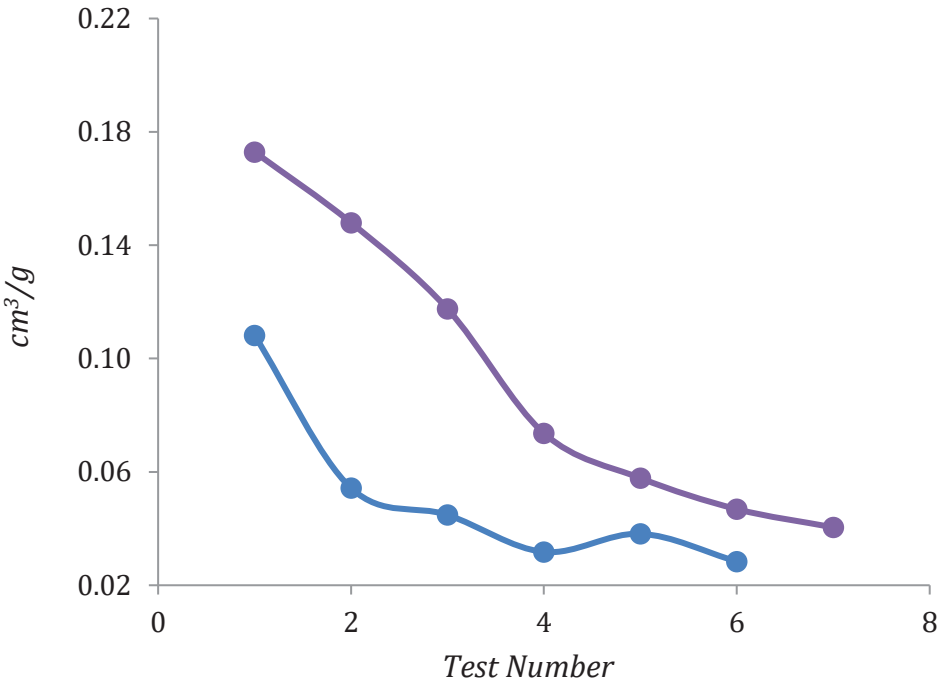

Annex 6

The graph below shows two experiments performed in a batch test for a conventional BaX zeolite. The different experiments can be distinguished by the symbol (square or triangle). The tests were performed simultaneously under the same conditions. The zeolite was also activated under the same conditions and therefore in both analyses the zeolite shows the same LOI of 4.98%. The orange color represents the adsorption of *ox*, blue represents adsorption of *px* and black is the sum of both isomers. As can be observed, the repeatability of the experimental data is good. However, for the last experimental point the analyses indicate a less precise value with respect to the quantity of *ox*, which can vary around 15%.